

**EFFECT OF RANDOM ANISOTROPY ON MAGNETIZATION  
REVERSAL IN CONTINUOUS AND DISCONTINUOUS THIN  
FILMS**

*By*

**NIRU CHOWDHURY**

**(Enrolment No. PHYS11201004013)**

**NATIONAL INSTITUTE OF SCIENCE EDUCATION AND  
RESEARCH BHUBANESWAR**

*A thesis submitted to the*

*Board of Studies in Physical Sciences*

*In partial fulfillment of requirements*

*For the Degree of*

**DOCTOR OF PHILOSOPHY**

*of*

**HOMI BHABHA NATIONAL INSTITUTE**



**June, 2016**

# Homi Bhabha National Institute

## Recommendations of the Viva Voce Board

As members of the Viva Voce Board, we certify that we have read the dissertation prepared by Niru Chowdhury entitled "Effect of random anisotropy on magnetization reversal in continuous and discontinuous thin films" and recommend that it may be accepted as fulfilling the dissertation requirement for the Degree of Doctor of Philosophy.



Date: 8/12/2016

Chairman - Dr. Bedangadas Mohanty



Date: 08/12/2016

Guide - Dr. Subhankar Bedanta



Date: 08/12/16

External- Dr. Anjan Barman



Date: 08/12/2016

Member - Dr. Kartikeswar Senapati



Date: 08/12/2016

Member - Dr. Pratap Kumar Sahoo

Final approval and acceptance of this dissertation is contingent upon the candidate's submission of the final copies of the thesis to HBNI.

I hereby certify that I have read this thesis prepared under my direction and recommend that it may be accepted as fulfilling the thesis requirement.

Date: 08/12/2016



Place: NISER, Bhubaneswar

Dr. Subhankar Bedanta  
(Thesis Supervisor)

## **STATEMENT BY AUTHOR**

This dissertation has been submitted in partial fulfillment of requirements for an advanced degree at Homi Bhabha National Institute (HBNI) and is deposited in the Library to be made available to borrowers under rules of the HBNI.

Brief quotations from this dissertation are allowable without special permission, provided that accurate acknowledgment of the source is made. Requests for permission for extended quotation from or reproduction of this manuscript in whole or in part may be granted by the Competent Authority of HBNI when in his or her judgment the proposed use of the material is in the interests of scholarship. In all other instances, however, permission must be obtained from the author.

**(Niru Chowdhury)**

## **DECLARATION**

I, hereby declare that the investigation presented in the thesis has been carried out by me. The work is original and has not been submitted earlier as a whole or in part for a degree / diploma at this or any other Institution / University.

**(Niru Chowdhury)**

## List of Publications arising from the thesis

### Journal:

1. “Study of magnetization reversal processes in a thin Co film”, **N. Chowdhury**, S. Bedanta and G. S. Babu, *J. Magn. Magn. Mat.*, **2013**, 336, 20–25.
2. “Effect of inter-particle interactions in magnetic nanoparticle ensembles”, S. Bedanta, **N. Chowdhury**, and W. Kleemann, *Sensor Letters*, **2013**, 11, 1-8.
3. “Controlling the anisotropy and domain structure with oblique deposition and substrate rotation”, **N. Chowdhury** and S. Bedanta, *AIP Advances*, **2014**, 4, 027104-1- 6.
4. “Controlling the size and relaxation dynamics of superferromagnetic domains”, **N. Chowdhury**, S. Bedanta, S. Sing and W. Kleemann, *J. Appl. Phys*, **2015**, 117, 153907-1-5.
5. “Study of magnetization relaxation in Co thin films prepared by substrate rotation”, **N. Chowdhury**, S. Mallick, S. Mallik and S. Bedanta, *Thin Solid Films*, **2016**, 616, 328-334.

### Conference Proceedings:

1. “Magnetization reversal study along easy and hard axes in a superferromagnet”, S. Bedanta, **N. Chowdhury** and S. Sing, *AIP Conf. Proc.*, **2012**, 1461, 98-103.

### Others:

1. “Interplay of uniaxial and cubic anisotropy in epitaxial Fe thin films on MgO (001) substrate”, S. Mallik, **N. Chowdhury** and S. Bedanta, *AIP Advances*, **2014**, 4, 097118-1-6.

### Manuscripts in preparation:

1. “Effect of dipolar coupling on domains in Co/AlO<sub>x</sub>/Co trilayers”, **N. Chowdhury**, S. Bedanta, G. S. Babu, A. Weber, T. Brückel, and M. K. Dalai.
2. “Occurrence of 360° domain walls: a competing effect of uniaxial and random anisotropy”, S. Bedanta, **N. Chowdhury**, O. Petravic, W. Kleemann, F. Kronast, A. Doran, A. Scholl, S. Cardoso, and P. P. Freitas.

(Niru Chowdhury)

**Dedicated to my mother**

## ACKNOWLEDGEMENTS

At the very outset I would like to express my deep and sincere gratitude to my thesis advisor Dr. Subhankar Bedanta for his continuous support, motivation, and guidance throughout my Ph.D. He was always there to improve my understanding of the subject matter, suggesting way out of the problems. His wide knowledge, logical way of thinking along with his scientific temper has been a great value to me. His inspiration, understanding, faith and encouragement have kept me going throughout the tenure. I would be eternally indebted for his motivations, timely advice, insightful discussions and suggestions which helped me shape the thesis.

I would also like to thank Dr. Gunda Santosh Babu for his scientific advices, guidance and discussion throughout the project.

My special thanks to all my labmates – Srijani, Sougata, Sukanata, Sagarika for their continuous help and support. The work place would not have been refreshing without them. I would also acknowledge Dr. Sudhanu Sekar Das and Dr. Braj Bhusan Singh for their kind elderly advices and help.

I duly acknowledge DST-DAAD for their funding to carry out the polarized neutron reflectivity measurements. I am thankful to Prof. Thomas Brückel for his collaboration and discussions. Having said this, I would like to express my heartfelt gratitude to Dr. Alexander Weber for his help and scientific discussion in the polarized neutron reflectivity and SQUID measurements. I am also grateful to Alexandra Steffen for her help in X-ray reflectivity measurements.

I acknowledge Prof. P. V. Satyam, Ashutosh Rath and Raghevendra Rao Juluri, I.O.P Bhubaneswar for their kind and sincere help in performing cross-sectional transmission electron microscopy.

I am thankful to Dr. Manas Dalai, National Physical Laboratory, New Delhi for secondary ion mass spectroscopy measurements and valuable discussions.

I am grateful to Mr. Vanarajsinh J. Solanki and Prof. Shikha Varma for their help in atomic force microscopy (AFM) measurements until the AFM in NISER was installed.

I thank Mr. Sovakara Sing for his technical help in preparation of samples, opening and maintenance of the multi-deposition preparation chamber.

I am also thankful to the summer students Swapna Sindhu Mishra and Debiprasad Pattnaik for their help in learning the OOMMF installations and commands. It was a pleasant experience to work with Ankur Das for MOKE calculations in Mathematica.

I would also like to thank my Doctoral Committee members Dr. Kartikeswar Senapati and Dr. Pratap Kumar Sahoo for their evaluation and feedbacks on the project. I would take this

opportunity to thank Dr. Bedangadas Mohanty Chairperson, School of Physical Sciences for his ever inspiring words.

Very special thanks to NISER and DAE for providing me this opportunity, infrastructure support and funding during the entire span of the research.

Finally, I would like to thank my family and friends (Sushree, Sanjima, Gargi, Prachi, Niladri, Pratibha) for their unconditional support and care. A special thanks goes to Mr. Sidhartha Rout for his continuous care and support all the way along the journey.

**Niru Chowdhury**

# CONTENTS

<b>STATEMENT BY AUTHOR</b> .....	i
<b>DECLARATION</b> .....	ii
<b>List of Publications arising from the thesis</b> .....	iii
<b>DEDICATIONS</b> .....	<b>Error! Bookmark not defined.</b>
<b>ACKNOWLEDGEMENTS</b> .....	v
<b>CONTENTS</b> .....	vii
<b>SYNOPSIS OF Ph. D. THESIS</b> .....	x
<b>LIST OF FIGURES</b> .....	xv
<b>LIST OF TABLES</b> .....	xxiii
<b>List of Abbreviations</b> .....	xxiv
<b>Chapter 1 : Introduction and fundamentals</b> .....	1
<b>1.1 Introduction:</b> .....	1
<b>1.2 Fundamentals:</b> .....	6
1.2.1 Exchange energy: .....	6
1.2.2 Magnetostatic or demagnetization energy: .....	7
1.2.3 Magnetic anisotropy: .....	9
1.2.4 Zeeman energy (External magnetic field):.....	16
<b>1.3 Magnetic domains and domain walls:</b> .....	17
<b>1.4 Magnetization reversal:</b> .....	23
1.4.1 Coherent rotation (Stoner-Wohlfarth model): .....	25
1.4.2 Reversal by domain wall motion:.....	27
<b>1.5 Inverted thin films:</b> .....	28
<b>1.6 Magnetization dynamics:</b> .....	29
<b>Chapter 2 : Experimental Techniques</b> .....	31

<b>2.1</b>	<b>Thin Film Deposition techniques:</b> .....	31
2.1.1	Sputtering: .....	32
2.1.2	Sample preparation using magnetron sputtering at NISER: .....	36
<b>2.2</b>	<b>Atomic Force Microscopy (AFM):</b> .....	38
<b>2.3</b>	<b>Secondary Ion Mass Spectroscopy (SIMS):</b> .....	41
<b>2.4</b>	<b>X-Ray Reflectivity (XRR):</b> .....	44
<b>2.5</b>	<b>Cross-section Transmission Electron Microscope (TEM):</b> .....	48
<b>2.6</b>	<b>Superconducting Quantum Interference Device (SQUID) magnetometer:</b> .....	49
<b>2.7</b>	<b>Magneto- Optic Kerr Effect (MOKE) fundamentals-</b> .....	51
2.7.1	MOKE Geometries: .....	54
2.7.2	MOKE magnetometer set up: .....	54
2.7.3	Magneto – optic Kerr effect microscopy: .....	58
<b>2.8</b>	<b>Polarized Neutron Reflectivity (PNR):</b> .....	61
2.8.1	Introduction: .....	61
2.8.2	Neutron scattering:.....	62
2.8.3	Reflectometer instrument: .....	66
<b>Chapter 3 : Magnetization reversal and relaxation dynamics in Co thin film</b> .....		69
<b>3.1</b>	<b>Introduction:</b> .....	69
<b>3.2</b>	<b>Sample preparation:</b> .....	72
<b>3.3</b>	<b>Results and discussion:</b> .....	73
3.3.1	Magnetization reversal in AlO <sub>x</sub> (3 nm)/Co (3.5nm)/AlO <sub>x</sub> (3 nm):.....	73
3.3.2	Magnetization reversal in Co (10 nm) thin films with oblique deposition and substrate rotation: 79	
<b>3.4</b>	<b>Conclusion-</b> .....	98
<b>Chapter 4 : Study of magnetization reversal in dipolarly coupled Co/AlO<sub>x</sub> multilayers</b>		
.....		100
<b>4.1</b>	<b>Introduction:</b> .....	100
<b>4.2</b>	<b>Sample preparation and experimental techniques:</b> .....	101
<b>4.3</b>	<b>Structural Characterization:</b> .....	102
<b>4.4</b>	<b>Magnetic Properties:</b> .....	105
4.4.1	Magnetization reversal of Co (10nm) single layer:.....	105
4.4.2	Study of magnetization reversal for Co (10 nm)/AlOX (t nm)/Co (10 nm) .....	107
<b>4.5</b>	<b>Conclusion-</b> .....	119
<b>Chapter 5 : Occurrence of 360° domain walls: a competing effect of uniaxial and random anisotropy</b> .....		120

<b>5.1</b>	<b>Introduction:</b> .....	120
<b>5.2</b>	<b>Sample Preparation:</b> .....	123
<b>5.3</b>	<b>Magnetization reversal and experimental observation of 360° DWs:</b> .....	124
<b>5.4</b>	<b>Micro-magnetic Simulations for 360° DWs along EA and HA:</b> .....	129
5.4.1	Micromagnetic simulations along EA: .....	129
5.4.2	Micromagnetic simulations along HA: .....	134
<b>5.5</b>	<b>Conclusion:</b> .....	136
<b>Chapter 6 : Controlling the size and relaxation dynamics of Superferromagnetic domains</b> .....		
<b>137</b>		
<b>6.1</b>	<b>Introduction:</b> .....	137
<b>6.2</b>	<b>Preparation for Superferromagnetic sample:</b> .....	141
<b>6.3</b>	<b>Angle dependent control of SFM domains:</b> .....	141
<b>6.4</b>	<b>Angle dependent magnetization relaxation in SFM –</b> .....	146
<b>6.5</b>	<b>Conclusion:</b> .....	150
<b>Chapter 7 : Summary and Outlook</b> .....		
<b>151</b>		
<b>Appendix</b> .....		
<b>155</b>		
<b>References</b> .....		
<b>156</b>		



# Homi Bhabha National Institute

## SYNOPSIS OF Ph. D. THESIS

- 1. Name of the Student: Niru Chowdhury**
- 2. Name of the Constituent Institution: National Institute of Science Education and Research, Bhubaneswar (NISER)**
- 3. Enrolment No. : PHYS11201004013**
- 4. Title of the Thesis: Effect of random anisotropy on magnetization reversal in continuous and discontinuous thin films.**
- 5. Board of Studies: Physical Sciences**

## SYNOPSIS

Magnetic thin films and nanostructures have been a subject of intense research for both physicists and engineers in last few decades. Within nanoscale, the materials can exhibit a great number of properties different from the ones in macroscale because of quantum size, quantum tunneling, and surface effects. Therefore, these systems can be tuned for various applications like data storage, magneto-resistive devices, magnetic sensing and magnetoelectronics. For optimizing the performance of these devices a better understanding of magnetization reversal, relaxation and domain structure is required. Similarly, the research on magnetic nanoparticles is quite vivid because it offers applications in various fields such as magnetic resonance imaging (MRI), hyperthermic treatment for malignant cells, site-specific drug delivery and manipulating cell membranes etc. Apart from applications, magnetic thin films are an excellent system for studying many fundamental physics such as magnetic domain and domain wall dynamics, inter-layer coupling etc.

A part of this thesis is devoted to understand the magnetization reversal for Co thin film having growth induced uniaxial anisotropy along with oblique deposition and substrate rotation ( $\omega$ ). For this purpose, Co films with 10 nm thickness have been prepared by sputtering with an oblique angle of incidence for 0, 10 and 20 rpm substrate rotations. Large grains in the form of chains were observed by atomic force microscopy (AFM) for 0 rpm substrate rotation. On increasing the substrate rotation, grain size gets reduced. Small correlated grains are observed for the film with 10 rpm substrate rotation whereas for the film with 20 rpm substrate rotation non-uniformly distributed island like structures were observed due to non-availability of sufficient time for the adatoms to relax. The average grain size of the sample with  $\omega = 0, 10$  and  $20$  rpm are  $138.9 \pm 11.7$  nm,  $23.4 \pm 1.2$  nm and  $38.5 \pm 1.2$  nm, respectively. The magnetization reversal was studied by magneto-optic Kerr effect (MOKE) based microscope in the longitudinal geometry. Strong uniaxial anisotropy with small misalignment of the local grain anisotropy was observed for Co (10 nm) thin film with  $\omega = 0$  rpm. The Co films prepared with  $\omega = 10$  and  $20$  rpm weakens the anisotropy but does not completely lead to isotropic films. However, rotation of substrates during thin film preparation increases the randomness in anisotropy. This dispersion in local anisotropy affects the domain structure. It was observed that rotation of substrate weakens the anisotropy and leads to high dispersion in local grain anisotropy resulting in ripple and labyrinth domains. For the inversion sector of the films, the magnetization was first observed by partial rotation which leads to the formation of ripple domains. Saturation of the sample was achieved by another type of large domains. The magnetization relaxation measurements were performed by negatively saturating the sample and then reversing the field to a positive constant applied magnetic field ( $H_M$ ) close to the coercive field ( $H_C$ ), where  $H_M/H_C \sim 0.995, 0.99, 0.985, \text{ and } 0.97$ . Keeping the magnetic field constant, the time evolution of domains were recorded. The constant magnetic field during magnetization relaxation implies the

constant Zeeman energy. Hence, effectively we observe the thermal energy activated magnetization reversal of the sample. The relaxation follows the Boltzmann fit for  $\omega = 0$  rpm indicating the effect of slow nucleation followed by fast domain wall motion under thermal activation energy. For  $\omega = 10$  rpm, the fast relaxation along easy axis (EA) followed the Fatuzzo-Labrune model (Single exponential function) indicating the nucleation dominated aftereffect followed by domain wall motion. For  $\omega = 20$  rpm, slow magnetization relaxation following double exponential function was observed. Hence, as the randomness in anisotropy increases, the reversal becomes slow and relaxation time increases.

However, the magnetization reversal and domain structure can be very different in multilayers compared to their single layer thin film. In magnetic multilayers where ferromagnetic layers (FM) are separated by non-magnetic layers (NM) i.e. [FM/NM/FM] can have different kind of interactions depending on the nature of non-magnetic spacer. For metallic spacers, depending on its thickness, exchange coupling shows oscillatory behavior due to Ruderman–Kittel–Kasuya–Yosida (RKKY) interactions. For insulating spacers, ferromagnetic layers (FM) will experience long-range dipolar interactions leading to an anti-parallel alignment of the magnetization of next nearest neighbors in the layers. It shows non-oscillatory monotonically decreasing behavior with increasing the insulating spacer thickness. We have studied the effect of dipolar coupling on [Co(10 nm)/AlO<sub>x</sub> (*t* nm)/Co(10 nm)] multilayers prepared on Si(100) substrates, where the thickness (*t*) of the insulating spacer (AlO<sub>x</sub>) has been varied from 3 to 270 nm. Uniaxial anisotropy with small random anisotropy was observed in all the samples. As mentioned earlier the uniaxial anisotropy was observed due to oblique deposition. Magneto-Optic Kerr Effect (MOKE) microscopy measurements showed double stepped hysteresis loops. Two different domain structures for the two Co layers were observed by MOKE microscopy even though were prepared under identical conditions. Interestingly, as the thickness of the spacer layer (AlO<sub>x</sub>) was increased, in

addition to longitudinal component, transverse magnetization has been observed. Hence to know the magnetization depth profile of the multilayer system, polarized neutron reflectivity (PNR) measurements were performed at TREFF reflectometer in Munich. PNR measurements indicate anti-parallel alignment of the two Co layers at the coercivity where the magnetization of the bottom Co layer first reverses. To understand the experimental observations, micromagnetic simulations were performed using Object Oriented Micromagnetic Framework (OOMMF) for Co(10 nm)/AlO<sub>x</sub>( $t$  nm)/Co(10 nm) with  $t = 3, 8$  and 90 nm. In these simulations, addition of small random anisotropy with uniaxial anisotropy lead to layer-by-layer reversal of magnetization and change in domain structure was observed confirming our observed experimental results.

Magnetization reversal in thin films can occur via two processes - formation of domains or coherent rotation. Domain formation depends on minimization of various energy factors such as exchange energy, magnetostatic energy, or crystalline anisotropy energy. Among various types of domain walls the observation of 360° domain walls (DWs) is rare. These walls separate the adjacent domains with parallel magnetization. A part of the thesis is devoted in understanding of the observed 360° DWs in [Co<sub>80</sub>Fe<sub>20</sub> (1.8 nm)/Al<sub>2</sub>O<sub>3</sub> (3 nm)]<sub>9</sub> by X-ray photoemission electron microscopy (XPEEM) and MOKE microscopy. Along EA, the 360° DWs were formed when two 180° DWs of opposite chirality merges. The domain walls are quite stable and required high magnetic field for annihilation. Along hard axis (HA), the coherent rotation of spins in opposite sense lead to the formation of 360° DWs. To understand the experimental observations, simulations were performed using OOMMF for [Co(1.8 nm)/Al<sub>2</sub>O<sub>3</sub>(3.6 nm)]<sub>2</sub>. Random anisotropy ( $K_r$ ) in addition to uniaxial anisotropy ( $K_u$ ) was incorporated in these simulations. We found that when random anisotropy is comparable to the uniaxial anisotropy, 360° DWs were formed by the combination of two 180° Néel walls along EA. These 360° DWs need a high magnetic field for annihilation as was observed

experimentally along EA. However, along HA, as the exchange energy could not outweigh the random anisotropy it breaks the symmetry of coherent rotation and leads to opposite sense of rotation in the nearby grains giving rise to the formation of  $360^\circ$  DWs. These results were successfully extended to the understanding of the 9 layers of  $[\text{Co}_{80}\text{Fe}_{20}$  (1.8 nm)/ $\text{Al}_2\text{O}_3$  (3 nm)] which mimics our real sample.

Further, a part of the thesis is devoted for understanding of magnetization reversal and relaxation for a discontinuous metal insulator multilayers (DMIM)  $[\text{Co}_{80}\text{Fe}_{20}$  (1.3 nm)/ $\text{Al}_2\text{O}_3$  (3 nm)]<sub>10</sub> showing superferromagnetic (SFM) state. SFM domain is similar to the ferromagnetic domain where the atomic spins are replaced by the superspins (net magnetic moment of the nanoparticles). Although such SFM domains have been observed by several groups but the understanding of the SFM domains and domain wall dynamics is still yet to be explored. In this thesis, we have studied the angular dependence of the magnetization reversal of SFM domains. Since, in addition to uniaxial anisotropy, the system has small random anisotropy, therefore, the ferromagnetic correlation strength decreases for directions away from the easy axis as evident from the reduction in domain size. By varying the angle ( $\theta$ ) between the magnetic field and the easy axis both domain sizes and shapes can be changed. The reversal process by magnetizing along the easy axis (EA) is governed via domain wall motion. However, upon approaching the hard axis (HA) at increasing  $\theta$  coherent rotation of superspins becomes the dominant process for the magnetization reversal. This leads to the reduction of domain size for increasing values of  $\theta$ . The relaxation of magnetization for various values of  $\theta$  revealed that the relaxation time increases with increasing  $\theta$ . The presence of small random anisotropy leads to compressed exponential behavior of the relaxation curves implying the presence of energy distribution barriers in magnetization reversal.

## LIST OF FIGURES

Figure 1.1: Schematic showing the GMR effect due to parallel and antiparallel alignment of magnetization of FM layers giving rise to low and high resistance, respectively. ....	2
Figure 1.2: Schematic of the stray field energy of a magnetic system. ....	7
Figure 1.3: Effect of shape anisotropy on the demagnetization energy when it is (a) perpendicular and (b) parallel to the film plane. ....	11
Figure 1.4: Schematic showing the oblique deposition geometry. The magnetrons in the multi-deposition unit used for thin film preparation of Co/AlO <sub>x</sub> series are at an angle of 30° w.r.t to the substrate normal (Figure 2.3). ....	14
Figure 1.5: Schematic showing the oblique deposition in which the incident beam at 60° from the right direction [5]. ....	15
Figure 1.6: Schematic representation of reduction of the magnetostatic energy by domain formation in a ferromagnet. ....	18
Figure 1.7: The schematic of (a) Bloch wall with spins rotating perpendicular and (b) Néel wall with spins rotating in-plane of the domain walls [20]. ....	21
Figure 1.8: Thickness dependence of energy of Bloch, Néel and cross tie walls [47]. ....	21
Figure 1.9: The schematic (a) 180° (b) 90° and (c) 360° DWs. ....	22
Figure 1.10: Schematic for spin orientation inside a 360° DW separating domains of parallel magnetization ....	22
Figure 1.11: Kerr microscopy domain images where domains are separated by (a) 180° [50], (b) 90° [51] and (c) 360° DWs [52] ....	23
Figure 1.12: A typical hysteresis loop showing the $M$ vs $H$ behavior of a ferromagnet. ....	24
Figure 1.13: Illustration of the coordinate system of a single domain particle for SW model. ....	26
Figure 1.14: Hysteresis curves for different $\phi$ (angle between applied magnetic field and easy axis) using SW model. ....	27
Figure 1.15: Schematic showing the precession and damping of magnetization vector. ....	30
Figure 2.1: Schematic for sputtering deposition technique. ....	33
Figure 2.2: Schematic showing the (a) balanced magnetron configuration and (b) unbalanced magnetron configuration [64]. ....	35
Figure 2.3: Outer view of the Multi-deposition UHV system at NISER procured from Mantis Deposition Ltd, U.K showing its various units. The 4 pocket e-beam evaporator is situated behind the Nanogen unit and hence is not visible. ....	36

Figure 2.4: Schematic of Atomic Force Microscopy (AFM).....	39
Figure 2.5: Graph showing the force of interaction between the tip and sample surface vs the distance between them [69].....	40
Figure 2.6: Schematic showing the effect of the bombardment of the primary beam on the sample. It produces neutral particles and secondary ions from the sample surface. Image adapted from [73]......	42
Figure 2.7: Schematic showing the components of SIMS [74]. .....	43
Figure 2.8: Scattering geometry for x-ray reflectivity. $\theta_i$ and $\theta_f$ are the angles of incidence and angle of reflection. $k_i$ and $k_r$ are the wave vectors of the incident and reflected beam. The momentum transfer vector is shown as $q$ . .....	45
Figure 2.9: Schematic showing the geometry of the pick-up coil of the SQUID. The graph on the right shows the theoretical behaviour of magnetic dipole with respect to sample length [81]. .....	50
Figure 2.10: Schematic of MOKE showing the formation of elliptically polarized light from the incident linearly s-polarized light. The minor and major axes of the ellipse has been marked as 'a' and 'b', respectively [85]. .....	52
Figure 2.11: Different geometries of MOKE: (a) Longitudinal, (b) Transverse, and (c) Polar mode.....	53
Figure 2.12: Schematic of MOKE magnetometer set up at NISER.....	55
Figure 2.13: Observation of magnetic domains using MOKE microscopy set up [21].....	58
Figure 2.14: Optical sketch of Kerr microscopy manufactured by Evico Magnetics Ltd., Germany [89]. .....	59
Figure 2.15: Schematic showing the scattering geometry for specular reflectivity of spin polarized neutron beam. For specular reflection angle of incidence is equal to angle of reflection ( $\alpha$ ).The y-direction is the non-spin-flip (quantization) axis for the neutrons and the x-direction is the spin-flip axis. The scattering vector $Q$ is parallel to the z-axis and perpendicular to the surface [92].....	62
Figure 2.16: Schematic of the reflectometer TREFF at neutron guide NL5-S, FRM II in Garching (Top view), F1 and F2 are the Flippers places before and after the sample respectively. P1 and P2 are the polarizer and analyser, respectively. [96] .....	67
Figure 3.1: Schematic of sample structure for $\text{AlO}_x$ (3 nm)/Co (10 nm)/ $\text{AlO}_x$ (3 nm) prepared by magnetron sputtering.....	72
Figure 3.2: XTEM image of Si (100)/ $\text{AlO}_x$ (3 nm)/Co (3.5 nm)/ $\text{AlO}_x$ (3 nm)/Co (3.5 nm)/ $\text{AlO}_x$ (3 nm).....	73

Figure 3.3: LMOKE hysteresis loops measurements performed for AlO<sub>x</sub> (3 nm)/Co (3.5 nm)/AlO<sub>x</sub> (3 nm) (a) EA, (b) 30° and (c) 60° and (d) HA at room temperature [109]. .....74

Figure 3.4: LMOKE domain images for AlO<sub>x</sub> (3 nm)/Co (3.5 nm)/AlO<sub>x</sub> (3 nm) along EA (A) – (D) and HA (E) – (H). The values of the magnetic field points are marked in Figure 3.3(a). .....74

Figure 3.5: Magnetic hysteresis for AlO<sub>x</sub> (3 nm)/Co (3.5 nm)/AlO<sub>x</sub> (3 nm) measured by SQUID magnetometer along the EA at 300, 250, 200, and 100 K, respectively.....75

Figure 3.6: Relaxation curve for AlO<sub>x</sub> (3 nm)/Co (3.5 nm)/AlO<sub>x</sub> (3 nm) measured at  $\mu_0H = -11.7$  mT. Images were taken by longitudinal MOKE and magnetic field was applied along EA. Images (b), (c), (d) and (e) corresponds to points 1, 2, 3 and 4 of Figure 3.6(a).....76

Figure 3.7: Magnetization relaxation curves for AlO<sub>x</sub> (3 nm)/Co (3.5 nm)/AlO<sub>x</sub> (3 nm) measured using LMOKE along EA for magnetic fields of -11.7 mT, -11.8 mT and -11.9 mT, respectively. The best fits yield  $\tau = 8.06, 4.87, \text{ and } 2.76$  s for measurements performed at  $\mu_0H_M = -11.7, -11.8, \text{ and } -11.9$  mT, respectively. ....77

Figure 3.8: Domain wall velocity vs the magnetic field for AlO<sub>x</sub> (3 nm)/Co (3.5 nm)/AlO<sub>x</sub> (3 nm) along EA at room temperature. The different modes of domain walls: creep, depinning and slide have been shown. The slide region has been fitted linearly and extrapolation to the field axis gives the depinning field. ....78

Figure 3.9: Surface topography imaged by atomic force microscopy for sample A (a), sample B (b), and sample C (c). All the images are in the same length scale which is shown in (a). 80

Figure 3.10: High resolution AFM image of sample B (a) and sample C (b).....81

Figure 3.11: Surface topography by AFM in tapping mode for Si/AlO<sub>x</sub> (3 nm) with  $\omega = 0, 10$  and  $20$  rpm shown in (a), (b), and (c), respectively. ....82

Figure 3.12: (a) Coercivity vs.  $\theta$  and (b)  $M_r/M_s$  vs.  $\theta$  for Sample A (red solid circles), Sample B (blue solid triangles) and Sample C (green solid stars) showing the uniaxial anisotropy behaviour.....82

Figure 3.13: Comparison of hysteresis loops measured along EA and HA by LMOKE at room temperature for sample A, B, and C shown in (a), (b) and (c) plots, respectively. ....85

Figure 3.14: Domain images for sample A, B and C are shown for  $\theta = 0^\circ$  (EA),  $30^\circ$ ,  $60^\circ$  and  $90^\circ$  (HA), respectively. The images are taken near the coercive fields for the respective angles and the samples. The Zoomed in image of the red dotted area in Figure 3.14(i) has been shown in Figure 3.15(a).....86

Figure 3.15: (a) zoomed-in image of the red area highlighted in Figure 3.14 is shown in the red box in (i) ( $60 \times 60 \mu\text{m}^2$ ), (b) and (c) are high resolution image ( $57 \times 52 \mu\text{m}^2$ ) for sample C along  $30^\circ$  and  $60^\circ$  w.r.t EA, respectively. ....87

Figure 3.16: (a) Hysteresis measured by LMOKE for sample C for  $\theta = 30^\circ$ . Domain images for the fields marked by points 1 to 8 in (a) are shown in (b) - (i), respectively. ....87

Figure 3.17: The schematic showing the fluctuations of magnetization for ripple domains (a) longitudinal and (b) transverse ripple. [59]. ....89

Figure 3.18: Hysteresis loops showing the magnetic fields (red dots) where the relaxation measurements have been performed for sample A (a), sample B (b), and sample C (c). ....89

Figure 3.19: Relaxation measurement by LMOKE microscope for sample A along EA. Figure (b) - (j) are domain images taken at 0, 4, 8, 10, 14, 21, 40, 92, 160 s at  $H_M = 8.2$  mT, marked by points 1 to 9 in Figure 3.19, respectively. ....91

Figure 3.20: Relaxation measurement by LMOKE microscope for sample B along EA. Fig. (b) - (j) are domain images taken at 0, 3, 7, 10, 18, 30, 60, 120, 180 s at  $H_M = 4.74$  mT, marked by points 1 - 9 in Figure 3.20(a), respectively. ....92

Figure 3.21: Relaxation measurement by LMOKE microscope for sample B along  $30^\circ$  w.r.t EA. Figure (b) - (j) are domain images taken at 0, 2, 5, 10, 60, 120, 150, 195, 300 s at  $H_M = 3.64$  mT marked by points 1 - 9 in Figure 3.21(a), respectively. ....93

Figure 3.22: Relaxation measurement by longitudinal Kerr microscope for sample C along EA. Fig. (b) - (j) are domain images taken at 0, 2, 5, 10, 41, 131, 302, 572, 892 s at  $H_M = 8.56$  mT, marked by points 1 - 9 in Figure 3.22(a), respectively. ....94

Figure 3.23: Magnetization relaxation data along with the fits for sample A (a) - (c), sample B (d) - (f), sample C (g) - (i) measured at  $H_M/H_C \sim 0.995, 0.985, \text{ and } 0.97$ , respectively. It should be noted that the DED fits here have been represented by dashed red curve to differentiate between the overlapping curves. ....96

Figure 4.1: The schematic of the sample structure showing two Co (10 nm) layers separated by the spacer  $\text{AlO}_x$  whose thickness ( $t$ ) was varied from 3 to 270 nm. ....102

Figure 4.2: Cross-sectional transmission electron microscopy (XTEM) images of (a) Si (100)/  $\text{AlO}_x$  (3 nm)/Co (10 nm)/ $\text{AlO}_x$  (23 nm)/Co(10 nm)/ $\text{AlO}_x$  (3 nm), high resolution image of (b) bottom Co layer and (c) spacer and top Co layer. ....103

Figure 4.3: XRR curves for sample D (a), sample E (b) and sample F (c). The experimental data is shown as open circles and the solid line is the simulated fits. ....104

Figure 4.4: Elemental depth profile measured by SIMS for sample D i.e. Si (100)/AlO<sub>x</sub> (3 nm)/Co (10 nm)/AlO<sub>x</sub> (8 nm)/Co(10 nm)/AlO<sub>x</sub> (3 nm).....105

Figure 4.5: Hysteresis (a) and domain images (b) – (e) measured by LMOKE microscopy along EA for AlO<sub>x</sub> (3 nm)/Co (10 nm)/AlO<sub>x</sub> (3 nm) [The Co target used was different than the one used for preparation of Co/AlO<sub>x</sub>/Co multilayers]. The field points corresponding to the domain images for (b) – (e) are shown by points 1 to 4 in Figure 4.5(a), respectively. ..106

Figure 4.6: Hysteresis (a) and domain images (b) – (e) measured by LMOKE microscopy along HA for AlO<sub>x</sub> (3 nm)/Co (10 nm)/AlO<sub>x</sub> (3 nm) [The Co target used was different than the one used for preparation of Co/AlO<sub>x</sub>/Co multilayers]. The field points corresponding to the domain images for (b) – (e) are marked by points 1 to 4 in Figure(a), respectively.....107

Figure 4.7: Angular dependence of (a) Coercivity vs.  $\theta$  (b)  $M_r/M_s$  vs.  $\theta$  for Co (10 nm)/ AlO<sub>x</sub>(3 nm)/Co (10 nm) showing the uniaxial anisotropy behaviour. Similar behaviour was observed for all samples of Co (10 nm)/AlO<sub>x</sub> ( $t$  nm)/Co (10 nm).....108

Figure 4.8: (a) Hysteresis measured by LMOKE microscope at room temperature for sample D along EA. Images (b) - (e) are domain images taken at fields marked by point 1 - 4 in Figure (a), respectively.....109

Figure 4.9: (a) Hysteresis measured by LMOKE microscope at room temperature for sample E along EA. Images (b) - (e) are domain images taken at fields marked by point 1 to 4 in Figure (a), respectively.....110

Figure 4.10: LMOKE ((a) – (d)) and TMOKE ((e) – (h),) hysteresis loops for samples D, E, F and G, respectively. It should be noted that sample G was prepared from different Co target. ....111

Figure 4.11: PNR measurements (open circles) and fits (solid lines) for  $\mu_0 H$  at (a) positive saturation, (b) -7 mT, (C) -18 mT for Co (10 nm)/AlO<sub>x</sub> (8 nm)/Co (10 nm). The corresponding measuring field points are marked as 1, 2, and 3 in Figure 4.8 (a). The schematics the magnetization vector orientation of the two Co layers for each field has been shown to its corresponding right column. The bottom and top Co layers are labelled as Co1 and Co2, respectively. ....113

Figure 4.12: Micromagnetic simulated hysteresis (a) and domain images (b to e) for Co (10 nm)/Al<sub>2</sub>O<sub>3</sub> (8 nm)/Co (10 nm) with  $K_u = 0.18 \times 10^6 \text{ J/m}^3$  and  $K_r = 0.1 \times 10^6 \text{ J/m}^3$ . The red and blue pixel corresponds to magnetization  $M_x < 0$  and  $M_x > 0$ , respectively. The suffix 1 and 2 for each domain image refers to the top and bottom Co, respectively. ....116

Figure 4.13: OOMMF simulated hysteresis for Co (10nm)/Al <sub>2</sub> O <sub>3</sub> (t nm)/Co (10nm) along EA, where t = 2, 8, and 90 nm..	117
Figure 4.14: Simulated domain images along EA for Co (10 nm)/Al <sub>2</sub> O <sub>3</sub> (t nm)/Co (10 nm) near coercive fields along EA, where t = 2, 8, and 90 nm with $K_u = 0.18 \times 10^6 \text{ J/m}^3$ and $K_r = 0.1 \times 10^6 \text{ J/m}^3$ . The red and blue pixel corresponds to magnetization $M_x < 0$ and $M_x > 0$ , respectively. The suffix 1 and 2 for each domain image refers to the top and bottom Co, respectively..	118
Figure 5.1: Schematic showing the core and the tail of the Néel walls with the magnetic [20].	121
Figure 5.2: Schematic of 360° DWs formed due to (a) opposite sense (unwinding) and (b) similar sense of rotation (winding) of Néel walls [20].	122
Figure 5.3: (a) Schematic of the sample Al <sub>2</sub> O <sub>3</sub> (3 nm)/[Co <sub>80</sub> Fe <sub>20</sub> (1.8 nm)/Al <sub>2</sub> O <sub>3</sub> (3 nm)] <sub>9</sub> , (b) schematic showing the coalescence of nanoparticles to form continuous thin films with overall uniaxial anisotropy and random anisotropy of the grains.	124
Figure 5.4: Coercivity (a) and $M_r/M_s$ (b) vs. $\theta$ for [Co <sub>80</sub> Fe <sub>20</sub> (1.8nm)/Al <sub>2</sub> O <sub>3</sub> (3 nm)] <sub>9</sub> showing the presence of uniaxial anisotropy behavior.	125
Figure 5.5: (a) LMOKE hysteresis loop for Al <sub>2</sub> O <sub>3</sub> (3nm)/[Co <sub>80</sub> Fe <sub>20</sub> (1.8nm)/Al <sub>2</sub> O <sub>3</sub> (3 nm)] <sub>9</sub> along EA. Figure (b) – (g) show the domain images along the positive branch of hysteresis for which the corresponding field points (1) – (6) are marked in Figure 5.5(a).	126
Figure 5.6: (a) Hysteresis measured by LMOKE microscopy along HA. Images (b) to (f) are domain images of the field points marked (1) to (5) respectively in the hysteresis. The zoomed (50 X 35 $\mu\text{m}^2$ ) in domain image of the highlighted area of the image (d) is shown in Figure 5.7. The thick black loop like features are the 360° DWs [52].	128
Figure 5.7: (a) The zoomed (50 X 35 $\mu\text{m}^2$ ) in domain image of the highlighted area in Figure 5.6(d) for positive branch of the hysteresis, (b) domain image for negative branch of the hysteresis, showing the 360° DWs (as white colored loops) separating parallel magnetization by the arrows in the respective images. [Note: both the images are in same scale].	128
Figure 5.8: Micromagnetic simulated hysteresis (A) and domain images (B to G) for [Co(1.8 nm)/Al <sub>2</sub> O <sub>3</sub> (3.6 nm)] <sub>2</sub> with $K_u = 0.15 \times 10^6 \text{ J/m}^3$ and $K_r = 0.1 \times 10^6 \text{ J/m}^3$ . The red and blue pixel corresponds to magnetization $M_x < 0$ and $M_x > 0$ . The suffix 1 and 2 for each domain image refers to the top and bottom Co layers, respectively.	130
Figure 5.9: The zoom in image showing the spins of the domain walls. The spins have similar sense of rotation across the two 180° DWs as shown the curved yellow arrow. The bold	

yellow arrow in the red and blue regions show the magnetization direction of the spins in the domains. ....131

Figure 5.10: OOMMF simulated hysteresis and the corresponding domain images showing formation of 360° DWs for [Co (1.8 nm)/Al<sub>2</sub>O<sub>3</sub> (3.6 nm)]<sub>2</sub> with (i)  $K_r = K_u = 0.1 \times 10^6 \text{ J/m}^3$  and (ii)  $K_r = 0.15 \times 10^6 \text{ J/m}^3$  and  $K_u = 0.1 \times 10^6 \text{ J/m}^3$ . The suffix 1 and 2 in the domain images corresponds for the top and the bottom layer of the Co.....132

Figure 5.11: OOMMF simulated hysteresis loop and domain images showing the reversal by 180° DW motion along EA for [Co (1.8 nm)/Al<sub>2</sub>O<sub>3</sub> (3.6 nm)]<sub>2</sub> with  $K_u = 0.2 \times 10^6 \text{ J/m}^3$  and  $K_r = 0.1 \times 10^6 \text{ J/m}^3$ .....133

Figure 5.12: OOMMF simulated Hysteresis (A) and domain images (B to G) along HA for [Co (1.8 nm)/Al<sub>2</sub>O<sub>3</sub> (3.6 nm)]<sub>2</sub> with  $K_u = 0.15 \times 10^6$  and  $K_r = 0.1 \times 10^6 \text{ J/m}^3$ . The red and blue pixels correspond to magnetization  $M_y < 0$  and  $M_y > 0$ , respectively. The suffix 1 and 2 in the domain images correspond to the top and the bottom Co layers, respectively.....135

Figure 6.1: Cross-sectional schematic of [Co<sub>80</sub>Fe<sub>20</sub> (1.3 nm)/Al<sub>2</sub>O<sub>3</sub> (3 nm)]<sub>10</sub> where the big particles are the Co<sub>80</sub>Fe<sub>20</sub> single domain nanoparticles and the small one are the glue particles responsible for tunnelling exchange coupling giving rise to SFM behaviour [7].....139

Figure 6.2: Schematic showing the SFM two oppositely aligned domains shown by large blue arrows. Each domain is formed by a group of single domain nanoparticles represented by the brown spheres [155].....140

Figure 6.3: Longitudinal magneto-optic Kerr effect (LMOKE) hysteresis for [Co<sub>80</sub>Fe<sub>20</sub> (1.3 nm)/ Al<sub>2</sub>O<sub>3</sub>(3 nm)]<sub>10</sub> measured along  $\theta = 0^\circ, 30^\circ, 45^\circ, 60^\circ, 75^\circ,$  and  $90^\circ$  at room temperature. The numbers shown in the hysteresis loops correspond to the domain images shown in Figure 6.4.....142

Figure 6.4: Domain images for [Co<sub>80</sub>Fe<sub>20</sub> (1.3 nm)/ Al<sub>2</sub>O<sub>3</sub> (3 nm)]<sub>10</sub> recorded with LMOKE microscopy with  $H$  directed along  $\theta = 0^\circ$  (EA),  $30^\circ, 45^\circ, 60^\circ,$  and  $90^\circ$  (HA) and  $H$  values as marked in Figure 6.3. ....144

Figure 6.5: Plot showing difference of the slope of the hysteresis for  $\theta = 0^\circ, 30^\circ, 45^\circ, 60^\circ, 75^\circ,$  and  $90^\circ$  with respect to the closing field of EA ( $\mu_0 H \sim 1 \text{ mT}$ ).....146

Figure 6.6: Magnetization relaxation curves for a SFM DMIM [Co<sub>80</sub>Fe<sub>20</sub>(1.3 nm)/ Al<sub>2</sub>O<sub>3</sub>(3 nm)]<sub>10</sub> measured with LMOKE microscopy with  $H$  along (a)  $\theta = 0^\circ$  (EA) at  $\mu_0 H = 0.53 \text{ mT}$  (open circles),  $30^\circ$  at  $\mu_0 H = 0.53 \text{ mT}$  (open triangles),  $60^\circ$  at  $\mu_0 H = 0.58 \text{ mT}$  (open rhombs), and (b)  $\theta = 75^\circ$  at  $\mu_0 H = 0.73 \text{ mT}$ . Solid lines are best fits to Eq. (6.2). Domain

images corresponding to the points marked (1) - (4) and (5) – (8) for the  $\theta = 60^\circ$  and  $75^\circ$  in Figure 6.6(a) and (b) are shown in Figure 6.7 and 6.8, respectively.....147

Figure 6.7: Domain images of magnetic relaxation recorded with  $H$  along  $\theta = 60^\circ$ . Images (a), (b), (c), and (d) were taken at  $t = 3, 8, 12$  and  $20$ s, respectively, and correspond to points 1, 2, 3 and 4 of Figure 6.6(a).....149

Figure 6.8: Domain images for magnetic relaxation recorded with  $H$  along  $\theta = 75^\circ$ . Images (a), (b), (c), and (d) were taken at  $t = 0, 4, 8,$  and  $15$  s, respectively, and correspond to points 5, 6, 7 and 8 of Figure 6.6(b).....150

## LIST OF TABLES

Table 1: Details of fitting parameters for relaxation measurements along EA at $H_M/H_C \sim 0.99$ .....	95
Table 2: Details of fitting parameters for relaxation measurements along EA at different $H_M/H_C$ .....	97
Table 3: Fitting parameters obtained for different angles using Eq. (6.2). ....	148
Table A: Showing the sample list at a glance for the Co/AlO <sub>x</sub> series.....	155

## List of Abbreviations

AFM	Atomic Force Microscopy
CCD	Charge coupled Device
CVD	Chemical Vapor Deposition
DC	Direct Current
DMIM	Discontinuous Metal Insulator Multilayer
DW	Domain Wall
EA	Easy Axis
FIB	Focused Ion beam
HA	Hard Axis
$H_c$	Coercive Field
$H_k$	Anisotropy Field
$H_M$	Measuring Field
$K_u$	Uniaxial Anisotropy Constant
$K_r$	Random Anisotropy Constant
LLG	Landau–Lifshitz–Gilbert
MOKE	Magneto-Optic Kerr Effect
$M_r$	Remanence Magnetization
$M_s$	Saturation Magnetization
NSF	Non-Spin Flip
OOMMF	Object-Oriented Micromagnetic Modeling Framework
PNR	Polarized Neutron Reflectivity
PVD	Physical Vapor Deposition
RF	Radio Frequency
RKKY	Rudermann-Kittel-Kasuya- and Yosida

SFM	Superferromagnetic
SF	Spin Flip
SQUID	Superconducting Quantum Interference Device
SSG	Superspin Glass
UHV	Ultra High Vacuum
XRR	X- Ray Reflectivity
XTEM	Cross-sectional Transmission Electron Microscopy

# Chapter 1 : Introduction and fundamentals

## 1.1 Introduction:

The understanding of magnetic thin films and nanostructures has led to many discoveries and applications, especially in the field of data storage technology. However, the properties at nanoscale can be very different as compared to their parent bulk because of quantum size effects, quantum tunnelling effects and high surface to volume ratio. These systems can therefore, be tuned for use in various applications like data storage and magnetoresistive devices, magnetic sensing and magnetoelectronic [1]. The read head of the hard drives and the magnetic random access memory (MRAM) devices are made up of magnetic trilayers where magnetic layers are separated by a non-magnetic layer called spin valves or magnetic tunnel junction, respectively [2]. Spin valve systems, used in read heads of the hard drives, consists of ferromagnetic layers (FM) separated by a non-magnetic (NM) conducting layer. In this case, one of the FM layers is pinned by an antiferromagnetic underlayer and behaves like a hard layer. However, the other FM layer is a free layer and the magnetization in this layer is easier to manipulate. The operational principle of such spin valve based read heads is the giant magnetoresistance (GMR) effect. The discovery of the GMR effect lead to the Nobel prize to Prof. Peter Grünberg and Prof. Albert Fert in 2007 [3]. GMR effect is basically obtaining tunable electrical resistance from maximum to minimum when the relative orientation of magnetization between the two FM layers are either parallel or anti-parallel, respectively. [4, 3]. Magnetic tunnel junctions are used in MRAM devices where two ferromagnetic layers: one hard magnetic and other soft magnetic are separated by non-magnetic insulating layers. These devices can be used as storage devices depending on the two states of high and low resistance based on the GMR effect arising due to spin-dependent

tunneling of electrons. These low and high resistance states can be used similar to 0 and 1 logic states of conventional electronics.

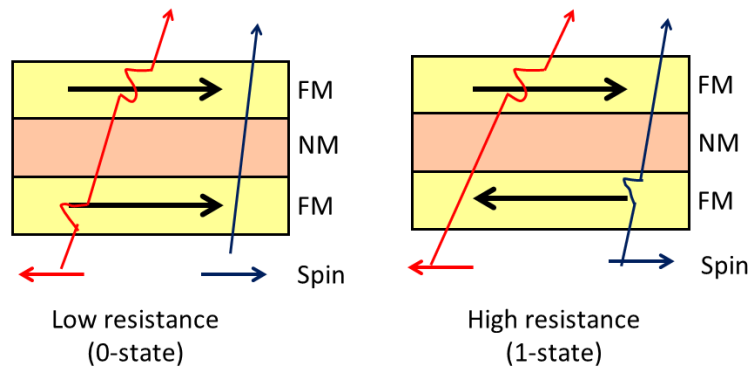


Figure 1.1: Schematic showing the GMR effect due to parallel and antiparallel alignment of magnetization of FM layers giving rise to low and high resistance, respectively.

Hence, for optimizing performance of these devices a better understanding of magnetization reversal, relaxation and domain structure is required. In particular, in MRAM high uniaxial anisotropy is required. One of the methods to induce and manipulate uniaxial anisotropy is to use oblique angle deposition of thin films [5, 6]. Other methods involve the application of magnetic field during deposition [7], post-annealing in the presence of magnetic field [8] etc. In the data storage and transfer technology, the relaxation rate of the magnetic thin films set the limits of the performance of the devices. Hence, it is relevant to know the effect of thermal activation energy and Zeeman energy in magnetization reversal of these devices to optimize their performance. Various models for magnetization relaxation have been proposed in past. For ferromagnetic thin films, the most widely used model is the Fatuzzo-Labrune model. This model was initially developed by Fatuzzo to investigate the relaxation in ferroelectric materials [9] and later Labrune [10] extended it to study relaxation in ferromagnetic thin films. However apart from applications, magnetic thin films are an excellent system for studying many fundamental physics such as magnetic domain and

domain wall dynamics, inter-layer coupling etc. Magnetic multilayers where ferromagnetic layers (FM) are separated by non-magnetic layers (NM) FM/NM/FM can have different kind of interactions depending on the nature of nonmagnetic spacer. For an insulating spacer long-range dipolar interactions will be present, leading to an antiparallel alignment of magnetization of next nearest neighbors in the layers. But if the spacer layer is metallic then due to conduction electrons the ferromagnetic layers will experience Ruderman–Kittel–Kasuya–Yosida (RKKY) interaction [11, 12, 13] in addition to the dipolar interaction. However if the system has any correlated roughness, for both the above cases, an additional Néel coupling, favoring parallel alignment of magnetization of layers will also be experienced [14]. Competition between these interactions can lead to modulated incommensurate phases.

Magnetization reversal in thin films and multilayers can be via formation of domains or by coherent rotation. Formation of domain walls in thin films depends on energy minimization of various energy factors such as exchange energy, magnetostatic energy, or crystalline anisotropy energy. Among various types of domain walls the observation of  $360^\circ$  domain walls (DWs) is rare.  $360^\circ$  DWs are formed due to the pinning centres in the magnetic thin film or by combination of two  $180^\circ$  Néel walls of the same chirality [15, 16].

Apart from thin films, magnetic nanoparticles also have wide applications in medical sciences for magnetic resonance imaging (MRI), hyperthermic treatment for malignant cells, site-specific drug delivery and manipulating cell membranes [17] etc. Single domain nanoparticles carry net spins denoted as “superspins” or “macrospins”, which in the case of ferromagnetic interaction are equal to the vector sum of all constituent atomic spins in the nanoparticle. Apart from technological applications, they are interesting systems to study the fundamental properties such as inter-particle interaction effects. By varying the concentration of nanoparticles the strength of the interactions can be tuned from superparamagnetism

(SPM), superspin glass (SSG) to superferromagnetism (SFM). The origin of such SFM domain state in DMIMs is generally believed to be due to strong dipolar interactions with additional tunneling exchange interaction [7].

Since, magnetization reversal, in general, is a topic of fundamental importance while implementing magnetic thin films or nanomaterials in storage devices and in other applications, hence, in this thesis we have studied the magnetization reversal for both continuous and discontinuous thin films. The major work of the thesis focuses on understanding and controlling the magnetization reversal, domain study, and relaxation for thin Co films with growth induced uniaxial anisotropy. With this understanding, the effect of interlayer coupling for continuous Co thin films in Co/AlO<sub>x</sub>/Co trilayers were studied using MOKE based microscope and polarized neutron reflectivity (PNR). Since, AlO<sub>x</sub> is an insulator, Co layers are expected to be dipolarly coupled. We also show that competing values of uniaxial and random anisotropy in soft magnetic multilayers of [Co<sub>80</sub>Fe<sub>20</sub>(1.8 nm)/Al<sub>2</sub>O<sub>3</sub>(3 nm)]<sub>9</sub> leads to the formation of non-trivial 360° domain wall (DWs). Further, a part of the thesis is devoted for an understanding of magnetization reversal and relaxation for a discontinuous metal insulator multilayer (DMIM) [Co<sub>80</sub>Fe<sub>20</sub>(1.3 nm)/Al<sub>2</sub>O<sub>3</sub>(3nm)]<sub>10</sub> showing superferromagnetic (SFM) state.

In this thesis, we have studied magnetization reversal in discontinuous and continuous thin films (single layer and multilayers). The main interest of study was to address the effect of random anisotropy on the magnetization reversal of magnetic thin films with uniaxial anisotropy. The thesis is organized as follows- **Chapter 1** reviews the concepts and basics of ferromagnetism, anisotropy and magnetization reversal, domains and types of domain walls etc. required to understand the results of this work. **Chapter 2** describes the experimental techniques used for preparation and characterization of the samples used in this thesis. **Chapter 3** presents the magnetization reversal of Co thin films with thickness  $t = 3.5$

and 10 nm. It is reported that random anisotropy can be induced by substrate rotation leading to inverted thin films. Complex domain structures were observed for films with high dispersion in anisotropy. The magnetic aftereffect relaxation revealed slow relaxation behavior for films with high dispersion. In **Chapter 4** the structural and magnetic properties of dipolarly coupled Co (10 nm) separated by insulating AlO<sub>x</sub> spacers will be presented. The effect of variation of coupling on the domain structure and reversal of these samples i.e Co(10 nm)/ AlO<sub>x</sub> (*t* nm)/Co (10 nm) were studied by varying *t* = 3 to 270 nm. LMOKE microscopy and PNR measurements revealed a layer-by-layer reversal of the Co layers. These results were also supported by the OOMMF simulations by incorporating a small random anisotropy along with uniaxial anisotropy. MOKE magnetometry revealed that for thickness *t* >23 nm, the transverse component of magnetization along with longitudinal component was observed. **Chapter 5** develops the understanding of the formation of 360° DWs observed experimentally in [Co<sub>80</sub>Fe<sub>20</sub> (1.8 nm)/Al<sub>2</sub>O<sub>3</sub> (3 nm)]<sub>9</sub>. It will be shown by OOMMF simulations that the competing effect of uniaxial and random anisotropy leads to the formation of 360° DWs. In **Chapter 6**, the angle-dependent magnetization reversal of a superferromagnetic system is studied. Decrease in ferromagnetic correlation strength due to the presence of small random anisotropy along with uniaxial anisotropy will be reported for angles away from the easy axis. Compressed exponential behavior due to the presence of this small random anisotropy was observed. Finally, the summary and the outlook is discussed in **Chapter 7**.

## 1.2 Fundamentals:

This section described some basic terms and concepts required to understand the results of this thesis.

### 1.2.1 Exchange energy:

The basic interaction that causes the ordering of molecular magnetic moment in a ferromagnetic material is the exchange interaction. Unlike long-range dipolar interaction, it is short range interaction of the order of  $10^3$  T as predicted by Weiss which was termed as molecular field by him. [18]. Heisenberg showed that exchange interaction is a quantum mechanical effect arising due to electrostatic interaction between the electrons of the nearby atoms [19]. Hence, exchange interaction manifests from Pauli Exclusion Principle as the electrons with the same spin will occupy different orbitals and hence will experience less coulomb repulsion. Whereas, the electrons with opposite spin can occupy same orbital and thus will experience less repulsive force. Since, the electrons are fermions, the total wave-function, consisting of the product of the spatial and spin part, needs to be antisymmetric. A system of two electrons can be in either in spin singlet or triplet with total spin  $S = 0$  and  $1$ , respectively. The energy difference between these two states gives the exchange energy. The Heisenberg exchange interaction energy for electron spins  $S_i, S_j$  is given by –

$$E_{ex} = -\frac{1}{2} \sum_{i,j} J_{ij} \hat{\mathbf{S}}_i \cdot \hat{\mathbf{S}}_j \quad (1.1)$$

where, where  $\hat{\mathbf{S}}_i$  and  $\hat{\mathbf{S}}_j$  are spin operators of electrons at the  $i^{\text{th}}$  and  $j^{\text{th}}$  site.  $J_{ij}$  is the exchange constant between them. Eq. 1.1 implies that for positive value of  $J_{ij}$ , spins of the corresponding electrons prefer to align parallel to each other. Hence, the ground state will be ferromagnetic. In case of negative value of  $J_{ij}$ , the spins will be aligned antiparallel to each other which occurs for antiferromagnetic materials. The strength of the exchange interaction is expressed as energy per unit volume. This exchange interaction macroscopically can be

expressed as a quadratic form of the first spatial derivatives of the magnetization vector which is also known as exchange stiffness. On microscopic scale, this stiffness energy is responsible for uniform magnetization [20].

The above exchange interaction is called direct exchange interaction since the wave functions of different electrons overlap to contribute to the exchange integral  $J$ . However, in multilayers, exchange interaction can also appear indirectly via conduction electrons called as RKKY interaction or via non-magnetic ion called as superexchange interaction.

### 1.2.2 Magnetostatic or demagnetization energy:

Magnetostatic energy originates due to the classical long-range dipolar interactions between the atomic magnetic dipoles in the solid. For an infinite magnetic body, the relation  $\mathbf{B} = \mu_0(\mathbf{H} + \mathbf{M})$  holds inside the system. However, for finite systems, especially for thin films and nanostructures, having uniform magnetization will lead to formation of charges on the surfaces. This will result in stray field energy outside the sample and a demagnetizing field  $\mathbf{H}_d$  (brown dotted arrows) opposite to the direction of its own magnetization inside the sample as shown in Figure 1.2. This demagnetizing field depends on the shape and hence is responsible for the shape anisotropy, in-plane anisotropy in thin films and formation of domains [21, 22] which will be discussed latter.

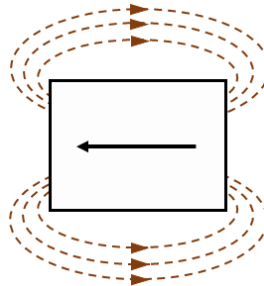


Figure 1.2: Schematic of the stray field energy of a magnetic system.

The energy of the system in its own stray field is given by  $E_{str}$ :

$$E_{str} = -\frac{1}{2} \int \mu_0 \mathbf{M} \cdot \mathbf{H}_{demag} dV \quad (1.2)$$

where,  $\mathbf{H}_{demag}$  is the demagnetizing field inside the magnetic system. For an ellipsoid the demagnetizing field is given as -

$$\mathbf{H}_{demag} = -N \mathbf{M} \quad (1.3)$$

where,  $N$  is the demagnetizing tensor and is shape dependent. Hence, using Eq. (1.3) in (1.2), the stray field energy over the volume  $V$  of the sample reduces to –

$$\begin{aligned} E_{str} &= \frac{1}{2} \mu_0 \int \mathbf{M} N \mathbf{M} dV \\ &= 1/2 \cdot V \mu_0 \mathbf{M} N \mathbf{M} \end{aligned}$$

An arbitrary direction of the magnetization with respect to the axes  $a$ ,  $b$  and  $c$  of an ellipsoid can be characterized by the direction cosines  $\alpha_a, \alpha_b$ , and  $\alpha_c$  [22]. Then the demagnetizing tensor ( $N$ ) is given by:

$$N = \begin{pmatrix} N_a & 0 & 0 \\ 0 & N_b & 0 \\ 0 & 0 & N_c \end{pmatrix} \quad (1.4)$$

with the condition that Trace  $N = 1$  (i.e.  $N_a + N_b + N_c = 1$ ). Hence, the stray field per unit volume energy reduces to [22]

$$E_{str} = 1/2 \cdot \mu_0 M^2 (N_a \alpha_a^2 + N_b \alpha_b^2 + N_c \alpha_c^2) \quad (1.5)$$

For thin film with magnetization  $\mathbf{M}$  at an angle  $\theta$  with respect to the surface normal i.e along  $z$ - axis,  $a = b = \infty$  and the demagnetizing tensor is given as -

$$N = \begin{pmatrix} 0 & 0 & 0 \\ 0 & 0 & 0 \\ 0 & 0 & 1 \end{pmatrix} \quad (1.6)$$

Therefore, the stray field energy density of the thin film will be reduced to -

$$E_{str} = 1/2 \cdot \mu_0 M^2 \cos^2 \theta \quad (1.7)$$

This stray field energy gives rise to shape anisotropy and in-plane magnetization in thin films which is discussed under shape, surface and interface anisotropy in the next section.

### 1.2.3 Magnetic anisotropy:

The Heisenberg exchange Hamiltonian for the energy of a ferromagnet does not depend on the spatial direction of the spins or magnetic moments. This would mean that magnetization should always vanish for zero magnetic field. However, this is not the case for real ferromagnetic thin film as there can be directional dependence of magnetic property/energy. This may lead to a preferred orientation of  $\mathbf{M}$  other than  $\mathbf{H}$ , creating an energetically favorable direction called easy axis (EA) and unfavorable direction called hard axis. Hence, in the absence of magnetic field, the magnetization of the ferromagnet will align along the EA. To rotate this magnetization in any other direction requires energy. This directional dependence of magnetic property of a ferromagnet is called magnetic anisotropy. The magnetic anisotropy is often in the order of  $\sim \mu\text{eV}/\text{atom}$  which is much smaller than the exchange energy of the order of  $10\text{-}10^3 \text{ meV}/\text{atom}$ . However, anisotropy energy is important as the direction of magnetization is determined by it and not by exchange energy. The role of exchange interaction is to align the magnetic moments parallel, no matter in which direction. Hence the understanding of anisotropy is important from fundamental as well as application point of view so that magnetic properties can be tailored for use in technology. Since a part of this thesis is devoted in understanding and modifying the anisotropy, domain structure and magnetization reversal of Co thin films with uniaxial anisotropy with different substrate rotations hence in the following section different anisotropies in thin films are discussed. Anisotropy in thin films can arise due to crystal symmetry which gives rise to magneto-crystalline anisotropy. It can also arise from stress, surface morphology or shape within the crystals. The magnetic anisotropy arises due to dipole-dipole interaction and the spin-orbit coupling. Dipole-dipole interaction is the origin for shape anisotropy and spin-orbit coupling is responsible for other anisotropies like magneto-crystalline, surface and magnetoelastic

anisotropy. Among these, only the magnetocrystalline anisotropy arising due to the crystal structure is intrinsic to a material.

### 1.2.3.1 Magnetocrystalline anisotropy:

It arises due to spin-orbit coupling in the crystal. The origin of the spin-orbit interaction is attributed to the coupling of the orbital moments of the electrons which arise from the electron motion around the nucleus and the spin angular momentum. This spin-orbit coupling is linked to the symmetry of the crystal lattice via the electric field (potential) of the crystal. This will lead to the energy contribution which depends on the relative orientation of the magnetization and the crystal symmetry giving rise to magneto-crystalline anisotropy. Hence, magnetization will tend to lie along certain crystallographic orientations which will be energetically favored. Phenomenologically, it is easier to describe the anisotropy as the direction cosines of the magnetization with respect to either rectangular coordinate axes or in terms of spherical harmonics. The magnetization direction w.r.t to the coordinate axis (or lattice primitive vectors) can be expressed as direction cosines ( $\alpha_i$ ) with  $\alpha_1^2 + \alpha_2^2 + \alpha_3^2 = 1$ . Hence magneto-crystalline energy density can be written in the form of

$$E_{anisotropy} = K \cdot f(\alpha_1, \alpha_2, \alpha_3)$$

Where,  $K$  is the anisotropy constant,  $f$  depends on the spatial symmetry of the lattice. Since there is no energy difference for oppositely magnetized systems, therefore,

$$E(\mathbf{M}) = E(-\mathbf{M})$$

$$E(\alpha_i) = E(-\alpha_i)$$

Thus, no odd terms of  $\alpha_i$  occur in the series expansion. Therefore, the general expression for energy reduces to [22]

$$E_{crys} = E_0 + \sum_{ij} b_{ij} \alpha_i \alpha_j + \sum_{ijkl} b_{ijkl} \alpha_i \alpha_j \alpha_k \alpha_l$$

The simplest example is uniaxial anisotropy where,  $E_{an} = K \sin^2(\alpha)$ . Uniaxial anisotropy can also be induced during growth by applying magnetic field, oblique deposition, post annealing in presence of magnetic field. The growth induced anisotropy will be discussed later in section 1.2.3.5 in detail.

### 1.2.3.2 Shape anisotropy:

Shape anisotropy has its origin due to long-range dipolar interaction. For a spherical magnetic particle, the energy needed to magnetize along any arbitrary direction is same. However, if the sample is not spherical then one or more specific directions occur which represent easy magnetization axes which are solely caused by the shape. A magnetic system of finite size will exhibit poles at its surfaces. This will result to a stray field outside it and experience an oppositely directed demagnetizing field inside the system. Hence, the strength of the demagnetizing field in case of thin films will be different along the directions parallel and perpendicular to the film plane. The strength of the demagnetizing field will be more in the direction perpendicular to the film plane (Figure 1.3(a)) compared to the direction parallel to the film plane (Figure 1.3(b)). Hence, the magnetization in a thin film will prefer to lie in the plane of the film.

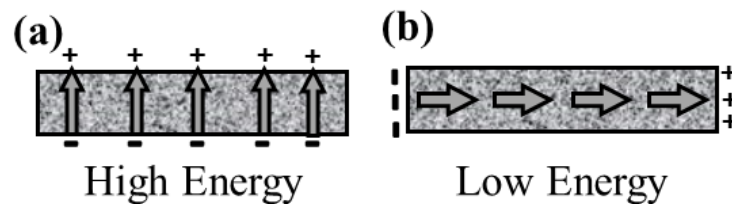


Figure 1.3: Effect of shape anisotropy on the demagnetization energy when it is (a) perpendicular and (b) parallel to the film plane.

Considering, thin film as a magnetic continuum and assuming it to be uniformly magnetized, the shape anisotropy can be given as [23, 22]-

$$E = \frac{1}{2} \mu_0 M_s^2 \cos^2 \theta \quad (1.8)$$

where,  $M_s$  is the saturation magnetization, the magnetization subtends an angle,  $\theta$ , to the plane normal. Hence, Eq. (1.8) implies that the shape anisotropy energy is minimum when the angle is  $90^\circ$  i.e. for in-plane orientation of magnetization.

### 1.2.3.3 Magnetoelastic anisotropy:

Magnetic properties like magnetocrystalline anisotropy of a ferromagnet can be altered in the presence of strain. It is opposite to the phenomenon of magnetostriction, where the dimensions of the sample alter due to the change in the direction of the magnetization. Hence, magneto-elastic or stress anisotropy can arise from the stress produced in the films during the deposition process, the difference in thermal expansion coefficients, due to mismatching of lattice parameters between the substrate and magnetic films (the adjacent layers) [24]. For a uniaxial system, the volume magnetoelastic energy is given by-

$$E_{ml} = -3\sigma\lambda_s \cos^2 \frac{\theta}{2} \quad (1.9)$$

where,  $\lambda_s$  is an isotropic magnetostriction coefficient and  $\theta$  is the angle between the magnetization  $M$  and  $\sigma$ . Therefore, Eq. 1.9 implies that the magnetoelastic energy is the product of stress ( $\sigma$ ) and the resulting value of magnetic strain or magnetostriction  $\lambda$

### 1.2.3.4 Surface and interface anisotropy:

In low dimensional systems, the broken symmetry at the surface or interfaces will also contribute to the effective anisotropy energy. Thus, the effective anisotropy of a thin film with thickness  $t$  can be separated into parts: one describing the volume and the other one describing the surface contribution given as [23, 22]-

$$K = K_{eff} = K_V + 2K_S/t \quad (1.10)$$

The factor 2 in above equation is to account for two identical surfaces bounding the layer.

From Eq. (1.10), it can be observed that for a critical thickness ( $t_c$ ) given by-

$$t_c = -2 K_S / K_V$$

The magnetization lies perpendicular to the film plane and above  $t_c$  it lies in the film plane [25]. This happens because below this critical thickness, the interface anisotropy, which is inversely proportional to the thickness, outweighs the volume contribution. Hence, it overcomes the demagnetization energy responsible for the in-plane anisotropy.

Magnetic anisotropy can be measured by the dynamic response of the system using Ferromagnetic resonance or BLS spectroscopy. Other techniques which use the static response of the system are MOKE magnetometry, torque magnetometry, SQUID magnetometry etc. However, it should be noted that using MOKE magnetometry, one cannot get directly the quantitative value of anisotropy as it does not measure directly the magnetization, however, the nature of the anisotropy can be obtained from MOKE. To get the value of the anisotropy energy one needs to assume a value of magnetization. Therefore, this method may lead to some error [23].

### **1.2.3.5 Growth induced anisotropy:**

Anisotropy in magnetic thin films can also be induced by applying a magnetic field during deposition, [26, 7] post-annealing (annealing in the presence of magnetic field) [8] or by oblique deposition [5]. The anisotropy induced in general is uniaxial in with the energy as:

$$E = -K_u \cos^2\theta$$

Where  $K_u$  is the anisotropy constant and  $\theta$  is the angle between the easy axis and the magnetization vector in the presence of magnetic field. The thin films studied in this thesis showed growth induces uniaxial anisotropy. The samples studied in this thesis can be categorized into two series-

- (1) The single and multilayers of  $\text{Co}/\text{AlO}_x$  thin films prepared by magnetron sputtering and
- (2) The multilayers of  $\text{Co}_{80}\text{Fe}_{20}/\text{Al}_2\text{O}_3$  prepared by focussed ion beam sputtering.

Samples prepared under the category (1) and (2) showed uniaxial anisotropy due to oblique angle deposition and applied magnetic field during growth, respectively.

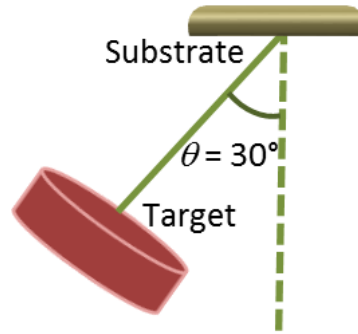


Figure 1.4: Schematic showing the oblique deposition geometry. The magnetrons in the multi-deposition unit used for thin film preparation of  $\text{Co}/\text{AlO}_x$  series are at an angle of  $30^\circ$  w.r.t to the substrate normal (Figure 2.3).

In oblique deposition, the incident flux from the target and the substrate normal are at an angle  $\theta > 0^\circ$  as shown in Figure 1.4. The Co films grown in this thesis were deposited at  $\theta = 30^\circ$ . Uniaxial anisotropy is induced by oblique deposition due to shadow deposition leading to the formation of an elongated chain like structure of the grains perpendicular to the incident flux as shown in Figure 1.5 [5]. To decrease the magnetostatic energy in such cases, the magnetization would prefer to lie along the length of the column leading to uniaxial anisotropy. It was also shown that these columnar structures of grains grow with a tilt towards the deposition angle [27]. Hence both the shape and strain anisotropies contribute to the effective anisotropy [5, 28].

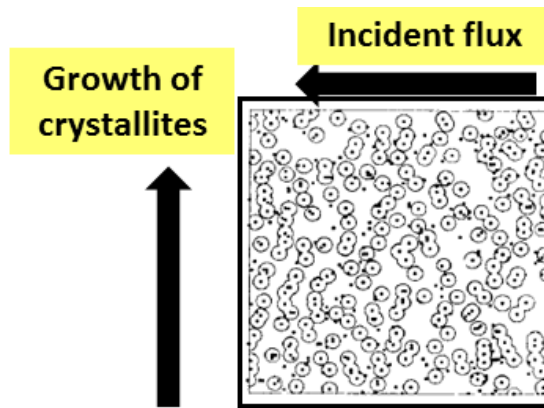


Figure 1.5: Schematic showing the oblique deposition in which the incident beam at  $60^\circ$  from the right direction [5].

For the case of field induced anisotropy, a magnetic field is applied parallel to the substrate plane during the deposition process. This induces the preferred direction of magnetization i.e. a uniaxial anisotropy along the field direction. A magnetic film when subjected to magnetic field leads to the directional ordering of magnetic moments along the field direction.

In the post-annealing process, the system is heated below the Currie temperature in the presence of magnetic field. The thermal energy allows atoms to diffuse and leads to the directional ordering of atomic pairs [29, 30, 31] and align them along the field to minimize the energy. As the sample is then cooled, this directional ordering is frozen giving rise to the preferred anisotropic direction along the magnetic field.

### **1.2.3.6 Random Anisotropy:**

Thin films may be classified as a single crystal, textured or polycrystalline. The polycrystalline and textures films are made up of crystallites/grains. The magnetization reversal of such films depends largely on the film microstructure and exhibit many interesting behaviours like random-anisotropy scaling [32], remanence enhancement [33],

micromagnetic localization [34], collapse of hard axis [35] etc. The randomness in magnetic systems can arise due to local dispersion anisotropy, grain size, stress etc. which varies over the structural correlation length (grain size)  $D$ . If the easy axes of the grains are completely random such that  $\langle\langle n(\mathbf{r}) \rangle\rangle = 0$ , then the nanostructures are isotropic. However, partially misaligned easy axis of grains are found in polycrystalline magnets [36] and in strained amorphous magnets [37]. Random anisotropy model was first presented by Alben where an effective anisotropy was observed due to the statistical averaging of the magneto-crystalline anisotropy of grains. It was shown by Imry *et al.* that presence of even weak random anisotropy will lead to unstable order parameter and the system will break into domains [38]. However, a system may have an induced uniaxial anisotropy in thin films or nanostructures where the constituent grains or structures have random anisotropy which effectively gives rise to uniaxial anisotropy. The magnetization reversal for such systems has not been studied in detail. Depending on the order of misalignment and exchange energy, the reversal mechanism can be different. If the randomness outweighs the exchange energy, then the rotational symmetry of the magnetization is broken [35] leading to collapse of hard axis, formation of ripple domains [39] or formation of  $360^\circ$  DWs [16]. However, a complete understanding of the magnetization reversal of the system with random anisotropy is not yet given.

#### 1.2.4 Zeeman energy (External magnetic field):

When an external magnetic field is applied to a ferromagnetic sample, then its potential energy arising from the interaction of the magnetization vector field with this external field  $\mathbf{H}_{Ext}$  is given as:

$$E_{Zeeman} = -\mu_0 \int_V \mathbf{M} \cdot \mathbf{H}_{Ext} dV \quad (1.11)$$

The Zeeman energy is at a minimum when all the magnetization ( $\mathbf{M}$ ) of the sample is aligned with the applied field. This means, that in the presence of magnetic field all the magnetic

moments try to align along the field. This energy is independent of the sample shape or the domain structure of the thin film but depends on the average magnetization of the sample.

Hence the total energy of the system is given by,

$$E = E_{exch} + E_{demag} + E_{anis} + E_{Zeeman} \quad (1.12)$$

### **1.3 Magnetic domains and domain walls:**

Weiss in 1907 proposed the existence of magnetic domains in ferromagnetic material. He suggested that, in its demagnetized state, a ferromagnetic material is composed of small regions which are magnetized in different directions [18]. Magnetic domains are formed to minimize the total energy which is a sum of exchange, demagnetization, anisotropy and Zeeman energy as given by Eq. (1.12). The exchange energy is minimum when the magnetic dipole moments are aligned parallel to each other. However, this increases the stray field energy or the demagnetization energy of the system. The high stray field energy for a uniformly magnetized system (Figure 1.6(a)) can be minimized by the formation of domains as shown in Figure 1.6(b). Even though this increases the exchange energy of the system, the total energy decreases as the dominant contribution is from magnetostatic energy. Landau and Lifshitz [40] suggested that the stray field energy can be reduced to zero by flux enclosure type domains shown in Figure 1.6(c). However, for domain pattern apart from magnetostatic energy, one needs to consider the anisotropy and exchange energies. The other contributions to energy arise from anisotropy and magnetostrictive energies, which influence the shape and size of domains.

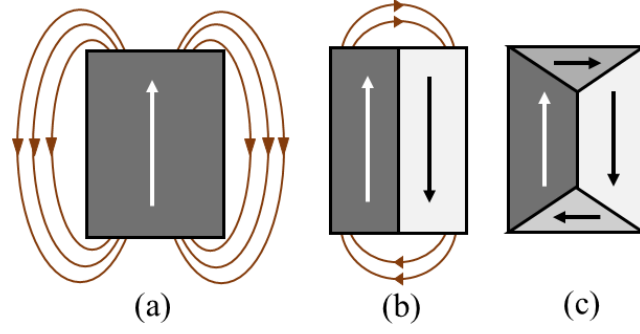


Figure 1.6: Schematic representation of reduction of the magnetostatic energy by domain formation in a ferromagnet.

The domains are separated by a region/boundary called domain wall first verified by Sixtus and Tonks [41]. Inside the domain walls, the direction of the magnetic moment changes continuously from one magnetization direction of one domain to other to minimize the exchange energy. This can be understood in the following way. The exchange energy between the two spins at an angle  $\theta$  is given by –

$$E = -2J\mathbf{S}_1 \cdot \mathbf{S}_2 = -2JS^2 \cos \theta$$

Therefore, the energy required to flip one spin is  $E = 2JS^2$  for  $\theta = \pi$ . However, for  $N$  number of spins, the angle between each spin will be  $\theta/N$ . Then the total exchange energy is distributed among each pair of spins over  $N$  lattice spacing and approximating  $\cos \theta = 1 - \frac{\theta^2}{2}$ , is given by-

$$\Delta E_{ex} = E_{ex} - E_{ex}^{\theta=0}$$

$$\Delta E_{ex}^{total} = N \cdot JS^2 \frac{\pi^2}{N^2} = JS^2 \frac{\pi^2}{N}$$

In a magnetic system of lattice constant ‘ $a$ ’, the number of spin rotation axes inside a Bloch wall is  $1/a^2$  per  $m^2$  which leads to an exchange energy of:

$$E_{ex}^{BW} = JS^2 \frac{\pi^2}{Na^2} \quad (1.13)$$

Therefore, it can be seen from Eq. (1.13) that exchange energy decreases as  $N$  increases. Hence, it introduces a gradual rotation of spins which tends to increase in width of the wall. This results in the spins pointing away from the easy axis thus increasing the anisotropy energy. The anisotropy energy given as  $E_{an} = K \sin^2(\theta)$ . For  $N$  spins, the anisotropy energy contribution will be summed as-

$$E_{ani}^{BW} = \sum_{i=1}^N K \sin^2 \theta_i \approx \frac{NKa}{2} \quad (1.14)$$

The anisotropy energy increases if the wall width increases. Since the anisotropy energy is minimized when the spins are aligned along easy axis, therefore, it tends to minimize the width of the wall. Hence, the width of the domain wall ( $\delta$ ) is decided by the minimization of the competing exchange energy and anisotropy energies [20]. The continuous rotation of spins in the domain wall was conceived by Bloch [42] and calculated by Landau and Lifshitz [40].

Depending on the spin structure inside the walls, the walls can be classified as Bloch wall or Néel wall. In Bloch walls, the magnetization rotates parallel to the plane of the wall as shown in Figure 1.7(a). Hence, there will be no magnetic charges inside the wall as the normal component of the magnetization on both sides of the walls are same [42]. However, these kinds of walls will create magnetic charges on the surface creating a demagnetizing field across the sample surface. Hence, Bloch walls are commonly observed for bulk materials as the demagnetization energy in such case will be minimum. The width of the domain wall is estimated by the minimization of the exchange and anisotropy energy density given in Eq. (1.13) and (1.14) by taking the first differentiation of the sum of these two energies w.r.t lattice spacing  $N$ . These results in effective wall width for Bloch wall ( $\delta$ ) as

$$\delta = Na = \pi S \sqrt{\frac{2J}{K_u a}} \quad (1.15)$$

$$\delta = \pi \sqrt{A/K}, \quad (1.16)$$

where, the constant  $A = \frac{2JS^2}{a}$  is called exchange stiffness. However, Bloch walls become energetically unfavourable in thin films where the width of the wall becomes comparable to the thickness of the film. In such cases, Néel walls are formed where the magnetization vector in the walls rotate perpendicular to the plane of the wall as shown in Figure 1.7(b). Hence, the demagnetization energy caused by the charges across the domain wall will be less than the Bloch wall [43]. The width of the Néel wall is approximately given as  $\delta_{DW} = \pi \sqrt{\frac{2A}{\mu_0 M_s^2}}$ , where  $M_s$  is the saturation magnetization [44]. In such type of walls the magnetostatic energy cannot be neglected as the residual charges in the DW will add up along the axis of the domain [20]. Due to this magnetostatic energy, the domain in multilayers can be very different from that of single layer. The stray field generated from the domain walls of one layer can affect the other layer [45]. Apart from Bloch and Néel wall, a third type of wall called cross-tie wall was experimentally observed by Huber *et al.* in permalloy films [46]. These walls occur for films with intermediate thickness. Unlike Bloch and Néel walls, these walls have complex two dimensional structures. It should be noted that Bloch and Néel wall have one dimensional structure. It can happen when the charges of the  $180^\circ$  Néel walls destabilizes it and energy is minimized by formation of cross- tie walls. These walls have a sequence of magnetic vortices and anti-vortices, arranged along a straight line [20]. Figure 1.8 shows the transition thickness dependence of Bloch wall to cross-tie to Néel walls w.r.t. domain wall energy. It can be seen that for thick films Bloch walls are favourable. On decreasing the thickness of the films, a transition occurs from Bloch wall to cross-tie and then to Néel walls (Figure 1.8).

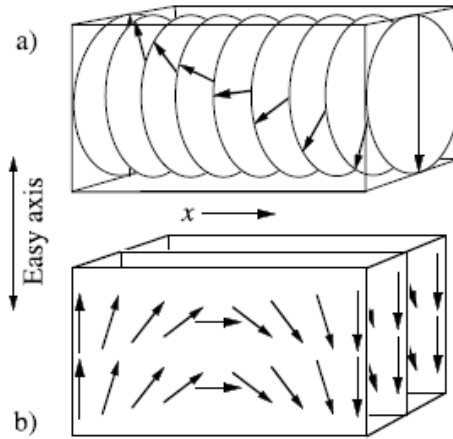


Figure 1.7: The schematic of (a) Bloch wall with spins rotating perpendicular and (b) Néel wall with spins rotating in-plane of the domain walls [20].

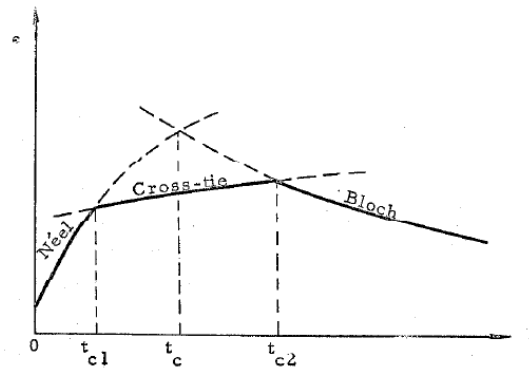


Figure 1.8: Thickness dependence of energy of Bloch, Néel and cross tie walls [47].

Depending on the magnetization direction of the neighboring domains, the domain walls (DWs) commonly observed in magnetic materials can be classified as  $180^\circ$ ,  $90^\circ$  and  $360^\circ$  DWs as shown schematically in Figure 1.9 (a), (b) and (c), respectively.  $180^\circ$  domain walls are the most commonly observed domain walls in magnetic materials with uniaxial anisotropy separating the domains with antiparallel magnetization (Figure 1.9(a)). In systems with cubic anisotropy, apart from  $180^\circ$  domain walls,  $90^\circ$  domains wall can also occur. These  $90^\circ$  domain walls separate the regions with perpendicular (in-plane) magnetization (Figure 1.9(b)) and are generally characterized by the zigzag boundaries to decrease the energy. For

example, having easy axis along  $[100]$  will have domain wall of  $180^\circ$  along  $[\bar{1}00]$  but will have  $90^\circ$  domain walls long  $[010]$  [48]. These cubic systems can sometimes have  $109^\circ$  and  $71^\circ$  domain walls along with  $180^\circ$  domain walls as observed in the case of Ni thin film along its easy axis i.e.  $\langle 111 \rangle$  [49]. Another non-trivial domain wall rarely observed is  $360^\circ$  DW which separates the domains having parallel magnetization (Figure 1.9(c)). The spins across these DW rotates by  $360^\circ$  as shown in Figure 1.10. The details of  $360^\circ$  DWs will be discussed later in Chapter 5. The example of  $180^\circ$ ,  $90^\circ$  and  $360^\circ$  observed in the real samples are shown in Figure 1.11(a), (b) and (c), respectively.

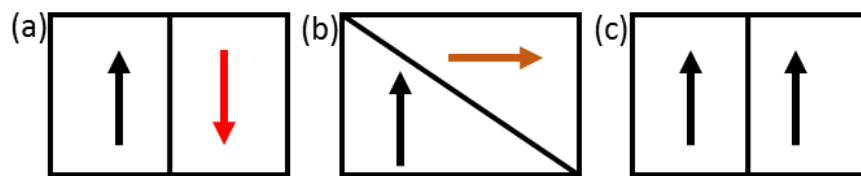


Figure 1.9: The schematic (a)  $180^\circ$  (b)  $90^\circ$  and (c)  $360^\circ$  DWs.

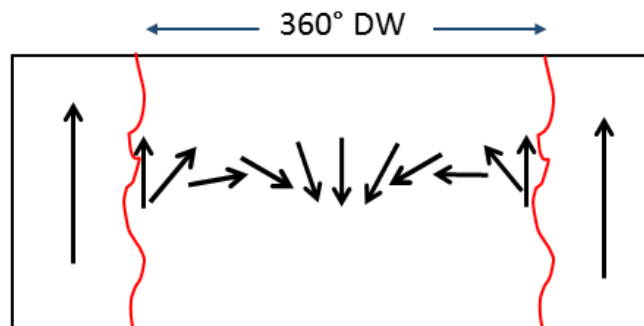


Figure 1.10: Schematic for spin orientation inside a  $360^\circ$  DW separating domains of parallel magnetization

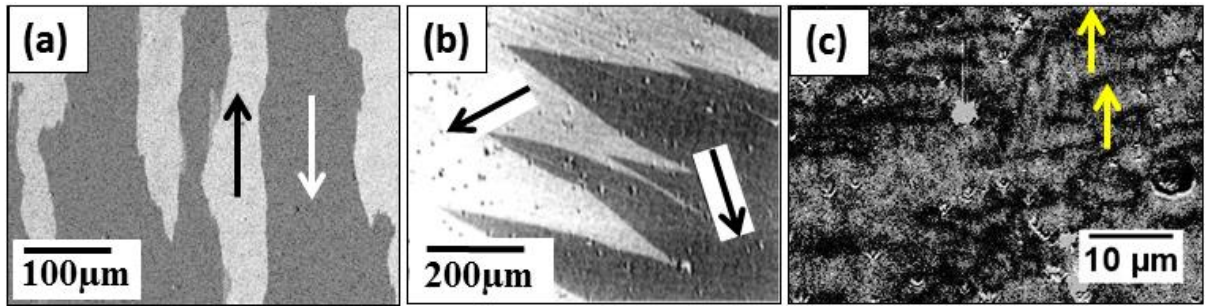


Figure 1.11: Kerr microscopy domain images where domains are separated by (a)  $180^\circ$  [50], (b)  $90^\circ$  [51] and (c)  $360^\circ$  DWs [52].

## 1.4 Magnetization reversal:

Magnetization reversal is the process in which the magnetization vector of the ferromagnetic system is reversed from one stable state to another under an external magnetic field. The magnetization does not follow the applied magnetic field linearly giving rise to hysteresis loop which can be measured by Magneto-Optic Kerr Effect (MOKE), SQUID, etc. Fundamental parameters like saturation magnetization ( $M_s$ ), coercive field ( $H_c$ ), remanent magnetization ( $M_r$ ), effective anisotropy constant ( $K$ ) required for characterizing the ferromagnetic material can be determined from the hysteresis loops of the system. Further, the knowledge of these parameters is also important for tailoring of various properties for the applications. Hysteresis is a nonlinear, non-equilibrium complex first order phase transition. The complexity also increases due to the effect of local microstructure, defects and morphology of the system. [53]. Therefore, magnetization reversal processes are related to the complex landscape of the free energy. A typical hysteresis curve is shown in Figure 1.12. It can be observed that the value of magnetization is not single-valued but gets branched for the fields less than the closure field  $H^*$  as shown in Figure 1.12. [54]. On applying field greater than the  $H^*$  results in saturation of the material where all the magnetic moments are aligned along the field and is in single domain state with value approximately equal to saturation magnetization ( $M_s$ ). On reversing the magnetic field from saturation magnetization ( $M_s$ ) to

zero, the magnetization of the system does not reduce to zero but retains some positive magnetization called remanent magnetization ( $M_r$ ) as shown in Figure 1.12.

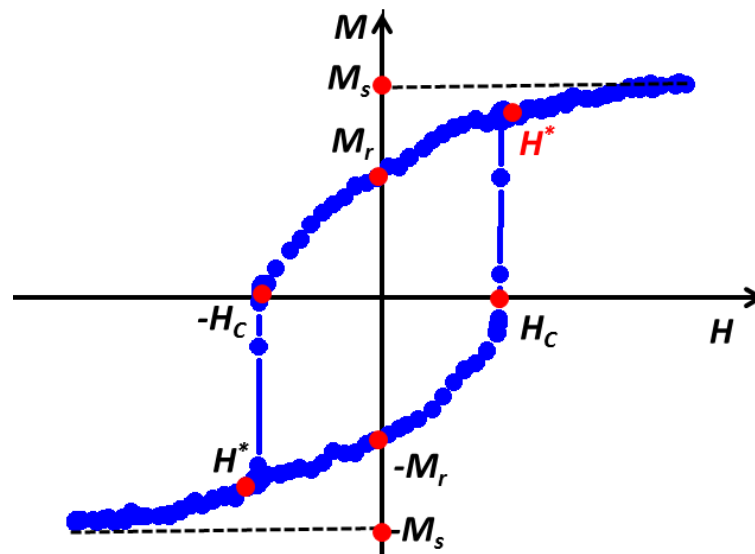


Figure 1.12: A typical hysteresis loop showing the  $M$  vs  $H$  behavior of a ferromagnet.

A magnetic field equal to the coercive field ( $-H_c$ ) in the reverse direction is required to reduce this  $M_r$  to zero. The coercive field  $H_c$  of a material is the field at which the net magnetization of the system is zero. It can be used as a property to measure the hardness of the material. Soft (hard) magnetic materials have small (large) values of  $H_c$  and hence exhibit a narrow (large) hysteresis loop. On increasing the field further in the reverse direction, negative saturation state is achieved. Another parameter that can be deduced from the hysteresis is its squareness ( $S$ ) which is defined as the ratio of the remanence to saturation magnetization i.e.  $S = M_r/M_s$ . The squareness along easy axis, in general, is close to unity with a square hysteresis loop. The angular dependence of Squareness for a sample gives the nature of the anisotropy of the system where for uniaxial systems it follows cosine function. Magnetization switching can occur via coherent rotation of spins or by nucleation and growth of reversed domains. These process can coexist and can be partly reversible or irreversible. One of the most relevant simplified cases of magnetization reversal for particles with uniform magnetization is given by Stoner-Wohlfarth (SW) model as discussed briefly below.

### 1.4.1 Coherent rotation (Stoner-Wohlfarth model):

This model describes the magnetization switching of single domain particles with uniaxial anisotropy with an ellipsoidal shape having saturation magnetization  $M_s$ . This theory neglects the spatial inhomogeneity in all directions and considers uniform magnetization of constant magnitude [55]. A magnetic particle is smaller than a critical radius becomes a single domain where all the atomic magnetic moments are parallel for the entire system. This implies that the contribution of exchange energy can be neglected as it will always be minimum due to the collinear alignment of spins. Therefore, on application of magnetic field, the free energy of the system will be given by sum of Zeeman and anisotropy energy –

$$E = K \sin^2 \theta - \mu_0 H M_s \cos(\phi - \theta) \quad (1.17)$$

Where, the first term is the anisotropy energy,  $K$  is the effective anisotropy constant due to the magneto-crystalline and shape anisotropy,  $\theta$  is the angle between the easy axis and the magnetization,  $\phi$  is the angle between the easy axis and the applied magnetic field as shown in Figure 1.13. The equilibrium position of magnetization can be deduced by minimizing the energy function (Eq. 1.17) with respect to  $\theta$  which is  $dE/d\theta = 0$ , which can be written as -

$$2K \sin \theta \cos \theta - \mu_0 H M_s \sin(\phi - \theta) = 0 \quad (1.18)$$

and the condition for this equilibrium to be stable requires  $d^2E/d\theta^2 > 0$ ; i.e

$$\frac{d^2E}{d\theta^2} = 2k(\cos^2 \theta - \sin^2 \theta) + \mu_0 H M_s \cos(\phi - \theta) = 0 \quad (1.19)$$

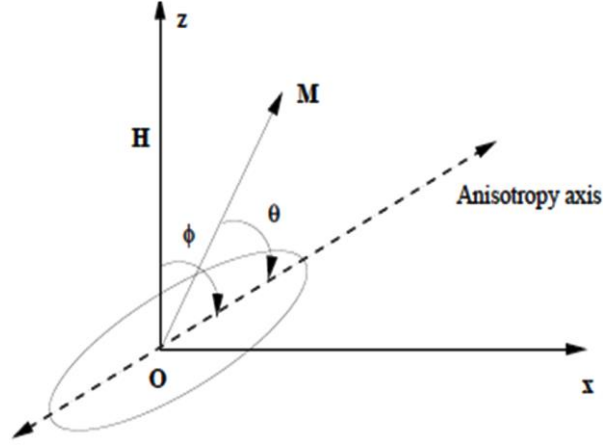


Figure 1.13: Illustration of the coordinate system of a single domain particle for SW model.

Solving Eq. 1.18 for hard axis (i.e.  $\phi = 90^\circ$ ), the equation reduces to –

$$2K(M/M_s) = \mu_0 H M_s \quad (1.20)$$

Putting  $M/M_s = m =$  reduced magnetization, it can be seen from Eq. (1.20) that the magnetization linearly follows the applied magnetic field and is via reversible rotation of the magnetic moments. The saturation field of the hard-axis ( $H_{sat}$ ), also called as anisotropy field ( $H_k$ ) occurs at –

$$H_k = 2K/\mu_0 M_s \quad (1.21)$$

Again, solving Eq. (1.18) for easy axis i.e.  $\phi = 0$ , at positive saturation field the magnetization is aligned along the global minima which is along the field direction. However when the field is reversed to the negative direction, the magnetization remains along the easy axis until the field is reversed to  $H_k$ , at which the reversal takes place by irreversible switching of the magnetization. The field at which this discontinuous jump occurs is called switching field. The switching field, also known as the *nucleation* field is the point of instability of the near saturation state [20]. This happens because the global energy minima now shifts to  $\phi = 180^\circ$  whereas  $\phi = 0^\circ$  becomes local minima. However, when applied field is at an angle away from easy axis ( $0^\circ < \phi < 90^\circ$ ), the magnetization reversal is first accompanied by reversible

rotation. This aligns the magnetization away from field direction but aligns it along the easy axis. On further increasing the field in the negative direction, the reversal takes place via irreversible discontinuous jump with magnetization. As the magnetization is still away from the field axis, the negative saturation takes place via rotation of magnetization towards the field direction. The angle dependent hysteresis for this model is shown in Figure 1.14. Even though SW model allowed easy modeling of magnetization reversal, its simple assumption of coherent rotation neglects the true picture of magnetization processes in the presence of imperfections.

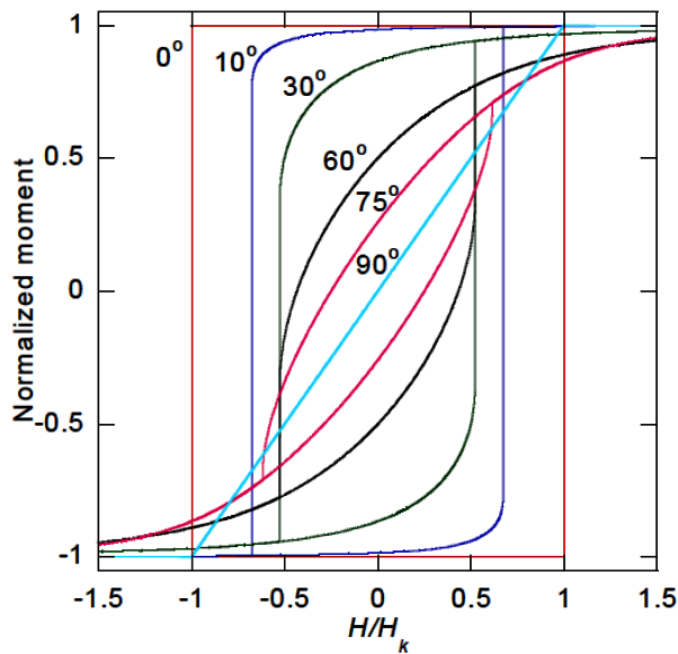


Figure 1.14: Hysteresis curves for different  $\phi$  (angle between applied magnetic field and easy axis) using SW model.

### 1.4.2 Reversal by domain wall motion:

The SW model holds good for a system where  $\nabla \mathbf{M} = 0$  which is generally the case for very small particles. It is, therefore, mostly used for understanding the reversal of the ensemble of non-interacting small particles having random orientation of EA which yields  $H_C = 0.48Ha$  and the remanence  $Mr = 0.5Ms$  [56]. This model predicts that the coercive field ( $H_C$ ) can be

estimated from the anisotropy field using  $H_k = 2K/M_s$ . However, for large particles above the critical radius reduced experimental value of the coercive field was observed. This is known as Brown paradox explained by the presence of defects or imperfections like dislocation, impurities etc. where domain walls might nucleate [57]. The probability of the presence of defects and hence nucleation of domains increases as the system size increases beyond single domain limit. Also, such system breaks down into domains to reduce the stray field energy. Hence, magnetization switching takes place via domain wall motion which can similar to rotation be reversible or irreversible depending on the amplitude of the magnetic field. When a demagnetized film is subjected to the small magnetic field, domains nearest to the direction of easy axis grow at the expense of the other domains and is reversible. On increasing the field as the domain wall moves, it may encounter defects. These defects pin the domain wall via magnetostatic coupling and hinders the motion of the domain walls. The translation motion of the domain wall becomes irreversible after it interacts with a defect. On increasing the field domain wall acquires the energy required to overcome the pinning potential. This can be observed as a small discontinuous jump in the hysteresis loop called as “Barkhausen effect”. On further increasing of the magnetic field, the Zeeman energy overcomes the anisotropy energy and this leads to the orientation of the spins along the applied field direction. The magnetic moments with increasing field are then aligned along the field.

## 1.5 Inverted thin films:

Thin films with uniaxial anisotropy, in general, have anisotropy field ( $H_K$ ) greater than the wall motion coercive field ( $H_c$ ) of the easy axis. As discussed earlier, the anisotropy field is the saturation field of the hard axis and can be deduced from  $H_K = 2K/M_S$  where  $K$  and  $M_S$  are the anisotropy energy and saturation magnetization, respectively [23]. However, it may happen that due to the presence of randomness in the system due to grain size, misalignment of local easy axis etc., the anisotropy field is less than or comparable to the coercive field of

easy axis. Such films in literature have been termed as “Inverted thin films” [58]. The inverted thin film arises due to local dispersion in anisotropy and is characterized by the formation of ripple domains. The dispersion in anisotropy can arise due to inhomogeneous strain between crystallites [59], different grain sizes [60], and insufficient magnetic field during deposition etc. [61]. These films are characterized by the formation of ripple and labyrinth domains. This topic will be discussed further in detail in Chapter 3 where the magnetization reversal and domain structure of inverted thin films due to the substrate rotation in Co thin films will be discussed.

## 1.6 Magnetization dynamics:

The magnetization reversal model discussed in previous sections 1.4.1 and 1.4.2 is based on the energy minimization where the change in magnetic field is slower than the system relaxation. It neglects the time evolution of magnetization and how the system will approach equilibrium states on changing the applied magnetic field. Therefore, one needs to consider the time evolution of magnetization given by Landau Lifshitz Gilbert (LLG) equation [62]. The equation of motion of a magnetic moment under the applied magnetic field as given by Landau–Lifshitz–Gilbert (LLG) equation is –

$$\frac{d\vec{M}}{dt} = -|\gamma|\vec{M} \times \vec{H}_{eff} + \alpha\vec{M} \times \frac{d\vec{M}}{dt} \quad (1.22)$$

where,  $M$  is the magnetization vector,  $\gamma$  is the gyromagnetic ratio, and  $\alpha$  is the Gilbert damping constant representing the dissipative relaxation mechanisms present in the system.

$\vec{H}_{eff}$  is given as -

$$\vec{H}_{eff} = -\mu_0^{-1} \frac{\partial E}{\partial \vec{M}} \quad (1.23)$$

The first term of the Eq. (1.22) gives the precession the magnetization vector along the direction of  $\vec{H}_{eff}$ . The second term describes the damping term which produces magnetization

relaxation towards the magnetic field as shown in Figure 1.15. During the damping process, the spins of the system precess and transfers the energy to the oscillations of the lattice of the bulk. This process may occur via spin-lattice or spin-orbit coupling. This LLG equation is in general used to simulate the hysteresis and domain structures in many simulating programs like Object Oriented Micromagnetic Framework (OOMMF) [63]. In this thesis work, we have performed OOMMF simulations to understand the magnetization reversal for multilayers which had random anisotropy along with uniaxial anisotropy. In Co (10 nm)/AlO<sub>x</sub> (*t* nm)/Co (10 nm) [where *t* = 3, 8, and 90 nm] multilayers it was used to understand the domain structure and layer-by-layer magnetization reversal of the system. It was also used to understand the formation of 360° DWs in multilayers of [Co<sub>80</sub>Fe<sub>20</sub> (1.8 nm)/Al<sub>2</sub>O<sub>3</sub> (3 nm)]<sub>9</sub> by changing the values of random and uniaxial anisotropy of the system.

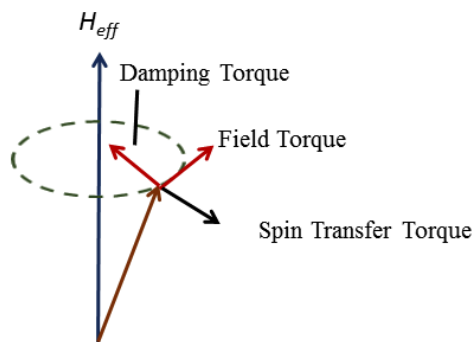


Figure 1.15: Schematic showing the precession and damping of magnetization vector.

## Chapter 2 : Experimental Techniques

In this chapter, the experimental techniques used to prepare and characterize the structural and magnetic properties of the samples are discussed. The continuous thin films of Co/AlO<sub>x</sub> were prepared by magnetron sputtering. The discontinuous [Co<sub>80</sub>Fe<sub>20</sub>/Al<sub>2</sub>O<sub>3</sub>]<sub>9</sub> multilayers were prepared by focussed ion beam (FIB) sputtering. The structural properties of the films were studied by using X- Ray Reflectivity (XRR) and Atomic Force Microscopy (AFM). To investigate the magnetic properties Magneto-Optic Kerr Effect (MOKE) based microscopy was used as major technique complemented by Polarized Neutron Reflectivity (PNR) and Superconducting Quantum Interference Device (SQUID).

### 2.1 Thin Film Deposition techniques:

The various methods for thin film deposition techniques can be broadly classified into two groups:

(a) Chemical Vapour Deposition (CVD) - In this process, thin films are grown by introducing volatile precursors in their vapor phase into the reaction chamber which react or decompose generally on a heated substrate. Various types of CVD process exist such as thermal (heat-assisted reactions), photo-assisted CVD (reactions promoted by higher frequency radiation such as UV light) and plasma-enhanced CVD (PECVD) etc.

(b) Physical Vapour Deposition (PVD) - In this process, the deposition material in solid form is vaporized or sputtered to form a flux of atoms or molecules, in a vacuum or low-pressure gaseous environment and is deposited on the substrate. The main categories for PVD are vacuum evaporation, sputtering and ion plating. The samples in this thesis were prepared by sputtering. Sputtering has several advantages over other techniques. The most important is that, it can be used to deposit any material, irrespective of its conductivity. It can be used to

deposit metals (conducting) as well as dielectrics. Metals can be sputtered using direct current (DC) sputtering. However, insulators or dielectrics, which are difficult to deposit using evaporation technique due to their high melting point, can be deposited using radio frequency (RF) sputtering. Other advantages of sputtering are -

(1) to prepare films with high uniformity of thickness over a larger area; (2) to have good adhesion to the substrate; (3) to obtain better reproducibility of films; (4) to achieve films with a same stoichiometry of the original target (5) the ability to control film thickness in a simple manner.

### **2.1.1 Sputtering:**

Sputtering is the process in which energetic ions produced from the gaseous plasma are bombarded to the target material and gets deposited on everything which is kept in their line-of-sight. The schematic of sputtering is shown in Figure 2.1. In our deposition unit, inert argon gas is used to create a plasma of argon ions. A negative voltage is applied to the target (cathode) which results in the formation of gaseous plasma. The positive argon ions from the plasma are accelerated to the negatively biased target. Due to the momentum transfer that occurs between the ions and sputter target, the atoms/ molecules get ejected along with the secondary electrons. These sputtered or ejected particles then get deposited on the substrate. The secondary electrons help in further ionizing the argon atoms which contributes in maintaining the plasma, thus making the sputtering process a self-sustained process.

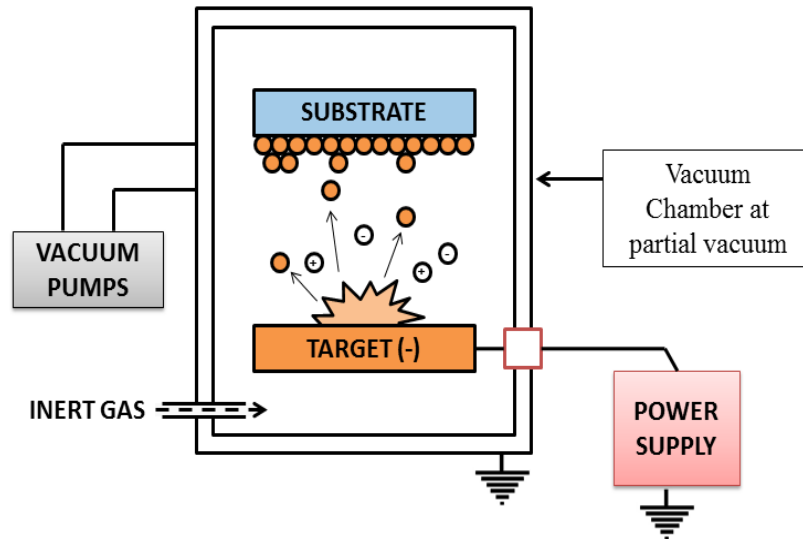


Figure 2.1: Schematic for sputtering deposition technique.

Various types of sputtering method exist depending on the requirement of the thin film preparation. The sputtering process explained above describes the DC diode sputtering. However, one cannot use DC sputtering for insulators as the positive charge will build up on the target surface resulting in plasma extinguishment. This can be avoided by using an alternating radio frequency (RF) power supply. For the negative half of the cycle i.e. when the target is negatively biased, the positively charged argon ions get attracted to the target and results in its sputtering and creating a positive charge on the target surface. In the positive half of the cycle, (i.e. when the target is positively biased) the electrons from the plasma get attracted to the target and neutralize it. Since the sputtering occurs only on one-half of the cycle, the rate for the RF sputtering is generally low compared to the DC sputtering. It should be noted that RF sputtering can be used for both metals and insulators.

For the preparation of the compound thin film, reactive gasses like oxygen or nitrogen can be used instead of inert gas to sputter the target material. This mode of sputtering is called reactive sputtering. In this process, the sputtered atoms react with the gasses to form the oxide or nitride films.

In conventional sputtering (diode sputtering), the rate of deposition is very less and it needs a high density of plasma which means that high argon pressure is required. To overcome this magnetron sputtering is used, where a permanent magnet is placed behind the target. In this method, the electric field applied to the target is perpendicular to the magnetic field. The trick of the magnetron is to use the magnetic field to trap the ejected secondary electrons which allow having (a) sputtering at low pressure and (b) high density of plasma resulting in better deposition rate. Conventionally, the magnet is designed such that one pole of the magnet is at the central axis of the target and the other is formed by the magnet at the outer ring of the target. The initial design for the magnetron sputtering was the one with balanced magnetron configuration, where the strength of the magnetic poles at the central axis and at the outer rings are equal and hence cancel each other [64]. However, in this configuration, the major drawback is that the plasma is confined to the vicinity of the target. This can be overcome by using an unbalanced magnetron where the strength of the poles are different resulting in some uncompensated flux directed towards the substrate. In this way, the plasma density gets enhanced in the vicinity of the substrate and eventually the ion bombardment also increase onto the substrate. Figure 2.2 shows the difference between the balanced and unbalanced magnetron configuration. Magnetron sputtering can be used in both DC and RF sputtering.

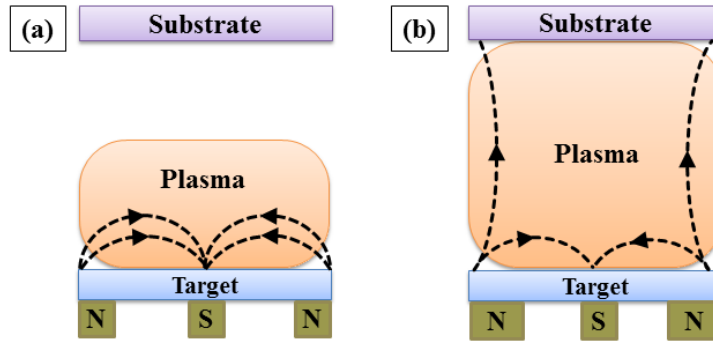


Figure 2.2: Schematic showing the (a) balanced magnetron configuration and (b) unbalanced magnetron configuration [64].

We have used DC magnetron sputtering for the preparation of Co thin films and RF magnetron sputtering for  $\text{AlO}_x$  thin films. It should be noted that since  $\text{AlO}_x$  is an insulator, therefore, RF sputtering was used to avoid the build-up of charges on the target surface. Another method for sputtering is to use focussed ion beams (FIB) for sputtering. This technique was used to prepare Discontinuous Metal Insulator Multilayers (DMIMs) of structure:  $\text{Glass}/\text{Al}_2\text{O}_3$  (3 nm)  $[\text{Co}_{80}\text{Fe}_{20}(t_n)/\text{Al}_2\text{O}_3$  (3 nm)] $_m$  with  $t_n = 1.3$  and 1.8 nm and  $m = 10$  and 9, respectively.  $t_n$  refers to the nominal thickness of  $\text{Co}_{80}\text{Fe}_{20}$  layer. A part of this thesis is focussed on investigating the magnetization reversal of these films. These samples were prepared by focused Xe- ion beam sputtering by the group of Prof. P. P. Freitas at INESC, Lisbon, Portugal. The films prepared with  $t_n = 1.3$  nm was below the in-plane percolation limit of the CoFe film. This behaves as an ensemble of single domain nanoparticles on  $\text{Al}_2\text{O}_3$  matrix showing superferromagnetic behavior [7]. However, it should be noted that  $t_n = 1.8$  nm was above the percolation limit of CoFe thickness (1.4 nm) and hence is continuous. The deposition was performed at  $200^\circ\text{C}$  with a rate of 0.012 and 0.032 nm/s, for  $\text{Al}_2\text{O}_3$  and  $\text{Co}_{80}\text{Fe}_{20}$  layer, respectively. The details of the preparation can be found in references [65, 155].

## 2.1.2 Sample preparation using magnetron sputtering at NISER:

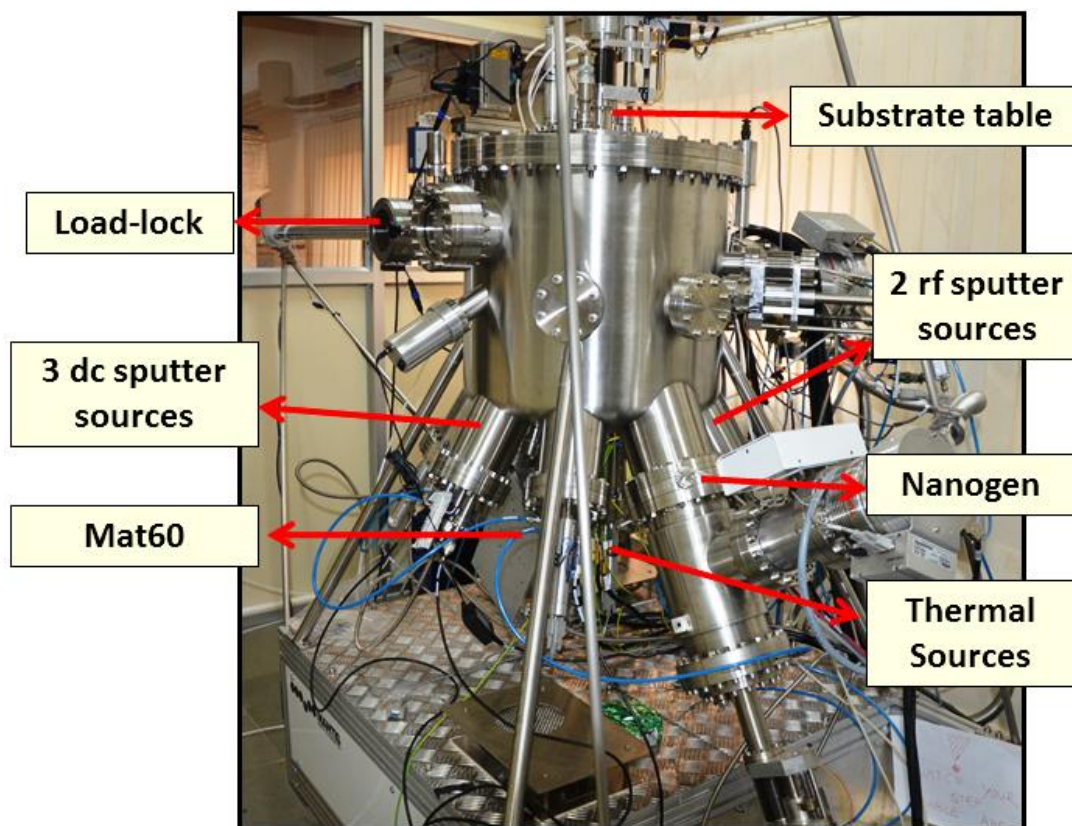


Figure 2.3: Outer view of the Multi-deposition UHV system at NISER procured from Mantis Deposition Ltd, U.K showing its various units. The 4 pocket e-beam evaporator is situated behind the Nanogen unit and hence is not visible.

The sputtering system used to prepare Co/AlO<sub>x</sub> thin films is a multi-deposition unit of the QPrep series from Mantis Deposition Ltd, U.K (Figure 2.3). The main chamber of the deposition unit is equipped with a load lock. This helps in transferring the sample to the main chamber without breaking its vacuum. In addition to the backing pump, the load lock, and the main chambers have separate turbo-molecular pumps so that the pressure of the system can be pumped down to UHV range.

The deposition unit contains-

- (i) 3 DC and 2 RF unbalanced magnetron sputtering guns.
- (ii) Two thermal evaporation sources where the target in the form of powder or pellet can be evaporated by resistive heating.
- (iii) A 4 pocket e-beam evaporator where the electron beam is used to heat the crucibles for evaporating the materials for thin film deposition.
- (iv) A nano-particle generator called 'Nanogen' which can produce nanoparticles inside the chamber under vacuum conditions. It should be noted the Nanogen is based on the principle of "terminated gas condensation" [66] or "Terminated cluster growth" process [67] in which the atoms produced by the sputtering is cooled down via collisions with inert gas atoms at high pressure leading to the agglomeration and formation of nanoparticles.
- (v) Mat60 unit which can be used for producing the nascent oxygen from the plasma of the molecular oxygen gas for preparing oxide based materials.

In the QPrep deposition system, each unit has its own shutter to prevent it from contamination of other materials during deposition. The substrate table is positioned on the top of the main chamber such that it is at the focus point of all the above mention units. Due to this geometrical construction of the main chamber, the angle between the substrate normal and the incident flux from the target are at  $30^\circ$  and is  $45^\circ$  w.r.t to the substrate plane (horizontal), except for thermal deposition which is at normal incidence. This oblique configuration of targets w.r.t to substrate normal leads to the growth induced magnetic uniaxial anisotropy in the deposited thin films [6]. Therefore, all the multilayers Co/AlO<sub>x</sub> prepared for our investigation had uniaxial anisotropy. This will be discussed in detail in chapter 3. The substrate table can be rotated up to 20 rpm to have a uniform thickness. It can be heated up to 800 °C by four halogen lamps present in the substrate table unit. The samples

were prepared on p and n-type doped Si (100) substrates. Prior to deposition, the Si (100) substrates were cleaned in acetone followed by isopropanol for 5 minutes each using an ultrasonic cleaner. It was then blow dried using nitrogen gas (5N purity). Next, the cleaned substrates were mounted inside the deposition chamber and were plasma cleaned for 30 seconds with Ar<sup>+</sup> prior to deposition. This was performed to remove any additional impurity if present on the substrate surface. However, the cleaned substrates of Si will still have the native SiO<sub>2</sub> layer. The parameters for plasma cleaning were pressure =  $1.5 \times 10^{-2}$  mbar, Ar flow = 75 sccm and RF power = 40 W. The AlO<sub>x</sub> layers were deposited at the rate of 0.07 Å/s at  $3 \times 10^{-3}$  mbar of Ar<sup>+</sup> pressure by RF magnetron sputtering with power of 120 W. The Co layer was deposited at the rate of 0.22 Å/s at  $4 \times 10^{-3}$  mbar of Ar<sup>+</sup> pressure by DC sputtering with power of 56 W.

Co thin film with sample structure of AlO<sub>x</sub> (3 nm)/Co (*t* nm)/AlO<sub>x</sub> (3 nm) were prepared where *t* = 3.5 and 10 nm, to study the magnetization reversal and the domain structures. To overcome the anisotropy due to oblique deposition, the samples with *t* = 10 nm of Co thickness were rotated with 10 and 20 rpm of substrate rotation ( $\omega$ ) throughout during the preparation. The magnetization relaxation and domain structures were studied in all these samples to understand the effect of the substrate rotation. The multilayers of structure AlO<sub>x</sub> (3 nm)/ Co (10 nm)/ AlO<sub>x</sub> (*t* nm)/ Co (10 nm)/ AlO<sub>x</sub> (3 nm) studied in this thesis were prepared on Si (100) substrates at room temperature. These Co(10nm)/ AlO<sub>x</sub> (*t* nm)/Co(10 nm) multilayers were prepared to investigate the effect of interlayer coupling by changing the spacer AlO<sub>x</sub> thickness from 3 to 270 nm.

## **2.2 Atomic Force Microscopy (AFM):**

In this thesis work, atomic force microscope (AFM) was used to study the surface morphology and grain structure of the Co thin films. AFM was invented in 1986 by Binnig,

Quate and Gerber [68] to extend the use of scanning tunneling microscopy (STM) for insulating samples.

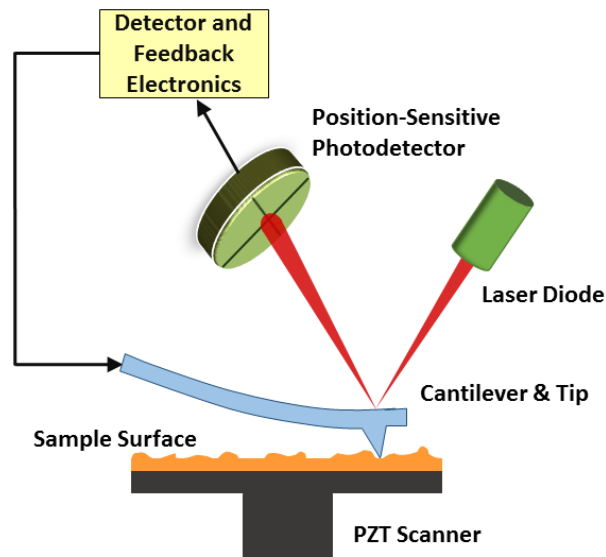


Figure 2.4: Schematic of Atomic Force Microscopy (AFM)

Figure 2.4 shows the schematic of an AFM set up. An AFM consists of a sharp probe (tip) made up of Si or silicon nitride integrated on a cantilever spring on which the light from laser falls on the cantilever and is reflected to a photodetector. The tip is scanned over the surface and depending on the distances between the tip and the sample surface, the interaction will be either long range attractive or short range repulsive forces. Therefore, any change of the surface height will change the force experienced on it and hence will deflect the cantilever accordingly. This deflection in the cantilever is measured by reflecting the laser beam to a 4-segment photodetector. The change in the intensity of the photodetector gives the topography of the surface. To maintain a constant sample to tip separation and to avoid any damage due to the sample - tip collision, an electronic feedback is given during the scanning of the surface. This feedback helps to maintain a constant force of interaction between the sample and the tip by using the piezo scanner.

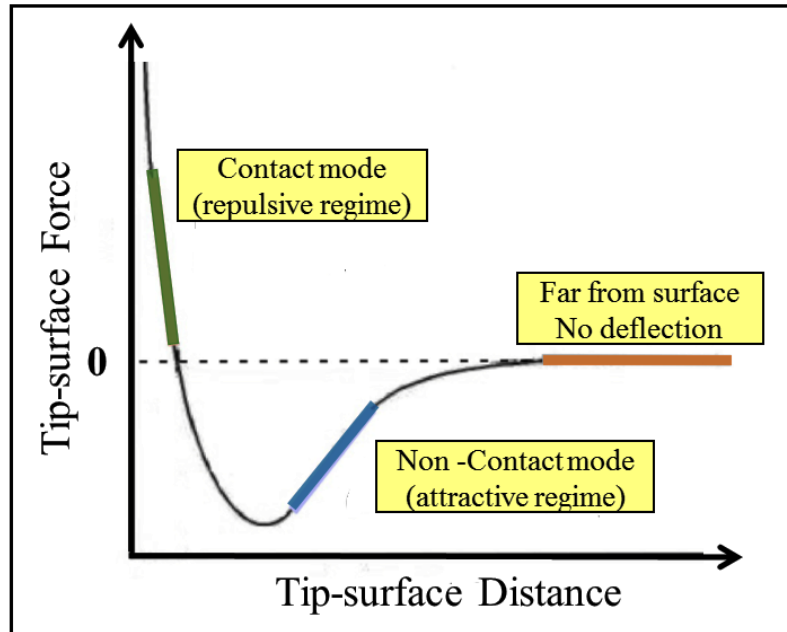


Figure 2.5: Graph showing the force of interaction between the tip and sample surface vs the distance between them [69].

AFM measurements can be performed in different modes – static mode (contact mode) and dynamic mode (tapping mode and non-contact mode), operating at various interaction forces depending on the tip to sample distance as shown in Figure 2.5. In contact mode, the tip is scanned in close contact over the sample surface. The force on the tip is in the repulsive region of the probe surface interaction as shown in Figure 2.5. In non-contact mode, the tip is held at a height of few nanometres above the sample surface such that the tip is close to the surface but does not touch it. Therefore, the tip experiences attractive Van der Waals forces from the sample and works in the attractive regime of the curve shown in Figure 2.5. However, it should be noted that the attractive forces in non-contact mode are weaker than that of contact mode. The measurements in this thesis were performed using tapping mode where the large amplitude of oscillations of the cantilever occurs. As the tip gets closer to the sample surface the forces acting on the cantilever results in the decrease in the oscillation’s amplitude. In this mode, it is required to have constant oscillation amplitude over the sample. This is achieved by the feedback loop which maintains the constant distance

between the sample surface and the tip. The feedback loop applies a voltage to the piezo which changes the cantilever height to maintain its constant distance from the sample surface and allows to acquire the topographic image of the sample.

The AFM Nano-observer from Concept Scientific Instrument (CSI) has been used to investigate the surface topography and the grain size of the Co films prepared with different substrate rotation. The measurements were performed in tapping mode. The tips used for the measurements were from AppNano which were made of Si having radius less than 10 nm. The force constant and the resonance frequency of the cantilever was 0.6 – 3.7 N/m and 43 – 81 kHz, respectively.

### **2.3 Secondary Ion Mass Spectroscopy (SIMS):**

Secondary ion mass spectrometry (SIMS) technique uses focused primary ion beam ( $\text{Cs}^+$ ,  $\text{O}^-$ ,  $\text{O}_2^+$ ,  $\text{Ar}^+$ ) of energy 0.5 -20 KeV to sputter off the sample surface and then analyzing the emitted secondary ions by ion mass spectroscopy. It can detect elements from hydrogen to uranium with the elemental detection limits ranging from parts per million to parts per billion which makes it the most surface sensitive technique. It can also measure isotopic ratios to a precision of 0.5 to 0.05% [70]. The primary beam on interaction with the sample results in sputtering of mostly neutral atoms or molecules, out of which a small percentage is ionized (Figure 2.6). To determine the elemental or isotopic composition, a mass spectrometer is used to measure the mass/charge ratios of the secondary ions. Depending on the dose of the primary ion, SIMS can be classified as static or dynamic SIMS. If the dose of the primary ion is such that the damage to the surface is negligible and considered to be non-destructive then it is called static SIMS. However, if the large dose of the primary ions per unit area is used to sputter into the bulk of the sample, then it is called dynamic SIMS. This mode of operation can be used for obtaining the chemical depth profiles of the system [71, 72].

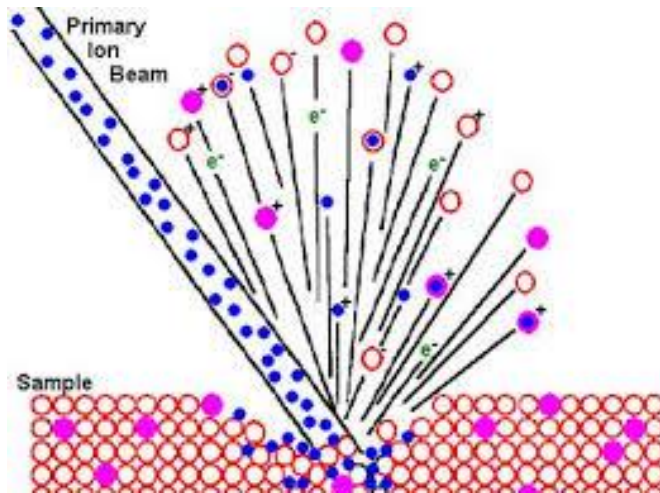


Figure 2.6: Schematic showing the effect of the bombardment of the primary beam on the sample. It produces neutral particles and secondary ions from the sample surface. Image adapted from [73].

SIMS measurements were performed on Co/ $\text{AlO}_x$  trilayers in dynamic time-of-flight mode to acquire the depth profile and interface of the layers. The measurements were performed using ION-TOF GmbH, at National Physical Laboratory, New Delhi. In order to get information about the depth, the time axis (x-axis) is calibrated or converted to the depth of the film by using a profilometer. In this case, the sputter crater depth is measured by the profilometer by dragging a stylus across the crater and noting vertical deflections.

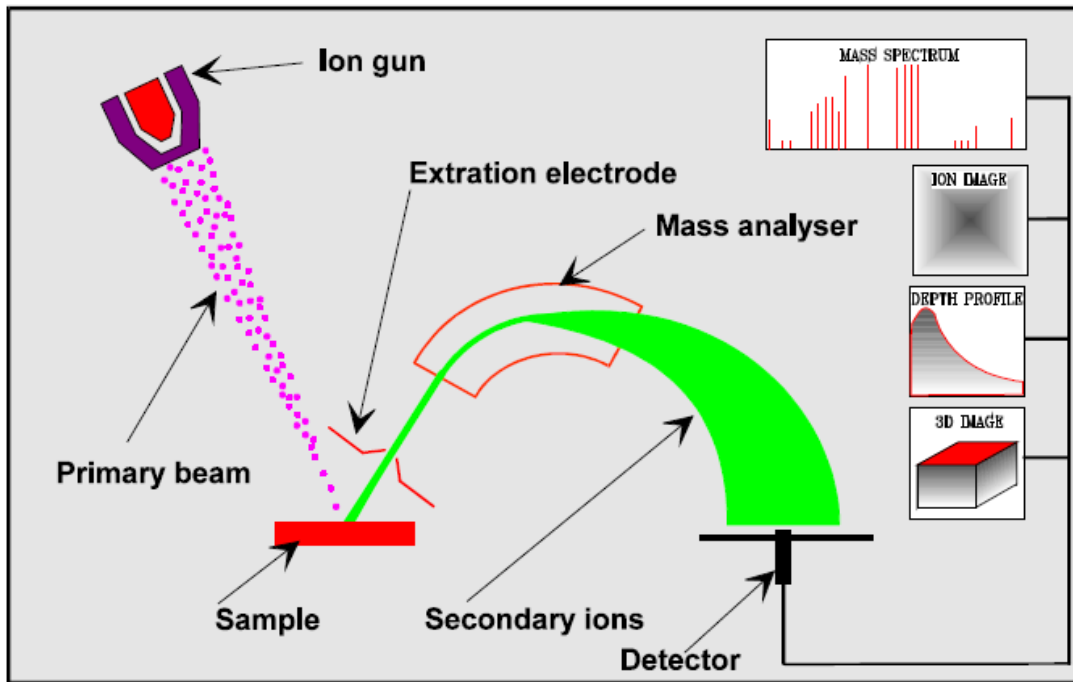


Figure 2.7: Schematic showing the components of SIMS [74].

Typical components of SIMS are shown in Figure 2.7. It consists of a primary ion gun which generates the primary ion beam using electron ionization of noble gasses or by surface ionization or by liquid metal ion gun. Since we had multilayers of Co/AlO<sub>x</sub>, the Cs<sup>+</sup> ions were used as primary beam to enhance the yield of electronegative O element. The energy of the Cs<sup>+</sup> ion beam was 25 KeV. The primary beam generated from the source is then accelerated and focused onto the sample by the primary ion column. A typical column consists of a mass filter, apertures, lenses and deflection plates. The mass filters allow removing the impurities in the ion beam. The shape of the primary beam and intensity is controlled by the electrostatic lenses and the apertures. The deflection plates help to steer the primary ion beam in passing through the center of the lenses, in positioning the beam, and in raster scanning the beam. It is then allowed to interact with the sample kept in a high vacuum in the sample chamber. The secondary ions produced are then extracted by into time-of-flight (TOF) mass analyzer by applying a high extraction voltage between the sample and the

extraction lens. It is very important to keep the potential difference between the sample and the extraction (immersion) lens to be constant in order to obtain a constant ion beam current. In the TOF mode of mass spectrometry, the ions with the same energy but different masses travel with different velocities. The generated ions are accelerated to a common energy by an electrostatic field which then travel over a drift path to the detector. In this way, the ions with different masses arrive at different time at the detector due to their variable velocities. Therefore in the TOF mode by measuring the flight time for each ion one can easily calculate its mass.

## **2.4 X-Ray Reflectivity (XRR):**

X-rays are a powerful non-destructive tool to study the microstructural properties of the thin films since its wavelength is comparable to the interatomic distances in solids. It can be used in diffraction or in reflectivity mode following Bragg's law:

$$n\lambda = 2d \sin \theta \quad (2.1)$$

where,  $d$  is the distance between adjacent atomic planes in solid,  $\lambda$  is the wavelength of x-rays and  $n$  is an integer that gives the order of interference. In diffraction mode it is used to obtain crystallographic information like lattice strain, crystal size and orientation relationship of a thin-film material. In reflectivity mode it can be used to find the thin film parameters like thickness of the layer and multilayers, density, and surface or interface roughness [75, 76]. XRR measurements can be performed on any thin film irrespective of its crystallinity i.e. it can be used on crystalline as well as amorphous thin films with the depth resolution from few atomic layers to several hundred nanometres. In this thesis XRR measurements were performed to find the thickness and roughness of the sample. These parameters were then used for analyzing the data obtained from polarized neutron reflectometry to find the magnetization depth profile of the multilayers.

The measurements were performed at JCNS, Forschungszentrum, Jülich using Bruker D8 with Cu  $K_\alpha$  radiation of wavelength 0.154 nm in specular reflectivity geometry where the angle of incidence is equal to the angle of reflection as shown in Figure 2.8. It should be noted that the angle of incidence and reflection is defined here with respect to the surface plane. In this mode, the X-ray beam is reflected from the sample at the grazing angle  $\theta$  and the intensity of the reflected beam is recorded by the detector at an angle of  $2\theta$ . In this mode one measures the momentum transfer vector  $\mathbf{q} = \mathbf{k}_r - \mathbf{k}_i$  along the surface normal as shown in Figure 2.8.

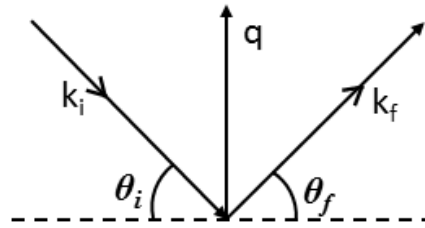


Figure 2.8: Scattering geometry for x-ray reflectivity.  $\theta_i$  and  $\theta_f$  are the angles of incidence and angle of reflection.  $k_i$  and  $k_r$  are the wave vectors of the incident and reflected beam. The momentum transfer vector is shown as  $q$ .

In x-ray reflectivity, the incident x-rays are reflected from the top and bottom interface of the films due to the change/difference in electron density which changes the refractive index of the medium. This leads to the formation of the interference pattern. Similar to Bragg's condition in diffraction (Eq. 2.1), constructive and destructive interference pattern gives rise to fringes which in this case are called as Kessing fringes. Using Bragg's law of diffraction, the thickness of the thin film can be calculated [76].

In the following section, the basic principles of x-ray reflectivity are briefly discussed. Consider an electromagnetic wave propagating through a medium of refractive index  $n(\mathbf{r})$ . Considering, the  $N$  atoms per unit cell as harmonic oscillators having resonance frequencies  $\omega_j$ , the refractive index is given by [77]-

$$n(\mathbf{r}) = 1 + N \frac{e^2}{\varepsilon_0 m} \sum_{j=1}^N \frac{f_j(\omega)}{\omega_j^2 - \omega^2 - 2i\omega\eta_j} \quad (2.2)$$

where  $\omega$  is the frequency of the incoming wave,  $e$  and  $m$  are the charge and mass of the electron, respectively. The  $\eta_j$  is the damping factor and the form factor  $f_j$  is the forced oscillation strength of the  $j^{\text{th}}$  atom.  $f_j$  is a complex number and can be expressed as,  $f_j = f_j^0 + f_j'(E) + i f_j''(E)$ , where  $f_j'(E)$  and  $f_j''(E)$  are dispersion and absorption corrections dependent on the energy of the radiation, respectively [77]. Since for x-rays  $\omega > \omega_j$ , the refractive index can be rewritten as –

$$n(\mathbf{r}) = 1 - \delta(\mathbf{r}) + i\beta(\mathbf{r}) \quad (2.3)$$

where,

$$\delta(\mathbf{r}) = \frac{\lambda^2}{2\pi} \rho(\mathbf{r}) \sum_{j=1}^N \frac{f_j^0 + f_j'(E)}{Z} \quad (2.4)$$

$$\beta(\mathbf{r}) = \frac{\lambda^2}{2\pi} \rho(\mathbf{r}) \sum_{j=1}^N \frac{f_j''(E)}{Z} = \frac{\lambda}{4\pi} \mu(\mathbf{r}) \quad (2.5)$$

$\rho(\mathbf{r}) = r_e \rho(\mathbf{r})$  is the scattering length density,  $r_e$  is the classical radius,  $\rho(\mathbf{r})$  is the electron density and  $\sum_j Z_j = Z$  is the total number of electrons present in the unitcell [77]. Now neglecting  $f_j'(E)$  and approximating  $f_j^0(E) \sim Z_j$ , Eqn. (2.2) may be rewritten as-

$$n(\mathbf{r}) = 1 - \frac{\lambda^2}{2\pi} \rho(\mathbf{r}) + i \frac{\lambda}{4\pi} \mu(\mathbf{r}) \quad (2.6)$$

where  $\mu(\mathbf{r})$  is the linear absorption coefficient. Typically,  $\delta$  is of the order  $10^{-6}$  and  $\beta$  is another one or two order of magnitude below this, therefore the refractive index for x-rays are slightly less than unity. Therefore, when x rays passes from air ( $n = 1$ ) to a medium ( $n < 1$ ) of higher electron density, at very small angles, it is possible to have total external reflection of the x ray beam. Hence the critical angle below which the total internal reflection occurs can be found by applying Snell–Descartes’ -

$$\cos \theta_c = n = 1 - \delta \quad (2.7)$$

Since, for x-ray reflectivity measurements, the critical angle for total external reflection is very small therefore,  $\cos \theta_c$  can be approximated as  $1 - \theta_c^2/2$ . As mentioned earlier, the value of  $\delta$  is very small, therefore Eq. 2.7 becomes

$$\theta_c^2 = 2\delta \quad (2.8)$$

Therefore, for all incident angle less than  $\theta_c$ , total external reflection occurs as a plateau in the reflectivity curve. For scattering experiments, it is convenient to work in reciprocal space where the incident and reflected waves are described by their wave vectors  $\mathbf{k}_i$  and  $\mathbf{k}_r$  and the scattering vector  $\mathbf{q}$  as shown in Figure 2.8. The momentum transfer vectors are -

$$q_z = \frac{2\pi}{\lambda} (\sin \theta_i + \sin \theta_f) \quad (2.9)$$

$$q_x = \frac{2\pi}{\lambda} (\cos \theta_i - \cos \theta_f) \quad (2.10)$$

Where, the z-axis is along the surface normal and x-axis lies in the plane parallel to the surface. Therefore, in this geometry,  $q_y = 0$ . For specular reflection of x rays we have,  $\theta_i = \theta_f = \theta$ . Hence,

$$q_z = \frac{4\pi}{\lambda} (\sin \theta) = 2k \sin \theta \quad (2.11)$$

Therefore, the total external reflection will occur for critical wave vector transfer at  $q_c = 2k \sin \theta_c$ . Using eq. 2.8 and using the approximate value of  $\delta$ , one gets the relation between the scattering length density and critical wave vector as follows -

$$q_c = \sqrt{16\pi\rho} \quad (2.12)$$

It should be noted that, critical wave vector depends only on the material properties.

Let us now discuss the case when the reflectivity of the x-rays incident on a smooth surface, it then gets split into reflected and the transmitted wave having wave vectors  $\mathbf{k}_r$  and  $\mathbf{k}_t$ . Since the refractive index for air is unity, the Fresnel coefficients for reflection ( $r$ ) and transmission ( $t$ ) will be same for s and p polarized light [78] given as:  $r = \frac{k_i - k_t}{k_i + k_t}$  and  $t = \frac{2k_i}{k_i + k_t}$ . Therefore the intensity of the reflected radiation ( $R$ ) is given as -

$$R = |r^2| = \left| \frac{q_z - \sqrt{q_z^2 - q_c^2 + 2i(2k)^2 \beta}}{q_z + \sqrt{q_z^2 - q_c^2 + 2i(2k)^2 \beta}} \right|^2 \quad (2.13)$$

It can be observed from Eq. (2.13), for  $q_z \gg q_c$ , the reflectivity curve follows  $\frac{1}{q^4}$  power law. For multilayers or superlattices, the reflectivity is calculated such that at each interface boundary conditions are satisfied. The reflection and transmission coefficients at each interface are added together to give the overall reflectivity and transmission coefficients. This can be calculation by using Parratt's recursion formula [79] or by using the matrix calculation.

## 2.5 Cross-section Transmission Electron Microscope (TEM):

Transmission electron microscope uses electron beam to image the morphology, microstructural properties like dislocations, grain boundaries etc. The working principle of TEM is similar to that of optical microscope with the difference that the light beam is replaced by an electron beam. TEM basically consists of (a) an illuminating system consisting of an electron gun producing electron beam by application of high voltage, (b) condenser system to produce focused monochromatic electron beam and (c) image recording system. The focussed electron beam on interacting with sample will result mostly in transmission and a part will be scattered. The transmitted beam then passes through the objective lenses to form the image. This image can be enlarged using the intermediate and

projector lenses before being projected onto the phosphor screen. The working principle and details of the TEM can be found in detail in Ref [80]. TEM can be performed in two ways – planar and cross-sectional. In this work cross sectional TEM are performed to investigate the microstructural properties of all layers of the sample. For this purpose, samples for performing cross-sectional TEM is prepared by cutting it in the plane and joining the two pieces by the glue. The samples are then thinned by mechanical polishing ion milling to the surface perpendicular to the surface of interest. To investigate the crystallinity of the samples, cross sectional TEM was performed on Si (100)/ AlO<sub>x</sub> (3 nm)/Co (3.5 nm)/AlO<sub>x</sub> (3 nm)/Co (3.5 nm)/AlO<sub>x</sub> (3 nm) and Si (100)/ AlO<sub>x</sub> (3 nm)/Co (10 nm)/AlO<sub>x</sub> (23 nm)/Co (10 nm)/AlO<sub>x</sub> (3 nm) samples using JEOL-2010, at Institute of Physics, Bhubaneswar.

## **2.6 Superconducting Quantum Interference Device (SQUID) magnetometer:**

SQUID magnetometers made up of superconducting coils (pick-up coils) and superconducting quantum interference device (SQUID) as flux detector can be used to measure magnetic sensitivity of the order of  $10^{-7}$  emu ( $10^{-10}$  Am<sup>2</sup>). SQUID consists of two superconductors separated by thin insulating layers to form two parallel Josephson junctions. The electrical current density through a Josephson junction depends on the phase difference  $\Delta\phi$  of the two superconducting wave functions. The voltage across the junction can be calculated by taking the time derivative of the  $\Delta\phi$ . This phase difference,  $\Delta\phi$  will be also affected by the magnetic flux  $\Phi$  passing through a superconducting ring. Hence, magnetic flux can be converted to an electrical voltage. Therefore, in SQUID magnetometers one does not directly measures the magnetization of the sample. The sample is placed in superconducting sensing coil, which is coupled through superconducting circuitry to the SQUID device (Figure 2.9). A superconducting electromagnet is used to generate magnetic

field. The sample vibrates up and down through the superconducting coils (pick-up coil). The magnetic moment of the sample produces a magnetic flux in the pick-up coil and hence induces an electric current in the detection coil. Any change in the detection coil will produce a persistent current in the detection circuit which will be proportional to the magnetic flux. Since the SQUID device can function as a magnetic flux to voltage converter, the variation in the current in the detection circuit produces the corresponding variations in SQUID output voltage which is proportional to the magnetic moment of the sample.

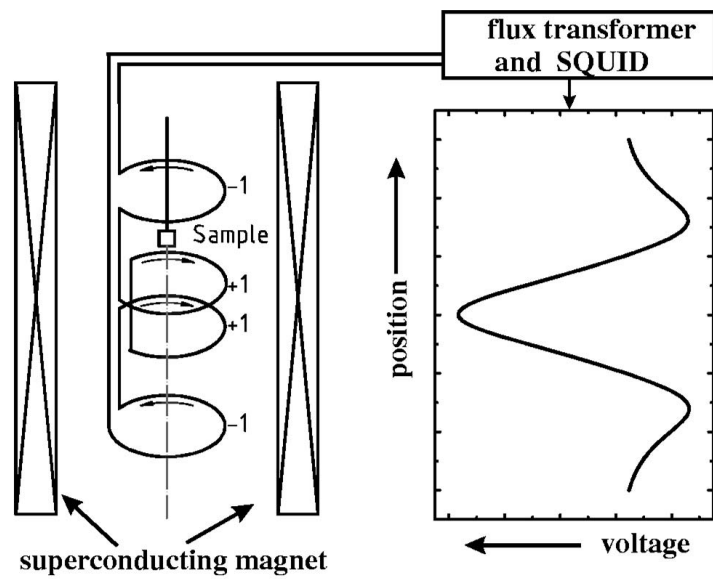


Figure 2.9: Schematic showing the geometry of the pick-up coil of the SQUID. The graph on the right shows the theoretical behaviour of magnetic dipole with respect to sample length [81].

The samples measured in this thesis were performed on MPSM SQUID VSM EverCool system from Quantum Design at JCNS, Forschungszentrum, Jülich and by VSM at IIT Guwahati. The  $M$  vs  $H$  measurements were performed at room temperature for easy and hard axis to know the magnetic moment and to calculate the anisotropy of the system.

## **2.7 Magneto- Optic Kerr Effect (MOKE) fundamentals-**

Magneto-Optic Kerr Effect (MOKE) is the change in polarization or intensity of the incident polarized light after being reflected from the surface of a magnetic sample [82]. It is similar to Faraday Effect, with the difference that in the later the change in polarization of the linearly polarized light occurs when the light is transmitted through the magnetic medium [83]. Depending on the detector at the end signal, MOKE can be used as magnetometer as well as microscope to view the domains in the magnetic thin films and multilayers. Apart from MOKE several other techniques like SQUID, MFM exists for studying the magnetic properties. However, MOKE is a popular technique to study magnetic properties of thin films and multilayers because of several advantages including the sensitivity down to monolayer resolution [84], high temporal and spatial resolution and its low cost. The time needed to measure a hysteresis loop and the acquisition of domain image in MOKE is significantly less compared to SQUID. However, it should be noted that the MOKE probes the magnetic properties locally whereas SQUID gives the magnetization from the whole sample. Even though, the resolution of the domain imaging using MOKE is limited by the wavelength of the visible light compared to other electron based techniques like Lorentz microscopy, Scanning electron microscopy with polarisation analysis (SEMPA) etc., yet the simplicity to combine it with in-situ experiments and low cost makes it a popular tool for studying the magnetic properties and domain imaging.

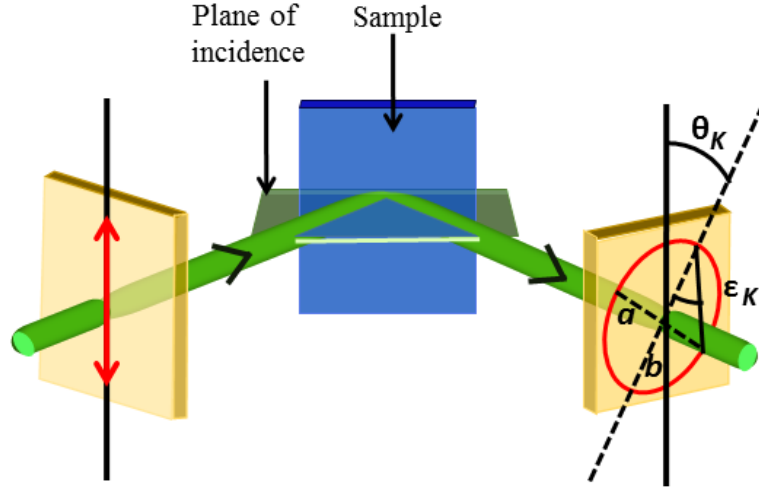


Figure 2.10: Schematic of MOKE showing the formation of elliptically polarized light from the incident linearly s-polarized light. The minor and major axes of the ellipse has been marked as ‘a’ and ‘b’, respectively [85].

Microscopically, MOKE description can be interpreted as circular birefringence. Linearly polarized light can be considered to be a superimposition of left and right circularly polarized light having same magnitude of angular momentum and opposite helicity. This light when incident on the non-magnetic thin film, will drive the electron in left and right circular motion with equal radius. The radius is proportional to the electric dipole moment. In presence of magnetic sample, an additional Lorentz force ( $F = q[E + (v \times B)]$ ) acts on the electrons. This force points toward or away from the circle’s centre for left or right circular motion, resulting in unequal radius of left and right circularly polarized light. The difference in the radii of the left – circularly and right-circularly polarized modes will give different dielectric constants resulting in the rotation of plane polarised light with Kerr rotation ( $\theta_K$ ) and ellipticity ( $\epsilon_K$ ) [86]. Figure 2.10 shows the change of linearly polarized light to elliptically polarized light with rotation ( $\theta_K$ ) and ellipticity ( $\epsilon_K$ ) on being reflected from the magnetic sample. The rotation ( $\theta_K$ ) is defined as the angle between the direction of polarization of incident beam and the major axis of the reflected elliptically polarized light.

Kerr ellipticity is defined as the ratio of major axis ( $b$ ) to minor axis ( $a$ ) of the ellipse i.e  $\epsilon_K = \arctan(b/a)$ . This Kerr rotation and ellipticity is proportional to the magnetization of the sample and varies linearly with it. However, macroscopically, the magneto-optic Kerr effect can be described by the dielectric properties of a medium. The dielectric property of a medium, characterized by a  $3 \times 3$  tensor ( $\epsilon_{ij}$  with  $i, j = 1, 2, 3$ ) can be decomposed into a symmetric and anti-symmetric part. The symmetric part of the dielectric tensor does not contribute to the magneto-optic effect and have equal diagonal elements for proper choice of coordinates. The antisymmetric off diagonal part of the dielectric tensor gives rise to magneto-optic effects. Therefore, the dielectric tensor describing the magnetic material is given as-

$$\tilde{\epsilon} = \epsilon \begin{pmatrix} 1 & -iQ_v m_z & iQ_v m_y \\ iQ_v m_z & 1 & -iQ_v m_x \\ -iQ_v m_y & iQ_v m_x & 1 \end{pmatrix}$$

where,  $Q_v$  is the Voigt constant and  $(m_x, m_y, m_z) = m$  is the normalized magnetization vector.

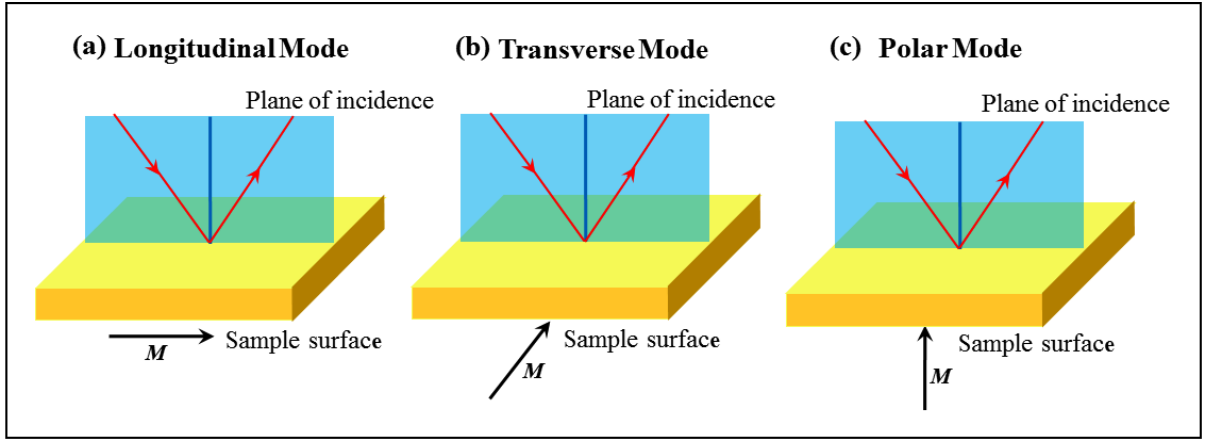


Figure 2.11: Different geometries of MOKE: (a) Longitudinal, (b) Transverse, and (c) Polar mode.

### 2.7.1 MOKE Geometries:

There can be three possible geometries for the MOKE classified according to the direction of magnetization and the plane of incidence are described below-

- **Longitudinal MOKE** - In this configuration the magnetization is parallel to both the plane of incidence and the sample surface as shown in Figure 2.11(a). In this effect, the linearly *s* or *p* - polarized light upon interaction with magnetization of the sample give elliptically polarized light and therefore one measures Kerr rotation ( $\theta_K$ ) and ellipticity ( $\varepsilon_K$ ) of the reflected light.
- **Transverse MOKE** - In this configuration the magnetization is perpendicular to the plane of incidence but parallel to the film surface as shown in Figure 2.11(b). However, in this transverse configuration one measures the change in intensity of the *p*- polarised after being reflected from the sample.
- **Polar MOKE** - This configuration is similar to longitudinal MOKE where the change in plane of polarisation and ellipticity is measured but the magnetization vector is perpendicular to the plane of the film plane as shown in Figure 2.11(c).

### 2.7.2 MOKE magnetometer set up:

Figure 2.12 shows the general MOKE set up used as magnetometer. Depending on the detector at the end signal, MOKE can be used as magnetometer as well as microscope.

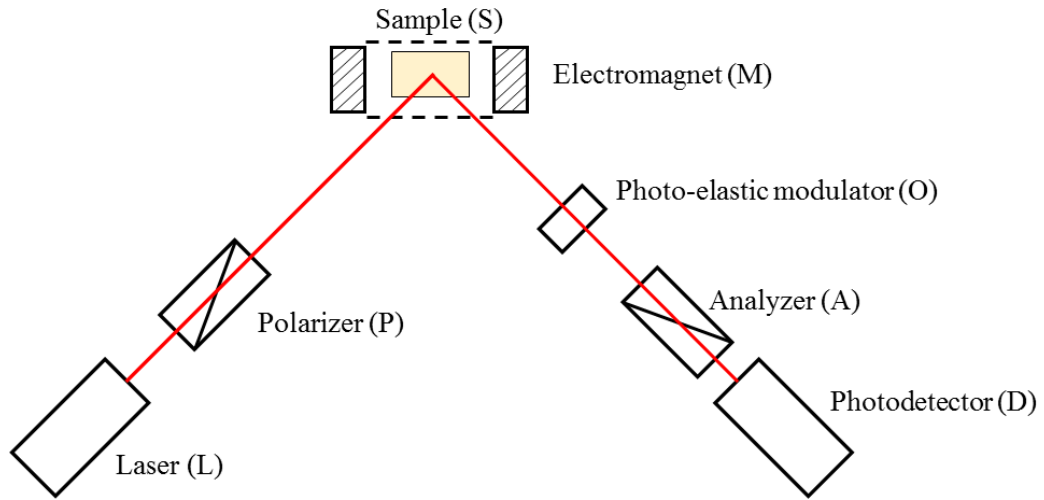


Figure 2.12: Schematic of MOKE magnetometer set up at NISER.

In the following section first, a brief description of MOKE set up is given and then the Kerr microscope setup is described. In general, the incident light from the laser (L) is *s* or *p* polarized by using the polarizer before the sample (S). In *s*-polarized light the electric field vector is polarized perpendicular to the plane of incidence where as in *p*-polarized light, the electric field vector is polarized parallel to the plane of incidence. This polarized light on interacting with the sample magnetization becomes elliptically polarized with rotation. The reflected light is then allowed to pass through the photo-elastic modulator which acts as quarter wave plate to account for the phase shift in the beam. The analyzer is kept at  $45^\circ$  w.r.t to the principle axis and the signal is detected at the photo detector. The setup has to be optimized and can be performed using the Jones Matrix calculation [87]. A room temperature MOKE magnetometer from Hinds instrument was used. It had a laser diode of wavelength = 635 nm. A maximum magnetic field of 100 mT can be applied in the plane of the sample. The other optical components were configured as described above. The action of various optical components used in MOKE magnetometer can also be expressed in terms of their respective Jones' matrices which can be used to optimize the signal to noise ratio of the measurements [87]. The matrix representation for polarizer [P] and analyser [A] with major transmission axis with the plane of incidence at  $\beta$  and  $\alpha$ , respectively can be represented as-

$$P = \begin{bmatrix} \cos^2\beta & \sin\beta\cos\beta \\ \sin\beta\cos\beta & \sin^2\beta \end{bmatrix} \quad (2.14)$$

$$A = \begin{bmatrix} \cos^2\alpha & \sin\alpha\cos\alpha \\ \sin\alpha\cos\alpha & \sin^2\alpha \end{bmatrix} \quad (2.15)$$

The sample matrix can be represented by [S] –

$$S = \begin{bmatrix} \tilde{r}_p & \tilde{r}_{ps} \\ \tilde{r}_{sp} & \tilde{r}_s \end{bmatrix} \quad (2.16)$$

where, the diagonal elements  $\tilde{r}_p = r_p e^{i\delta_p}$  and  $\tilde{r}_s = r_s e^{i\delta_s}$  are independent of magnetization and the off-diagonal elements  $\tilde{r}_{ps} = -\tilde{r}_{sp} = r_{ps} e^{i\delta_{ps}} = -r_{sp} e^{-i\delta_{sp}}$  contributes to the magneto – optic effects. For the PEM [O] at an angle of  $0^\circ$  or  $90^\circ$  w.r.t to plane of incidence is given by-

$$O = \begin{bmatrix} e^{i\phi/2} & 0 \\ 0 & e^{-i\phi/2} \end{bmatrix} \quad (2.17)$$

where,  $\phi = \phi_0 \sin \omega t$ . Therefore, the reflected amplitude of the electric field vector will be given as [87]-

$$\begin{bmatrix} E_p \\ E_s \end{bmatrix}^r = [A][O][S][P] \begin{bmatrix} E_p \\ E_s \end{bmatrix}^i, \quad (2.18)$$

and the signal detected at the photodetector (D) will be given as :

$$I \propto |E^r|^2 \quad (2.19)$$

The MOKE magnetometer from Hinds instrument in our laboratory had PEM with  $\omega = 50$  kHz and  $\phi_0 = 2.405$ . For longitudinal MOKE, s-polarized light is used and therefore,  $\beta = \pi/2$ , Eq. (2.14) reduces to -

$$P = \begin{bmatrix} 0 & 0 \\ 0 & 1 \end{bmatrix} \quad (2.20)$$

And therefore, using Eq. 2.20 in 2.18 gives -

$$\begin{bmatrix} E_p \\ E_s \end{bmatrix} = \begin{bmatrix} \cos^2 \alpha & \sin \alpha \cos \alpha \\ \sin \alpha \cos \alpha & \sin^2 \alpha \end{bmatrix} \begin{bmatrix} e^{i\phi/2} & 0 \\ 0 & e^{-i\phi/2} \end{bmatrix} \begin{bmatrix} \tilde{r}_p & \tilde{r}_{ps} \\ \tilde{r}_{sp} & \tilde{r}_s \end{bmatrix} \begin{bmatrix} 0 & 0 \\ 0 & 1 \end{bmatrix} \begin{bmatrix} 0 \\ 1 \end{bmatrix} \quad (2.21)$$

As described by Yang *et al.*, the Fresnel reflection coefficients of off-diagonal elements for [S] for two media separated by a single boundary can be expressed as [88] –

$$\tilde{r}_p = \frac{\mu_1 N_2 \cos \theta_1 - \mu_2 N_1 \cos \theta_2}{\mu_1 N_2 \cos \theta_1 + \mu_2 N_1 \cos \theta_2} + \frac{i \mu_1 \mu_2 N_1 N_2 \cos \theta_1 \sin \theta_2 m_x Q}{\mu_1 N_2 \cos \theta_1 + \mu_2 N_1 \cos \theta_2} \quad (2.22)$$

$$\tilde{r}_{ps} = - \frac{i \mu_1 \mu_2 N_1 N_2 \cos \theta_1 (m_y \sin \theta_2 + m_z \cos \theta_2)}{(\mu_1 N_2 \cos \theta_1 + \mu_2 N_1 \cos \theta_2)(\mu_2 N_1 \cos \theta_1 + \mu_1 N_2 \cos \theta_2) \cos \theta_2} \quad (2.23)$$

where,  $\theta_1$  and  $\theta_2$  are angles of incidence,  $N_1$  and  $N_2$ ;  $\mu_1$  and  $\mu_2$  are the complex refractive indices and permittivities of air and the material, respectively.  $Q$  is the Voigt constant proportional to magnetization,  $\theta_1$  and  $\theta_2$  are angle of incident and refraction [88].

In below analysis, Fourier decomposition of  $\cos(\phi(t))$  and  $\sin(\phi(t))$  as:  $\cos(\phi) = J_0(\phi_0) + 2 \sum_{m=1}^{\infty} J_{2m}(\phi_0) \cos(2m\omega t)$ , and  $\sin(\phi) = 2 \sum_{m=0}^{\infty} J_{2m+1}(\phi_0) \sin((2m+1)\omega t)$ , has been used for PEM matrix expansion respectively. The intensity for the reflected beam can be calculated from Eq. (2.21) and then using Eq. (2.19) which gives:

$$I \propto r_{ps}^2 \cos^2 \alpha + r_s^2 \sin^2 \alpha + r_s r_{ps} \cos(\delta_{ps} - \delta_s + \phi) \sin(2\alpha) \quad (2.24)$$

Eq. (2.24) shows that the first two terms are constant and can be considered as constant background. Considering the intensity upto first harmonic gives as -

$$I_1 = r_{ps}^2 \cos^2 \alpha + r_s^2 \sin^2 \alpha + r_{ps} r_s (-\sin(\delta_{ps} - \delta_s) 2J_1(\phi_0) \sin[\omega t]) \sin 2\alpha \quad (2.25)$$

Hence, from Eq. (2.25), it can be seen that only longitudinal component ( $m_y$  in present discussion as the system co-ordinates described by Yang *et al.* has been used [88]) affect the

intensity of the magnetization. To know the maximum signal for the MOKE set up we need to find the values  $r_{ps}$  and  $r_s$  from Eq. (2.22) and (2.23). The MOKE set-up in our case had  $\omega = 50$  kHz and  $\phi_0 = 2.405$ ,  $\theta_1 = \pi/4$ , and hence from Snell's law  $\theta_2 = \sin^{-1}[\frac{N_1}{N_2} \sin \theta_1]$ . For simplicity, considering  $\mu_1 = \mu_2 = 1$ ;  $N_1 = 1$ ,  $N_2 = 2.45 + 4.41i$ , it was calculated that the maximum intensity occurred when analyser angle ( $\alpha$ ) was at  $45^\circ$  and  $135^\circ$ . Hence, the measurements in this thesis were performed keeping the analyser angle at  $45^\circ$ .

### 2.7.3 Magneto – optic Kerr effect microscopy:

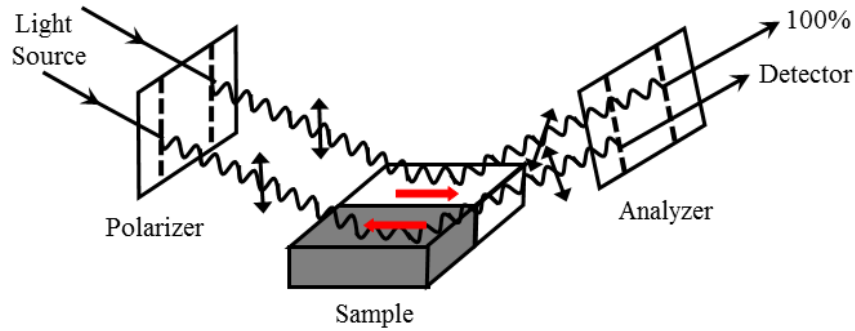


Figure 2.13: Observation of magnetic domains using MOKE microscopy set up [21].

The magnetic properties and domain imaging of the samples in this thesis were measured using MOKE microscopy. The basic principle for Kerr microscope is similar to that of MOKE magnetometer with detector replaced by a camera to obtain the domain images. The formation of domains in Kerr microscope is schematically shown in Figure 2.13. The light from the source is linearly polarized by the polarizer and then incident on the magnetic sample. Let us consider that there are two domains in the sample with the opposite magnetization. The magnetization of one domain is along positive x-direction while that of the other is in negative x-direction (Figure 2.13). Therefore, polarization of the incident light on being reflected from these two domains will be oppositely rotated. Now, if the analyzer axis is aligned such that it allows the transmittance of light from the first domain, then this

will result a bright intensity in the camera image. However, as the analyzer is now not aligned with the polarization axis of the light reflected from the second domain, it will therefore appear as dark in the image. Hence, bright and dark contrasts of the domain image corresponding to opposite magnetization of the sample are observed.

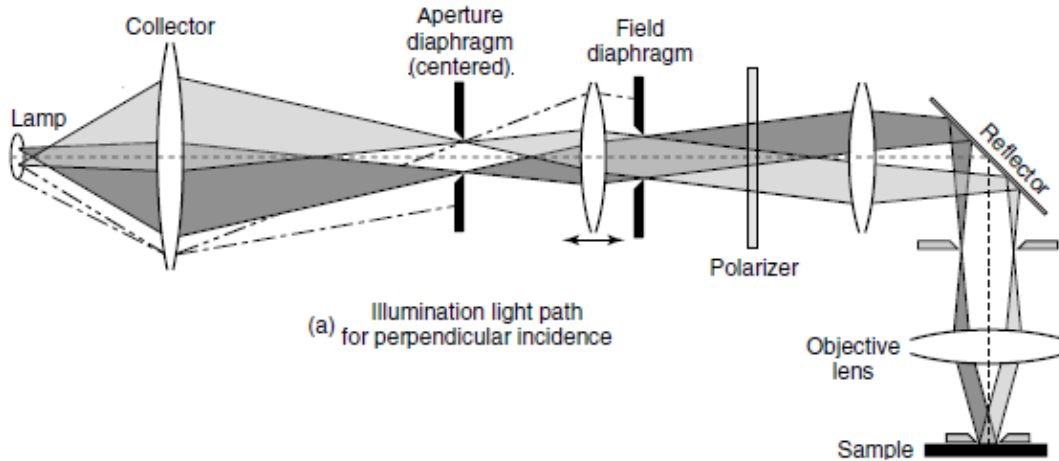


Figure 2.14: Optical sketch of Kerr microscopy manufactured by Evico Magnetics Ltd., Germany [89].

The Kerr microscope used to image the domains in this thesis is manufactured by Evico Magnetics Ltd., Germany. It is based on the MOKE principle with the detector replaced by a camera to image the domains. An external magnetic field can be applied by using an electromagnet with a Kepco power source. A maximum of 1300 mT and 900 mT magnetic field can be applied for in- plane and out-of-plane of the sample surface, respectively. The sample stage can be rotated in plane from 0 to 360° with the step resolution of 1 degree. This enables us to study the angle dependent magnetic properties like magnetic anisotropy, hysteresis and domain imaging.

The microscope consists of a Xenon lamp and is based on Köhler illumination technique [89]. The Kerr microscope set up schematically is shown in Figure 2.14. The light from the xenon lamp is passed through a collector lens to focus on the plane of the aperture

diaphragm. This aperture diaphragm can be used to select the sensitivity of the MOKE microscopy. For example, for polar Kerr effect the iris diaphragm is placed at centre. However, for longitudinal mode, the iris diaphragm is made off-centred and the slit aperture is aligned parallel to the plane of the incidence. The light from the slit is allowed to pass through the polarizer to have linearly polarized light. It is allowed to fall on the reflector and then down to the sample through the objective. The resolution of the microscope is determined by the numerical aperture (NA) of the microscope ( $NA = n \sin \alpha$ ), where  $n$  is the refractive index of the medium between objective and the sample,  $\alpha$  is one half angular opening of the objective [89]. Hence, to increase the resolution one can use the immersion oil having  $n = 1.5$  as the medium between the objective lens and the sample. In the present set up of Kerr microscope, the highest numerical aperture (1.4) is obtained by using 100X oil immersion objective. This gives the maximum resolution depending on the wavelength of the light used. The light from the objective is reflected back to the beam splitter and then to the compensator and analyser. The compensator placed on the reflected side of the light beam acts as a variable quarter wave plate. This converts the elliptically polarized light into a linearly polarized one by changing the phase of the constituent orthogonal components (ordinary and extraordinary) of the wave [89]. The light intensity is then recorded by the CCD camera. It is also possible to measure the hysteresis and record simultaneous domain images at each point of the hysteresis. The net grey value of the domain image is proportional to the net magnetization. The software also allows for the background subtraction so that the effect from topography is reduced. There is also a provision of image contrast enhancement in the software which can be used during measurements. Latter the contrast can also be increased by using the software Image J. Recently the Kerr microscope was upgraded, where the Xenon lamp was replaced by eight LEDs. The measurements performed in this thesis are mostly by Xenon lamp.

## 2.8 Polarized Neutron Reflectivity (PNR):

### 2.8.1 Introduction:

Neutrons are neutral spin half particles. However according to de Broglie theory, they can have wavelength of  $\lambda = h/mv$ . Since the wavelength of neutron is comparable to atomic spacing therefore, just like x-rays, they can also be used in determination of structural information like crystal structure and atomic spacing. However, in contrast to x-rays which interact with electrons of the atoms, neutrons interact with the nuclei of the sample via strong nuclear forces at short distances. Hence, neutrons are sensitive equally to light and heavy atoms; therefore they can distinguish between the different isotopes of the material and have better contrast variation for the neighbouring elements of the periodic table as compared to x-rays. Due to this property neutrons can probe samples containing hydrogen, carbon or oxygen next to any other heavier atom. Neutrons being neutral particles have large penetration depth and hence can be used to study the bulk properties of the sample and biological materials. Since the energies of the thermal neutrons are comparable to the elementary excitations of the solids, they can be used to investigate lattice excitations, molecular vibrations and dynamics of atomic motion.

However, the true advantage of neutrons over x-rays lies in the fact the neutrons have magnetic moment ( $\mu_n$ ), it can therefore interact with the magnetic moment of the sample. It was first shown by G. P. Flecher that neutrons can be used to probe surface magnetism [90]. This makes neutrons a useful tool to probe the magnetic properties like spin ordering, micro-magnetic structures, magnetic fluctuations, the coupling between different magnetic sites etc. Hence, the effective potential of a neutron on interacting with nucleus will have additional interaction term of the form  $V_m = -\mu_n \cdot \mathbf{B}$  in addition to neutron-nucleus interaction potential.

It was shown by S. J. Blundell, the neutrons with polarized beam can be used to study the magnetization vector profile of a multilayer system [91]. Polarized neutron reflectivity (PNR) was used in this thesis to study the magnetization depth profile of Co/AlO<sub>x</sub>/Co trilayers. In the following section we briefly describe the theory and instrument used for PNR.

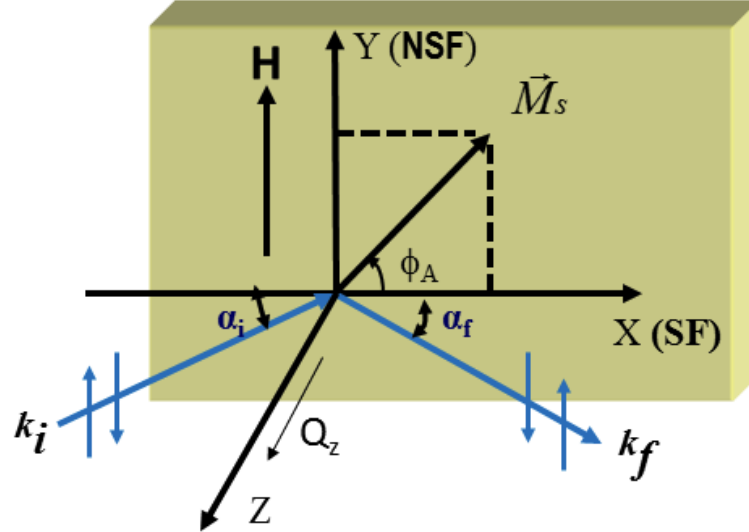


Figure 2.15: Schematic showing the scattering geometry for specular reflectivity of spin polarized neutron beam. For specular reflection angle of incidence is equal to angle of reflection ( $\alpha$ ). The y-direction is the non-spin-flip (quantization) axis for the neutrons and the x-direction is the spin-flip axis. The scattering vector  $Q$  is parallel to the z-axis and perpendicular to the surface [92].

## 2.8.2 Neutron scattering:

Considering the wave property of neutrons, it interacts with the materials as a continuous solid of refractive index  $n$ . Therefore, standard optical equations for reflectivity will also be valid for neutron reflectivity. Hence, for unpolarised neutrons, the refractive index will be defined similar to x-rays [92] –

$$n = 1 - \frac{2\pi}{k^2} N b_{coh} = 1 - \frac{2\pi}{\hbar} V_n \quad (2.26)$$

Where,  $b_{coh}$  is the coherent scattering length and  $V_n$  is the neutron-nucleus pseudo potential. Since neutrons have magnetic moment, the refractive index of a ferromagnetic material will be given by –

$$n(Q) = 1 - \frac{2\pi}{\hbar} (V_n \pm V_m) \quad (2.27)$$

where,  $V_m$  is the magnetic potential. The sign (+) and (–) stands for the parallel and antiparallel alignment of the initial neutron polarization to the magnetization [90]. Eq. (2.27) shows that the refractive index of magnetic material depend on the relative orientation of  $\mathbf{B}$  with the neutron spin. Therefore, a bifurcation of refractive index and hence the reflectivity occurs in magnetic materials. This allows to analyse the nuclear and magnetic density profile in the sample.

The scattering geometry for a typical reflectometry experiment is shown in Figure 2.15. For specular reflectivity, angle of incidence ( $\alpha_i$ ) is equal to angle of exit ( $\alpha_f$ ), then the scattering vector along normal to the surface (along z axis) is given as:

$$Q_z = \mathbf{k}_f - \mathbf{k}_i = \frac{4\pi \sin \alpha_i}{\lambda} \quad (2.28)$$

where,  $\mathbf{k}_i$  and  $\mathbf{k}_f$  are the incident and final wave vectors, respectively. In reflectivity measurements, range of  $Q_z$  can be spanned either by keeping angle of incidence fixed ( $\alpha_i$ ) and changing the wavelength, or by choosing a fixed wavelength by and varying the angle of incidence ( $\alpha_i$ ) [93]. In general, for most of the materials, the reflectivity is unitary up to a value of  $Q_c = \sqrt{16\pi N(b_{coh} \pm \rho_m)}$  of order  $0.01\text{\AA}^{-1}$ , where  $b_{coh}$  is the coherent scattering length,  $N$  is the atomic number density and  $\rho_m$  is the magnetic scattering length related to the magnetic induction of the sample [94]. Therefore, total external reflection occurs for  $Q_z < Q_c$ . After the plateau of total reflections the neutron reflectivity decreases rapidly with a mean

asymptotic  $Q_z^{-4}$  dependence. In a magnetic multilayer system the reflectivity in the  $Q_z \gg Q_c$  range is well described using the first Born approximation:

$$R \approx \frac{1}{Q_z^4} \left| 4\pi \sum_{l=1}^L [(Nb)_l - (Nb)_{l-1}] \exp(iQ_z d_l) \right|^2 \quad (2.29)$$

where  $d_l$  is the distance of the  $l^{\text{th}}$  layer's top interface below the surface [ 94].

Before the neutrons interact with the magnetic sample and the surrounding magnetic field the neutron can be considered as a plane wave. Hence the interaction potential will not be affected by the lateral coordinates. Therefore, the interaction potential will vary only as a function of the depth (along Z axis) which reduces 3 dimensional Schrödinger equation to 1 dimensional equation. Assuming in-plane magnetization for a magnetic sample, the magnetization may point in any in-plane direction at an angle  $\phi$  with respect to the scattering plane (the applied field is directed perpendicular to the scattering plane). In neutron scattering by atoms, two main interactions occur. The first is the short-range nuclear interaction of the neutron with the atomic nucleus (the nuclear scattering). The second one is the Zeeman interaction of the magnetic moment of the neutron with the magnetic field produced by spin and orbital magnetic moments of the electrons. Therefore the effective potential with the  $i^{\text{th}}$  layer of a stratified medium can be expressed as form of-

$$V_{i,eff} = V_{i,n} + V_{i,m} \quad (2.30)$$

Where  $V_n$  is the nuclear interaction which is spin independent and is given as  $\frac{2\pi\hbar^2}{m} Nb_n$ ,  $V_m$  is magnetic scattering potential related to the magnetic moment of the neutron and magnetic induction of  $\mathbf{B}$  inside the material which is given as -

$$V_m = -\boldsymbol{\mu}_n \cdot \mathbf{B} \quad (2.31)$$

Where,  $\mathbf{B} = \mathbf{B}_{spin} + \mathbf{B}_{orbital}$ . Therefore Eq. 2.30 reduces to -

$$V_{eff} = \frac{2\pi\hbar^2}{m} Nb_n + \mu_N \vec{\sigma} \cdot \vec{B} \quad (2.32)$$

Therefore,

$$V \propto (\rho_n \pm \rho_m), \quad (2.33)$$

where,  $N$  is the number density,  $b$  is the coherent nuclear scattering length,  $\mathbf{B}$  is the magnetic field of the specimen,  $m$  is the mass of the neutron and  $\sigma$  is the operator associated with the Pauli-spin matrices and  $\mu_N$  is the neutron magnetic moment. The  $\pm$  in Eq. 2.33 indicates the spin up and down states of the incident neutron. Therefore, the scattering-length densities (SLD) of a magnetic material are either the sum or the difference of the nuclear ( $\rho_n$ ) and magnetic ( $\rho_m$ ) components. [93]. The reflectivity can be calculated by applying the time independent Schrödinger equation for the neutron wavefunction inside and outside the sample. The neutron wavefunction can be expressed as a linear combination of the two spin states of the neutrons given as [93]:

$$|\psi(r)\rangle = |\psi^+(r)|\chi^+\rangle + |\psi^-(r)|\chi^-\rangle = \begin{pmatrix} \psi^+ \\ \psi^- \end{pmatrix}$$

The equation can be solved by considering the spin dependences of the scattering potential and the neutron wave function giving rise to non-spin flip (NSF) and spin flip (SF) scattering. The NSF scattering amplitude can be expressed as  $\rho_n \pm \rho_m \cos \Phi_A$  provides the information about the magnetization component  $M$  parallel or anti-parallel to the applied field. The SF channels measures  $\rho_m^2 \sin^2 \Phi_A$  i.e. magnetization perpendicular to the applied field [93]. Therefore, the change in effective potential occurs only from the y- component of the sample magnetization. The x- component of magnetization, without changing the potential causes a perturbation of the polarization and over some optical path length results in the flipping of the neutron spin from the (+) to the (-) state or vice versa. Hence, the Y axis is the NSF axis along which the magnetic field is applied and the X-axis is the SF-axis which may flip the neutrons from one potential to the other. Spin flip is a purely magnetic property and does not occur in coherent nuclear scattering. Hence combining the x and y components of magnetization vector from NSF and SF, respectively, one can get net magnetization vector

[76]. Therefore, the specular reflectivities in the NSF channels ( $R^{++}$  and  $R^{--}$ ) are due to periodicities of the structure and magnetization components collinear to  $\mathbf{H}$ , whereas reflectivities in the SF channels ( $R^{+-}$  and  $R^{-+}$ ) are exclusively of magnetic origin and correspond to in-plane magnetization components perpendicular to  $\mathbf{H}$  [93].

### 2.8.3 Reflectometer instrument:

A free neutron has a mean life of 900 s, therefore they are produced during experiments either by fission of uranium 235 nuclei by a chain reaction or by spallation where heavy nuclei are bombarded with high energy protons [95]. The neutrons produced at the reactor core is slowed down via inelastic collision by passing them through the moderator. This increases their wavelengths such that they are comparable to the interatomic spacings of the solids. Such neutrons known as thermal neutrons. The measurements in this thesis were performed for Co/AlO<sub>x</sub>/Co multilayers at TREFF reflectometer at FRM 2, in Munich which allows having simultaneous polarization analysis measurements. The schematic of the instrument is shown in Figure 2.16. A neutron on interacting with a nucleus can either be absorbed or scattered. Therefore neutron guides are required to transfer the neutrons away from the reactor to the instrument. For this purpose neutron wave guides made up of supermirrors consisting of thin layers of e.g. Ni and Ti enclosing the flight path of a neutron is used. The principle of the neutron guide is based on total the external reflection phenomenon which transports the neutrons to the end of the guide without allowing them to leave the guide. Spin polarized neutron beams for the experiments are achieved by the use of magnetic supermirrors which can provide spatially narrow beams of limited divergence. A supermirror (SM) is a stack of multilayers with gradually increasing value of the  $d$  (artificial periodicity) spacing. Since it is before the sample we call it as polarizer (P1 in Figure 2.16). The spin of the neutrons are flipped using the spin flipper (F1 in Figure 2.16) in which the neutron polarization vector processes around the flipping field in accordance to Lamour

precession. This precession can be parallel or antiparallel to the field depending on the spin state of the neutron. Hence the incident beam can be polarized for up spin or down spin accordingly. Now on interaction with the magnetic induction of the sample, the spin state of the neutron may change. A second flipper (F2 in Figure 2.16) after the sample verifies whether or not the neutron spin has been flipped during the reflectivity process. Hence we can have 4 possible cross scattering  $R^{++}$ ,  $R^{-}$ ,  $R^{+}$  and  $R^{--}$  depending on the incident and final spin state of the neutron where the first +/- sign stands for incident neutron state and the second +/- for the final neutron state. The  $R^{++}$  and  $R^{--}$  are called non-spin flip reflectivity. The final polarization state of the neutron is tested via a second supermirror called analyser (P2 in Figure 2.16) in the exit beam.

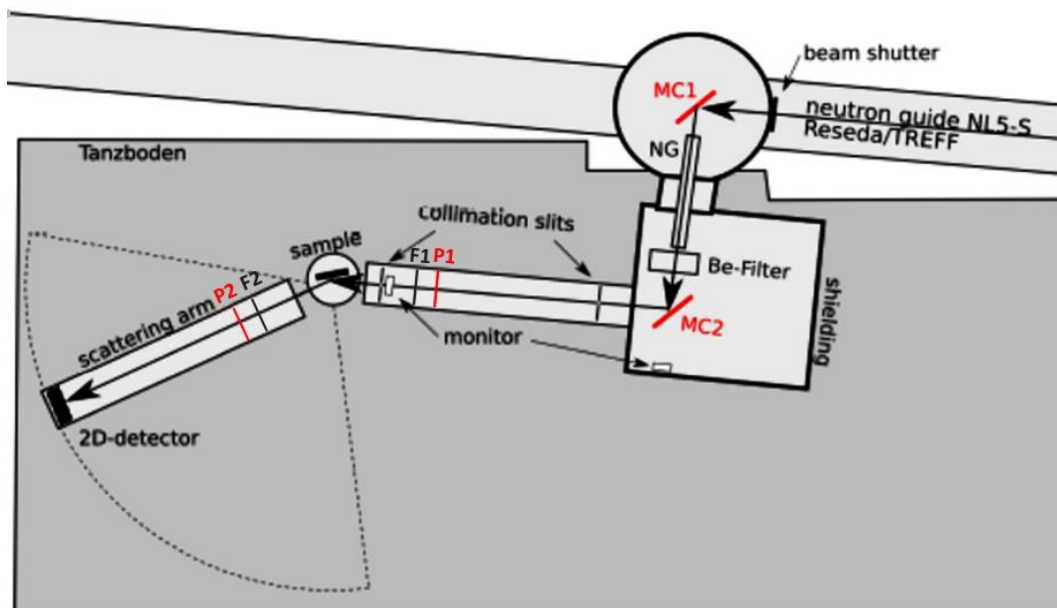


Figure 2.16: Schematic of the reflectometer TREFF at neutron guide NL5-S, FRM II in Garching (Top view), F1 and F2 are the Flippers places before and after the sample respectively. P1 and P2 are the polarizer and analyser, respectively. [96]

The reflectivity measurements for  $\text{Co}/\text{AlO}_x/\text{Co}$  were performed as a function of incident angle by keeping the wavelength of the neutrons fixed ( $4.73 \text{ \AA}$ ). It was then converted to reciprocal mapping and hence a plot of scattering vector vs intensity was obtained. This was

then fitted using GenX software with the prior information of thickness, density and roughness obtained from the x-ray measurements. The fits can give the magnetization depth profile of the sample.

## **Chapter 3 : Magnetization reversal and relaxation dynamics in Co thin film**

### **3.1 Introduction:**

Understanding and tailoring of anisotropy in magnetic thin films has been interesting due to its application in data storage devices and magnetoresistive devices. For optimizing the performance of these devices a high uniaxial anisotropy is desired. In particular, in plane uniaxial anisotropy is required in magnetoresistive random access memory and read head assemblies of the hard drive [97]. From the fundamental point of view, anisotropy plays an important role in determining the magnetic properties of thin films. As discussed in Chapter 1, various anisotropies such as magnetocrystalline, shape, surface and strain anisotropy can contribute to the net anisotropy in magnetic thin films. Anisotropy can be induced in a magnetic film by oblique deposition [5], applying a magnetic field during deposition, [7] post annealing (annealing in the presence of a magnetic field or magnetic annealing) [8] etc. details of which have been discussed in section 1.2.3.5 of Chapter 1. When the film is grown with an oblique angle of deposition, the self-shadowing and steering effects lead to the chain-like formation of grains giving rise to a preferred direction of anisotropy [5, 98, 99, 100, 101]. For small angles between the incident beam flux and the substrate normal, the easy axis (EA) lies perpendicular to the beam direction [5, 102] but for angles greater than  $75^\circ$ , the EA gets reoriented in the direction parallel to the incident flux [102]. The net anisotropy of the film will depend on the total contribution of the shape anisotropy of the grains as well as the inherent magneto-crystalline anisotropy of the system. Hence, the surface morphology plays an important role in determining the anisotropy and magnetic properties of the film.

However, in some applications e.g. in microwave devices [103, 104] and in fundamental studies it is desirable to overcome the anisotropy. One method is to rotate the substrate so that homogenous thickness and the isotropic thin film is obtained. Kim *et al.* showed that coercive field increases with increasing the rotational speed of the substrate [105]. Since the magnetization reversal strongly depends on the microstructure of the ferromagnetic films, therefore, it can be different for obliquely grown films and those with substrate rotations. It will be shown in this section that substrate rotation induces dispersion in anisotropy and hugely affects the switching mechanism, domain structures and also the thermally activated relaxation.

In the data storage and transfer technology, the relaxation rate of the magnetic thin films set the limits of the devices' performance. It is also important to know the thermal stability of the data storage system. Hence, they may be optimized being aware of the contribution of thermal activation energy and Zeeman energy in magnetization reversal which can be effectively studied as magnetization relaxation. For a constant Zeeman energy, the thermal activation results in overcoming the energy barrier arising due to the inhomogeneities like defects and pinning centres along with magnetic anisotropies in thin films for domain nucleation and its propagation. The most commonly used model to explain magnetic relaxation for ferromagnetic thin films is the Fatuzzo-Labrune model. This model was initially developed by Fatuzzo to investigate the relaxation in ferroelectric materials [9] and later Labrune [106] extended it to study relaxation in ferromagnetic thin films. This model describes the thermally activated reversal via domain nucleation and domain wall motion. It is based on the single energy barrier where the circular domains grow isotropically with initial radius  $r_c$ . It considers the probability of both - domain nucleation and domain wall motion. The nucleation rate was assumed to decrease exponentially by Fatuzzo and was given as  $n(t) = e^{(-Rt)}$ . The speed ( $v$ ) of the growth of the circular domains at a given time  $t$  and

nucleated at a time  $\tau$ , is given as:  $s(t - \tau) = \pi v^2(t - \tau)^2$ . The time dependent relaxation for this model was given as [107]-

$$B(t') = \exp(-k^2(2 - 2(t' + k^{-1}) + (t' + k^{-1})^2 - 2e^{t'}(1 - k^{-1}) + (1 - t')) \quad (3.1)$$

where  $t' = Rt$  and  $k = v/Rr_c$ . Here,  $R$  is the nucleation probability per unit time and  $r_c$  is the radius of the nuclei. The parameter  $k$  determines the shape of the magnetization relaxation curve depending on the dominant reversal process. For low values of  $k$ , reversal process will be mainly via nucleation. However, for large values of  $k$ , the reversal will be governed mainly by domain wall motion. In the limit of long time range, Eq. (3.1) reduces to

$$B(t) = \exp(-(Rt/\tau(k))^{\beta(k)})$$

where,  $\tau(k)$  and  $\beta(k)$  depends on  $k$ . However, in the case of polycrystalline ferromagnetic film, are in general inhomogeneous and have variation in local properties like anisotropy, exchange coupling, defects etc. This will violate the assumption of having smooth circular domains and the nucleation rate may not follow exponential behaviour. Hence, the reversal can be expressed as a compressed or stretched exponential behavior indicating that this model is not complete. For example, the compressed exponential fit has been used to describe the slow relaxation of a ferromagnetic film due to the distribution of energy barriers in Au/Co/Au films [108]. Hence, understanding magnetization relaxation in for thin films with random anisotropy is also of fundamental importance. In the following section, magnetization reversal for films with uniaxial and random anisotropy induced due to substrate rotation are studied.

### 3.2 Sample preparation:

Magnetization reversal and domain structures were studied for Co thin films with two different thickness of Co were prepared on Si (100) substrates at room temperature with the following structures –

(a) Si(100)/AlO<sub>x</sub>(3 nm)/Co(3.5 nm)/AlO<sub>x</sub>(3 nm)

(b) Si(100)/AlO<sub>x</sub>(3 nm)/Co(10 nm)/AlO<sub>x</sub>(3 nm)

The QPrep multideposition unit from Mantis Deposition Ltd., UK was used to prepare these samples. The base pressure inside the sputtering chamber was better than  $5 \times 10^{-8}$  mbar. This deposition unit had an angle of  $30^\circ$  between the substrate normal and the incident flux. As was discussed in sections 1.2.3.5 and 2.1.2 a growth induced in-plane uniaxial anisotropy due to oblique deposition was observed. The schematic for sample structure has been shown in Figure 3.1. To overcome this anisotropy, sample structure described in Figure 3.1 was rotated during deposition with substrate rotation ( $\omega$ ) = 10 and 20 rpm. The details of sample cleaning and deposition conditions have been described in Chapter 2, section 2.1.2. The magnetic properties of these samples are discussed below.

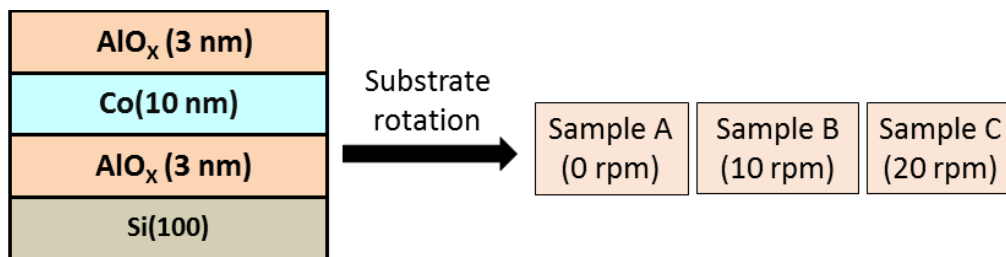


Figure 3.1: Schematic of sample structure for AlO<sub>x</sub> (3 nm)/Co (10 nm)/AlO<sub>x</sub> (3 nm) prepared by magnetron sputtering.

### 3.3 Results and discussion:

#### 3.3.1 Magnetization reversal in $\text{AlO}_x$ (3 nm)/Co (3.5nm)/ $\text{AlO}_x$ (3 nm):

##### 3.3.1.1 Study of magnetization switching and domain structure:

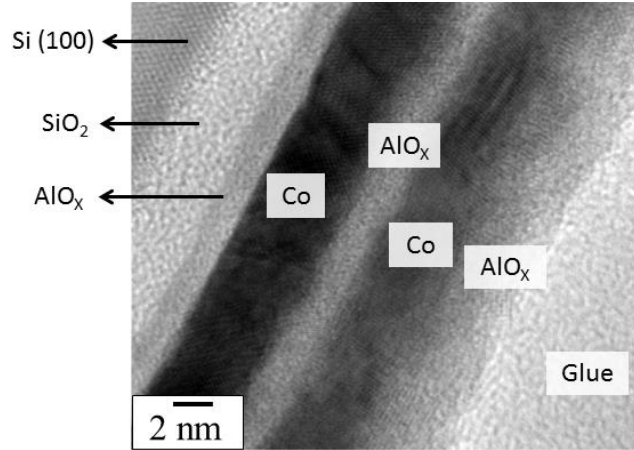


Figure 3.2: Cross-sectional transmission electron microscopy image of  $\text{Si (100)/ AlO}_x$  (3 nm)/Co (3.5 nm)/ $\text{AlO}_x$  (3 nm)/Co (3.5 nm)/ $\text{AlO}_x$  (3 nm).

The sample structure was similar to that shown in Figure 3.1 with Co thickness equal to 3.5 nm. Cross-sectional transmission electron microscopy (XTEM) on a bilayer sample of  $\text{Co (3.5 nm)/AlO}_x$  (3 nm)/Co (3.5nm) thin film is shown in Figure 3.2. This sample was prepared with the conditions similar to the single Co thin film. It was observed that Co (3.5 nm) was continuous and had polycrystalline structure (Figure 3.2). Magnetic hysteresis curves were measured by means of a Superconducting Quantum Interference Device (SQUID) based vibrating sample magnetometer (VSM-SQUID, Quantum Design) at various temperatures for the EA. However, angle dependent magnetic properties and domain structures were characterized by longitudinal magneto-optic Kerr effect (LMOKE) microscopy at room temperature. The sample stage of the MOKE microscope is such that it can be rotated with an accuracy of  $\sim 1^\circ$  and hence the angle between the magnetic field and the EA can be varied. Figure 3.3(a) – (d) shows the hysteresis loops measured by LMOKE microscopy along EA,  $30^\circ$ ,  $60^\circ$  and along the hard axis (HA), respectively. It can be observed

that the loop shape changes from square to S- shape and a gradual decrease of coercive field on going from the EA (0°) towards the HA (90°). This implies the presence of uniaxial anisotropy. The coercive fields  $\mu_0 H_c$  along EA, 30°, 60° and HA are ~ 14.6, 11.4, 10.5 and 4.5 mT, respectively.

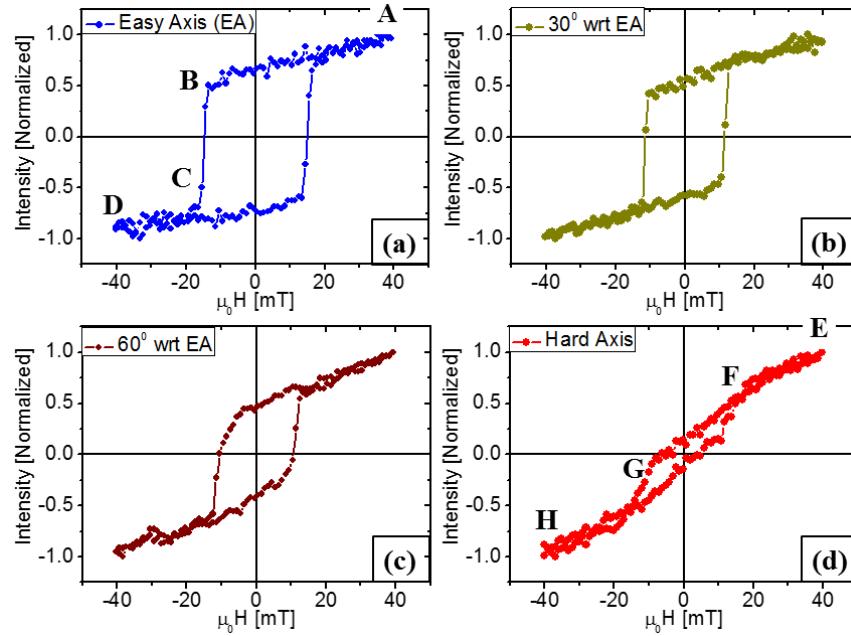


Figure 3.3: LMOKE hysteresis loops measurements performed for  $\text{AlO}_x$  (3 nm)/Co (3.5 nm)/ $\text{AlO}_x$  (3 nm) along (a) EA, (b) 30° and (c) 60° and (d) HA at room temperature [109].

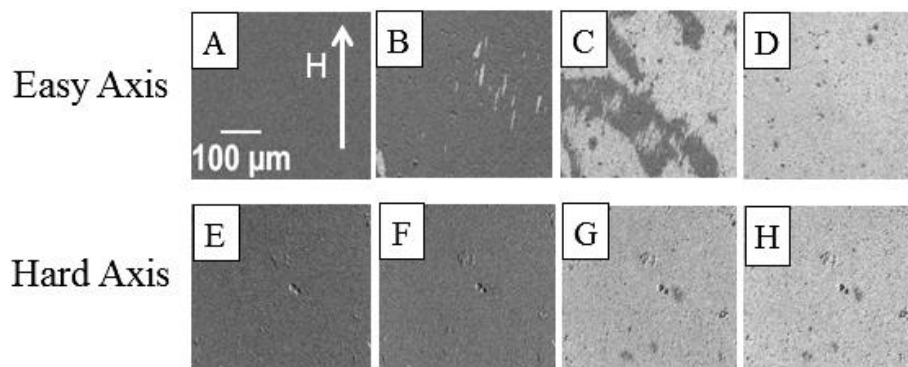


Figure 3.4: LMOKE domain images for  $\text{AlO}_x$  (3 nm)/Co (3.5 nm)/ $\text{AlO}_x$  (3 nm) along EA (A) – (D) and HA (E) – (H). The values of the magnetic field points are marked in Figure 3.3(a).

Domain images from MOKE microscopy reveals domain nucleation followed by domain wall motion along EA (Figure 3.4(a) – (d)) and coherent rotation along HA as shown by domain images in (Figure 3.4(e) – (f)).

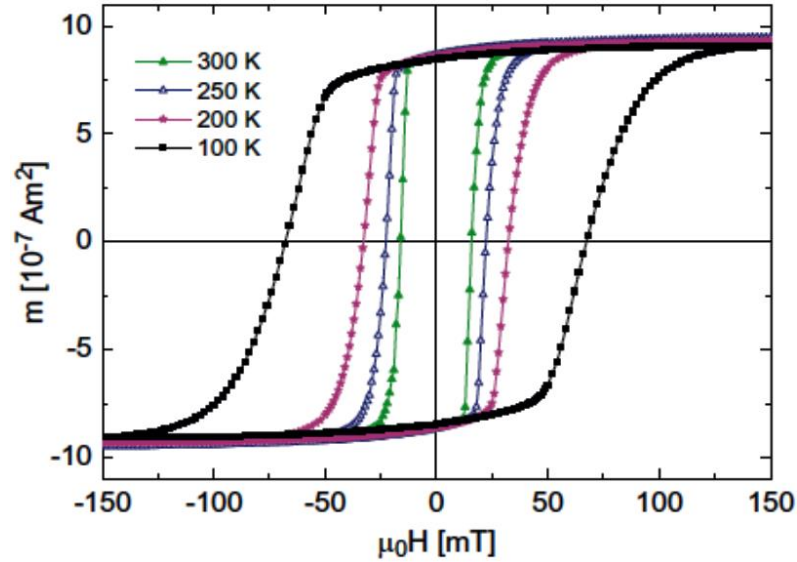


Figure 3.5: Magnetic hysteresis for  $\text{AlO}_x$  (3 nm)/Co (3.5 nm)/ $\text{AlO}_x$  (3 nm) measured by SQUID magnetometer along the EA at 300, 250, 200, and 100 K, respectively.

Temperature dependent hysteresis loops were performed using SQUID magnetometer along EA for 300, 250, 200 and 100 K as shown in Figure 3.5. Rounded hysteresis loops indicate soft ferromagnetism, which partly demagnetizes in zero field via domain formation as in permalloy or  $\mu$  metal. The coercivity increases with decrease in temperature as expected for a ferromagnetic thin film.

### 3.3.1.2 Magnetization relaxation:

In order to understand more about the magnetization reversal processes along the EA, relaxation measurements were performed. The sample was first saturated by negative DC magnetic field and then the field was reversed to a positive constant applied magnetic field called as measuring field ( $H_M$ ) close to the coercive field ( $H_C$ ). Keeping the magnetic field

constant, the time evolution of domains were recorded. The constant magnetic field during magnetization relaxation implies the constant Zeeman energy. Hence, effectively the time evolution of thermally activated magnetization reversal of the sample is observed by recording the domain images. The net gray scale value obtained from these domain images, being proportional to the magnetization of the sample, was then extracted by using ImageJ software. The normalized net intensity was then plotted as a function of time to study the magnetic relaxation.

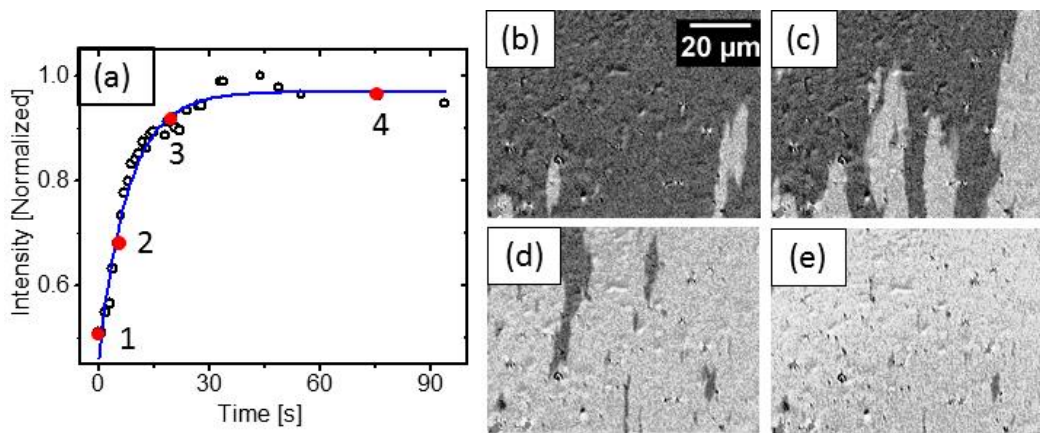


Figure 3.6: Relaxation curve for  $\text{AlO}_x$  (3 nm)/Co (3.5 nm)/ $\text{AlO}_x$  (3 nm) measured at  $\mu_0 H = -11.7$  mT. Images were taken by longitudinal MOKE and magnetic field was applied along EA. Images (b), (c), (d) and (e) corresponds to points 1, 2, 3 and 4 of Figure 3.6(a).

Figure 3.6(a) shows the relaxation measurement for  $\mu_0 H = -11.7$  mT. Initially, the reverse domain nucleates as shown in Figure 3.6(b). Further with time, domain wall motion with subsequent nucleation of new reverse domains (Figure 3.6(c) and (d)) leads to positive saturation (Figure 3.6(e)). Therefore, the reversal occurs via domain nucleation followed by domain wall motion. Such reversal processes are well corroborated with the Fatuzzo - Labrune model as discussed in introduction of this chapter. The experimental data in Figure 3.6(a) can be fitted (the solid line) using the equation:

$$M = M_0 - M_1 \exp(-t/\tau) \quad (3.2)$$

where, the fitting parameters are,  $M_0 = 0.967$ ,  $M_1 = 0.506$ , and  $\tau = 8.059$  s. However, if the Zeeman energy is increased by increasing the strength of the applied magnetic field then the magnetization relaxation time decreases as shown in Figure 3.7. These relaxation curves were fitted with Fatuzzo - Labrune model and the best fit yields  $\tau = 8.06$ ,  $4.87$ , and  $2.76$  s for  $\mu_0 H_M$  of  $11.7$ ,  $11.8$  and  $11.9$  mT, respectively. Hence, the relaxation time decreases with increase in magnetic field i.e. Zeeman energy.

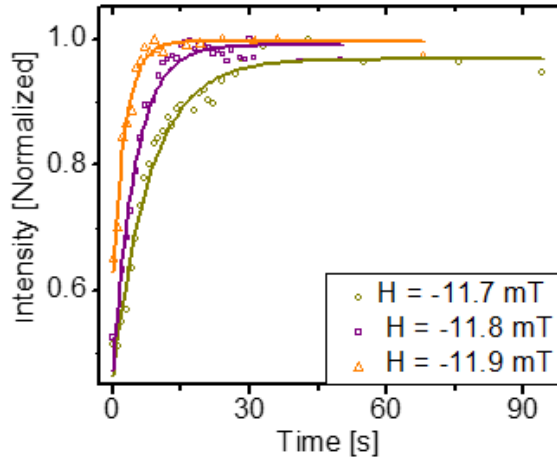


Figure 3.7: Magnetization relaxation curves for AlO<sub>x</sub> (3 nm)/Co (3.5 nm)/AlO<sub>x</sub> (3 nm) measured using LMOKE along EA for magnetic fields of -11.7 mT, -11.8 mT and -11.9 mT, respectively. The best fits yield  $\tau = 8.06$ ,  $4.87$ , and  $2.76$  s for measurements performed at  $\mu_0 H_M = -11.7$ ,  $-11.8$ , and  $-11.9$  mT, respectively.

### 3.3.1.3 Domain wall dynamics:

Other way of representing the relaxation dynamics is to observe the different modes of domain walls of a pinned ferromagnetic film by plotting the velocity of the domain wall vs the applied magnetic field. The velocity for each field was calculated from the domain images taken during relaxation as displacement along the x-direction divided by time. It is well established that with increasing the magnetic field different modes of domain wall

motion can be observed [110]. Figure 3.8 shows the plot for velocity vs applied field along EA showing different modes of domain wall motion i.e. creep, depinning and slide.

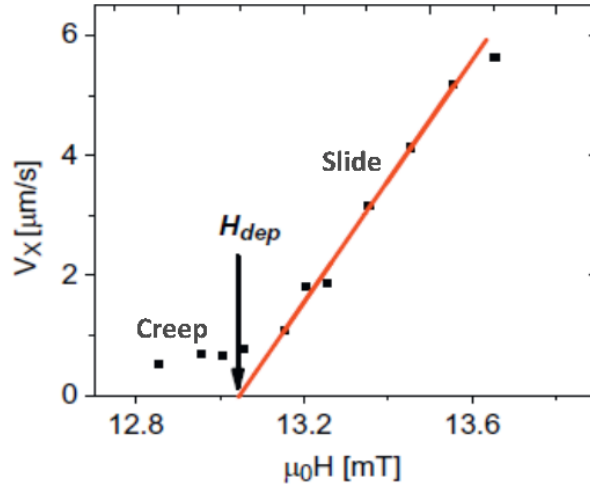


Figure 3.8: Domain wall velocity vs the magnetic field for  $\text{AlO}_x$  (3 nm)/Co (3.5 nm)/ $\text{AlO}_x$  (3 nm) along EA at room temperature. The different modes of domain walls: creep, depinning and slide have been shown. The slide region has been fitted linearly and extrapolation to the field axis gives the depinning field.

It is well established that for  $T = 0$ , at all fields below depinning field ( $H_{dep}$ ), the velocity is always zero and the domain walls are always pinned resulting in the sharp transition from creep to slide. However, at finite temperatures due to thermally activated motion the depinning transition gets smeared. Hence, at any non-zero field  $H < H_{dep}$ , a finite velocity will be observed. This thermally activated region is called creep [111]. From Figure 3.8 it can be observed that in the range of  $\mu_0 H_{ext}$  from 13.15 to 13.64 mT, velocity increases linearly with field, which implies that the wall motion is in the slide regime. Extrapolating the linear fit, the intercept to the field axis gives the depinning field  $H_{dep} \sim 13.04$  mT. Above  $H_{dep}$ , i.e. in the slide regime, the field strength becomes sufficient to overcome the pinning forces. As discussed earlier, in slide region velocity,  $v = \mu H$ , can be derived from the Landau-Lifshitz-Gilbert equation of motion. The coefficient of mobility is given as:  $\mu = \frac{\gamma \Delta}{\alpha}$ , where  $\Delta$

is the domain wall width,  $\alpha$  is the damping constant and  $\gamma$  is the Gyromagnetic ratio. The damping parameter  $\alpha$ , results in dissipation and is responsible for limiting the wall velocity in this region. However, it should be noted that at high fields the domain wall velocity becomes very high and it becomes very difficult to measure in our image window of Kerr microscope.

Hence, it can be concluded that that magnetization reversal was governed by nucleation followed by domain wall motion along the EA. However, coherent rotation was observed during magnetization reversal measured along the HA. The relaxation of magnetization in constant dc magnetic field measured along the EA show exponential behaviour which according to Fatuzzo – Labrune model indicates domain nucleated dominant process. The relaxation time decreases when the applied magnetic field strength is increased. Domain wall velocity plotted as a function of constant dc magnetic field shows creep and slide regime from which the depinning transition was extracted [109].

In the later part of the thesis, in order to study the interlayer coupling of Co/AlO<sub>x</sub> multilayers the thickness of the Co layer was taken as 10 nm to achieve better contrast in Kerr microscopy measurements. For this purpose, magnetic properties like anisotropy, domain structure and magnetization relaxation of Co (10 nm) single layer films with oblique deposition and with substrate rotation were studied and is described in the following section.

### **3.3.2 Magnetization reversal in Co (10 nm) thin films with oblique deposition and substrate rotation:**

As discussed earlier, the magnetic thin films prepared in the QPrep deposition chamber showed uniaxial anisotropy due to the shadow deposition. One method to overcome this anisotropy and obtain isotropic film is to rotate the substrate during deposition. However, the substrate rotation may lead to variation in the local properties increasing the dispersion of anisotropy in the thin film. This will affect the magnetization reversal of the magnetic thin

films. Hence, in this section the effect of random anisotropy on magnetization reversal, domain structure and magnetic aftereffect relaxation on Co (10nm) thin films is discussed.

For this purpose AlO<sub>x</sub> (3 nm)/Co (10 nm)/AlO<sub>x</sub> (3 nm) on Si (100) with different substrate rotations ( $\omega$ ) = 0, 10, and 20 rpm were prepared at room temperature as described in sample preparation section. The samples prepared with  $\omega$  = 0, 10, and 20 rpm are labelled as sample A, B, and C, respectively (Figure 3.1).

### 3.3.2.1 Structural characterization:

Cross-sectional transmission electron microscopy (XTEM) on a bilayer sample of Co (10 nm)/AlO<sub>x</sub> (20 nm)/Co (10 nm) thin film prepared with the conditions similar to sample A is shown in Figure 4.2 of chapter 4. It was observed that Co thin film with 10 nm was continuous and had polycrystalline structure.

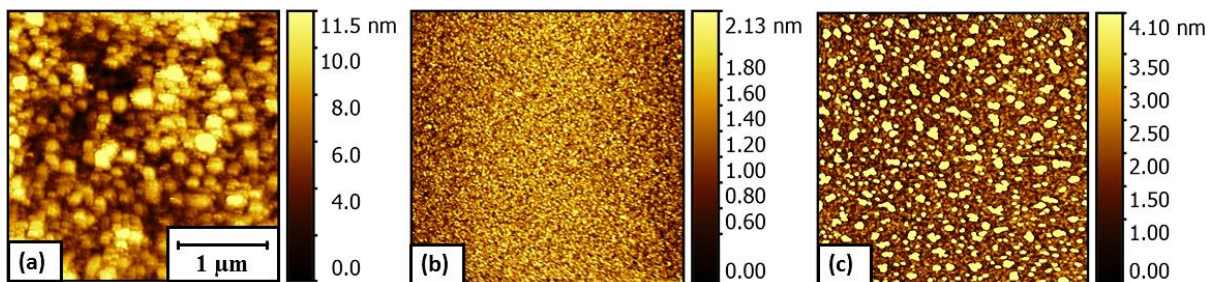


Figure 3.9: Surface topography imaged by atomic force microscopy for sample A (a), sample B (b), and sample C (c). All the images are in the same length scale which is shown in (a).

Figure 3.9 shows the surface morphology of the three samples measured ex-situ in tapping mode by atomic force microscopy (AFM). It is observed that the grains for sample A (Figure 3.9(a)) are larger compared to sample B (Figure 3.9(b)) and C (Figure 3.9(c)). Figure 3.9(b) shows a uniform distribution of small grains over the surface of sample B which can be ascribed to the substrate rotation during deposition. For better visualization of the grains

high resolution image of sample B is shown in the inset of Figure 3.10(a). However, Figure 3.9(c) shows that the grains for sample C are not uniformly distributed and formed island-like structures. The high resolution image of sample C (Figure 3.10(b)) indicates that the islands consist of 3 to 4 grains. It is known that Co on  $\text{Al}_2\text{O}_3$  follows Volmer-Weber growth mechanism in which three-dimensional islands nucleate and the film is formed by the coalescence of these structures [112]. Hence, in sample C, due to the higher substrate rotation (20 rpm) during the deposition the adatoms might not have sufficient time to relax which leads to the formation of island-like structures. The average grain size of sample A, B, and C are  $138.9 \pm 11.7$  nm,  $23.4 \pm 1.2$  nm, and  $38.5 \pm 1.2$  nm, respectively.

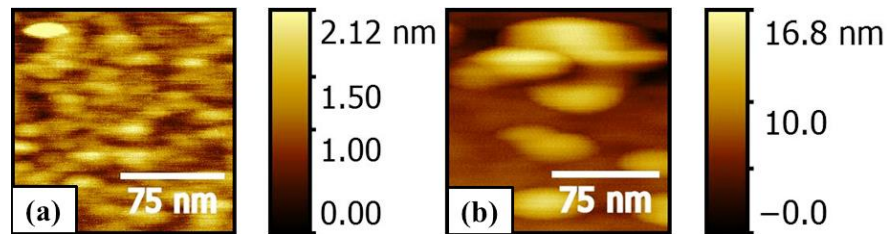


Figure 3.10: High resolution AFM image of sample B (a) and sample C (b).

The decrease in grain size for samples B and C can be explained as an effect of substrate rotation during growth. In order to check the effect of  $\text{AlO}_x$  as the buffer layer on the growth of Co, we have prepared single 3 nm of  $\text{AlO}_x$  film on Si(100) substrate with  $\omega = 0, 10,$  and 20 rpm. Figure 3.11(a) shows that the  $\text{AlO}_x$  layer prepared on Si with  $\omega = 0$  rpm is discontinuous. However,  $\text{AlO}_x$  film prepared with  $\omega = 10$  rpm becomes continuous (Figure 3.11(b)). Further increase of  $\omega$  from 10 to 20 rpm had a minimal effect on the surface morphology of  $\text{AlO}_x$  (Figure 3.11(c)). However, it should be noted that Co growth gets strongly affected by the substrate rotation when  $\omega$  is changed from 10 to 20 rpm as evident from the islands in Figure 3.9(c) as explained above.

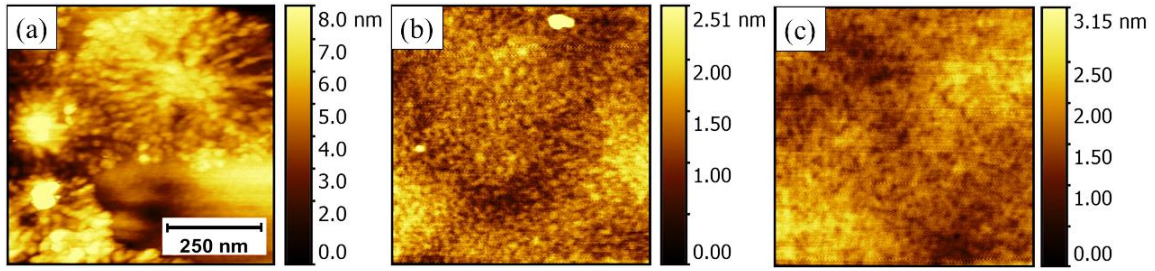


Figure 3.11: Surface topography by AFM in tapping mode for Si/AlO<sub>x</sub> (3 nm) with  $\omega = 0, 10$  and  $20$  rpm shown in (a), (b), and (c), respectively.

### 3.3.2.2 Study of magnetic properties due to randomness in film:

#### 3.3.2.2.1 Effect on anisotropy, magnetization switching and domain structures:

In-plane angle dependent static hysteresis measurement with simultaneous domain imaging was performed using longitudinal MOKE (LMOKE) microscope. The angle ( $\theta$ ) was varied between the EA and the external magnetic field by rotating the sample holder. From these hysteresis loops the values of coercive field and squareness ( $R_s$ , defined as  $M_r/M_s$  where  $M_r$  = remanent magnetization and  $M_s$  = saturation magnetization) [section 1.4] were extracted for each angle and plotted as shown in Figure 3.12(a) and (b) respectively.

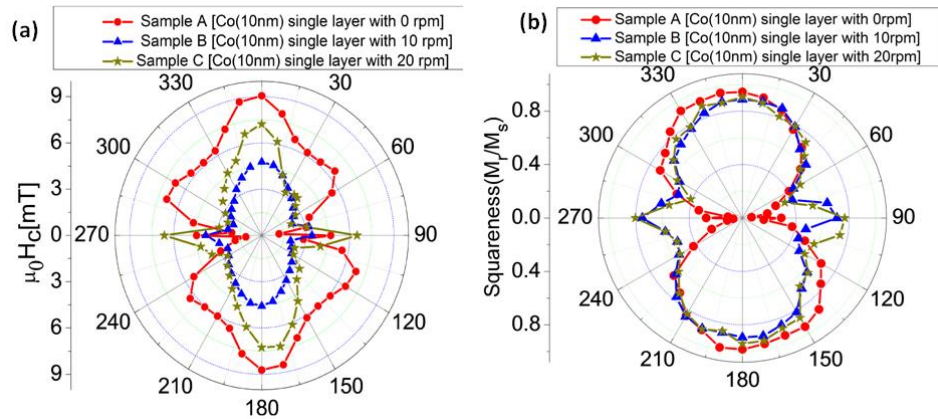


Figure 3.12: (a) Coercivity vs.  $\theta$  and (b)  $M_r/M_s$  vs.  $\theta$  for Sample A (red solid circles), Sample B (blue solid triangles) and Sample C (green solid stars) showing the uniaxial anisotropy behaviour.

It can be observed from Figure 3.12(a) that the plot for sample A, shows two global minima and four local minima which implies that in addition to a strong uniaxial magnetic anisotropy due to shadow effect, there exists weak intrinsic magnetocrystalline anisotropy [98]. The presence of strong uniaxial anisotropy is the result of oblique angle deposition. As already mentioned that in the QPrep deposition unit the angle between the substrate normal and the incident flux from the target is at 30°. Hence a uniaxial anisotropy is induced [5, 97]. On rotating the substrate, even though the anisotropy for sample B and C decreases it does not completely gives isotropic film. The uniaxial anisotropy behavior for Sample B and C can be observed in Figure 3.12(a) shown by the green color stars and blue color triangles. The anisotropy comparison can be better visualized in Figure 3.12(b) which shows the plot for angular dependence of squareness  $R_s$ . The existence of EA and HA for sample A can be clearly inferred from Figure 3.12(b). It can be observed that the change in squareness (Figure 3.12(b)) for sample B and C is small. This implies that even though we have rotated the sample to get isotropic film, a very weak uniaxial anisotropy still exists.

In general, the uniaxial anisotropy behavior of thin films is expected to follow  $|\cos \theta|$  which is the geometric projection of the easy axis magnetization onto the field axis. However, from Figure 3.12(a) and (b), a peak near HA is observed for all the three samples. This peak arises due to the misalignment of local grain anisotropy as explained by Idigoras *et al.* by using two grain Stoner-Wohlfarth model [35]. The energy for two exchanged coupled ( $J$ ) grains with magnetization  $m_1$  and  $m_2$ , anisotropy constants  $K_1$  and  $K_2$  with unit vectors  $n_1$  and  $n_2$  is given as –

$$E = -Jm_1 \cdot m_2 - H(m_1 + m_2) - \frac{1}{2}K_1(m_1 \cdot n_1)^2 - \frac{1}{2}K_2(m_2 \cdot n_2)^2 \quad (3.3)$$

For in-plane anisotropy assuming  $K_1 = K_2$  for grains with the same material, Eq. 3 reduces to-

$$E = -J \cos(\theta_1 - \theta_2) - H [\cos(\theta_1 - \beta) + \cos(\theta_2 - \beta)] - \frac{1}{2} K_1 [\cos^2(\theta_1 - \omega/2) + \cos^2(\theta_1 + \omega/2)]$$

where,  $\theta_1$ ,  $\theta_2$  and  $\beta$  are the angles with respect to the average anisotropy direction and  $\omega$  is the misalignment between the grains [35]. Idigoras *et al.* showed experimentally and theoretically that the height and width of the peak increases with the increase in disorder.

It has been shown that for HA reversal, below a certain critical misalignment of the EA of the grains, the exchange coupling dominates the misalignment of the anisotropy of the grains. Hence, as predicted by Stoner-Wohlfarth theory the grains follow the coherent rotation in the same sense of direction. However, above a certain degree of misalignment of the grain axis, the exchange coupling is not sufficient enough to overcome the randomness and hence the grains may rotate in opposite sense leading to the enhancement of the remanent magnetization and therefore a peak along HA [35]. From Figure 3.12(b), it can be observed that the height and width of the peak increase abruptly from 0 to 10 rpm but the change is minimal when  $\omega$  is increased from 10 to 20 rpm. It is evident that increase in substrate rotation during deposition results in misalignment and dispersion in local grain anisotropy. The uniaxial anisotropy of sample A can also be evident by comparing the hysteresis loops along EA and HA as shown in Figure 3.13(a). The loop shape suggests that along EA domain wall motion occurs by correlated switching of grains due to strong inter-granular exchange coupling [54, 113] and by coherent rotation along HA. The hysteresis loops for EA and HA for sample B and C are shown in Figure 3.13(b) and (c), respectively. It provides a direct visualization of squareness i.e.  $M_r/M_s$  for all the three samples. It can be observed from graphs that the squareness of HA increases with rotation. To calculate and quantify the anisotropies, SQUID measurements were performed at IITG along the HA. The values of the anisotropy was extracted using the formula:  $K = \mu_0 H M_s / 2$ , where  $H$  is the saturation field along the HA [23]. The values extracted from SQUID measurements for sample A, B and C

are  $6.28 \times 10^2$ ,  $4.45 \times 10^2$ ,  $5.49 \times 10^2$  J/m<sup>3</sup>, respectively. It indicates that sample B is the most isotropic which is consistent with AFM and MOKE analysis.

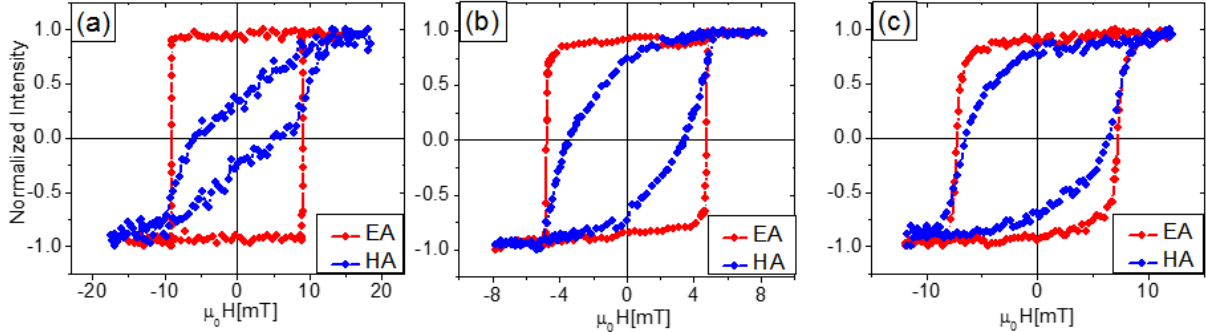


Figure 3.13: Comparison of hysteresis loops measured along EA and HA by LMOKE at room temperature for sample A, B, and C shown in (a), (b) and (c) plots, respectively.

It can also be observed from Figure 3.13(a) that the saturation field (anisotropy field  $H_k$ ) of HA is greater than the coercive field of the EA which is the case for general thin film. However, from Figure 3.13(b) and (c), it can be observed that the anisotropy field is comparable to coercive field for samples B and C which are characteristics of an inverted film [58]. The value of  $H_k$  can be deduced from the saturation field of HA as discussed in chapter 1 [23, 114]. This means that for inverted thin films, the ratio of  $H_C/H_K > 1$ . However, according to Methfessel *et al.* depending on the ratio of  $H_C/H_K$ , a film may be inverted in a certain angle range above the EA [58]. This implies that increase in the ratio of  $H_C/H_K$  should result in the decrease in the angle between the EA and inversion sector. In this angle range, the magnetization reversal for the small applied field is accompanied by rotation leading to the formation of ripple domains. As evident from Figure 3.13(b) and (c), the ratio of  $H_C/H_K \sim 1$  and hence the inversion sector of the film will be few degrees away from the EA. It will be later shown that this affects the domain structure and the relaxation process in the films.

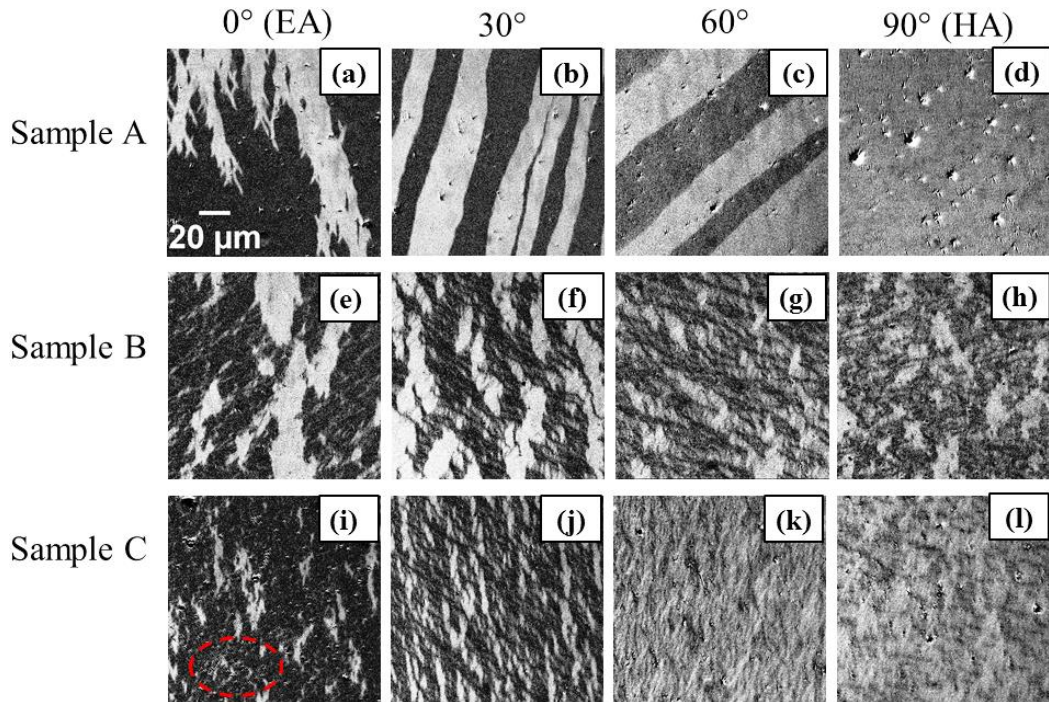


Figure 3.14: Domain images for sample A, B and C are shown for  $\theta = 0^\circ$  (EA),  $30^\circ$ ,  $60^\circ$  and  $90^\circ$  (HA), respectively. The images are taken near the coercive fields for the respective angles and the samples. The Zoomed in image of the red dotted area in Figure 3.14(i) has been shown in Figure 3.15(a).

Inverted thin films are the signature of inhomogeneous anisotropy distribution which affects the domain structures as discussed below. Domain structures for all the samples were studied by performing longitudinal Kerr microscopy obtained during hysteresis loop measurements and is shown in Figure 3.14. It was observed that reversal for sample A along EA,  $30^\circ$  and  $60^\circ$  (Figure 3.14) were corroborated by domain wall motion and nucleation. However, along HA (Figure 3.14(d)) no domains were observed during magnetization reversal for Sample A. Hence, the magnetization reversal was due to coherent rotation of spins. For sample B and sample C we observe ripple domains superimposed on patch like domains for EA. As we increase the angle from EA labyrinth domains are observed for sample B and sample C which is characteristic of an inverted film. Figure 3.15(a) shows the zoomed image for the area marked in Figure 3.14(i) and Figure R 3.15(j) and (k) shows high resolution images of

sample C for  $30^\circ$  and  $60^\circ$ , respectively. The images clearly show the labyrinth pattern. The origin of such labyrinth domains in samples B and C arise due to local dispersion in anisotropy in Co film due to the substrate rotation [6].

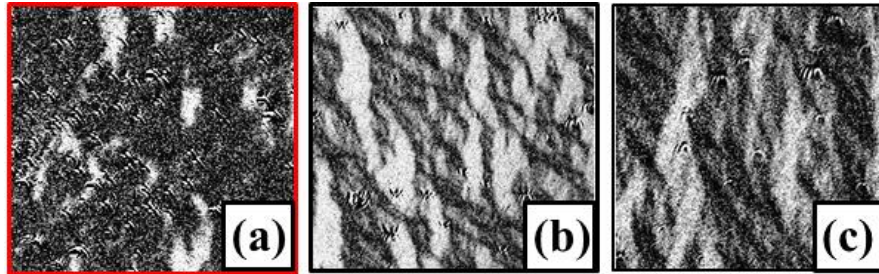


Figure 3.15: (a) zoomed-in image of the red area highlighted in Figure 3.14 is shown in the red box in (i) ( $60 \times 60 \mu\text{m}^2$ ), (b) and (c) are high resolution image ( $57 \times 52 \mu\text{m}^2$ ) for sample C along  $30^\circ$  and  $60^\circ$  w.r.t EA, respectively.

The detailed magnetization reversal along with hysteresis and domain images for  $30^\circ$  w.r.t EA for sample C is shown in Figure 3.16. Initially, the magnetization reverses by partial rotation giving rise to magnetization ripple domains (Figures 3.16(c, d)) [58]. Theoretically, formation of these ripple domains were ascribed to the presence of statistical fluctuations of anisotropy of the grains in the films. [115, 59].

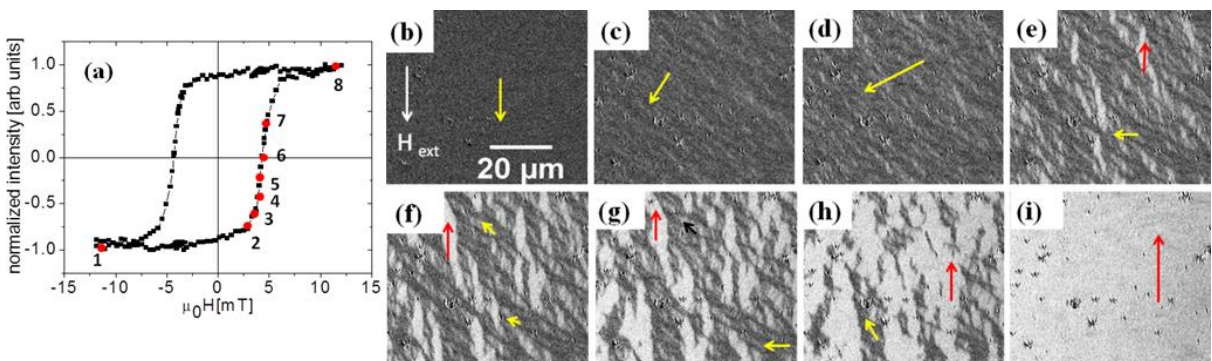


Figure 3.16: (a) Hysteresis measured by LMOKE for sample C for  $\theta = 30^\circ$ . Domain images for the fields marked by points 1 to 8 in (a) are shown in (b) - (i), respectively.

These ripples can be such that either the wave-front normal of the local fluctuations of the magnetization directions are parallel (longitudinal) to the average magnetization ( $m_0$ ), or are perpendicular (transverse) to  $m_0$  as shown in Figure 3.17(a) and (b) respectively [59]. However, the stray field energy due to the magnetic charge density will be less in longitudinal modulation compared to the transverse modulation (Figure 3.17). Hence, the major contribution arises from the longitudinal ripple waves as shown in the domain image Figure 3.16(c) and (d). On further increasing the field, a blocked state with the formation of labyrinth domains indicating the polycrystalline nature of the films are formed (Figure 3.16(e)). Finally, with an increase in the field, reversal is completed by domain wall motion as higher fields are required to move the domain walls formed. It can be seen from Figure 3.16(h) that these domain walls are present even at higher fields. These blocking and incoherent switching processes are undesirable in devices which require rapid switching of magnetization and hence must be avoided [20]. Similar magnetization reversal was observed for both samples B and C, when the magnetic field was applied for angles greater than  $30^\circ$  w.r.t EA. This observation suggests the existence of high dispersion in local anisotropy as observed in inverted films [58, 61]. In our case, we attribute the variation in local anisotropy to the misalignment of grains due to the substrate rotation.

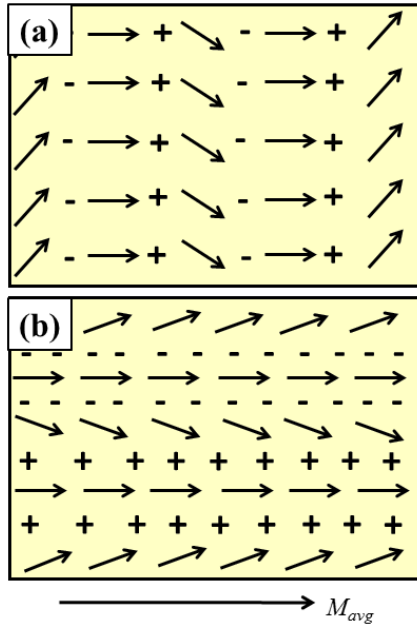


Figure 3.17: The schematic showing the fluctuations of magnetization for ripple domains (a) longitudinal and (b) transverse ripple. [59].

### 3.3.2.2.2 Effect on magnetization relaxation:

To understand the magnetization reversal further, magnetization relaxation measurements were performed as already described in section 3.3.1.2 [116]. Figure 3.18(a), (b), and (c) shows the hysteresis loops along EA for samples A, B, and C, with coercive fields ( $H_C$ ) of 8.28, 4.78 and, 8.65 mT, respectively. The nucleation fields ( $H_N$ ) observed from the Kerr microscopy images were found to be 8.23, 4.64, and 7.55 mT for sample A, B, and C, respectively.

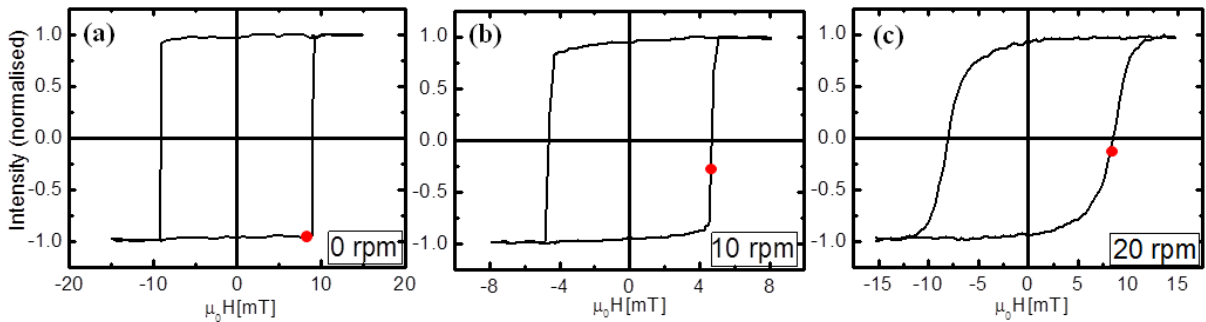


Figure 3.18: Hysteresis loops showing the magnetic fields (red dots) where the relaxation measurements have been performed for sample A (a), sample B (b), and sample C (c).

The magnetization relaxation measurements were performed as per the following procedure. First, the sample was negatively saturated in a uniform dc magnetic field. Subsequently, the field was reversed to  $H_M < H_C$ . Temporal evolution of the domains was recorded at  $H_M$ . Application of constant magnetic field (Zeeman energy) ensured that the magnetization reversal was governed by the thermal activation energy. The net gray scale value of the domain images was extracted by using the ImageJ software.

The relaxation data has been fitted using Boltzmann (Eq. (3.4)), single exponential decay (SED) (Eq. (3.5)) and double exponential decay (DED) (Eq. (3.6)) functions. These three functions have the following forms:

$$I(t) = I_F + (I_I - I_F) / [1 + \exp((t-t_0)/\tau)] \quad (3.4)$$

$$I(t) = I_F + I_I' \exp(-t/\tau) \quad (3.5)$$

$$I(t) = I_F + I_1 \exp(-t/\tau_1) + I_2 \exp(-t/\tau_2) \quad (3.6)$$

where,  $I(t)$  is the measured Kerr intensity,  $I_I$  is the initial Kerr intensity at time  $t=0$ ,  $I_F$  is the final Kerr intensity at saturation.  $\tau$ ,  $\tau_1$ ,  $\tau_2$  are the relaxation time constants;  $I_I'$ ,  $I_1$ ,  $I_2$  are the amplitudes of the corresponding exponents, and  $t_0$  is the time corresponding to the mean intensity of Eq. (3.4). In Figure 3.19 to 3.23, the experimental data of the relaxation measurements for all the samples are represented by black hollow circles whereas the blue, green and red curves represent the fits for Boltzmann, SED, and DED functions, respectively. Table 1 shows the values of reduced  $\chi^2$  and coefficient of determination (cod)  $r^2$  for all the fits. The least value of reduced  $\chi^2$  and the maximum value of cod  $r^2$  has been considered as the best fit for all the cases.

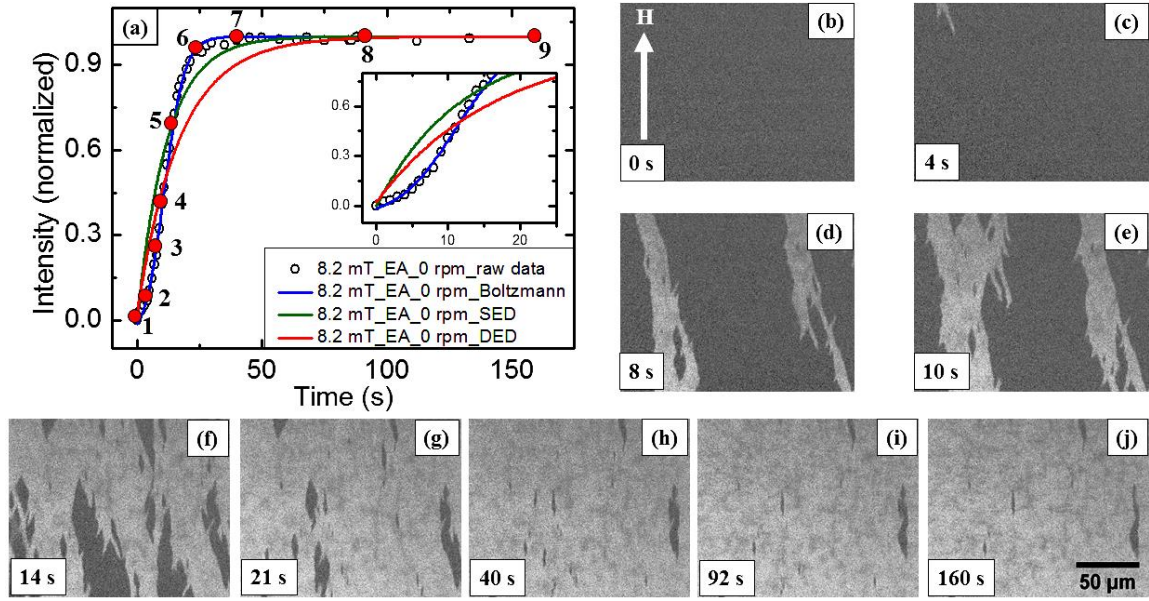


Figure 3.19: Relaxation measurement by LMOKE microscope for sample A along EA. Figure (b) - (j) are domain images taken at 0, 4, 8, 10, 14, 21, 40, 92, 160 s at  $H_M = 8.2$  mT, marked by points 1 to 9 in Figure 3.19, respectively.

Figure 3.19 shows the relaxation measurement along with the simultaneous domain imaging at  $H_M = 8.2$  mT along EA for sample A. In this case,  $H_M < H_N$  because the reversal for sample A is sharp i.e.  $H_N \sim H_C$  (Figure 3.18(a)). Figure 3.19(a), reveals that the data points for sample A is sharp i.e.  $H_N \sim H_C$  (Figure 3.18(a)). Figure 3.19(a), reveals that the data points are best fitted to the Boltzmann function which yields  $\tau = 4.00 \pm 0.09$  s. The initial slow nature of the relaxation is attributed to the fact that the domains started nucleating after a few seconds ( $t = 4$  s) of keeping the field at  $H_M$  (Figure 3.19(c)). The sharp increase in relaxation after a few seconds is due to the fast domain wall motion (Figure 3.19(d) - (g)). This fast relaxation is an effect of high exchange coupling due to the large size of grains as observed in Figure 3.9(a). While approaching the saturation at time  $t \geq 40$  s, the domain wall motion becomes slow which yields the flat nature of the relaxation (Figure 3.19(h) - (j)). The relaxation measurement performed for sample A along  $30^\circ$  away from EA (not shown here) was also best fitted to Boltzmann function (Eq. (3.4)) with  $\tau = 15.58 \pm 0.25$  s. Therefore, the relaxation became slow while moving away from EA.

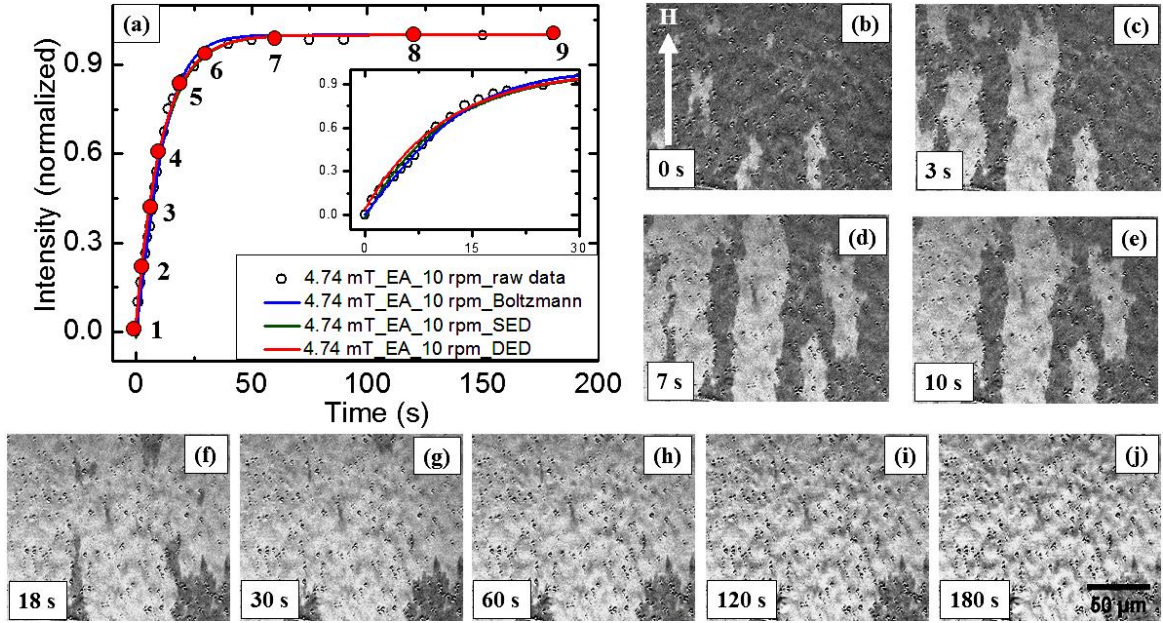


Figure 3.20: Relaxation measurement by LMOKE microscope for sample B along EA. Fig. (b) - (j) are domain images taken at 0, 3, 7, 10, 18, 30, 60, 120, 180 s at  $H_M = 4.74$  mT, marked by points 1 - 9 in Figure 3.20(a), respectively.

Figure 3.20 shows the relaxation measurement for sample B along EA at  $H_M = 4.74$  mT. The reversal for sample B is slow (Figure 3.18(b)) i.e.  $H_N$  is well below  $H_C$  and hence  $H_M$  (4.74 mT)  $>$   $H_N$  (4.64 mT). From Figure 3.20(a), it appears that the fits are equivalent for all the three functions. Nevertheless, we found that the value of reduced  $\chi^2$  is maximum and  $\text{cod } r^2$  is minimum for DED among all the three functions (see Table 3.1). Therefore, DED function was not considered to be the best fit. Further, we note that from table 3.1, the values of reduced  $\chi^2$  and  $\text{cod } r^2$  are comparable for Boltzmann and SED functions. However, the error in  $\tau$  was 7.18% and 2.64% for Boltzmann and SED function, respectively. Since the error in  $\tau$  was least for SED function, it was chosen as the best fit for sample B with  $\tau = 11.11 \pm 0.29$  s. This SED function is also known as the Fatuzzo-Labrune model [9, 106] as described in section 1.1 of chapter 1. It indicates that the magnetization reversal mechanism is governed by nucleation dominated aftereffect followed by domain wall motion as observed from the domain images in Figure 3.20(b) - (j). The initial data points of sample

B (Figure 3.20(a)) did not exhibit the slow relaxation behavior as compared to sample A (Figure 3.20(a)). Since  $H_M$  (4.74 mT)  $>$   $H_N$ , the domains were nucleated before the field was fixed at  $H_M$  (Figure 3.20(b)). Here, the domain walls propagate very fast under the influence of thermal activation energy and the relaxation curve flattens as it reaches saturation.

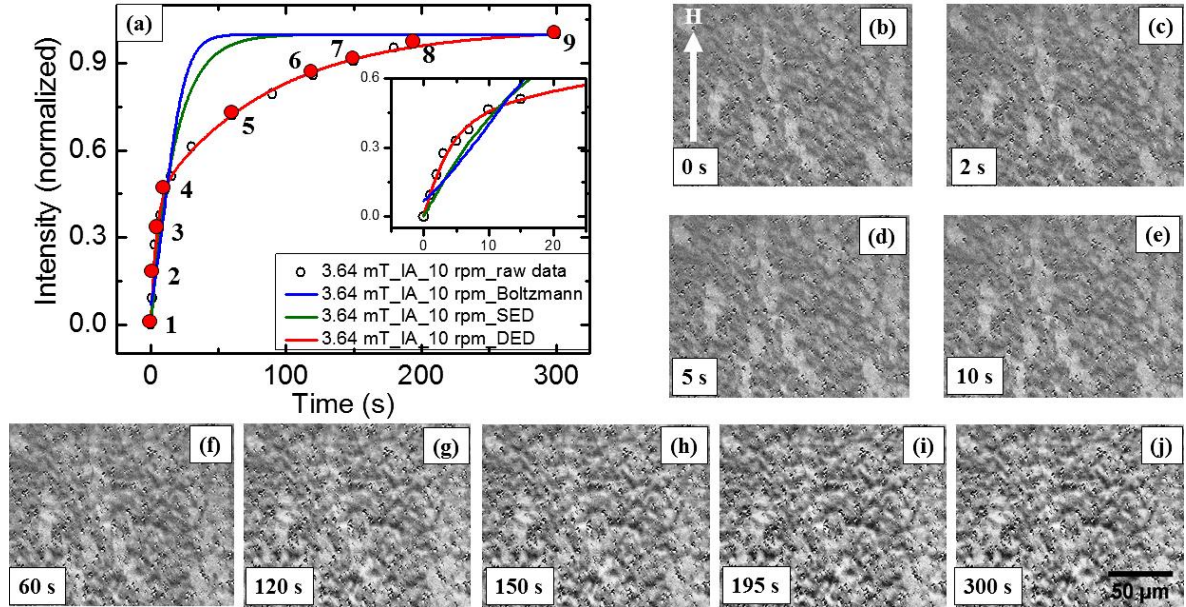


Figure 3.21: Relaxation measurement by LMOKE microscope for sample B along  $30^\circ$  w.r.t EA. Figure (b) - (j) are domain images taken at 0, 2, 5, 10, 60, 120, 150, 195, 300 s at  $H_M = 3.64$  mT marked by points 1 - 9 in Figure 3.21(a), respectively.

The relaxation data for sample B along  $30^\circ$  from EA is shown in Figure 3.21(a). It was best fitted with DED function (Eq. 3.6). The value of the relaxation time constants  $\tau_1$  and  $\tau_2$  were  $4.12 \pm 0.42$  s and  $93.39 \pm 9.28$  s, respectively. However, it should be noted that according to Methfessel *et al.*, depending on the ratio of  $H_C/H_K$ , a film is inverted in a certain angle range above the EA [58]. This implies that increase in the ratio of  $H_C/H_K$  should result in the decrease in the angle between the EA and inversion sector. It should be noted that  $30^\circ$  w.r.t EA of sample B is already in the inversion sector as observed by the formation of ripple domains as shown in Figure 3.14(f) and its high resolution image Figure 3.15(b) [6]. Therefore, the energy present in the system (Zeeman and thermal activation) is not sufficient

to overcome the energy barrier of the random distribution of the grain anisotropy which results in the slow relaxation (Figure 3.21(b) – (j)).

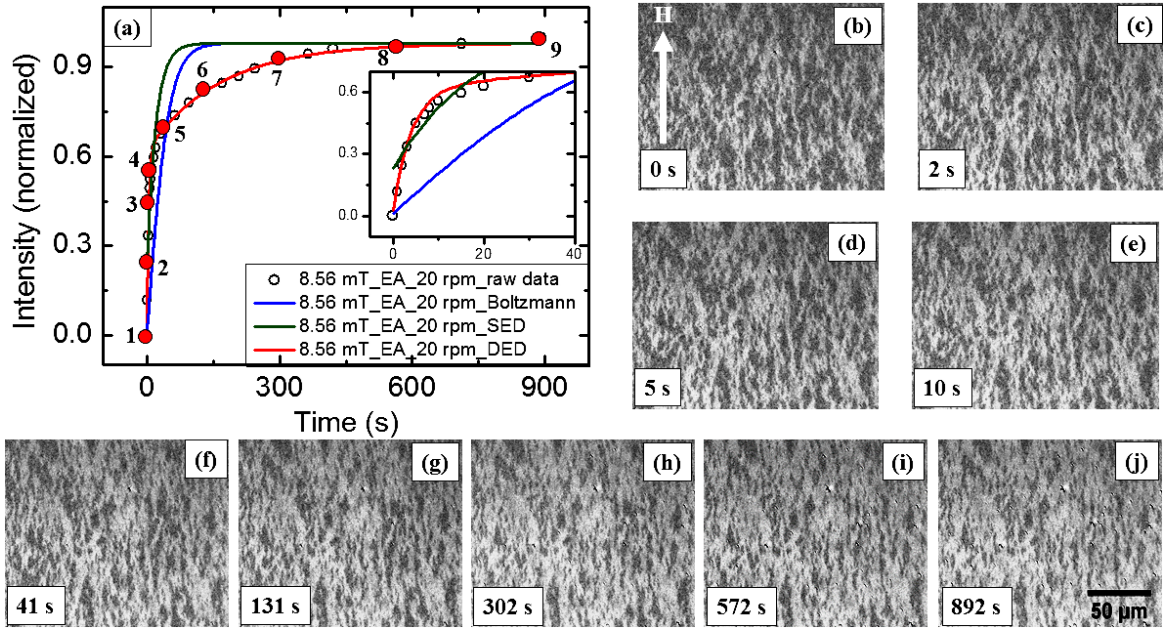


Figure 3.22: Relaxation measurement by longitudinal Kerr microscope for sample C along EA. Fig. (b) - (j) are domain images taken at 0, 2, 5, 10, 41, 131, 302, 572, 892 s at  $H_M = 8.56$  mT, marked by points 1 - 9 in Figure 3.22(a), respectively.

Figure 3.22 depicts the relaxation behavior and the corresponding domain images of sample C along EA at  $H_M = 8.56$  mT. The data points were best fitted (red curve) using DED function (Eq. 3.6). From the DED fit the extracted relaxation time constants  $\tau_1$  and  $\tau_2$  are  $4.09 \pm 0.14$  and  $166.90 \pm 9.17$  s, respectively. Both the exponent of the DED function (Eq. 3.6) can be derived from the Boltzmann function (Eq. 3.4) by considering the time limits  $t-t_0 \gg \tau$  and  $t-t_0 < \tau$ . Figure 3.9 reveals that the average grain size in sample C is less than sample A but more than sample B. However, the grains in sample C were not uniformly distributed and formed island-like structures (Figure 3.10(b)) which cause the slow nature of the relaxation behavior. The initial few seconds of relaxation is relatively faster because the applied  $H_M$  is high in comparison to  $H_N$ . However, due to the high dispersion of grains, it is unfavorable to overcome the large energy barriers to saturate the sample. Hence, sufficient

thermal activation energy is required to overcome the energy barriers leading to the slow relaxation of the second exponential part of DED. For sample C, the relaxation performed along 30° away from EA (data not shown) was best fitted by DED behavior which yields higher relaxation times.

Table 1: Details of fitting parameters for relaxation measurements along EA at  $H_M/H_C \sim 0.99$

		<b>Boltzmann Fit</b>	<b>SED Fit</b>	<b>DED Fit</b>
<b>Sample A (0 rpm) EA</b>	$(\chi^2)_{\text{red}}$	$1.44 \times 10^{-4}$	$6.72 \times 10^{-3}$	$7.10 \times 10^{-3}$
	$(r^2)_{\text{cod}}$	0.999	0.953	0.953
	$\tau_1$	$4.00 \pm 0.09$ s	$14.15 \pm 0.92$ s	$15.01 \pm 1.69$ s
	$\tau_2$			$20.02 \pm 2.29$ s
	Best Fit	✓		
<b>Sample B (10 rpm) EA</b>	$(\chi^2)_{\text{red}}$	$4.50 \times 10^{-4}$	$5.52 \times 10^{-4}$	$9.87 \times 10^{-4}$
	$(r^2)_{\text{cod}}$	0.996	0.995	0.991
	$\tau_1$	$7.75 \pm 0.11$ s	$11.11 \pm 0.29$ s	$13.55 \pm 0.98$ s
	$\tau_2$			$11.29 \pm 0.29$ s
	Best Fit		✓	
<b>Sample B (10 rpm) IA</b>	$(\chi^2)_{\text{red}}$	$7.07 \times 10^{-3}$	$6.52 \times 10^{-3}$	$2.05 \times 10^{-4}$
	$(r^2)_{\text{cod}}$	0.949	0.950	0.999
	$\tau_1$	$24.40 \pm 6.90$ s	$21.51 \pm 3.59$ s	$4.12 \pm 0.42$ s
	$\tau_2$			$93.39 \pm 9.28$ s
	Best Fit			✓
<b>Sample C (20 rpm) EA</b>	$(\chi^2)_{\text{red}}$	$8.14 \times 10^{-3}$	$7.76 \times 10^{-3}$	$2.15 \times 10^{-4}$
	$(r^2)_{\text{cod}}$	0.912	0.912	0.997
	$\tau_1$	$9.40 \pm 1.23$ s	$29.86 \pm 4.92$ s	$4.09 \pm 0.14$ s
	$\tau_2$			$166.90 \pm 9.17$ s
	Best Fit			✓

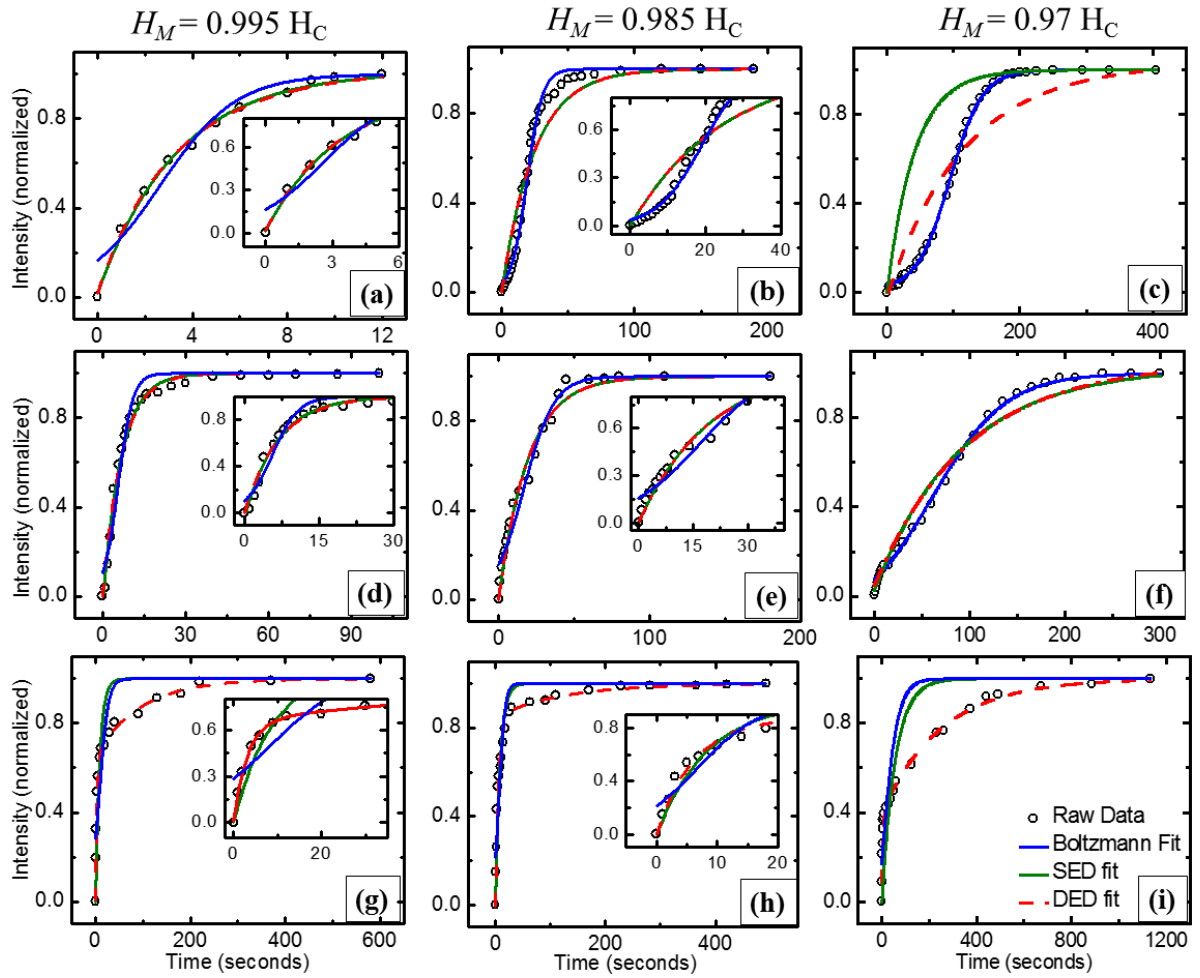


Figure 3.23: Magnetization relaxation data along with the fits for sample A (a) - (c), sample B (d) - (f), sample C (g) - (i) measured at  $H_M/H_C \sim 0.995$ ,  $0.985$ , and  $0.97$ , respectively. It should be noted that the DED fits here have been represented by dashed red curve to differentiate between the overlapping curves.

The relaxation data for sample A for  $H_M/H_C \sim 0.995$ ,  $0.985$  and  $0.97$  are shown in Figure 3.23(a), (b) and (c), respectively. The relaxation behavior at  $H_M/H_C \sim 0.995$  is best fitted (green curve) with SED function (Figure 3.23(a)). In this case  $H_M > H_N$  and hence, the relaxation is fast. However, the relaxation behavior at  $H_M/H_C \sim 0.985$  and  $0.97$  follows Boltzmann function (Figure 3.23(b) and (c)) which is similar to the behavior at  $H_M/H_C \sim 0.99$  (Figure 3.19(a)). The relaxation data for sample B, best fitted to SED function at  $H_M/H_C \sim 0.995$  and  $0.985$ , are shown in Figure 3.23(d) and (e), respectively. This behavior is

consistent with the relaxation at  $H_M/H_C \sim 0.99$  (Figure 3.20(a)). However for sample B, at  $H_M/H_C \sim 0.97$ , the relaxation follows Boltzmann function (Figure 3.23(f)). The relaxation data for sample C is best fitted (red dashed curve) to DED function at  $H_M/H_C \sim 0.995, 0.985,$  and  $0.97$  shown in Figure 3.23(g), (h), and (i), respectively. This behavior is similar to the relaxation at  $H_M/H_C \sim 0.99$  (Figure 3.22(a)). Table 3.2 shows the values of  $\tau$ , reduced  $\chi^2$  and cod  $r^2$  for all the fits at  $H_M/H_C \sim 0.995, 0.985,$  and  $0.97$ .

Table 2: Details of fitting parameters for relaxation measurements along EA at different  $H_M/H_C$

	$H_M/H_C$		<b>Boltzmann Fit</b>	<b>SED Fit</b>	<b>DED Fit</b>
<b>Sample A</b> <b>(0 rpm)</b>	0.995	$(\chi^2)_{\text{red}}$ $(r^2)_{\text{cod}}$ $\tau_1$ $\tau_2$ Best Fit	$4.67 \times 10^{-3}$ 0.954 $1.62 \pm 0.22$ s	$3.89 \times 10^{-4}$ 0.996 $3.33 \pm 0.08$ s  ✓	$4.02 \times 10^{-4}$ 0.996 $1.32 \pm 0.67$ s $3.66 \pm 0.14$ s
	0.985	$(\chi^2)_{\text{red}}$ $(r^2)_{\text{cod}}$ $\tau_1$ $\tau_2$ Best Fit	$1.40 \times 10^{-3}$ 0.990 $5.85 \pm 0.25$ s  ✓	$9.94 \times 10^{-3}$ 0.930 $24.66 \pm 1.54$ s	$1.01 \times 10^{-2}$ 0.928 $24.66 \pm 15.41$ s $24.66 \pm 1.71$ s
	0.97	$(\chi^2)_{\text{red}}$ $(r^2)_{\text{cod}}$ $\tau_1$ $\tau_2$ Best Fit	$1.58 \times 10^{-4}$ 0.999 $24.58 \pm 0.35$ s  ✓	$9.98 \times 10^{-2}$ 0.399 $41.60 \pm 17.09$ s	$1.55 \times 10^{-2}$ 0.907 $115.19 \pm 2.69$ s $115.19 \pm 2.91$ s
<b>Sample B</b> <b>(10 rpm)</b>	0.995	$(\chi^2)_{\text{red}}$ $(r^2)_{\text{cod}}$ $\tau_1$ $\tau_2$ Best Fit	$4.00 \times 10^{-3}$ 0.963 $2.63 \pm 0.26$ s	$1.29 \times 10^{-3}$ 0.988 $6.54 \pm 0.21$ s  ✓	$1.86 \times 10^{-3}$ 0.980 $6.91 \pm 0.54$ s $6.91 \pm 0.54$ s

	0.985	$(\chi^2)_{\text{red}}$ $(r^2)_{\text{cod}}$ $\tau_1$ $\tau_2$ Best Fit	$3.00 \times 10^{-3}$ 0.976 $9.96 \pm 0.76$ s	$1.70 \times 10^{-3}$ 0.986 $19.55 \pm 0.77$ s ✓	$1.80 \times 10^{-3}$ 0.985 $19.54 \pm 1.54$ s $19.54 \pm 1.54$ s
	0.97	$(\chi^2)_{\text{red}}$ $(r^2)_{\text{cod}}$ $\tau_1$ $\tau_2$ Best Fit	$4.80 \times 10^{-4}$ cod $r^2 = 0.990$ $\tau = 41.94 \pm 3.15$ s ✓	$1.80 \times 10^{-3}$ 0.988 $112.99 \pm 10.23$ s	$2.00 \times 10^{-3}$ 0.988 $2.15 \pm 0.03$ s $112.99 \pm 10.65$ s
<b>Sample C</b> <b>(20 rpm)</b>	0.995	$(\chi^2)_{\text{red}}$ $(r^2)_{\text{cod}}$ $\tau_1$ $\tau_2$ Best Fit	$1.70 \times 10^{-2}$ 0.804 $9.13 \pm 2.72$ s	$1.30 \times 10^{-2}$ 0.850 $8.90 \pm 1.36$ s	$2.53 \times 10^{-4}$ 0.997 $3.15 \pm 0.21$ s $96.61 \pm 8.56$ s ✓
	0.985	$(\chi^2)_{\text{red}}$ $(r^2)_{\text{cod}}$ $\tau_1$ $\tau_2$ Best Fit	$7.30 \times 10^{-3}$ 0.920 $5.23 \pm 0.84$ s	$3.70 \times 10^{-3}$ 0.959 $8.52 \pm 0.58$ s	$1.00 \times 10^{-3}$ 0.989 $5.91 \pm 0.27$ s $123.78 \pm 31.08$ s ✓
	0.97	$(\chi^2)_{\text{red}}$ $(r^2)_{\text{cod}}$ $\tau_1$ $\tau_2$ Best Fit	$1.86 \times 10^{-2}$ 0.797 $49.14 \pm 6.46$ s	$3.00 \times 10^{-2}$ 0.668 $55.46 \pm 11.58$ s	$3.01 \times 10^{-4}$ 0.997 $4.50 \pm 0.16$ s $253.39 \pm 8.33$ s ✓

### 3.4 Conclusion-

Hence, it can be concluded that oblique deposition leads to uniaxial anisotropy in Co thin films. Substrate rotation during growth weakens this uniaxial anisotropy but does not completely give isotropic properties. However this moderate change in anisotropy affects the domain structure of the ferromagnet. It may give rise to inverted thin films and leads to formation of ripple and labyrinth domains. Magnetic aftereffect relaxation measurements reveal that the samples can be classified into two types: (i) sample A ( $\omega = 0$  rpm) and B ( $\omega = 10$  rpm) having uniform grains and low dispersion and (ii) sample C ( $\omega = 20$  rpm) with high dispersion and non-uniform grain distribution. The first type of samples follows either Boltzmann or single exponential decay behavior depending on the amplitude of the applied

magnetic field. However, the second type follows double exponential behavior irrespective of the amplitude of the applied magnetic field. This implies that the dispersion in thin films limits the relaxation and magnetic switching time [116].

## Chapter 4 : Study of magnetization reversal in dipolarly coupled Co/AlO<sub>x</sub> multilayers

### 4.1 Introduction:

In the previous chapter, magnetization reversal of Co thin film with oblique deposition and substrate rotation has been studied. However, magnetization reversal for two ferromagnetic films separated by a spacer layer is expected to be different than its single layer. The interactions between the ferromagnetic layers (FM) separated by a non-magnetic spacer (NM) will depend on the nature of the spacer layer. For FM layers separated by metallic spacer like Co/Ru, Co/Cr and Fe/Cr systems, depending on the thickness of the spacer layer, exchange coupling and the magnetoresistance shows oscillatory behaviour [117, 118]. For such systems where the ferromagnetic layers are separated by metallic spacers, the coupling is attributed to *Ruderman-Kittel-Kasuya-Yosida* (RKKY) coupling. It is an indirect exchange coupling which occurs through the itinerant electrons of the metals. It shows the oscillatory behaviour due to the Fermi surface of the metallic spacer [119, 120, 121]. For insulating spacer, in the ultrathin limit, an exponential decreasing interaction related to electron tunnelling may be anticipated between the two ferromagnetic layers [13, 122]. Interlayer exchange coupling for insulating spacers was theoretically explained by introducing the concept of complex Fermi surface [13, 123, 124]. A unified theory of metallic and insulating spacers was proposed by Bruno where it was shown that interlayer coupling decreases with increase in temperature for metallic spacers but it increases for insulating spacers. For the large thickness of the insulating spacer, one expects dipolar interaction leading to an anti-parallel alignment of the ferromagnetic layers. Dipolar energy between two magnetic dipoles ( $m_1$  and  $m_2$ ) is given by –

$$E = \frac{\mu_0}{4\pi r^3} \left[ m_1 \cdot m_2 - \frac{3}{2} (m_1 \cdot r)(m_2 \cdot r) \right]$$

where,  $\mu_0$  is the permeability of free space and  $r$  is the distance from the center of the two dipoles. However, correlated roughness at the interfaces may lead to ferromagnetic coupling (Neel Orange-peel coupling) as suggested by Néel [14]. It was observed that uncorrelated roughness may lead to biquadratic coupling leading to 90° coupling between the magnetic layers [125]. It is believed to arise due to high roughness or magnetic impurities in the spacer layers which mediates the coupling between the two ferromagnetic layers. Mathematically, the interaction energy for interlayer coupling can be expressed as -

$$E = -J_1(m_1 \cdot m_2) - J_2 (m_1 \cdot m_2)^2$$

where,  $J_1$  is the bilinear coupling constant whose sign (+ or -) depends on the type of interaction (antiferromagnetic or ferromagnetic),  $J_2$  is the biquadratic coupling. This term gives rise to non-collinear alignment of the magnetization vectors  $m_1$  and  $m_2$  [125]. Apart from metallic and insulating spacers, interlayer exchange coupling has also been studied for semiconductor [126, 127] and antiferromagnetic spacers [128, 129, 130]. The competition between interlayer interactions may lead to modulated incommensurate phases [112]. In this chapter, the magnetization reversal of dipolarly coupled Co layers with uniaxial and random anisotropy have been studied. The coupling induces a layer-by-layer magnetization reversal.

## 4.2 Sample preparation and experimental techniques:

The multilayers of AlO<sub>x</sub> (3 nm)/[Co( 10 nm)/AlO<sub>x</sub> ( $t$  nm)/Co (10 nm)/AlO<sub>x</sub> (3 nm) on Si (100) substrates were prepared by magnetron sputtering in the UHV chamber manufactured by Mantis Deposition Ltd., UK. The Co and AlO<sub>x</sub> layers were prepared by DC and RF sputtering as described in Chapter 2, section 2.1.2. The schematic for sample structure is shown in Figure 4.1. The thickness of the spacer AlO<sub>x</sub> ( $t$ ) was varied from 3 to 270 nm to study the effect of dipolar coupling with increasing the spacer thickness.

Specifically, samples with  $t = 3, 8, 23, 33, 45, 90, 130$  and  $270$  nm were prepared. However, it should be noted that the sample for  $t = 270$  nm was prepared with different Co target. The details of the sample structure with its name for Co/ $\text{AlO}_x$  series used in Chapter 3 and Chapter 4 has been shown in Table A of the Appendix. Though the measurements were taken on many samples, but the results from few of them have been discussed in detail in this thesis and have been labelled accordingly.

The structural characterization was performed using cross sectional transmission electron microscopy (XTEM), X-ray reflectivity (XRR), and Secondary ion mass spectroscopy (SIMS). The magnetization properties were studied by LMOKE magnetometry and microscopy, and the magnetization depth profile by polarized neutron reflectivity (PNR). To qualitatively understand the experimental observations micromagnetic simulations were performed using object oriented micromagnetic framework (OOMMF).

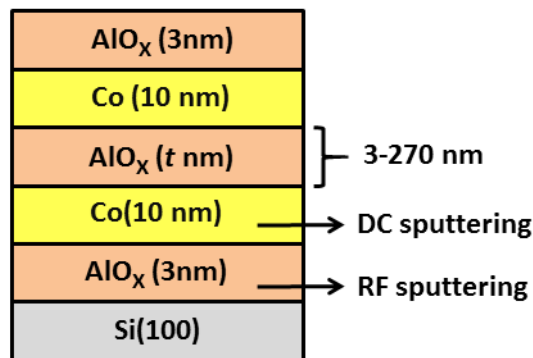


Figure 4.1: The schematic of the sample structure showing two Co (10 nm) layers separated by the spacer  $\text{AlO}_x$  whose thickness ( $t$ ) was varied from 3 to 270 nm.

### 4.3 Structural Characterization:

Cross sectional transmission electron microscopy (XTEM) was performed at Insititute of Physics, Bhubaneswar to know the layer quality and crystallinity. Figure 4.2 shows the XTEM image of a representative sample - Si (100)/  $\text{AlO}_x$  (3 nm)/Co (10 nm)/ $\text{AlO}_x$  (23 nm)/Co(10 nm)/ $\text{AlO}_x$  (3 nm).

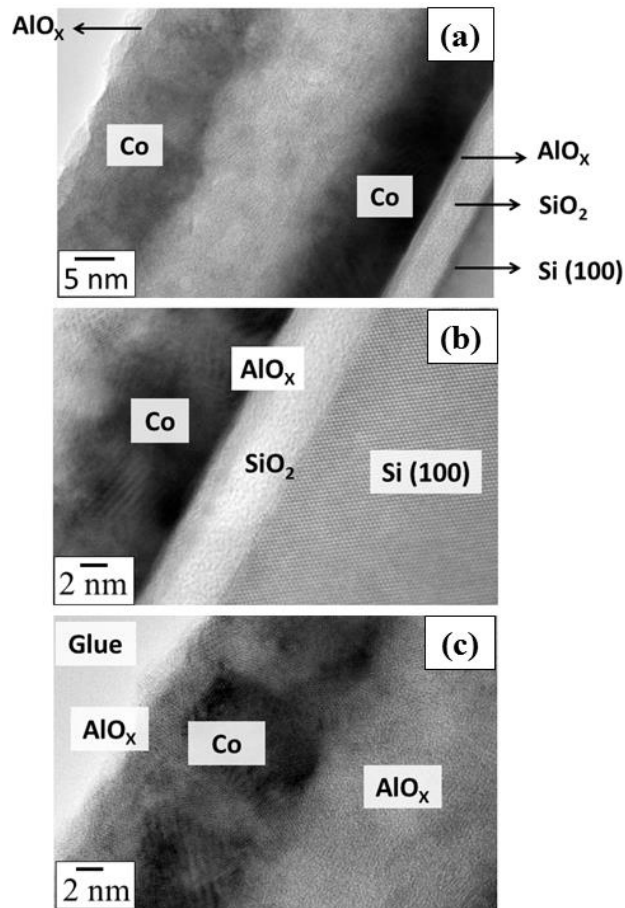


Figure 4.2: Cross-sectional transmission electron microscopy (XTEM) images of (a) Si (100)/ AlO<sub>x</sub> (3 nm)/Co (10 nm)/AlO<sub>x</sub> (23 nm)/Co(10 nm)/AlO<sub>x</sub> (3 nm), high resolution image of (b) bottom Co layer and (c) spacer and top Co layer.

Figure 4.2(a) shows the XTEM image of the sample with its native SiO<sub>2</sub>. The high resolution XTEM images reveal that both the bottom and top Co layers as shown in Figure 4.2(b) and (c), respectively, have polycrystalline structure. Since all the samples discussed in this chapter has been prepared in similar conditions to the one shown above (Figure 4.2), it is expected that for other samples similar crystallinity will be followed. From here on for the ease of discussion samples with  $t = 8, 90, 130$  and  $270$  nm are labelled as sample D, E, F, and G, respectively.

In order to determine accurately the layer thickness, roughness, and density of the samples, specular X-ray reflectivity (XRR) measurements were performed. The measured

data was simulated and fitted using GenX which uses the differential evolution algorithm. It can be used for fitting of X-ray as well as neutron reflectivity data using Parratt recursion formula [131]. Figure 4.3(a), (b) and (c) shows the XRR measurements for sample D, E, and F, respectively. The model for simulation had Si substrate with its native oxide ( $\text{SiO}_2$ ) along with the sample structure  $\text{AlO}_x$  (3 nm)/Co (10 nm)/ $\text{AlO}_x$  ( $t$  nm)/Co(10 nm)/ $\text{AlO}_x$  (3 nm) where  $t = 8, 90, 130$  nm. From the fits, the thicknesses of the Co layers were found to be  $11 \pm 1$  nm. The values of top and bottom  $\text{AlO}_x$  were found to be  $3 \pm 0.5$  nm. The values of spacer layers were found to be 8, 90, 130 nm from the fits of Figure 4.3(a), (b), and (c), respectively. The XRR fits revealed there was no interdiffusion at the interfaces. It should be noted that the densities of  $\text{Al}_2\text{O}_3$  is quite less than the bulk value, which may happen due to some oxygen deficiencies.

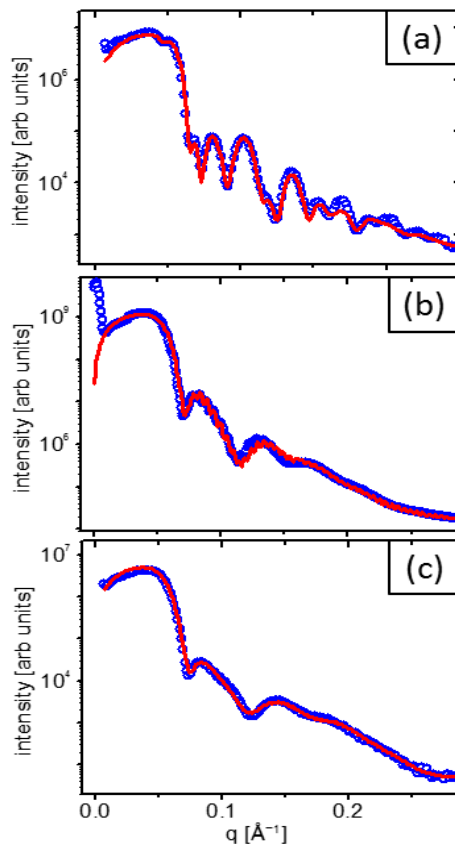


Figure 4.3: XRR curves for sample D (a), sample E (b) and sample F (c). The experimental data is shown as open circles and the solid line is the simulated fits.

Secondary ion mass spectroscopy (SIMS) was performed at National Physical laboratory, New Delhi to know the quality of the layers and the elemental (Al, O and Co) profile in the multilayers grown. It should be noted that SIMS is a qualitative technique. The measurement was performed using  $\text{Cs}^+$  as primary ions to enhance the yield of oxygen. The elemental profile of SIMS data for sample D is shown in Figure 4.4. The full width at half maxima for each layer intersected with each other indicating no interdiffusion. It should be noted that the graph in Figure 4.4 is in log scale. The other samples of Co/ $\text{AlO}_x$ /Co were prepared with similar growth conditions. Therefore it is expected that the other samples have no interdiffusion.

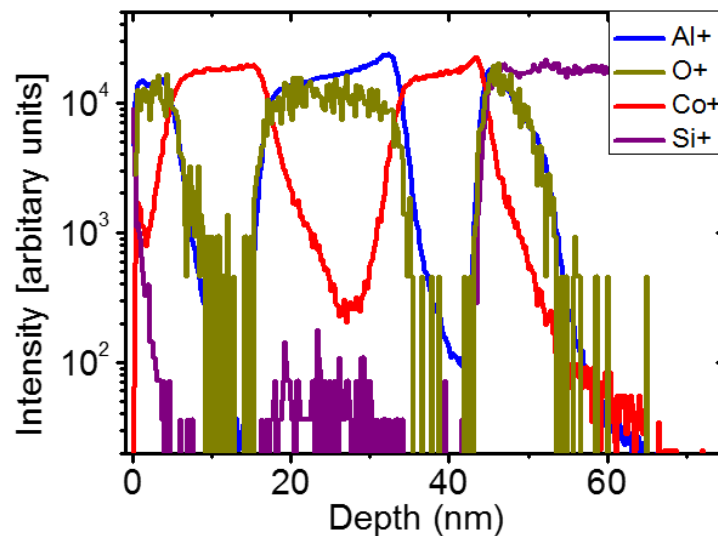


Figure 4.4: Elemental depth profile measured by SIMS for sample D i.e. Si (100)/ $\text{AlO}_x$  (3 nm)/Co (10 nm)/ $\text{AlO}_x$  (8 nm)/Co(10 nm)/ $\text{AlO}_x$  (3 nm).

## 4.4 Magnetic Properties:

### 4.4.1 Magnetization reversal of Co (10nm) single layer:

Effect of dipolar coupling on the magnetization reversal of the Co layers with increasing the spacer layer was studied by Kerr magnetometry and microscopy. It should be noted that the Co target used to prepare these series of Co/ $\text{AlO}_x$ /Co trilayers was different

than that used for the results shown in chapter 3. Hence, a Co (10 nm) single layer with structure Si(100)/AlO<sub>x</sub>(3 nm)/Co(10 nm)/AlO<sub>x</sub>(3 nm) was prepared and characterized by MOKE microscopy. It showed similar properties to the one discussed in chapter 3 except there was little variation in the domain structure. The hysteresis and the domain structure along EA is shown in Figure 4.5(a) and 4.5(b) – (e), respectively. Similar to the previous case, the reversal occurs via domain wall motion along easy axis (EA). The domains here are large and striped.

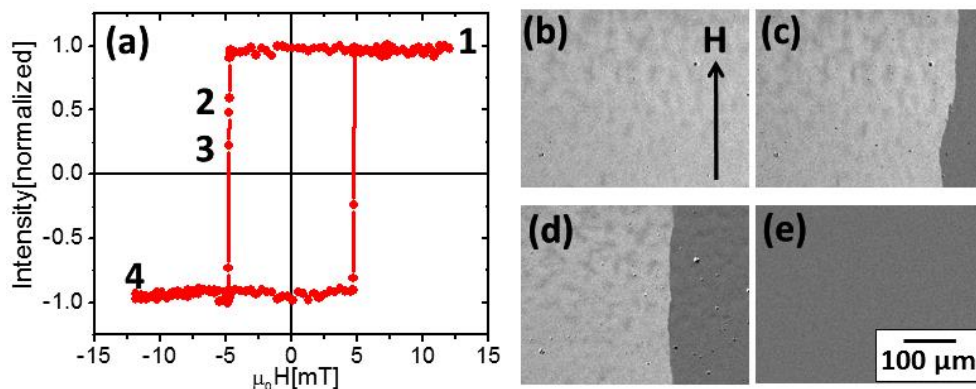


Figure 4.5: Hysteresis (a) and domain images (b) – (e) measured by LMOKE microscopy along EA for AlO<sub>x</sub> (3 nm)/Co (10 nm)/AlO<sub>x</sub> (3 nm) [The Co target used was different than the one used for preparation of Co/AlO<sub>x</sub>/Co multilayers]. The field points corresponding to the domain images for (b) – (e) are shown by points 1 to 4 in Figure 4.5(a), respectively.

Along hard axis (HA), the reversal was governed by coherent rotation as shown by the *S*-shaped hysteresis (Figure 4.6(a)) and the contrast change of the domain images of Figure 4.6(b) – (e). The field points for the images of Figure 4.6(b) – (e) are marked in hysteresis (Figure 4.6(a)).

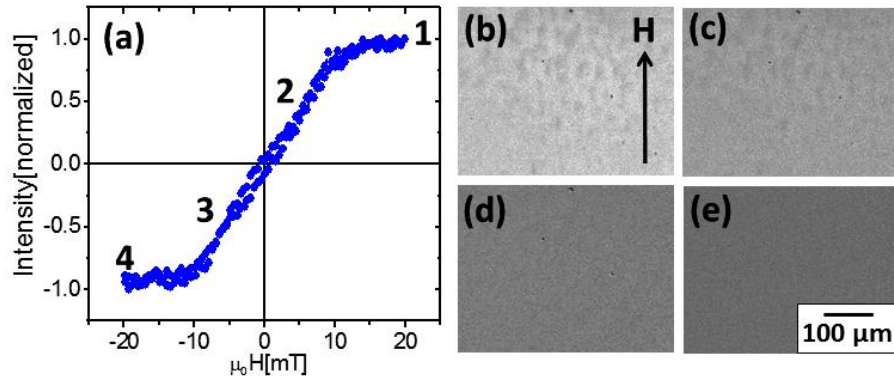


Figure 4.6: Hysteresis (a) and domain images (b) – (e) measured by LMOKE microscopy along HA for  $\text{AlO}_x$  (3 nm)/Co (10 nm)/ $\text{AlO}_x$  (3 nm) [The Co target used was different than the one used for preparation of Co/ $\text{AlO}_x$ /Co multilayers]. The field points corresponding to the domain images for (b) – (e) are marked by points 1 to 4 in Figure(a), respectively.

## 4.4.2 Study of magnetization reversal for Co (10 nm)/ $\text{AlO}_x$ ( $t$ nm)/Co (10 nm)

### 4.4.2.1 Presence of uniaxial and random anisotropy:

In – plane magnetization measurements were performed using LMOKE microscopy and magnetometry for Co(10nm)/ $\text{AlO}_x$  ( $t$  nm)/Co(10nm) where  $t$  was varied from 3 to 270 nm. As discussed in Chapter 3, due to the geometrical construction of the deposition chamber, the angle between the substrate normal and the incident flux from the target is at  $30^\circ$ . Hence, a growth induced in-plane uniaxial anisotropy was observed in all the Co (10nm)/ $\text{AlO}_x$ ( $t$  nm)/Co (10nm) samples where  $t = 3$  to 270 nm. The in-plane angle dependence of coercivity and Squareness  $R_s$ , defined as  $M_r/M_s$  where  $M_r$  = remanent magnetization and  $M_s$  = saturation magnetization for Co (10nm)/ $\text{AlO}_x$  (3 nm)/Co (10nm) are shown in Figure 4.7(a) and (b), respectively. It should be noted that a peak near HA is observed in both Figure 4.7(a) and (b). This peak arises due to the misalignment of local grain anisotropy as explained in detail in Chapter 3, section 3.3.2.2. All the samples with the trilayers of Co (10nm)/ $\text{AlO}_x$  ( $t$  nm)/Co (10nm) showed similar behaviour.

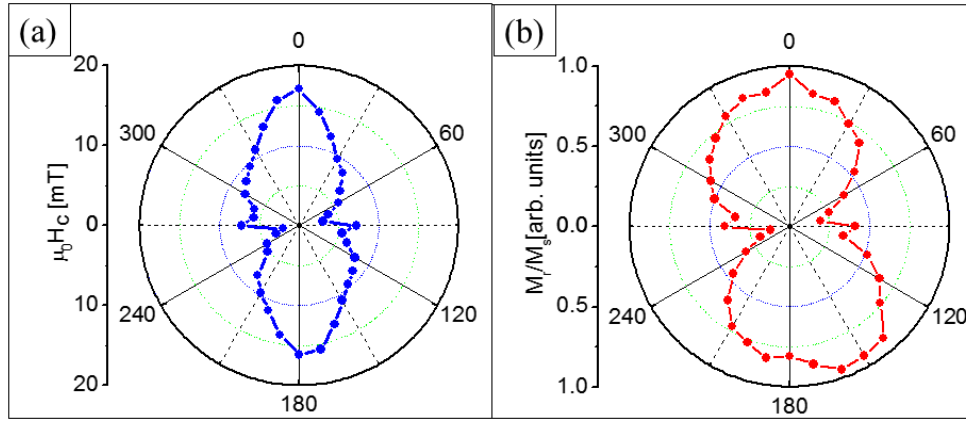


Figure 4.7: Angular dependence of (a) Coercivity vs.  $\theta$  (b)  $M_r/M_s$  vs.  $\theta$  for Co (10 nm)/ AlO<sub>x</sub>(3 nm)/Co (10 nm) showing the uniaxial anisotropy behaviour.

Similar behaviour was observed for all samples of Co (10 nm)/AlO<sub>x</sub> ( $t$  nm)/Co (10 nm).

#### 4.4.2.2 MOKE microscopy and magnetometry-

To understand the effect of dipolar coupling on the magnetization reversal of Co layers, LMOKE microscopy measurements with simultaneous domain imaging were performed. The hysteresis loops measured along EA by MOKE microscopy for all the samples showed two stepped hysteresis loops. Figure 4.8 shows the two stepped hysteresis loop along EA with its domain images for sample D. At positive saturation,  $\mu_0 H = 40$  mT (Figure 4.8(a), point 1), a single domain state with black contrast shown in Figure 4.8(b) is observed. As the applied field is increased in the negative direction, the first magnetization reversal is observed at  $\mu_0 H = -4.2$  mT (point 2 of Figure 4.8(a)). This reversal is accompanied by large domains as shown in Figure 4.8(c). It can also be observed from the domain image in Figure 4.8(c) that some fine domains have nucleated in the region where reversal has already occurred. This may happen due to the magnetostatic coupling of the domains in the layers. On further increasing the magnetic field, the second reversal occurs round  $\mu_0 H = -13.5$  mT (point 3) accompanied by fine domains (Figure 4.8(d)) and finally gets saturated. Figure 4.8(e) with complete white contrast shows the negative saturation state at

$\mu_0 H = -40$  mT. The step in the hysteresis and their corresponding different domains indicates layer-by-layer reversal of the two Co layers in the sample. The change in the domain structure of the two Co layers indicates the effect of interlayer coupling on the Co layers. It should be noted that these Co layers were prepared in identical conditions with the same thickness.

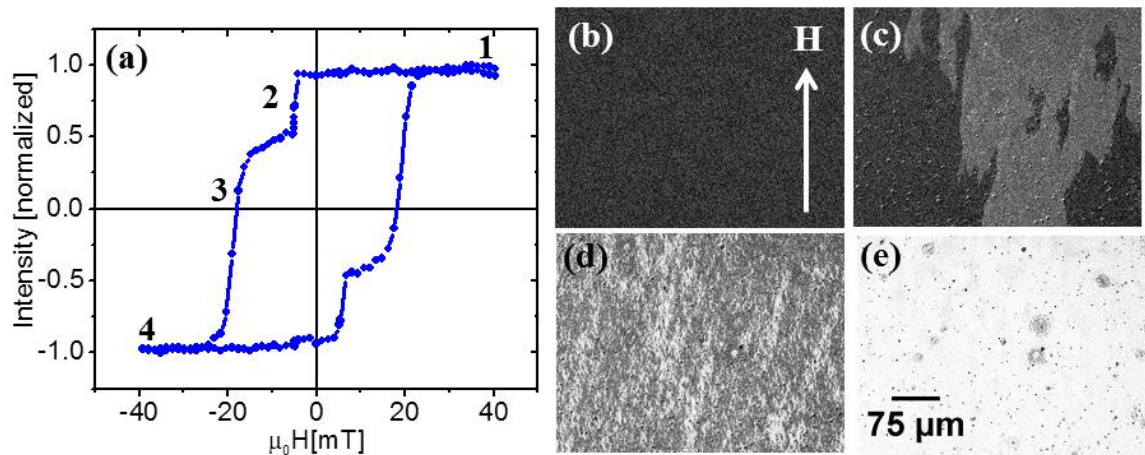


Figure 4.8: (a) Hysteresis measured by LMOKE microscope at room temperature for sample D along EA. Images (b) - (e) are domain images taken at fields marked by point 1 - 4 in Figure (a), respectively.

On increasing the spacer thickness of the spacer layers, transverse component of magnetization reversal was observed. The hysteresis for one such case is shown for sample E in Figure 4.9(a). It shows the hysteresis loop and the domain images corresponding to the points (1 – 4) are shown in Figure 4.9(b) - (e), respectively. As the field is reversed from positive saturation to negative field (point 2 in Figure 4.9(a)) a small transverse component of magnetization is observed which looks like a hump in the hysteresis. The reversal is accompanied by large stripe domains (Figure 4.9(c)). The boundaries of these domains have been highlighted in yellow for having a better visualization. The second reversal is accompanied by small branched domains (Figure 4.9(d), point 3). Hence, similar to sample

D, two types of domains indicating layer-by-layer reversal of the Co thin films was observed. However, comparing Figure 4.8(a) and Figure 4.9(a) it can be observed that with an increase in thickness the second reversal, which may be due to top Co layer, becomes sharper.

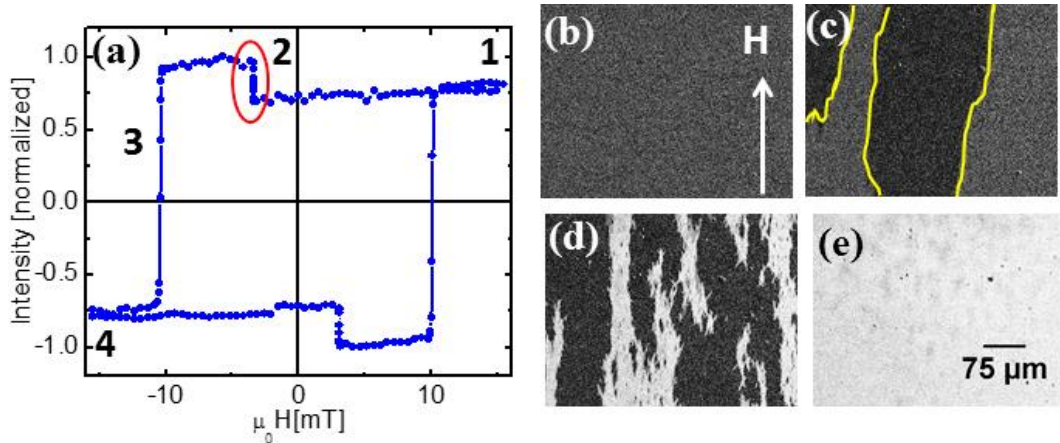


Figure 4.9: (a) Hysteresis measured by LMOKE microscope at room temperature for sample E along EA. Images (b) - (e) are domain images taken at fields marked by point 1 to 4 in Figure (a), respectively.

MOKE magnetometry in both longitudinal and transverse mode was performed for sample D, E, F and G to confirm the transverse component of the magnetization. Figure 4.10(a) – (d) and (e) - (h) shows the hysteresis loops for LMOKE and TMOKE for samples D, E, F and G, respectively. For sample D, stepped hysteresis loop for LMOKE (Figure 4.10(a)) and TMOKE (Figure 4.10(e)) are observed. However, this transverse component of magnetization was also observed by LMOKE and TMOKE measurements for higher thickness of  $t = 90, 130,$  and  $270$  nm as evident from Figure 4.10(b) – (d) and (f) – (h), respectively. Also, with increase in thickness, the saturation field decreases for samples E, F and G (Figure 4.10(a) – (c)). However, it should be noted that even though  $t = 270$  nm showed strong transverse signal and did not follow the trend of decreasing of the saturation field. This may happen as it was prepared by different Co target and hence may have little

different microstructural properties. The transverse component of magnetization was observed for samples with  $t > 23$  nm.

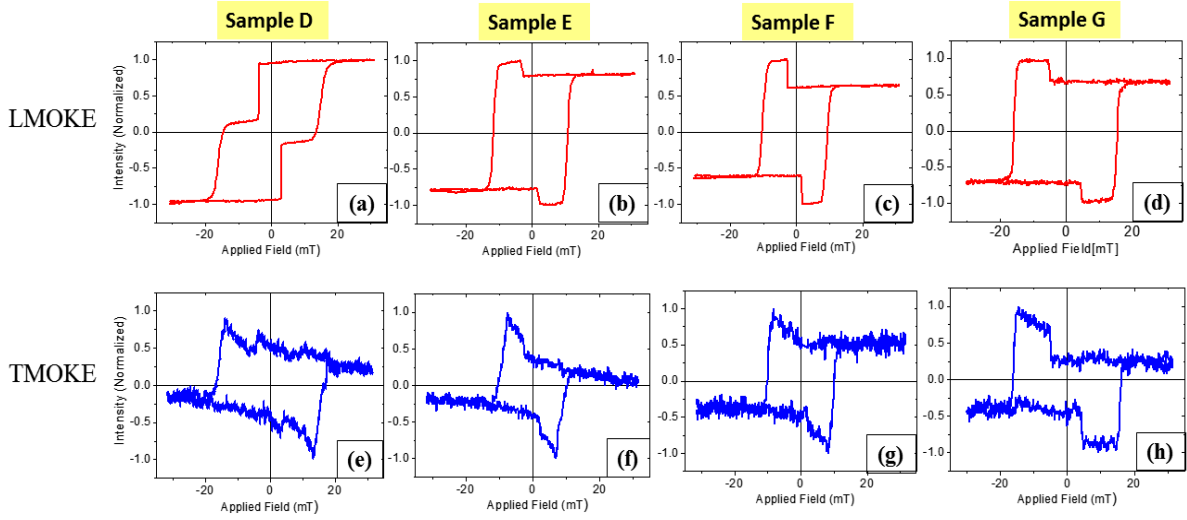


Figure 4.10: LMOKE ((a) – (d)) and TMOKE ((e) – (h),) hysteresis loops for samples D, E, F and G, respectively. It should be noted that sample G was prepared from different Co target.

The observation of transverse component and a decrease in saturation field can be understood by considering the decrease of dipolar coupling between the two Co layers with an increase in spacer thickness. Dipolar coupling decreases monotonically with increasing the spacer layer thickness [132, 133]. The magnetization reversal can hence be understood assuming the stray field from the bottom Co layer will affect the top Co layer. For lower thickness, the Co layers will be coupled magnetostatically, they will therefore, need a high field for saturation [134]. This coupling will also restrict the reversal of the layers and thus only longitudinal magnetization will be present. However, for very thin spacer layers,  $t = 3$  nm, coupling due to pin holes may also be present. It is generally difficult to separate the effect of pinning on magnetization reversal along with other coupling mechanisms. Labrune *et al.* showed theoretically that for the dipolarly coupled Co (20 nm) layers in a bilayer magnetic systems, the saturation field decreases with increasing in spacer thickness. On

increasing the spacer thickness, i.e. for weakly coupled systems and in the absence of any exchange coupling, each Co layer of the stack can individually respond to the change in the magnetic field [134]. This reduces the saturation field which is valid for our case also. It is expected that for decoupled Co layers, magnetization reversal behaviour will be similar to that of single layer behaving like a single ferromagnet. The coercive and saturation field will be expected to be close to the values of Co single layer (Figure 4.5(a)) [50]. Therefore, at higher thickness ( $t > 23$  nm) appears that a weak coupling still exists and hence leads to contribution of transverse magnetization. Since using MOKE microscopy and magnetometry, it is difficult to know the magnetization depth profile, therefore, Polarized neutron reflectivity (PNR) measurements were performed to elucidate the layer-by-layer magnetization state.

#### 4.4.2.3 Polarized Neutron Reflectivity (PNR):

PNR measurements under small angles were performed to study the magnetization depth profile of the Co layers. The measurements were performed in specular mode at TREFF reflectometer in FRM2, Munich. As discussed in Chapter 2, section 2.8, the momentum transfer along Z-axis is given by -

$$q_z = (4\pi \sin \theta) / \lambda, \quad (4.1)$$

where,  $q_z$  = momentum transfer perpendicular to the surface and where  $\lambda = 0.48$  nm is the neutron wavelength. As discussed in section 2.8 of chapter 2, four cross sections,  $R^{++}$ ,  $R^{--}$ ,  $R^{+-}$ , and  $R^{-+}$  can be measured. The plus and minus signs indicate polarizations of the incident and scattered neutrons parallel or antiparallel to the applied external field, respectively. The non-spin-flip (NSF) scattering amplitude [ $R^{++}$ ,  $R^{--}$ ] provides structural and magnetic information whereas spin-flip (SF) [ $R^{+-}$ ,  $R^{-+}$ ] gives only magnetic information and correspond to in-plane magnetization components perpendicular to the neutron polarization.

The non-spin flip (NSF) scattering measurements for sample D was performed at room temperature. The magnetic field was applied along EA and was parallel to the sample

plane. The layer thickness, roughness, and densities were taken from the XRR fits discussed in section 3. Figure 4.11(a), (b), and (c) shows the non-spin flip measurements (open circles) along with the fits (solid lines) for sample D at fields 100 mT, -7 mT, and -18 mT, respectively. The fitting for each data set was performed using GenX [135] software based on Parratt's formalism [136]. For fitting the PNR data, the thickness, roughness and densities were used from the XRR fits of sample D. However, while refining the fits the densities and roughness was varied slightly.

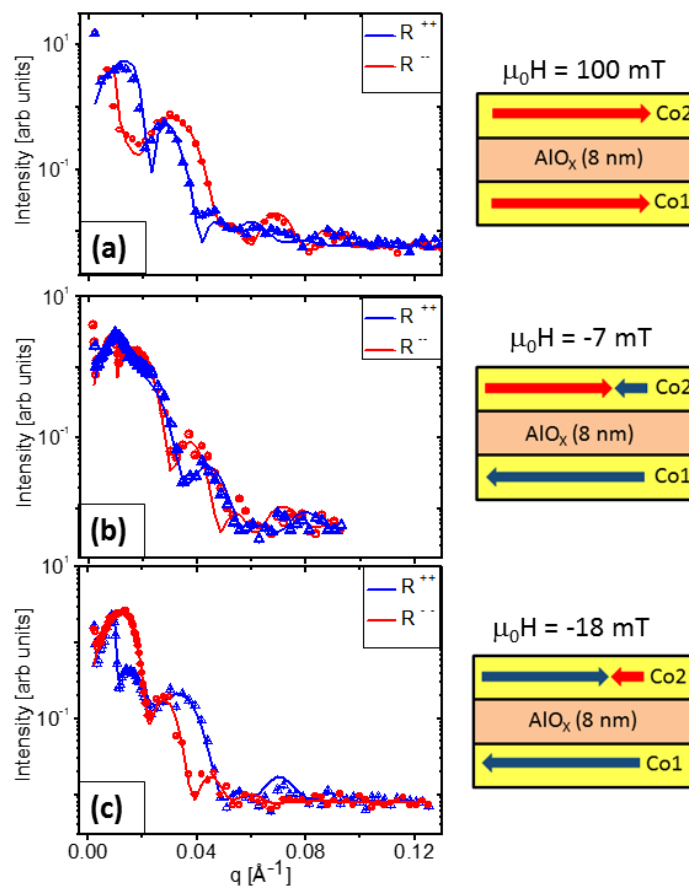


Figure 4.11: PNR measurements (open circles) and fits (solid lines) for  $\mu_0 H$  at (a) positive saturation, (b) -7 mT, (c) -18 mT for Co (10 nm)/AlO<sub>x</sub> (8 nm)/Co (10 nm). The corresponding measuring field points are marked as 1, 2, and 3 in Figure 4.8 (a). The schematics the magnetization vector orientation of the two Co layers for each field has been shown to its corresponding right column. The bottom and top Co layers are labelled as Co1 and Co2, respectively.

The fits of PNR data at positive saturation (Figure 4.11(a)) reveals that both the Co layers are saturated along the field direction. It can be observed from Figure 4.11(a) that near total reflection plateau around  $q \sim 0.01 \text{ \AA}^{-1}$ ,  $R^{++} > R^{--}$ . This indicates the positive magnetization state of the sample where both the Co layers are effectively saturated along the field direction. The PNR data for  $\mu_0 H = -7 \text{ mT}$  (the step in the hysteresis in Figure 4.8(a)) is shown in Figure 4.11(b). For small  $q$ , near total reflection plateau, the intensity of  $R^{++}$  is nearly equal to  $R^{--}$ . This indicates the sample to be in nearly demagnetized state. From the simulations, it was found that at this field, the magnetization of the bottom Co layer (Co1) has reversed completely as shown schematically in the right of Figure 4.11(b). Hence, the large stripe domain in Kerr microscopy image (Figure 4.8(c)) corresponds to the reversal of the bottom layer of the Co. The PNR fits at this field reveals that the Co top layer has also partially reversed (20%). This may arise since  $\text{AlO}_x$  is an insulator, hence the only coupling present can be dipolar coupling, which may result in the stray field of the domains from the bottom Co layer and affect the top Co layer. On further increasing the field to  $-18 \text{ mT}$ , from Figure 4.11(c) it can be observed that near total reflection plateau around  $q \sim 0.013 \text{ \AA}^{-1}$ , the  $R^{--} > R^{++}$ . This indicates the sample is now negatively magnetized. From the fits, it was found that the magnetization of the top layer reverses. Hence, from the PNR measurements, layer-by-layer reversal of the Co layers due to dipolar coupling was confirmed [50].

#### 4.4.2.4 Micromagnetic simulations:

In order to understand the magnetization reversal observed in the experiments, micromagnetic simulations were performed using object oriented micromagnetic framework (OOMMF) [63]. The system consists of two Co layers of equal thickness (10 nm) separated by an insulating spacer to account for  $\text{AlO}_x$  layer of the real sample. The OOMMF simulations were performed for different spacer layer ( $t$ ) = 2, 8, and 90 nm. The lateral size of the sample was 304 nm x 304 nm. The cell size was defined to be  $3.2 \times 3.2 \times 2 \text{ nm}^3$ . The

saturation magnetization was assumed to be  $1.44 \times 10^6$  A/m. As discussed in section 4.4.2.1 all the samples showed uniaxial anisotropy and small random anisotropy due to the misalignment for grain anisotropy as evidenced from the peak around the hard axis (Figure 4.7) [35]. Hence, account for the variation in local anisotropy of the misalignment of grains in the real sample, a small random anisotropy ( $K_r$ ) apart from uniaxial anisotropy ( $K_u$ ) was incorporated in the simulations. This random anisotropy was such that it only gives rise to the randomness in the direction of the anisotropy keeping its magnitude constant. The values of uniaxial and random anisotropy chosen were  $K_u = 0.18 \times 10^6$  J/m<sup>3</sup> and  $K_r = 0.1 \times 10^6$  J/m<sup>3</sup>, respectively. The micromagnetic model OOMMF is based on minimization of the energy by using Landau- Lifshitz-Gilbert equation as described in section 1.6 of chapter 1 [137]. The magnetic energy per unit cell is given by –

$$\frac{d\mathbf{M}}{dt} = -|\gamma|\mathbf{M} \times \mathbf{H}_{\text{eff}} - \frac{|\gamma|\alpha}{M_s} \mathbf{M} \times (\mathbf{M} \times \mathbf{H}_{\text{eff}})$$

where,  $\vec{M}$  is the magnetization vector,  $\gamma$  is the gyromagnetic ratio, and  $\alpha$  is the Gilbert damping constant,  $\vec{H}_{\text{eff}}$  is the effective magnetic field.

The magnetization reversal for  $t(\text{Al}_2\text{O}_3) = 8$  nm is first discussed in detail and then a comparison of hysteresis and domain images near coercive field will be summarized. Figure 4.12(a) shows the OOMMF simulated hysteresis for  $t = 8$  nm along the EA. A two stepped hysteresis similar to the the experimental loop (Figure 4.8(a)) was observed. The domain images for top and bottom Co layers are shown as Figure 4.12(b1) – (e1) and that of bottom layer is shown in Figure 4.12(b2) – (e2) marked as points (b) to (e) respectively, in Figure 4.12(a). Red and the blue pixel of the domain image refers to the magnetization component  $M_x < 0$  and  $M_x > 0$ , respectively. The simulation was performed by negatively saturating the sample and then reversing the field to positive direction. As the field is reversed towards positive direction, the bottom Co layer reverses (Figure 4.12(c2)) and the stray field

originating from it affects the top layer (Figure 4.12(c1)). On further increasing the field to point d (Figure 4.12(a)), the bottom Co layer is completely reversed whereas the top Co layer is still negatively magnetized. This is consistent with the experimental observations of the Kerr microscope and PNR data. The PNR data in Figure 4.11(b) revealed the antiparallel alignment of the two Co layers. On increasing the field, the top Co layer reverses (Figure 4.12(e1)). Hence, OOMMF simulation reveals layer-by-layer magnetization reversal of the Co layers due to dipolar coupling with small random anisotropy which qualitatively explains the observations of Kerr microscope and PNR measurements.

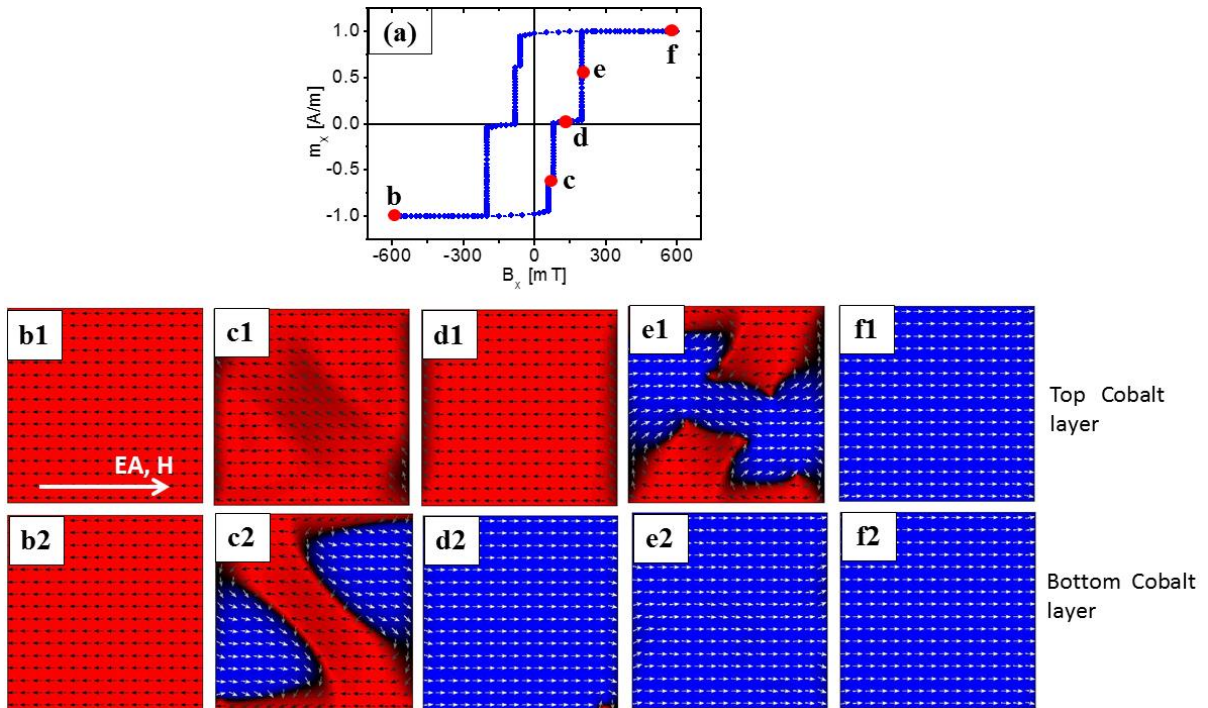


Figure 4.12: Micromagnetic simulated hysteresis (a) and domain images (b to e) for Co (10 nm)/Al<sub>2</sub>O<sub>3</sub> (8 nm)/Co (10 nm) with  $K_u = 0.18 \times 10^6 \text{ J/m}^3$  and  $K_r = 0.1 \times 10^6 \text{ J/m}^3$ . The red and blue pixel corresponds to magnetization  $M_x < 0$  and  $M_x > 0$ , respectively. The suffix 1 and 2 for each domain image refers to the top and bottom Co, respectively.

For understanding the thickness dependence of the spacer layer on magnetization reversal of the dipolarly coupled Co(10 nm) layers OOMMF simulations were performed by varying the

spacer thickness. Figure 4.13 shows the longitudinal component of magnetization of the simulated hysteresis loops for  $t = 2, 8, 90$  nm for understanding the thickness dependence of the spacer layer on magnetization reversal of the dipolarly coupled Co(10 nm) layers. Two stepped hysteresis loops were observed for all the cases. As discussed above in detail, the first ( $H_{C1}$ ) and second reversal ( $H_{C2}$ ) in all the hysteresis of Figure 4.13 corresponds to the magnetization reversal of the bottom and the top Co layer, respectively. This is consistent with the MOKE experimental observation. On increasing the thickness of the spacer layer, the saturation field decreases which was also observed by MOKE magnetometry (Figure 4.10). This indicates the reduction of coupling as explained in section 4.4.2.2.

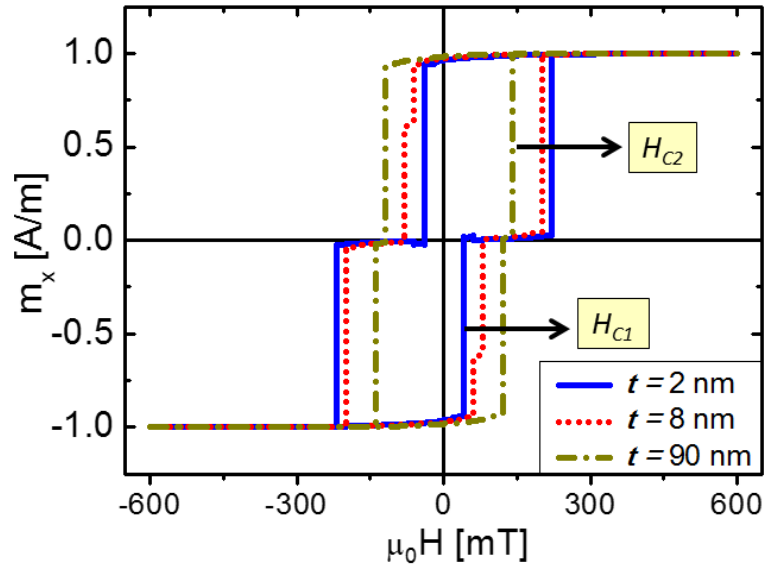


Figure 4.13: OOMMF simulated hysteresis for Co (10nm)/Al<sub>2</sub>O<sub>3</sub> ( $t$  nm)/Co (10nm) along EA, where  $t = 2, 8,$  and  $90$  nm.

The domain structure with increasing thickness of the spacer layer along EA for  $H \sim H_c$  is shown in Figure 4.14. It can be observed that the domain structure for  $t = 90$  nm is different compared to  $t = 2$  and  $8$  nm. Hence, the dipolar coupling affects the domains structure which was also evident from Kerr microscopy domain images. However, it should be noted that in simulations it is not possible to get different domains in the two Co layers for the same

thickness and the transverse magnetization unlike experiment decreased with increasing the spacer thickness (data not shown). However, it is worth mentioning that for systems with only dipolar coupling and no randomness it was qualitatively possible to achieve the trend of transverse magnetization. However, it was neither possible to observe the layer-by-layer magnetization reversal nor the decreasing trend of the saturation field for such cases where  $K_r$  was made zero.

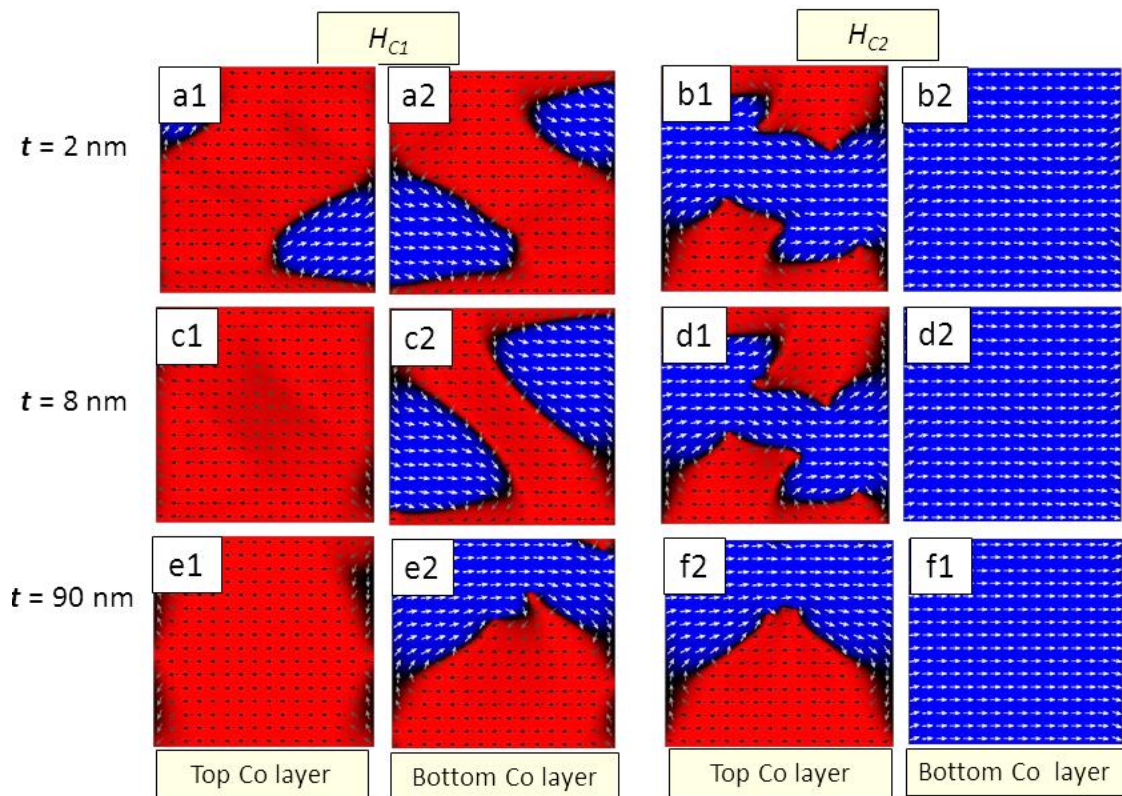


Figure 4.14: Simulated domain images along EA for Co (10 nm)/Al<sub>2</sub>O<sub>3</sub> ( $t$  nm)/Co (10 nm) near coercive fields along EA, where  $t = 2, 8,$  and  $90$  nm with  $K_u = 0.18 \times 10^6$  J/m<sup>3</sup> and  $K_r = 0.1 \times 10^6$  J/m<sup>3</sup>. The red and blue pixel corresponds to magnetization  $M_x < 0$  and  $M_x > 0$ , respectively. The suffix 1 and 2 for each domain image refers to the top and bottom Co, respectively.

## **4.5 Conclusion-**

In summary, in this chapter magnetization reversal and the effect of interlayer coupling in dipolarly coupled Co layers have been studied. Layer-by-layer magnetization reversal of the Co layers was evidenced by Kerr microscope and PNR measurements. The results were supported by OOMMF simulations in which uniaxial and random anisotropy was incorporated along with the dipolar coupling. On increasing the thickness of the spacer layer, decrease in dipolar coupling leading to transverse component of magnetization along with longitudinal magnetization component was observed.

# **Chapter 5 : Occurrence of 360° domain walls: a competing effect of uniaxial and random anisotropy**

## **5.1 Introduction:**

In previous chapters, it has been discussed that the magnetization reversal in multilayers of Co/AlO<sub>x</sub> (Chapter 4) can be different than that of single ferromagnetic Co film (Chapter 3). Magnetic multilayers where ferromagnetic (FM) layers are separated by non-magnetic spacer layers (NM) have been used in data storage devices like read-head of hard drives and magnetic random access memories (MRAMs), [138, 139]. Magnetization reversal can occur via domain wall (DW) motion or coherent rotation as discussed in section 1.4 of Chapter 1. Manipulating domains and DWs in magnetic thin films gives an alternative approach to use them in data storage technology. For example, in racetrack memory, the domains can be restricted along the length of the wires by the shape anisotropy. Hence, two opposite directions of magnetization along the length of the wire will be possible and can be used as 0 or 1 state. These two states can be used for DW logic [140, 141] and memory devices [142]. DWs can propagate on the application of magnetic field or spin polarized electric current. The reliable and controlled movement of DWs has to be used in racetrack memory for the storage devices [142, 143].

It is desirable that these devices e.g magnetic tunnel junctions, racetrack memory etc. have reliable and uniform magnetization reversal. However, the performance can be impaired by the local microstructure like the presence of pinning centers or defects. As discussed in chapter 3, the presence of inhomogeneity or randomness affects the magnetization reversal by the formation of complex domain structures. The magnetization relaxation time increases with increase in randomness. Hence, these inhomogeneities must be avoided to achieve a faster response of the devices. The presence of this random anisotropy may lead to the

formation of DWs [144]. Among various types of domain walls, the formation of  $360^\circ$  DWs has been reported in past by several authors [145, 146, 16]. Presence of these walls must be avoided as it hinders the magnetization reversal, reduces its reproducibility and requires high field for annihilation [147]. Therefore, for improving and engineering the performance of devices, it is necessary to understand the magnetic properties like domain structure, magnetization reversal of the magnetic thin films constituting these devices.

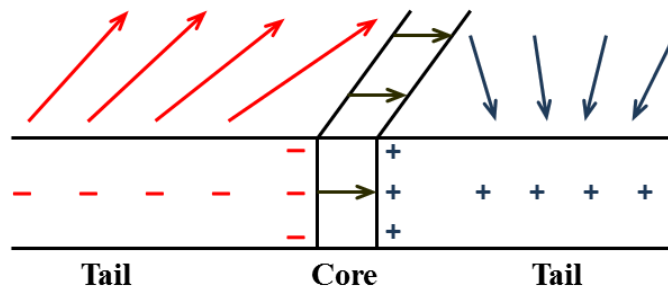


Figure 5.1: Schematic showing the core and the tail of the Néel walls with the magnetic [20].

Formation of domains depends on energy minimization of various energy factors such as exchange energy, magnetostatic energy and anisotropy energy as explained in section 1.3 of chapter 1. Different types of DWs like  $180^\circ$ ,  $90^\circ$ ,  $360^\circ$  etc. can exist as described in section 1.3 [20]. Among these the observation of  $360^\circ$  DWs is rare.  $360^\circ$  DWs separate the domains with parallel magnetization as has been shown in Figure 1.9 of chapter 1. Across these DWs, the spins inside them rotates by  $360^\circ$ . These walls are formed in continuous thin films when Bloch lines present in a  $180^\circ$  Néel walls gets pinned at structural inhomogeneities or defects in an exchange biased film [39, 148]. It can also be formed by merger of two  $180^\circ$  Néel DWs. The Néel walls consists of a core and a large tail as shown in Figure 5.1 [20]. The magnetic charges developed in the tail of one the Néel wall can interact magnetostatically with the other Néel walls present in the sample. The two bounding Néel walls of  $360^\circ$  DWs

can either attract or repel depending on the charges developed on the tails. For the Néel walls with opposite magnetic charges having opposite sense of rotation will attract each other and can be easily annihilated. These walls are called unwinding walls as shown in Figure 5.2(a). However, the interacting walls with similar rotational sense will repel each other due to the opposite polarity on the overlapping tails. These walls, called winding DWs, under the influence of magnetic field can merge to form  $360^\circ$  DW as shown in Figure 5.2(b). These winding walls are stable and will require high magnetic field for annihilation [20, 47].

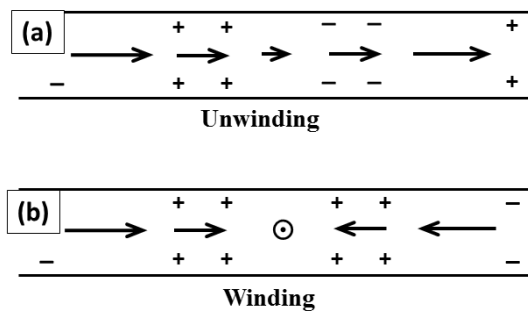


Figure 5.2: Schematic of  $360^\circ$  DWs formed due to (a) opposite sense (unwinding) and (b) similar sense of rotation (winding) of Néel walls [20].

However,  $360^\circ$  DWs can also be formed in the absence of defects [147, 148]. It was shown that even without inclusion, formation of  $360^\circ$  DWs were possible due to the presence of the dispersion of EA in permalloy films [149]. This dispersion can be treated as self perturbation leading to edge curling in opposite direction and hence formation of  $360^\circ$  DWs [145, 149]. Hehn *et al.* predicted that the curling in magnetic tunnel junction will depend on the the variation of the local anisotropy, thermal fluctuations and by the torque created by the dipolar field of the hard magnetic layer [145]. In some cases they can be formed due to the magnetization rotation of nearby grains in opposite direction due to the presence of the distribution of EA in the film [16, 148, 149, 150].  $360^\circ$  DWs were also observed both theoretically and experimentally in patterned thin films like ellipses [145], rings [151] and nanowires [152, 153].

Even though  $360^\circ$  DWs has been considered to be undesirable in data storage technology, it is still being explored for its probable applications. Marco *et al.* proposed to use the stability of  $360^\circ$  DWs as a future sensor application with special spin valve geometries [154]. They showed the formation, transportation and storage of  $360^\circ$  DWs in free permalloy layer of spin. This was achieved by joining a large circular element to a long and thin stripe of smaller area. However, the observed change in resistance was only 0.5%. Concentric  $360^\circ$  DWs were formed in the free layer of MTJ by repeated switching of the free layer [16]. The authors claimed the number of nested  $360^\circ$  DW loops can be used to track history and hence, the number of magnetization reversals of the device. The authors attributed the formation of  $360^\circ$  DWs to the inhomogeneities which gives rise to magnetic dispersion in grain and produces a preferential sense of rotation by breaking the local symmetry. Similar to other reports, formation of  $360^\circ$  DWs due to defects were also observed for this case [16]. Hence, a systematic study of the formation and annihilation of these  $360^\circ$  walls is an important issue. In this work, the effect of randomness on the formation of  $360^\circ$  DWs have been discussed. It is shown that the presence of high random anisotropy in a system can be one of the reasons for the formation of the  $360^\circ$  DWs.

## 5.2 Sample Preparation:

The sample  $\text{Al}_2\text{O}_3$  (3 nm)/  $[\text{Co}_{80}\text{Fe}_{20}$  (1.8 nm)/  $\text{Al}_2\text{O}_3$  (3 nm)]<sub>9</sub> (Figure 5.3(a)) was prepared on float glass by the group of Prof. P. P. Freitas at INESC, Lisbon, Portugal. This sample was prepared in continuation of the series where the thickness of the  $\text{Co}_{80}\text{Fe}_{20}$  ( $t_n$ ) was varied from 0.5 to 1.8 nm keeping  $\text{Al}_2\text{O}_3$  thickness constant at 3 nm [26]. It was observed that CoFe on  $\text{Al}_2\text{O}_3$  has Volmer - Weber growth and was discontinuous for thickness below 1.4 nm and continuous above it [155].

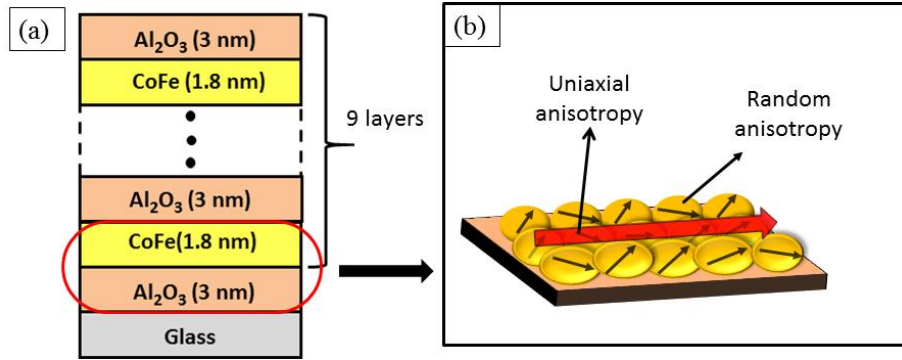


Figure 5.3: (a) Schematic of the sample  $\text{Al}_2\text{O}_3(3 \text{ nm})/[\text{Co}_{80}\text{Fe}_{20}(1.8 \text{ nm})/\text{Al}_2\text{O}_3(3 \text{ nm})]_9$ , (b) schematic showing the coalescence of nanoparticles to form continuous thin films with overall uniaxial anisotropy and random anisotropy of the grains.

These samples were prepared at a substrate temperature of 200 °C by Focussed Xe - Ion Beam (FIB) sputtering as described in section 2.1 of chapter 2. The deposition rate for  $\text{Al}_2\text{O}_3$  and  $\text{Co}_{80}\text{Fe}_{20}$  was 0.12 and 0.32 Å/s, respectively [26, 155]. To induce an in-plane anisotropy, a magnetic field of 10 mT was applied during the growth of the sample. Since the magnetic field was not strong enough, a small random anisotropy with an overall in-plane uniaxial anisotropy is expected due to the granularity of the CoFe thin film as shown in Figure 5.3(b). The detailed structural and magnetic properties of the discontinuous metal insulator multilayers have been studied in ref [155]. However, in this chapter, the magnetization reversal and formation 360° DWs due to the presence of random anisotropy in percolated metal insulator multilayer (MIM) is discussed.

### 5.3 Magnetization reversal and experimental observation of 360° DWs:

Angle-dependent hysteresis measurements were performed by using MOKE microscopy in the longitudinal mode. The plot for angle vs coercive field and squareness is shown in Figure 5.4 (a) and (b), respectively. It confirms the presence of uniaxial anisotropy

induced by application of magnetic field during film growth. A detailed magnetization reversal investigation was performed by experiments and simulations (OOMMF) along the EA and HA.

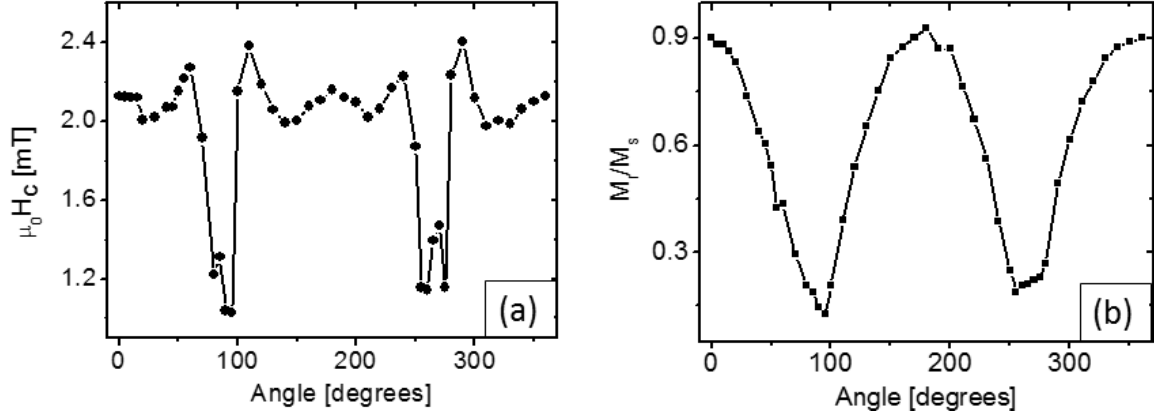


Figure 5.4: Coercivity (a) and  $M_r/M_s$  (b) vs.  $\theta$  for  $[\text{Co}_{80}\text{Fe}_{20} (1.8 \text{ nm})/\text{Al}_2\text{O}_3 (3 \text{ nm})]_9$  showing the presence of uniaxial anisotropy behavior.

The hysteresis measured along the EA by LMOKE microscopy at room temperature is shown in Figure 5.5(a). The narrow hysteresis loop with small coercive field indicates that sample is soft magnetic. The domain images on changing the field from negative to positive saturation are shown in Figure 5.5(b) – (g) with their corresponding field points marked as (1) – (6) in Figure 5.5(a). The sample at negative saturation (point 1, Figure 5.5(a)) shows that the sample is homogeneously black and hence implies single domain state (Figure 5.5(b)) with the net magnetization along the direction of the field. As the field is reversed from negative saturation to a small positive field (point 2,  $\mu_0 H \sim -1.80$  mT), domains of reverse magnetization represented by gray shade start to nucleate as shown in Figure 5.5(c). On further increasing the field, the reversal is accompanied by DW motion as shown by Figure 5.5(d) for  $\mu_0 H \sim -1.98$  mT. It should be noted that the black and gray scales of the domain images indicates the negative and positive magnetization, respectively. Since the sample has 9 layers of  $\text{Co}_{80}\text{Fe}_{20} (1.8 \text{ nm})/\text{Al}_2\text{O}_3 (3 \text{ nm})$ , one may expect layer-by-layer reversal of the  $\text{Co}_{80}\text{Fe}_{20}$  layers as was reported by Bedanta *et al.* for the sample  $t_n = 1.6 \text{ nm}$  of the same

series [112]. This is also evident from Figure 5.5(e) which has gray contrast with a small region of white contrast shown by the square. The magnetization reverses further via DW motion as shown in Figure 5.5(f) for  $\mu_0 H \sim -2.38$  mT (point 5 of Figure 5.5(a)). Finally, with an increase in the field, the sample gets completely saturated. It should, however, be noted that by using Kerr microscopy, it is not possible to know the exact magnetization depth profile and hence the reversal of individual layers. Magnetization reversal for this sample was also studied by X-ray photoemission electron microscopy (XPEEM) by Dr. S Bedanta [52].  $360^\circ$  DWs having irregular structure were observed. These walls were stable and present even around saturation. For a better understanding of the experimental observation, OOMMF simulations were performed where a random anisotropy in addition to uniaxial anisotropy was incorporated. This will be discussed in the next section of this chapter.

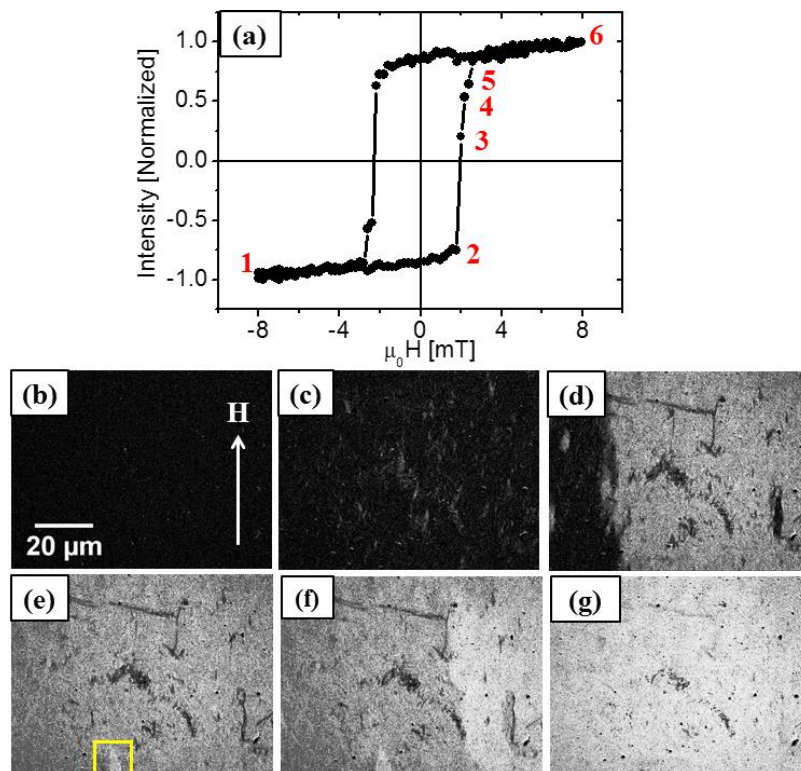


Figure 5.5: (a) LMOKE hysteresis loop for  $\text{Al}_2\text{O}_3(3 \text{ nm})/[\text{Co}_{80}\text{Fe}_{20} (1.8 \text{ nm})/\text{Al}_2\text{O}_3(3 \text{ nm})]_9$  along EA. Figure (b) – (g) show the domain images along the positive branch of hysteresis for which the corresponding field points (1) – (6) are marked in Figure 5.5(a).

360° DWs were also observed along the HA by LMOKE microscopy. The hysteresis and domain images are shown in Figure 5.6(a) and Figure 5.6(b) to (f), respectively. The sample was negatively saturated till -16 mT and then the magnetic field was reversed. The S- shape of the hysteresis loop Figure 5.6(a) indicates coherent rotation of magnetization reversal. The domain images during reversal are shown in Figure 5.6(b)-(f) with their corresponding field points (1) - (5) marked in the hysteresis (Figure 5.6(a)). At negative saturation (point 1) the sample is in single domain state as observed from the uniform gray color of the domain image of Figure 5.6(b). As the field is reversed, nucleation of fine domains is observed at 1 mT which is shown in Figure 5.6(c). On further increasing the magnetic field, a thick black loop like feature called as 360° DWs with the same gray scale on either side is observed as shown in the domain Figure 5.6(d) at  $\mu_0H = 3.07$  mT [52]. These walls existed till 4 mT as shown in Figure 5.6(e) and then were annihilated. The zoomed in image of the 360° DWs in the area highlighted in Figure 5.6(d) is shown in Figure 5.7(a). The black loop like features perpendicular to the field direction is the 360° DWs. Figure 5.7(b) shows the domain image of 360° DWs (white loop like features) for the negative branch of the hysteresis. It has to be noted that both the domain images are in same scale and for the same area of the sample. The 360° DWs formed at HA may arise due to the difference in the sense of the rotation of the magnetization of the grains [16] which occurs due to the dispersion of anisotropy of grains. This breaking of local symmetry occurs as the nearest EA of the grains are aligned antiparallel. Hence, the exchange coupling responsible for coherent rotation will not be sufficient to overcome the energy barrier due to the randomness as explained in section 3.3.2.2 of Chapter 3 [35]. The local magnetization of the grains will have antiparallel magnetization at remanence mostly aligned towards EA which on increasing the field results in the formation of 360° DWs still preserving the opposite sense of rotation. This was also confirmed by OOMMF simulations performed using the same parameters as

that for EA. The details of the results and discussion for OOMMF simulations for the understanding of experimental results are discussed in next section.

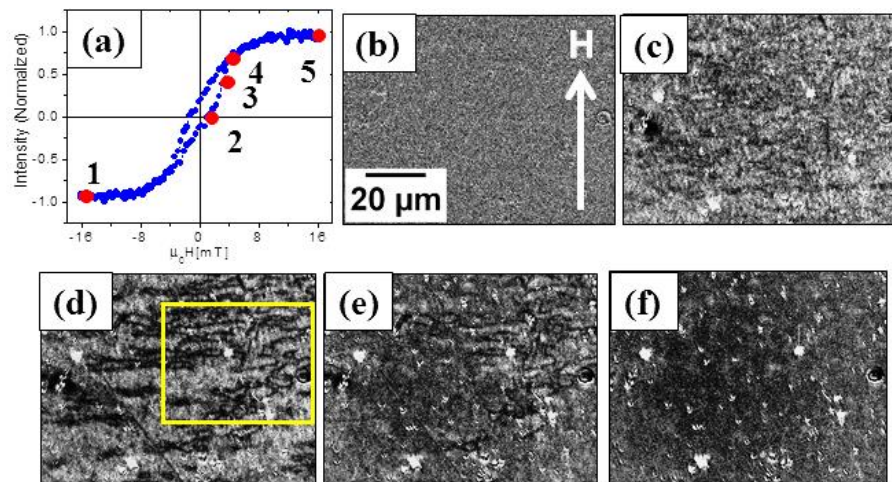


Figure 5.6: (a) Hysteresis measured by LMOKE microscopy along HA. Images (b) to (f) are domain images of the field points marked (1) to (5) respectively in the hysteresis. The zoomed ( $50 \times 35 \mu\text{m}^2$ ) in domain image of the highlighted area of the image (d) is shown in Figure 5.7. The thick black loop like features are the  $360^\circ$  DWs [52].

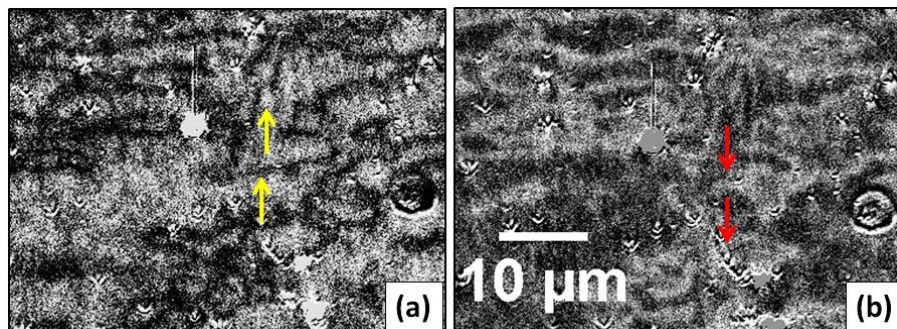


Figure 5.7: (a) The zoomed ( $50 \times 35 \mu\text{m}^2$ ) in domain image of the highlighted area in Figure 5.6(d) for positive branch of the hysteresis, (b) domain image for negative branch of the hysteresis, showing the  $360^\circ$  DWs (as white colored loops) separating parallel magnetization by the arrows in the respective images. [Note: both the images are in same scale].

## 5.4 Micro-magnetic Simulations for 360° DWs along EA and HA:

In order to understand the experimental observation of the magnetization reversal process in MIM, micromagnetic simulations using Object Oriented Micromagnetic Framework (OOMMF) were performed [63] for [Co (1.8 nm)/Al<sub>2</sub>O<sub>3</sub> (3.6 nm)]<sub>n</sub>, with  $n = 2$  along EA and HA. This understanding was extended for  $n = 9$  bilayers. The lateral size of the sample was 304 x 304 nm<sup>2</sup>. The cell size was defined to be 3.2 x 3.2 x 1.8 nm<sup>3</sup>. The saturation magnetization was assumed to be 1.44 x 10<sup>6</sup> A/m which corresponds to the bulk value of the Co [112]. As discussed previously, the MIM has uniaxial anisotropy ( $K_u$ ) and a non-negligible random anisotropy ( $K_r$ ) induced due to the growth technique used. Hence, a random anisotropy ( $K_r$ ) apart from uniaxial anisotropy ( $K_u$ ) was incorporated in OOMMF simulations. This random anisotropy was such that it only gives rise to the randomness around the direction of the uniaxial anisotropy keeping its magnitude constant to account for the dispersion in local anisotropy of the grains in the real sample. The model is based on the minimization of the energy by using Landau- Lifshitz-Gilbert equation as described in chapter 1, section 1.6 [137]. The magnetic energy per unit cell is given by –

$$\frac{d\vec{M}}{dt} = -|\gamma|\vec{M} \times \vec{H}_{eff} + \alpha\vec{M} \times \frac{d\vec{M}}{dt} \quad (5.1)$$

where,  $\vec{M}$  is the magnetization vector,  $\gamma$  is the gyromagnetic ratio, and  $\alpha$  is the Gilbert damping constant,  $\vec{H}_{eff}$  is the effective magnetic field.

### 5.4.1 Micromagnetic simulations along EA:

The simulations were performed along EA by varying the values of  $K_u$  and  $K_r$ . 360° DWs were formed when random anisotropy was comparable or greater than the uniaxial anisotropy ( $K_u \sim K_r$  or  $K_u < K_r$ ). However, for  $K_u \gg K_r$ , no 360° DWs were observed. The results for these three cases are discussed below in detail.

**5.4.1.1  $K_u = 0.15 \times 10^6 \text{ J/m}^3$  and  $K_r = 0.1 \times 10^6 \text{ J/m}^3$ : random anisotropy is smaller but comparable to uniaxial anisotropy:**

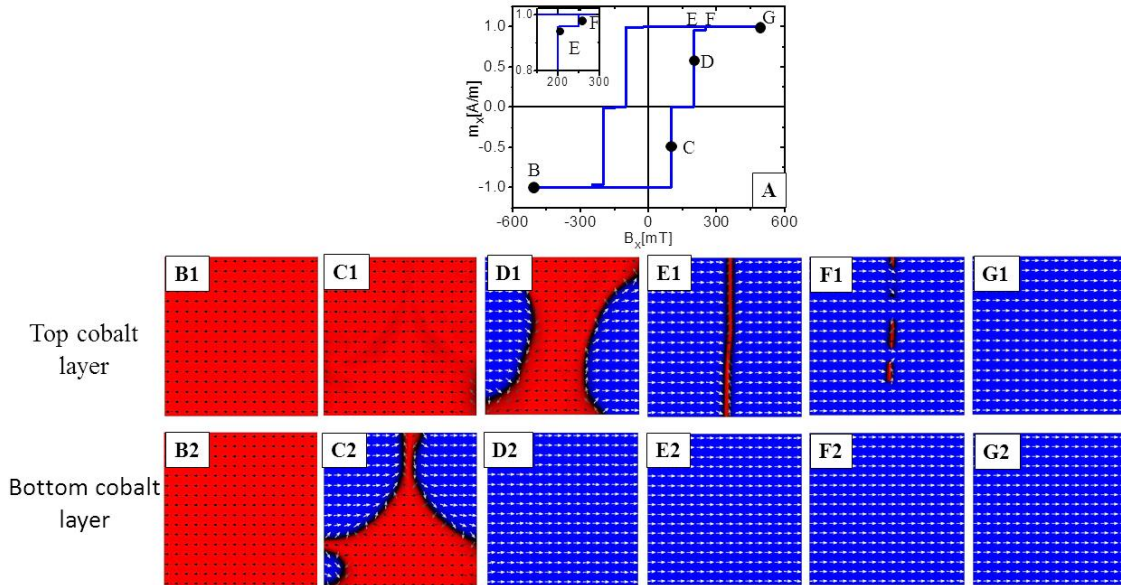


Figure 5.8: Micromagnetic simulated hysteresis (A) and domain images (B to G) for  $[\text{Co} (1.8 \text{ nm})/\text{Al}_2\text{O}_3 (3.6 \text{ nm})]_2$  with  $K_u = 0.15 \times 10^6 \text{ J/m}^3$  and  $K_r = 0.1 \times 10^6 \text{ J/m}^3$ . The red and blue pixel corresponds to magnetization  $M_x < 0$  and  $M_x > 0$ . The suffix 1 and 2 for each domain image refers to the top and bottom Co layers, respectively.

Figure 5.8 shows the hysteresis loop and the domain images of the two Co layers for the field points (B) to (G) marked in the hysteresis loops. The values of uniaxial and random anisotropy were taken to be  $K_u = 0.15 \times 10^6 \text{ J/m}^3$  and  $K_r = 0.1 \times 10^6 \text{ J/m}^3$ , respectively. Red and the blue pixel of the domain image refers to the magnetization component  $M_x < 0$  and  $M_x > 0$ , respectively. The simulation was performed by negatively saturating the sample and then reversing the field towards positive direction. As the field is increased, the bottom layer reverses first Figure 5.8 C2 and is completely saturated. Further, from Figure 5.8 D1, it can be observed that two  $180^\circ$  DWs come close to each other. These walls are formed by merger of domain walls with a similar sense of rotation as shown in the spin-resolved zoomed in domain image of Figure 5.9 (a). It is also noticed that high field is required for

annihilation (Figure 5.8 E1 and F1) which was also observed experimentally by XPEEM images.

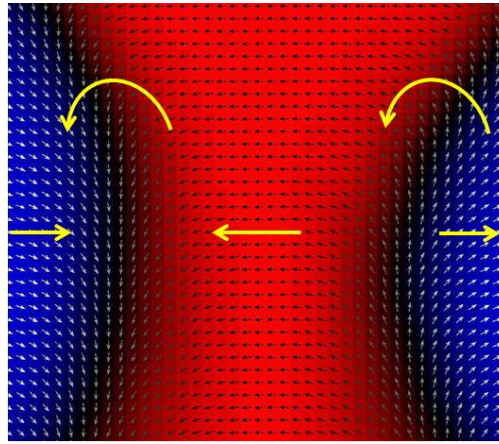


Figure 5.9: The zoom in image showing the spins of the domain walls. The spins have similar sense of rotation across the two  $180^\circ$  DWs as shown the curved yellow arrow. The bold yellow arrow in the red and blue regions show the magnetization direction of the spins in the domains.

**5.4.1.2 Random anisotropy is equal to ((i)  $K_u = K_r = 0.1 \times 10^6 \text{ J/m}^3$ ) or comparable but greater than uniaxial anisotropy ((ii)  $K_u = 0.1 \times 10^6 \text{ J/m}^3$  and  $K_r = 0.15 \times 10^6 \text{ J/m}^3$ ):**

Similar results were observed for  $K_u = K_r = 0.1 \times 10^6 \text{ J/m}^3$  and  $K_u = 0.1 \times 10^6 \text{ J/m}^3$  and  $K_r = 0.15 \times 10^6 \text{ J/m}^3$  as shown in Figure 5.10 (i) and (ii), respectively. Similar to the case (1), two  $180^\circ$  DWs merged (B1 of Figure 5.10 (i) and (ii)) to form  $360^\circ$  DWs (C1 of Figure 5.10 (i) and (ii)). It should be noted that unlike  $180^\circ$  DWs these walls did not propagate with the field. The  $360^\circ$  DWs were stable and required high field for annihilation. The flat region shown in the insets of the hysteresis of Figure 5.10 (i) and (ii) just below saturation gives the field range in which the  $360^\circ$  DWs were stable. This was also evident from the respective domain images of D1 of Figure 5.10 (i) and (ii). On further increasing the field, all the spins were aligned along the field resulting in the saturation. Hence,  $360^\circ$  DWs were observed due

to the presence of random anisotropy and in the defect free region. However, when  $K_u \gg K_r$ , no  $360^\circ$  DWs are observed as discussed in the next point.

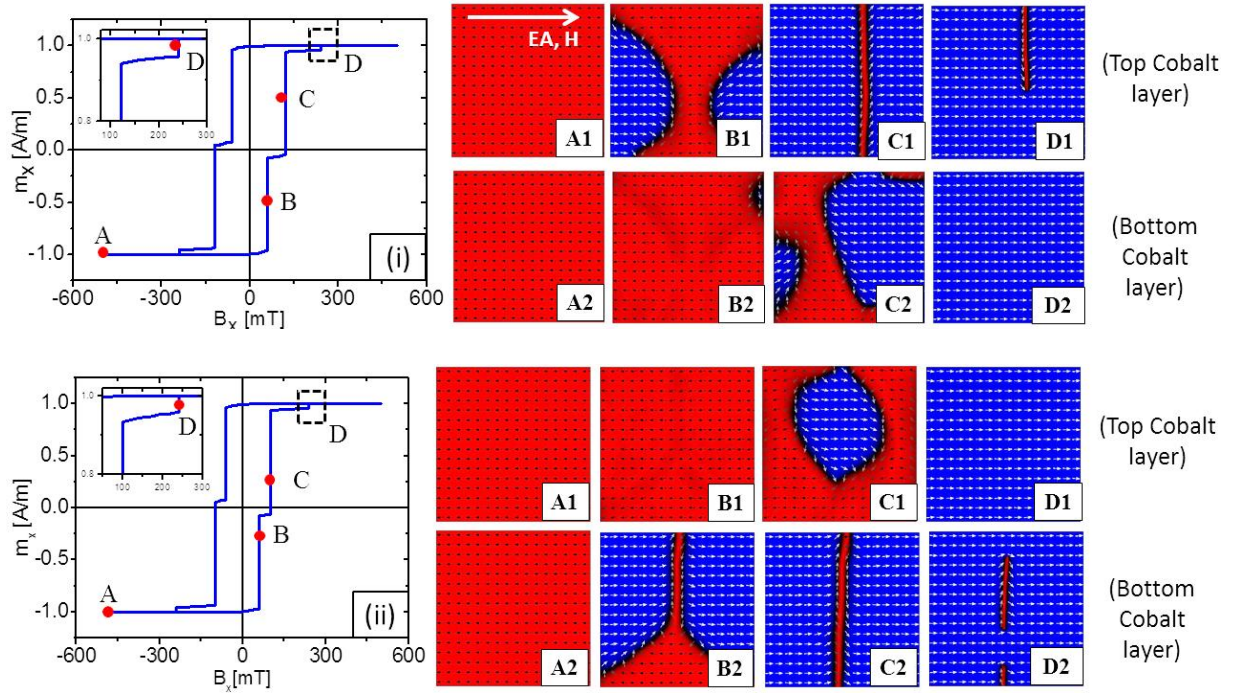


Figure 5.10: OOMMF simulated hysteresis and the corresponding domain images showing formation of  $360^\circ$  DWs for  $[\text{Co} (1.8 \text{ nm})/\text{Al}_2\text{O}_3 (3.6 \text{ nm})]_2$  with (i)  $K_r = K_u = 0.1 \times 10^6 \text{ J/m}^3$  and (ii)  $K_r = 0.15 \times 10^6 \text{ J/m}^3$  and  $K_u = 0.1 \times 10^6 \text{ J/m}^3$ . The suffix 1 and 2 in the domain images corresponds for the top and the bottom layer of the Co.

#### 5.4.1.3 $K_u = 0.2 \times 10^6 \text{ J/m}^3$ and $K_r = 0.1 \times 10^6 \text{ J/m}^3$ : random anisotropy is small compared to uniaxial anisotropy:

Let's now consider the case when the uniaxial anisotropy is strong compared to the random anisotropy i.e.  $K_u \gg K_r$ . Hence, all the parameters were kept same as described in above case (1) and (2), OOMMF simulations were performed for  $K_u = 0.2 \times 10^6 \text{ J/m}^3$  and  $K_r = 0.1 \times 10^6 \text{ J/m}^3$ . The hysteresis and its domain images are shown in Figure 5.11. It is evident from the domain images that the reversal was governed by the propagation of  $180^\circ$  DWs in both the Co layers.

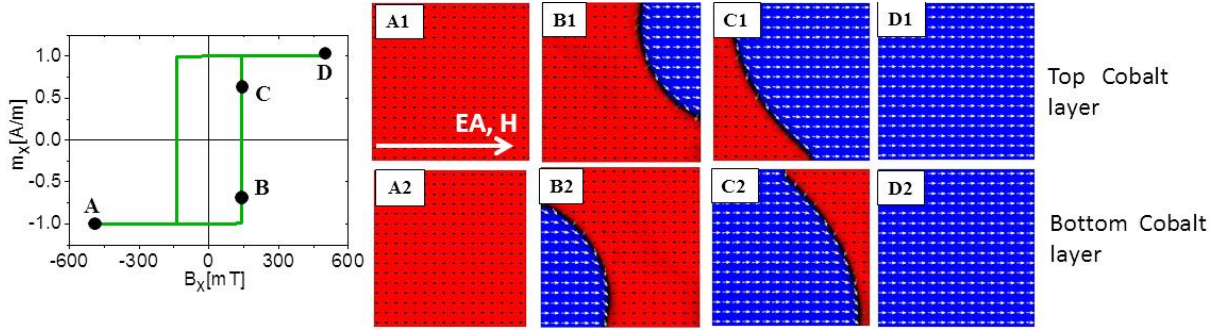


Figure 5.11: OOMMF simulated hysteresis loop and domain images showing the reversal by  $180^\circ$  DW motion along EA for  $[\text{Co} (1.8 \text{ nm})/\text{Al}_2\text{O}_3 (3.6 \text{ nm})]_2$  with  $K_u = 0.2 \times 10^6 \text{ J/m}^3$  and  $K_r = 0.1 \times 10^6 \text{ J/m}^3$ .

Of all the cases discussed above, the most relevant for the real sample is the one discussed is case I where  $K_r$  is less but comparable to  $K_u$ . Hence, for the simulations discussed hereafter the values of  $K_u$  and  $K_r$  are chosen to be  $0.15 \times 10^6 \text{ J/m}^3$  and  $0.1 \times 10^6 \text{ J/m}^3$ , respectively. Simulations were also performed for two Co (1.8 nm) layers separated by large spacer thickness of  $\text{Al}_2\text{O}_3$  (108 nm) with  $K_u = 0.15 \times 10^6 \text{ J/m}^3$  and  $K_r = 0.1 \times 10^6 \text{ J/m}^3$ . Formation of  $360^\circ$  DWs were also observed for this case (not shown here). Since the thickness of the spacer is large, the effect of inter-layer dipolar coupling for the formation of  $360^\circ$  DWs can be neglected in this case.

Hence, it can be concluded that  $360^\circ$  DWs can be formed along EA when the random anisotropy is comparable or greater than the uniaxial anisotropy. The walls are formed by merger of two  $180^\circ$  DWs of similar rotation. The random anisotropy in the real film can arise from the dispersion in the local EA due to the weak applied magnetic field during the deposition. The argument for the two layers also holds good for  $[\text{Co}(1.8 \text{ nm})/\text{Al}_2\text{O}_3(3.6 \text{ nm})]_9$  which approximately mimics the real sample is shown in next section.

### 5.4.2 Micromagnetic simulations along HA:

The OOMMF simulations along HA was performed for [Co (1.8 nm)/Al<sub>2</sub>O<sub>3</sub>(3.6 nm)]<sub>2</sub> by keeping all the parameters same as described for those along EA. The values of  $K_u$  and  $K_r$  were chosen to be  $0.15 \times 10^6$  and  $0.1 \times 10^6$  J/m<sup>3</sup>, respectively. The EA axis was considered to be along x-axis and the magnetic field was applied along the HA i.e. y-direction. Figure 5.12 (A) shows the OOMMF simulated hysteresis. Its S- shape indicates that magnetization reversal occurs via typical coherent rotation as was also experimentally observed by the Kerr microscopy hysteresis (Figure 5.4(a)). Images shown in Figure 5.12 B1, B2 to G1, G2 are the simulated domain images with their corresponding field points marked in the hysteresis (Figure 5.12(A)). The suffix 1 and 2 in the domain images corresponds to the top and the bottom Co layers, respectively. For negative saturation, all the spins of both the Co layers were saturated along HA (-y direction) as shown by domain Figure 5.12 B1 and B2. On reversing the field, the films breaks up into two regions with opposite sense of rotation (Figure 5.12 C1 and C2). This can be seen from the two regions (i) and (ii) of the top Co layer. The rotation of the region (i) of the top Co layer is anticlockwise whereas that of (ii) is clockwise. Similarly, the rotation of the region (iii) and (iv) of the bottom Co layers have opposite sense of rotation. This occurs due to high value of random anisotropy which induces a dispersion in the direction of the local EA. As already discussed in Chapter 3, for high randomness or misalignment (i.e.  $J/K_u \ll K_r$ ), the EA of the neighbouring grains may be aligned nearly antiparallel [35]. In such scenario, the exchange energy which induces coherent rotation will not be able to outweigh the random anisotropy. This breaks the symmetry of coherent rotation and hence rotation on either sense will be equally favourable. This leads to opposite sense of rotation in the nearby regions as discussed above. On approaching the remanence, the spins in the two regions of each of the Co layer are aligned along the EA and are antiparallel to each other as shown in Figure 5.12 D1 and D2. As

already discussed, the magnetization reversal for applied magnetic field at an angle to EA, the magnetization vector will rotate and align along the EA. However, since the random anisotropy is comparable to uniaxial anisotropy in this case, the opposite sense of rotation will lead to antiparallel alignment of the region (i) and (ii) of the top Co layer as shown in Figure 5.12 D1. This was also true for the bottom Co layer as shown for the region (iii) and (iv) of Figure 5.12 D2. On further increasing the field in the positive direction, this different rotation sense continues (Figure 5.12 E1 and E2) and leads to the formation of  $360^\circ$  DWs. Once formed, these walls were annihilated gradually under increasing magnetic field (Figure 5.12 F2) leading to saturation.

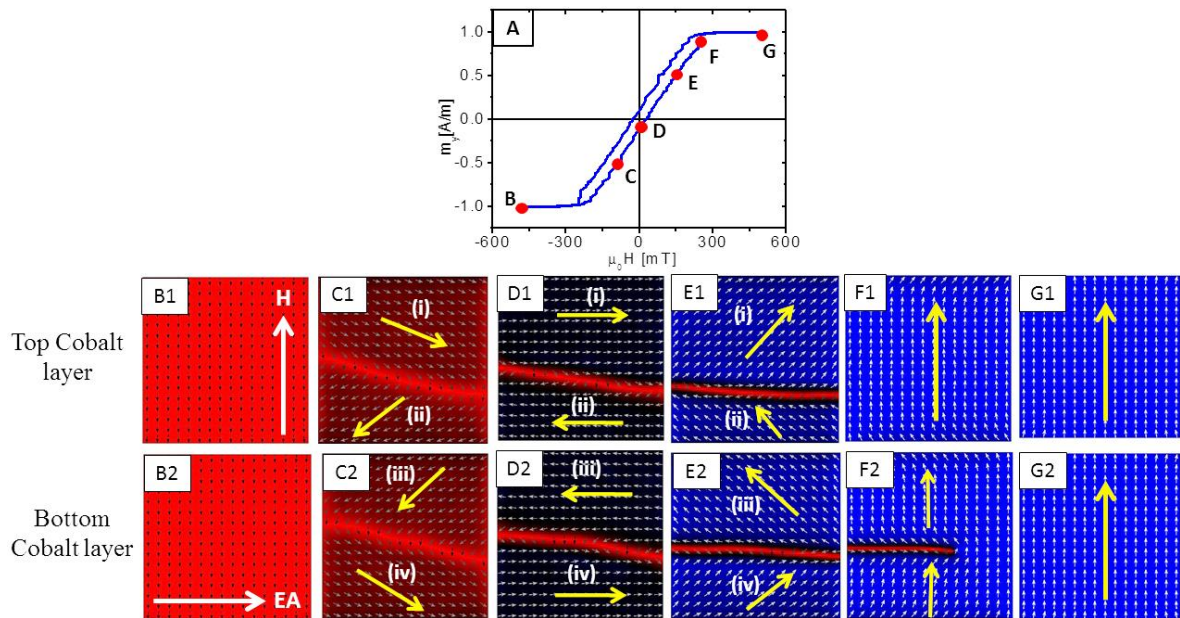


Figure 5.12: OOMMF simulated Hysteresis (A) and domain images (B to G) along HA for  $[\text{Co (1.8 nm)/Al}_2\text{O}_3 (3.6 \text{ nm})]_2$  with  $K_u = 0.15 \times 10^6$  and  $K_r = 0.1 \times 10^6 \text{ J/m}^3$ . The red and blue pixels correspond to magnetization  $M_y < 0$  and  $M_y > 0$ , respectively. The suffix 1 and 2 in the domain images correspond to the top and the bottom Co layers, respectively.

## **5.5 Conclusion:**

Hence, it can be summarized that the presence of random anisotropy comparable to uniaxial anisotropy can lead to the formation of non-trivial  $360^\circ$  DWs. Along EA, the  $360^\circ$  DWs were formed by merger of two  $180^\circ$  DWs. The DWs are quite stable and required high magnetic field for annihilation. Along HA, the coherent rotation of spins in opposite sense lead to the formation of  $360^\circ$  DWs.

# Chapter 6 : Controlling the size and relaxation dynamics of Superferromagnetic domains

## 6.1 Introduction:

Since magnetic nanoparticles have potential applications in various fields such as magnetic resonance imaging (MRI), magnetic refrigerants, hyperthermic treatment for malignant cells, site specific drug delivery and manipulating cell membranes etc., hence they have been subject of interest for research for last few decades. These nanoparticles below a critical size ( $r_c$ ) becomes single domain. The critical radius is given by –

$$r_c \approx 36 \frac{(AK_u)^{1/2}}{\mu_0 M_s^2}$$

where  $A$  is the exchange constant,  $K_u$  is the uniaxial anisotropy energy constant,  $\mu_0$  is the permeability of the material, and  $M_s$  is the saturation magnetization. [44, 156] These single domain nanoparticles carry net spins which is equal to the sum of all constituent atomic spins and are denoted as “superspins” or “macrospins”. The interaction in an ensemble of nanoparticles can be varied by changing the concentration of nanoparticles. For a system consisting of dilute and hence non-interacting nanoparticles will show superparamagnetic (SPM) behaviour. The relaxation for such systems was described by Néel- Brown model [157,158]. At high temperature the superspin fluctuate along their easy axis but at low temperatures it appeared to be blocked on a time scale given by the experiment. The magnetization reversal of non-interacting single domain particles was first examined by Stoner and Wohlfarth [55]. This theory was developed by assuming the coherent rotation of the magnetization of each particle. At high concentration of nanoparticles strong, dipolar interactions can be experienced. In this case the blocking at low temperature can be overcome by collective freezing in the case of a superspin glass (SSG) [159, 159, 161] for intermediate

concentrations. At high concentration, but below physical percolation, a ferromagnetic state called superferromagnetic (SFM) [162, 163, 164] can be observed.

In this context DMIMs such as  $[\text{Co}_{80}\text{Fe}_{20}(t_n)/\text{Al}_2\text{O}_3(3\text{ nm})]_{10}$  has been proven to be an ideal system to exhibit variety of magnetic properties such as superparamagnetism (SPM), superspin glass (SSG) and superferromagnetism (SFM) by varying the nominal thickness ( $t_n$ ) of the ferromagnetic layer [159]. It has been shown that in a DMIM sample with  $t_n = 0.5$  nm the superspins experience negligible interparticle interactions leading to SPM blocking behavior [165]. However, for DMIMs with  $0.5 \leq t_n \leq 0.9$  nm the superspins experience non-negligible interparticle interactions and undergo SSG freezing [166]. With increasing coverage,  $1.0 \leq t_n \leq 1.4$  nm, the nanoparticles experience strong interactions leading to a SFM domain state. A superferromagnetic (SFM) domain can be defined as a domain similar to ferromagnetic domain where the long range collective behaviour arises due to supermoments of the individual nanoparticles. Hence, the difference between the conventional ferromagnetic film and SFM is that the atomic moments are replaced by the supermoments of the individual nanoparticles [155]. Schematically the collective ferromagnetic behaviour giving rise to SFM domains is shown in Figure 6.2. The domains consist of a group of single domain ferromagnetic nanoparticles with average magnetization of each region shown by the large blue arrows. Unlike the structure of domain walls in thin films, the structure of walls separating the SFM domains are not yet understood.

In past several groups have reported indirect evidence of SFM e.g. Sankar *et al.* showed the ferromagnetic correlation below 150 K in Co-SiO<sub>2</sub> granular thin film by ac-susceptibility and small angle neutron scattering (SANS) measurements [167]. This correlated ordering was attributed to the dipolar coupling between the Co nanoparticles. Indirect evidences of SFM domain state for DMIMs were initially concluded from the characteristics similar to conventional continuous thin film. For example, SFM system

showed dynamic hysteresis loops measured by MOKE magnetometry, [168] different dynamic modes (relaxation, creep, slide, switching) of domains wall motions observed from Cole -Cole plots extracted from the ac-susceptibility [7, 161, 169], polarized neutron reflectometry [169], aging and memory effects measured in the magnetic relaxation [170] etc. However, real-time imaging of SFM domains was achieved by synchrotron based photoemission electron microscopy (XPEEM) and Kerr microscopy [7].

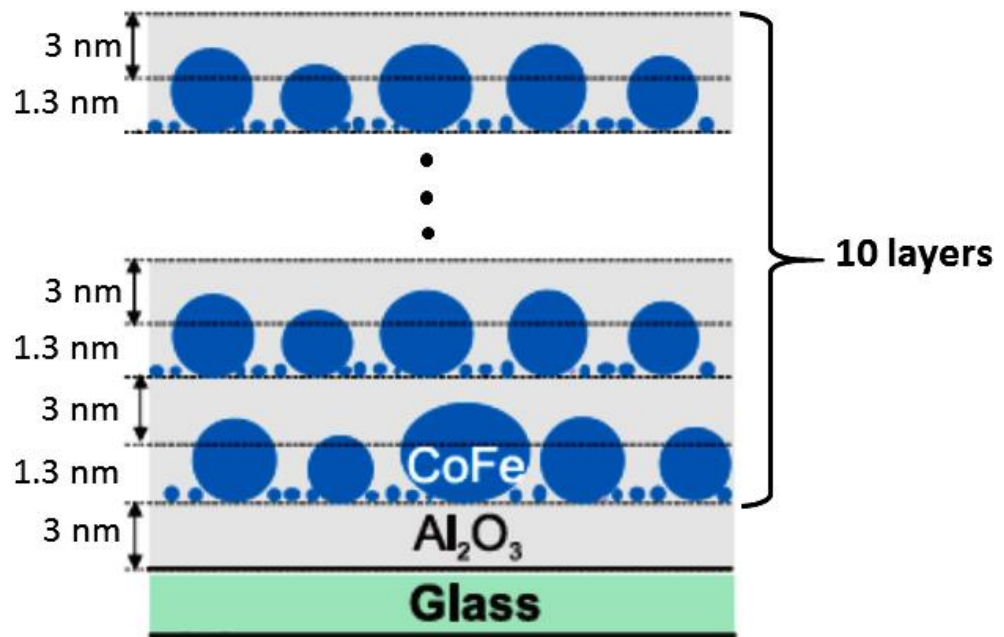


Figure 6.1: Cross-sectional schematic of  $[\text{Co}_{80}\text{Fe}_{20} (1.3 \text{ nm})/\text{Al}_2\text{O}_3 (3 \text{ nm})]_{10}$  where the big particles are the  $\text{Co}_{80}\text{Fe}_{20}$  single domain nanoparticles and the small one are the glue particles responsible for tunnelling exchange coupling giving rise to SFM behaviour [7].

The origin of SFM state in the DMIM was attributed to the dipolar coupling along with the weak tunnelling exchange coupling which was mediated by the glue particles as shown in Figure 6.1 [7]. These glue particles are the small residual atomic clusters which form due to the Volmer-Weber-Type growth of CoFe on Al<sub>2</sub>O<sub>3</sub> matrix (Figure 6.1) [155]. However, SFM domain-like states have also been observed in purely dipolarly coupled

systems [171, 172, 173]. In addition, calculations have shown that higher order multipolar interactions arising due to irregular particle shape might be a reason for the stable SFM domain state [174].

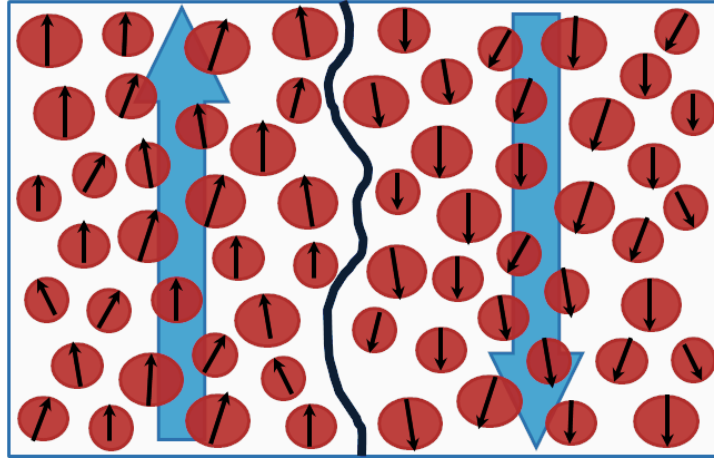


Figure 6.2: Schematic showing the SFM two oppositely aligned domains shown by large blue arrows. Each domain is formed by a group of single domain nanoparticles represented by the brown spheres [155].

However, many challenges in this field for example, understanding the nature and structure of superferromagnetic domain walls are yet to be explored. Further, the magnetization reversal process is of a fundamental importance while implementing in applications, it needs to be understood in SFM systems. For example, recording media demand miniaturization of domain size while keeping the media grains ferromagnetically coupled. Continuous thin films have been under investigation for this purpose for a few decades now. Recently, Arregi *et al.* [113] have demonstrated that by changing the angle between the applied field and the easy anisotropy direction, the magnetization reversal correlation length can be varied. Studying a uniaxial Co thin film deposited on Si substrate, the authors demonstrated a temperature independent pathway for the control of domain size. Therefore, in this work, a new approach to control the size of domains and magnetization reversal in superferromagnetic systems has been explored.

## 6.2 Preparation for Superferromagnetic sample:

The sample  $\text{Al}_2\text{O}_3(3 \text{ nm})/[\text{Co}_{80}\text{Fe}_{20} (1.3 \text{ nm})/\text{Al}_2\text{O}_3 (3 \text{ nm})]_{10}$  was prepared on float glass by focussed Xe- ion beam sputtering as discussed in section 2.1.1 of Chapter 2. However, the thickness  $t = 1.3 \text{ nm}$  was below the percolation limit.  $\text{Co}_{80}\text{Fe}_{20}$  on  $\text{Al}_2\text{O}_3$  follows Volmer-Weber which leads to the formation of discontinuous layer of spherical  $\text{Co}_{80}\text{Fe}_{20}$  nanoparticles for the nominal thickness below  $1.8 \text{ nm}$  [7]. An in-plane uniaxial anisotropy was induced by applying a magnetic field of  $\mu_0 H = 10 \text{ mT}$  during the deposition process. The structural and magnetic properties have been discussed in detail in reference [155]. It was shown that this sample has a Curie temperature of  $T_c \sim 510 \text{ K}$ . Hence, the sample was found to be superferromagnetic at room temperature [169]. The direct evidence of the presence of SFM domains were given by synchrotron based photoemission electron microscopy (XPEEM) and Kerr microscopy [7].

## 6.3 Angle dependent control of SFM domains:

The induced uniaxial anisotropy due to the application of magnetic field during growth was confirmed in past by ferromagnetic resonance [155]. Although SFM domains have been observed in past but the understanding of the SFM domains and domain wall dynamics is still yet to be explored. In this regard, angle dependent static hysteresis, domain shape and size, and relaxation were investigated. It should be noted that the angle dependent relaxation will be discussed in next section. These angle depended magnetization measurements were performed using MOKE microscopy similar to that described in section 3.3.2.2.1 of chapter 3.

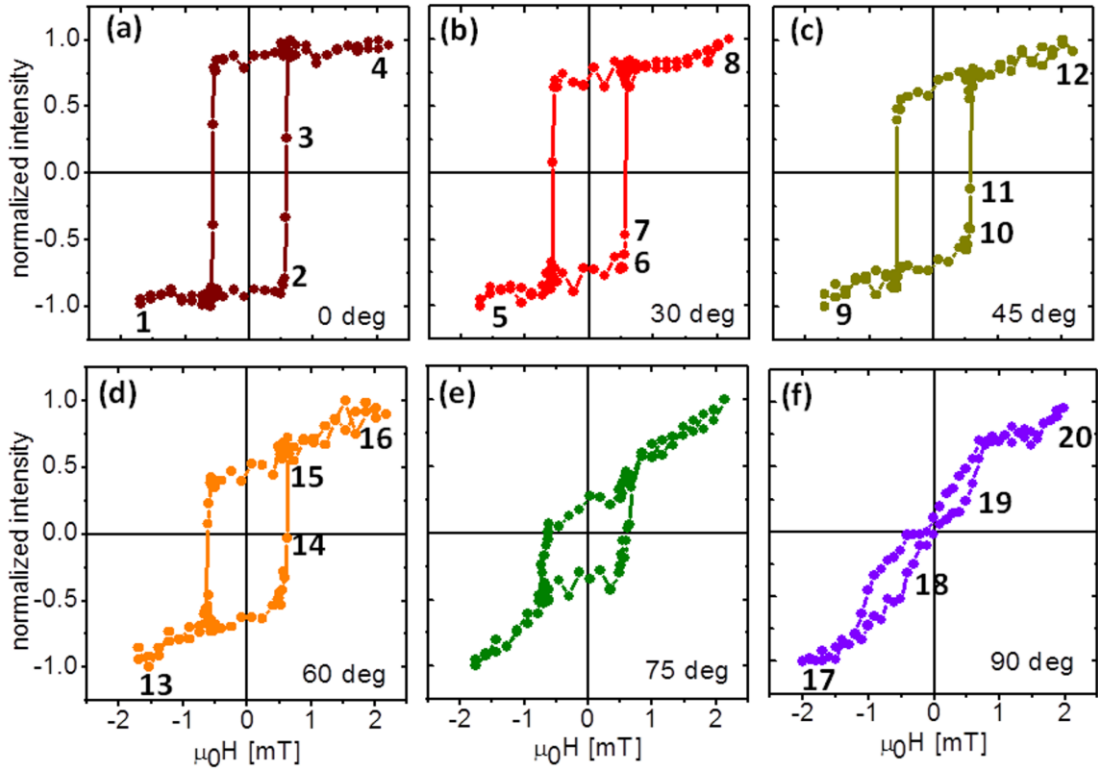


Figure 6.3: Longitudinal magneto-optic Kerr effect (LMOKE) hysteresis for  $[\text{Co}_{80}\text{Fe}_{20} (1.3 \text{ nm})/ \text{Al}_2\text{O}_3(3 \text{ nm})]_{10}$  measured along  $\theta = 0^\circ, 30^\circ, 45^\circ, 60^\circ, 75^\circ,$  and  $90^\circ$  at room temperature. The numbers shown in the hysteresis loops correspond to the domain images shown in Figure 6.4.

The angle dependent hysteresis loops for  $\theta = 0^\circ$  (EA),  $30^\circ, 45^\circ, 60^\circ, 75^\circ,$  and  $90^\circ$  (HA) are shown in Figure 6.3(a) – (f), respectively. A rectangular hysteresis loop with sharp jump at coercive field was observed along EA (Figure 6.3(a)). This sharp jump implies correlated reversal of all the nanoparticles governed by domain wall motion. This was also verified from the domain images of the EA shown in Figure 6.4.1 (negative saturation) to 6.4.4 (positive saturation). The corresponding field points for these domain images have been marked in Figure 6.3(a) as points 1 – 4. The uniform black image of Figure 6.4.1 implies that the sample is negatively saturated. As the field is reversed along positive direction, domain nucleation followed by domain wall motion is observed from Figure 6.4.2 and 6.4.3. The domains observed reveal “stripe”-type shapes, while their average width is a few tens of

micrometers. This means several hundred/thousands of nanoparticles (diameter  $\sim 5$  nm) constitute the SFM domain. When the field is increased from point 2 to point 3 in Figure 6.3(a), the domains grow sideways accompanied by nucleation of new domains (see Figure 6.4.2 and 6.4.3).

It is observed that for angles away from EA (i.e. for increasing values of  $\theta$ ) the hysteresis loop shape changes from square to *S*-shaped. This implies that for these angles, reversal is initially accomplished by coherent rotation and then followed by domain wall motion up to  $\theta = 60^\circ$ . A finite linear increase in all the hysteresis were observed even after the loop got closed. This finite slope indicates the onset of coherent rotation processes of the superspins, which need much higher fields to achieve saturation. However, a small slope observed along EA can be attributed to the presence of paramagnetic “glue” particles in the SFM system which thus requires high magnetic field to saturate (Figure 6.1) [7, 165]. However, the slope increases as the angle  $\theta$  between EA and applied magnetic field is increased as the rotation of nanoparticles also contributes to the slope towards the saturation. Domain images for off-easy axis fields for  $30^\circ$ ,  $45^\circ$  and  $60^\circ$  are shown in Figure 6.4.5 - 6.4.8, 6.4.9 - 6.4.12 and 6.4.13 - 6.4.16, respectively. It can be observed from these images that domain size reduces as  $\theta$  is increased and at  $\theta = 60^\circ$ , a significant decrease in domain size compared to EA is observed. Hence, in SFM systems correlated switching of nanoparticles occurs along the easy axis, while it decreases as we move away from the easy axis [175]. This is clearly evident from the domain images shown in Figure 6.4.7 and 6.4.11 as compared to Figure 6.4.3.

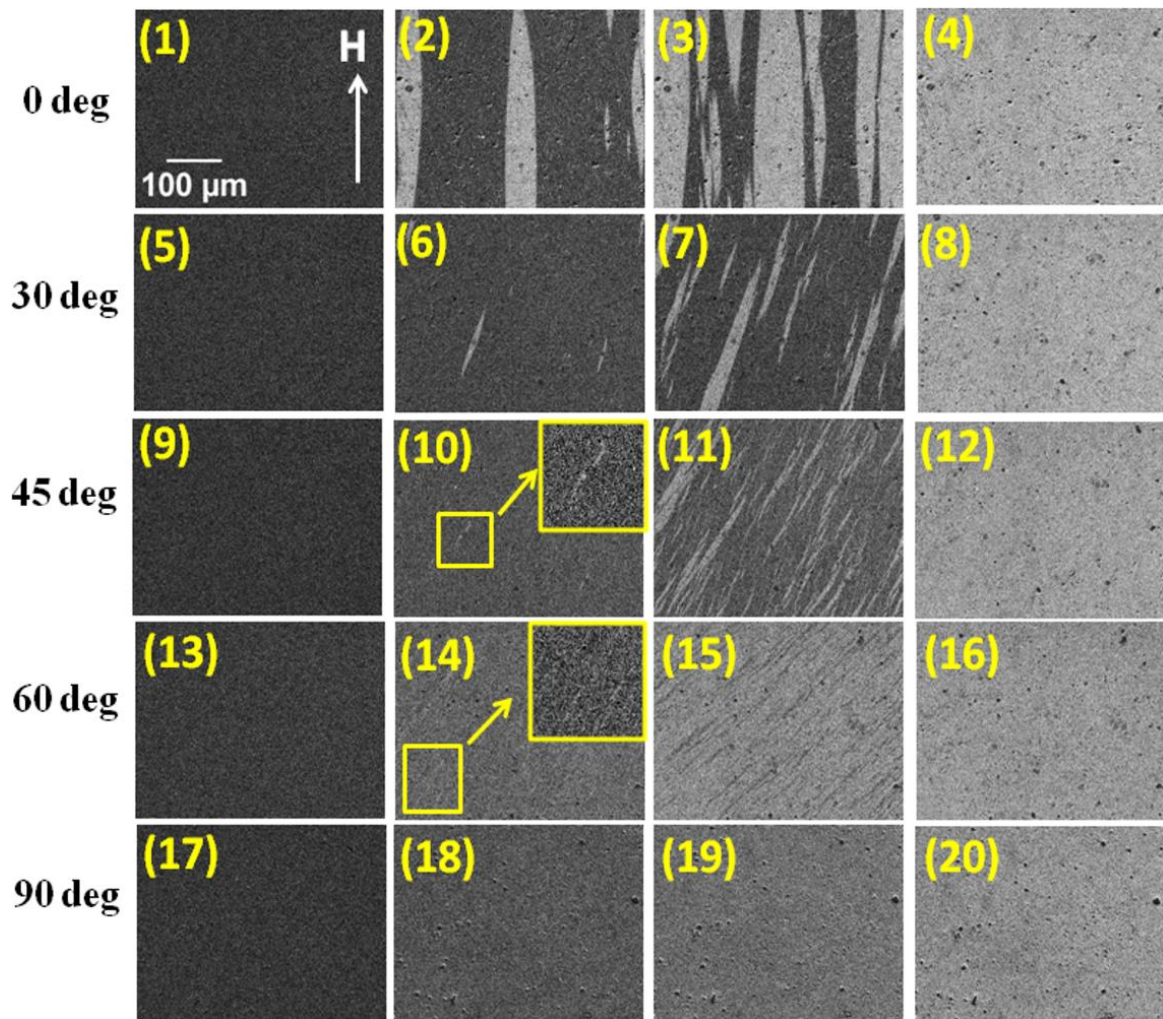


Figure 6.4: Domain images for  $[\text{Co}_{80}\text{Fe}_{20} (1.3 \text{ nm})/ \text{Al}_2\text{O}_3 (3 \text{ nm})]_{10}$  recorded with LMOKE microscopy with  $H$  directed along  $\theta = 0^\circ$  (EA),  $30^\circ$ ,  $45^\circ$ ,  $60^\circ$ , and  $90^\circ$  (HA) and  $H$  values as marked in Figure 6.3.

This decrease in domain size can be understood in analogy to the suppression of magnetic reversal correlation as observed in poorly crystalline films, where partial misalignment of crystallographic grains is encountered [113]. The difference in continuous and SFM system is that the continuous thin films will have grains with direct exchange coupling. However, the SFM system is mediated by a weak indirect tunneling exchange coupling via the glue particles with strong dipolar interactions between the nanoparticles. Due to this weak indirect exchange coupling, the nanoparticles in SFM will show small

random anisotropy in addition to the field induced uniaxial anisotropy. Therefore, the magnetization reversal of SFM can be understood in analogous to poorly crystalline thin films with weak exchange coupling as was discussed by Arregi *et al.* [113]. Hence, as  $\theta$  is increased away from easy axis, the exchange energy becomes weaker but the magnetic disorder becomes dominant and the energy barriers increase resulting in decorrelated reversal for higher angles.

The hard axis loop indicates that the magnetization reversal occurs essentially via coherent rotation. This was evident by the *S*-shaped hysteresis loop of Figure 6.3(f) for which merely a continuous change in the gray scale of the corresponding images is observed from Figure 6.4.17 - 6.4.20. However, the existence of very small sized domains of the order of a few tens of nanometers (*i.e.* a few superspins wide) is not excluded for the hard axis, since such small domains cannot be visualized by Kerr microscopy due to its limited spatial resolution.

On the present SFM sample we have observed clear hysteresis with finite loop area for angles  $\theta \leq 75^\circ$ . In the perpendicular configuration,  $\theta = 90^\circ$  (Figure 6.3(f)), the magnetization varies linearly and virtually without hysteresis. Here the classic result of a bulk magnet with uniaxial anisotropy constant  $K_u$  seems to apply, where

$$M(H) = (M_s^2/2K_u)H \quad \text{for } |\mathbf{H}| \leq H_C = (2K_u/M_s), \quad (6.1a)$$

$$M(H) = M_s \quad \text{for } |\mathbf{H}| > H_C. \quad (6.1b)$$

Within errors we find  $\mu_0 H_C \approx 1$  mT, which is close to the values found from the hysteresis loops (Figure 6.3(a) – (e)). It seems reasonable to assume coherent rotation of the individual nanoparticle magnetization, where statistical smearing of the coercive field,  $\Delta(\mu_0 H_C) \approx \pm 0.5$  mT, hints at a wide statistical distribution. Similar results were observed on lithographically produced regular arrays of virtually non-interacting rectangular permalloy

nanoparticles of planar dimension  $1.5 \times 0.2 (\mu\text{m})^2$  [176]. The above discussions can also qualitatively interpreted by plotting the difference of the slope of the hysteresis for each angle with respect to the closing field of EA ( $\mu_0 H \sim 1 \text{ mT}$ ). The corresponding plot is shown in Figure 6.5. The slope of the graph increases almost linearly and then flattens around  $75^\circ$ . This implies that the slope of the hysteresis for SFM increases on increasing  $\theta$  implying that the reversal at higher  $\theta$  is governed by coherent rotation process. This will be better evident from the magnetic aftereffect relaxation measurements discussed in next section.

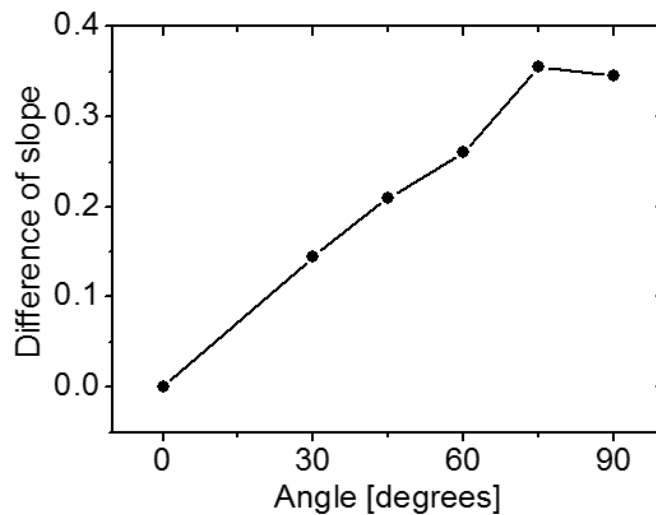


Figure 6.5: Plot showing difference of the slope of the hysteresis for  $\theta = 0^\circ, 30^\circ, 45^\circ, 60^\circ, 75^\circ,$  and  $90^\circ$  with respect to the closing field of EA ( $\mu_0 H \sim 1 \text{ mT}$ ).

#### 6.4 Angle dependent magnetization relaxation in SFM –

In order to understand the magnetization reversal in SFM in detail, angle dependent magnetization relaxation was measured using LMOKE microscopy. These measurements were performed for each angle as described in section 3.3.2.2.2. It should be noted that for every angle the ratio of the applied field to the coercive field was kept constant. Figure 6.6 shows the relaxation curves for  $\theta = 0^\circ, 30^\circ$  and  $60^\circ$ . The curves were fitted with a compressed exponential formula

$$M = M_0 + M_I \left( 1 - \exp(-t/\tau)^\beta \right), \quad (6.2)$$

where  $M_0 + M_I$  is the normalized saturation magnetization,  $\tau$  is the relaxation time obtained from the fit, and  $\beta > 1$  a compressing exponent as introduced by Adjanoh *et al.* [108]. Here the very fast dynamics ( $< 1$  s) of the initial switching from  $-(M_0 + M_I)$  to  $+M_0$  has not been taken into account.

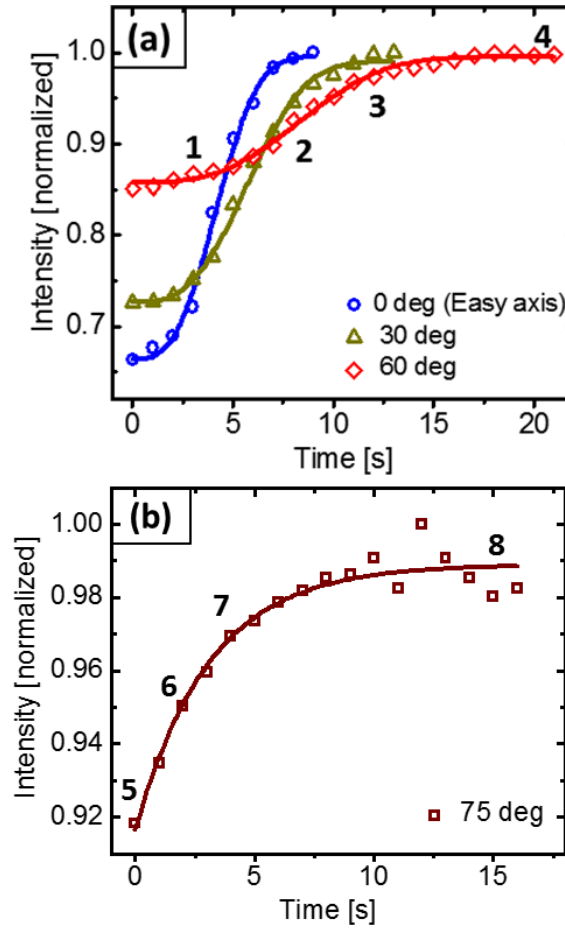


Figure 6.6: Magnetization relaxation curves for a SFM DMIM  $[\text{Co}_{80}\text{Fe}_{20}(1.3 \text{ nm})/\text{Al}_2\text{O}_3(3 \text{ nm})]_{10}$  measured with LMOKE microscopy with  $\mathbf{H}$  along (a)  $\theta = 0^\circ$  (EA) at  $\mu_0 H = 0.53 \text{ mT}$  (open circles),  $30^\circ$  at  $\mu_0 H = 0.53 \text{ mT}$  (open triangles),  $60^\circ$  at  $\mu_0 H = 0.58 \text{ mT}$  (open rhombs), and (b)  $\theta = 75^\circ$  at  $\mu_0 H = 0.73 \text{ mT}$ . Solid lines are best fits to Eq. (6.2). Domain images corresponding to the points marked (1) - (4) and (5) - (8) for the  $\theta = 60^\circ$  and  $75^\circ$  in Figure 6.6(a) and (b) are shown in Figure 6.7 and 6.8, respectively.

From the fittings using Eq. (6.2), the compressed exponent  $\beta=3$  was found for  $\theta = 0^\circ, 30^\circ$  and  $60^\circ$ , which gives the S-shaped nature of the graphs shown in Figure 6.6(a). However, for  $\theta = 75^\circ$  the best fit yields  $\beta=1$ , which gives rise to an exponential curve. The relaxation times for  $\theta = 0^\circ, 30^\circ$  and  $60^\circ$  were observed to be 4.72, 6.51, and 9.51 s, respectively. This indicates that the relaxation time increases as  $\theta$  is increased away from the easy axis. It should be noted that the relaxation time decreases with increasing applied field (*viz.* Zeeman energy) and temperature (*viz.* thermal energy). The parameters obtained from the fittings of the magnetization relaxation using Eq. (6.2) have been summarized in Table 6.1.

Table 3: Fitting parameters obtained for different angles using Eq. (6.2).

Angle ( $\theta$ )	$M_0$	$M_1$	$\beta$	$\tau$ [s]
$0^\circ$ (Easy axis)	$0.66 \pm 0.01$	$0.33 \pm 0.01$	$3.0000 \pm 0.0003$	$4.72 \pm 0.13$
$30^\circ$	$0.73 \pm 0.01$	$0.26 \pm 0.01$	$3.0000 \pm 0.0002$	$6.51 \pm 0.13$
$60^\circ$	$0.860 \pm 0.002$	$0.138 \pm 0.002$	$3.0000 \pm 0.0001$	$9.51 \pm 0.16$
$75^\circ$	$0.916 \pm 0.005$	$0.0725 \pm 0.0091$	$1.00000 \pm 0.00006$	$3.09 \pm 0.63$

From the S-shaped nature of these graphs in Figure 6.6(a), it can be concluded that the magnetization reversal is dominated by domain wall motion [108]. As the time was increased the number of domain nucleation sites increased as confirmed by the domain images for  $\theta = 60^\circ$  shown in Figure 6.7(a) – (b). During the initial few seconds of reversal very few domains nucleate as observed in the zoomed-in image in the left panel of Figure 6.7(a) at time  $t = 3$ s. With further increase in time the number of domain nucleation sites increases followed by domain wall motion (Figure 6.7(b) and 6.7(c) at  $t = 8$  and 12s, respectively) leading to saturation at  $t = 20$ s (Figure 6.7(d)) due to thermal activation as the Zeeman energy is fixed.

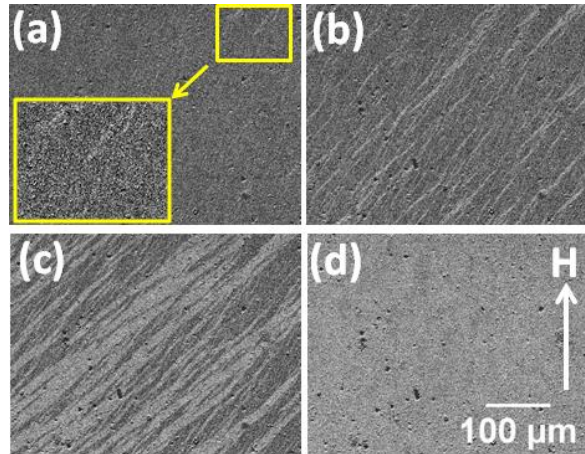


Figure 6.7: Domain images of magnetic relaxation recorded with  $H$  along  $\theta = 60^\circ$ . Images (a), (b), (c), and (d) were taken at  $t = 3, 8, 12$  and  $20$ s, respectively, and correspond to points 1, 2, 3 and 4 of Figure 6.6(a).

However, it can be observed from Figure 6.6(b) that the relaxation for  $\theta = 75^\circ$  does not reveal an  $S$ -shape. The fitting parameters to Eq. (6.2) are  $\beta = 1.00000 \pm 0.00006$  and  $\tau = (3.09 \pm 0.63)$  s, respectively. With  $\beta = 1$  for  $\theta = 75^\circ$ , Eq. (6.2) reduces to a simple exponential. This implies that the reversal is dominated by domain nucleation as also observed by the domain images in Figure 6.8 [108]. The magnetic relaxation for initial few seconds (Figure 6.8(a)) for  $\theta = 75^\circ$ , shows a gradual change in gray contrast followed by nucleation of very fine domains (Figure 6.8(b) and (c) at  $t = 4$  and  $8$  s, respectively). This is also consistent with the explanations discussed for Figure 6.3, 6.4 and 6.5.

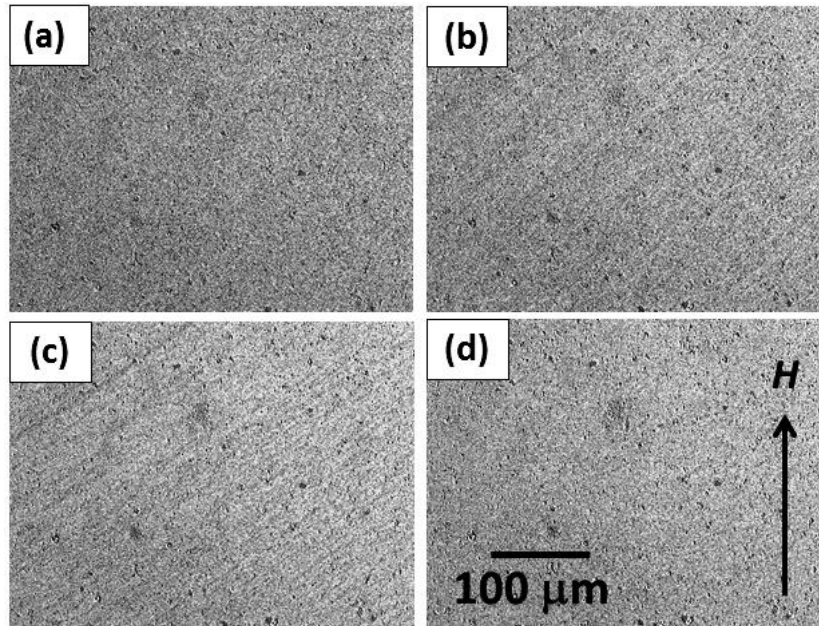


Figure 6.8: Domain images for magnetic relaxation recorded with  $H$  along  $\theta = 75^\circ$ . Images (a), (b), (c), and (d) were taken at  $t = 0, 4, 8,$  and  $15$  s, respectively, and correspond to points 5, 6, 7 and 8 of Figure 6.6(b).

## 6.5 Conclusion:

Hence, it can be concluded that the reversal process along the easy axis (EA) for a SFM shows a strongly correlated reversal accompanied by domain nucleation and domain wall motion. The magnetic correlation length decreases as the angle  $\theta$  between magnetic field and easy axis is increased. Remarkably, a quite strong magnetic saturation after-effect occurs beyond the coercive field  $\pm H_C$ . This is attributed to the final magnetic alignment of single superspins, which are subject to statistical fluctuations of their local magnetization. It has also been shown that the dynamics of the SFM domains can be varied by changing the angle between the easy axis and the applied magnetic field.

## Chapter 7 : Summary and Outlook

Primarily this work was focussed on understanding the magnetization reversal in granular thin films, multilayers, and nanoparticles which depends on the microstructural properties like anisotropy and its local dispersion, exchange energy, grain size and its distribution, coupling in multilayers etc. These factors affect the reversal and leads to complicated metastable domain structures during the magnetization reversal.

For this purpose, initially magnetization reversal, domain wall dynamics and relaxation were studied in Co(3.5 nm) and Co(10 nm) thin films prepared by magnetron sputtering. Kerr microscopy and magnetometry was used as the major characterization technique for studying magnetic properties. Growth induced uniaxial anisotropy due to oblique deposition was observed in these samples. Magnetization reversal is governed by domain wall motion and coherent rotation along easy and hard axes, respectively. The magnetic aftereffect relaxation measurements revealed domain wall motion dominated reversal for both the systems. Different modes of domain walls: creep, depinning and slide were observed for Co(3.5 nm) thin film. However, it should be mentioned that the range of the velocity appeared to be order less than generally observed in past by other groups. This may happen as at high fields the domain wall velocity becomes very high and it becomes very difficult to measure in our image window of Kerr microscope. Therefore, no attempt was made to calculate the domain wall width from the linear fits of the slide regime. In future, a stroboscopic set-up may be used with a pulsed field generator to study these modes, walker breakdown which occurs at very high field.

A part of this work shows that a dispersion in anisotropy (random anisotropy) can be induced in Co (10nm) thin film with uniaxial anisotropy by rotating the substrates with 10 and 20 rpm during their growth. In general, dispersion in anisotropy was observed in soft

magnetic films like permalloy [5] or in exchange biased films [61]. It was observed that with increase in substrate rotation, the films do not completely become isotropic and the dispersion in local grain anisotropy increases. For large randomness, the exchange coupling between grains responsible for correlated reversal will not be able to overcome the energy distribution. This will lead to formation of ripple domains due to incoherent switching and/or a blocked state of labyrinth domains during the magnetization reversal. Such blocked states must be avoided in thin films when used in device applications as it limits the rapid switching of magnetization required. Magnetic aftereffect relaxation measurements performed on these films revealed that relaxation process becomes slow with increasing randomness which in turn increases with substrate rotation. The effect of grain distribution on magnetization relaxation was also observed. For the sample prepared with 20 rpm rotation, the non-uniform distribution of grains (island like structures) showed that after nucleation of the domains, thermal energy was not sufficient to overcome the energy barriers, resulting in slow relaxation rate.

The magnetization reversal and domain structure can be very different in multilayers compared to their single layer film. In this work magnetization reversal of dipolarly coupled magnetic multilayers in Co (10 nm)/AlO<sub>x</sub> (*t* nm)/Co (10 nm) system was studied by varying thickness (*t*) of the AlO<sub>x</sub> spacer layer. Uniaxial anisotropy with small random anisotropy similar for single Co (10 nm) thin film was observed for all the multilayered samples. The structural characterization was performed using cross-sectional TEM, XRR and SIMS revealing polycrystalline nature of Co films with no interdiffusion. The magnetization reversal was studied by MOKE microscopy and magnetometry. Specifically, LMOKE microscopy was used to image the domain structure of the two Co layers. Layer-by-layer magnetization reversal was observed for all the samples. The observation from Kerr microscopy was confirmed by PNR measurements. PNR analysis revealed that the bottom Co

layer reverses first and then the top Co layer reverses. Two different domain structures corresponding to the two Co layers were observed by MOKE microscopy. It should be noted that the two Co layers were prepared under identical conditions. This shows the effect of dipolar interlayer coupling on magnetization reversal in magnetic multilayers. On increasing the thickness of the spacer layer, dipolar coupling weakens which leads to different domain structure. Also, for  $t > 23$  nm, transverse component of magnetization was observed and the saturation field decreased. Layer-by-layer magnetization reversal was also supported by OOMMF simulations. We considered a small random anisotropy along with uniaxial anisotropy in the simulations. However, in future one can explore the effect of change of thickness of the Co layer, the change in the number of bilayers in Co/AlO<sub>x</sub> multilayers.

In this thesis we have also studied the topic of 360° DWs. Among various types of domain walls the observation of 360° domain walls (DWs) is rare. These walls separate the domains with parallel magnetization. 360° DWs were observed in metal- insulator multilayer [Co<sub>80</sub>Fe<sub>20</sub> (1.8 nm)/Al<sub>2</sub>O<sub>3</sub> (3 nm)]<sup>9</sup>. Micromagnetic simulations suggest that formation of 360° DWs can be attributed to the presence of local random anisotropy which is comparable to the uniaxial anisotropy. In such cases, along EA, the 360° DWs are formed due to merger of two 180° DWs. However, along HA, 360° DWs are formed as the spins do not follow coherent rotation with magnetic field. When the random anisotropy ( $K_r$ ) in the simulations is comparable to uniaxial anisotropy, it cannot outweigh the exchange anisotropy. This results in opposite sense of rotation of the spins leading to the formation of 360° DWs. Therefore, we show that 360° DWs can be formed due to the competing effect of uniaxial and random anisotropies present in the magnetic thin films. Other parameters affecting the formation of these walls, like exchange stiffness, magnetic layer thickness etc. are yet to be explored theoretically. In future, one can explore the transport properties of these domain walls by both theory and experiment.

A small part of the thesis also reports the understanding of magnetization reversal and relaxation for a discontinuous metal insulator multilayers (DMIM)  $[\text{Co}_{80}\text{Fe}_{20} (1.3 \text{ nm})/\text{Al}_2\text{O}_3 (3 \text{ nm})]_{10}$  showing superferromagnetic (SFM) state. SFM domain is similar to ferromagnetic domain where the atomic spins are replaced by the superspins of single domain nanoparticles. It was observed that due to random anisotropy, the ferromagnetic correlation strength decreases for directions away from the easy axis as evident from reduction in domain size. The presence of small random anisotropy leads to compressed exponential behavior of the relaxation curves presence of energy distribution barriers in magnetization reversal. In future, one can try to verify different modes of domain wall motion, Walker breakdown to have the evidence of the domain wall existence in these systems.

## Appendix

Since various systems were studied in this thesis, the table A in this appendix gives the list of samples belonging to Co/AlO<sub>x</sub> at a glance. Though the measurements were taken on many samples, but the results from few of them have been discussed in detail in this thesis. They have been labelled accordingly and are shown in Table A.

Table A: Showing the sample list at a glance for the Co/AlO<sub>x</sub> series.

Sample structure on Si (100)/ AlO <sub>x</sub> (3 nm)/ [ <i>sturcture</i> ]/ AlO <sub>x</sub> (3 nm)	Sample Name	Substrate Rotation ( $\omega$ ) in rpm
Co (3.5 nm)	-	0
Co (10 nm)	Sample A	0
Co (10 nm)	Sample B	10
Co (10 nm)	Sample C	20
Co (10 nm)/AlO <sub>x</sub> (3 nm)/ Co (10 nm)	-	0
Co (10 nm)/AlO <sub>x</sub> (8 nm)/ Co (10 nm)	Sample D	0
Co (10 nm)/AlO <sub>x</sub> (23 nm)/ Co (10 nm)	-	0
Co (10 nm)/AlO <sub>x</sub> (33 nm)/ Co (10 nm)	-	0
Co (10 nm)/AlO <sub>x</sub> (45 nm)/ Co (10 nm)	-	0
Co (10 nm)/AlO <sub>x</sub> (90 nm)/ Co (10 nm)	Sample E	0
Co (10 nm)/AlO <sub>x</sub> (130 nm)/ Co (10 nm)	Sample F	0
Co (10 nm)/AlO <sub>x</sub> (270 nm)/ Co (10 nm)	Sample G	0

## References

1. M. Johnson, *J. Magn. Magn. Mater.* **156**, 321-324 (1996).
2. M. N. Baibich, J. M. Broto, A. Fert, F. N. Van Dau, F. Petroff, P. Eitenne, G. C. A. Friederich, and J. Chazelas, *Phys. Rev. Lett.* **61**, 2472 (1988).
3. P. Grünberg, R. Schreiber, and Y. Pang, M. B. Brodsky and H. Sowers, *Phys. Rev. Lett.* **57**, 19 (1986).
4. J. Barnaś, A. Fuss, R. E. Camley, P. Grünberg, and W. Zinn, *Phys. Rev. B* **42**, 8110 (1990).
5. D. O. Smith, M. S. Cohen, G. P. Weiss, *J. Appl. Phys.* **31**, 1755 (1960).
6. N. Chowdhury, and S. Bedanta, *AIP Advances* **4**, 027104 (2014).
7. S. Bedanta, Eimuller, W. Kleemann, J. Rhensius, F. Stromberg, E. Amaladass, S. Cardoso, and P. P. Freitas, *Phys. Rev. Lett.* **98**, 176601 (2007).
8. M. Takahashi and T. Kono, *J. Phys. Soc. Jpn.* **15**, 936 (1960).
9. E. Fatuzzo, *Phys. Rev.* **127**, 1999 (1962).
10. M. Labrune, S. Andrieu, F. Rio, P. Bernstein, *J. Magn. Magn. Mater.* **80**, 211-218 (1989).
11. M. A. Ruderman and C. Kittel, *Phys. Rev.* **96**, 99 (1954).
12. K. Yosida, *Phys. Rev.* **106**, 893 (1957).
13. J. C. Slonczewski, *Phys. Rev. B* **39**, 10, 6995 (1989).
14. L. Néel, *Acad. Sci., Paris, C. R.* **255**, 1676 (1962).
15. L. J. Heyderman, H. Niedoba, H. O. Gupta and I. B. Puchalska, *J. Magn. Magn. Mater.* **96**, 125 (1991).
16. K. J. O'Shea, K. Rode, H. Kurt, D. McGrouther and D. A. MacLaren, *J. Phys D: Appl. Phys* **48**, 055001 (2015).
17. C. C. Berry and A. S. G. Curtis, *J. Phys. D: Appl. Phys.* **36**, R198 (2003).

18. P. Weiss, L'Hypothèse du champ Moléculaire et de la Propriété Ferromagnétique (The hypothesis of the molecular field and the property of ferromagnetism), *J. Phys. Theor. Appl.* **6**, 661 (1907).
19. W. Heisenberg, *Z. Physik* **69**, 287-297 (1931).
20. A. Hubert and R. Schäfer, *Magnetic Domains*, Springer (2000).
21. Nicola A Spaldin, *Magnetic Materials Fundamentals and Applications*, Second Edition, Cambridge University Press (2011).
22. Mathias Getzlaff, *Fundamentals of Magnetism*, Springer (2007).
23. M.T. Johnson, , P. J. H. Bloemen, F. J. A. den Broeder and J. J .de Vries, *Rep. Prog. Phys.* **59**, 1409-1458 (1996).
24. D. Sander, *Rep. Prog. Phys.* **62**, 809 (1999).
25. F. J. A. den Broeder, W. Hoving and P. J. H. Bloemen, *J. Magn. Magn. Mater.* **93**, 562–70 (1991).
26. G. N. Kakazei, Yu. G. Pogorelov, A. M. L. Lopes, J. B. Sousa, S. Cardoso, P. P. Freitas, M. M. Pereira de Azevedo, and E. Snoeck, *J. Appl. Phys.* **90**, 4044 (2001).
27. Y. Hoshi, E. Suzuki, and M. Naoe, *J. Appl. Phys.* **79**, 4945 (1996).
28. J. L. Bubendorff, S. Zabrocki, G. Garreau, S. Hajjar, R. Jaafar, D. Berling, A. Mehdaoui, C. Pirri and G. Gewinner, *Europhys. Lett.* **75**, 119 (2006).
29. B. S. Berry and W. C. Pritchett, *Phys. Rev. Lett.* **34**, 1022 (1975).
30. L Néel, *Comp Rend* **237**, 1613 (1953).
31. S Taniguchi, *Sci Rept. RITU A7*, 269 (1955).
32. E. M. Chudnovsky, W. M. Saslow and R. A. Serota, *Phys. Rev. B* **33**, 251 (1986).

33. R. Coehoorn , D. B. de Mooij, J. P. W. B. Duchateau and K. H. J. Buschow, J. Physique Coll. **49**, C8, 669 (1988).
34. R. Skomski J. Appl. Phys. **83**, 11, 6503 (1998).
35. O. Idigoras, A. K. Suszka, P. Vavassori, P. Landeros, J. M. Porro, and A. Berger, Phys. Rev. B **84**, 132403 (2011).
36. J. P. Liu, C. P. Luo, Y. Liu and D. J. Sellmyer, Appl. Phys. Lett. **72**, 483 (1998).
37. D. C. Jiles, Introduction to Magnetism and Magnetic Materials (London: Chapman and Hall), Second Edition (1998).
38. Y Imry, and Shang-keng Ma, Phys. Rev. Lett. **35**, 21, 1399 (1975).
39. D. O. Smith, and K. J. Harte, J. Appl. Phys. **33**, 1399 (1962).
40. L.D. Landau, E. Lifshitz, Phys. Z. Sowjetunion **8**, 153–169 (1935).
41. K.J. Sixtus, and L. Tonks, Phys. Rev. **37**, 930–958 (1931).
42. F. Bloch, Z. Phys. **74**, 295 (1932).
43. L. Néel, C.R. Acad. Sci. Paris **241**, 533–536 (1955).
44. R. C. O'Handley, Modern Magnetic Materials: Principles and Applications. Wiley-Interscience, (2000).
45. S. Middelhoek, J. Appl. Phys. **37**, 3 (1966).
46. E. E. Huber, Jr., D. O. Smith, and J. B. Goodenough, J. Appl. Phys. **29**, 294 (1958).
47. R C Collette, Thesis, California Institute of Technology, California (1964).
48. S. Chikazumi, Physics of Ferromagnetism, second edition, Oxford University Press, (1997).
49. S. Chikazumi, Phys. Rev. **85**, 918 (1952).
50. N. Chowdhury, S. Bedanta, G. S. Babu, A. Weber, T. Brückel, and M. K. Dalai (unpublished).

51. Shi-shen Yan, R. Schreiber, P. Grünberg, R. Schäfer, *J. Magn. Magn. Mater.* **210**, 309 -315 (2000).
52. S. Bedanta, N. Chowdhury, O. Petravic, W. Kleemann, F. Kronast, A. Doran, A. Scholl, S. Cardoso, and P. P. Freitas (unpublished).
53. D. J. Sellmyer, D. Shindo, *Handbook of Advanced Magnetic Materials 11, Nanostructural Effects* edited by Yi Liu (2006).
54. A Berger, *Physica B* 407, 1322–1329 (2012).
55. E. C. Stoner and E. P. Wohlfarth, *Philos. Trans. London Ser. A* 240, 599 (1948).
56. R Skomski, *Nanomagnetics, J. Phys.: Condens. Matter* 15, R841–R896 (2003).
57. A. Aharoni, *Phys. Rev.* 119, 1 (1960).
58. S. Methfessel, S. Middelhoek, and H. Thomas, *J. Appl. Phys.* 32, 1959 (1961).
59. K. J. Harte, *J. Appl. Phys.* 39, 1503 (1968).
60. H. Hoffmann, *J. Appl. Phys.* 35, 1790 (1964).
61. J. McCord, R. Schäfer, R. Mattheis, K. -U. Barholz, *J. Appl. Phys.* 93, 5491 (2003).
62. G. Bertotti, *Hysteresis in Magnetism for Physicists, Materials Scientists, and Engineers*, Academic Press, Inc, San Diego, California, (1998).
63. M. J. Donahue and D. G. Porter, *OOMMF User's Guide*, National Institute of Standards and Technology, Gaithersburg, MD, (1999), Version 1.23.
64. P.J. Kelly, R.D. Arnell, *Vacuum* 56, 159-172 (2000).
65. S. Cardoso, V. Gehanno, R. Ferreira, and P.P. Freitas, *IEEE Trans. Magn.* 35, 2952 (1999).
66. <http://www.mantisdeposition.com/?url=nanoparticlesources>
67. C. Clavero, J. L. Slack, and A. Anders, *J. Phys. D: Appl. Phys* 46, 362001 (2013).

68. G. Binnig, C. F. Quate, and Ch. Gerber, *Phys. Rev. Lett.*, 56, 9, 930 (1986).
69. <http://www.teachnano.com/education/AFM.html>
70. P. Williams, *Ann. Rev. Mater. Sci.* 15, 517-548 (1985).
71. H.J. Liebl, *Anal.Chem.* 46, 22A, (1974).
72. H. W. Werner, *Vacuum* 22, 11, 613-617 (1972).
73. <http://www.nt.ntnu.no/users/floban/KJ%20%203055/Surface/SIMS.htm>
74. <http://www.ed.ac.uk/files/imports/fileManager/SIMS4.pdf>
75. S. K. Sinha, E. B. Sirota, S. Garoff, and H. B. Stanley, *Phys. Rev. B* 38, 2297 (1988).
76. H. Zabel, *Appl. Phys. A.* 58, 159 (1994).
77. K. M. Zimmermann, der Universität Dortmund, Thesis, (2005).
78. M. Born and E. Wolf, *Principles of Optics*, Pergamon, Oxford, (1993).
79. L. G. Paratt, *Phys. Rev.* 95, 359 (1954).
80. L. Reimer, *Transmission Electron Microscopy*, (Springer Series in Optical Sciences, Vol. 34), Ed. D. L. MacAdam, (Springer-Verlag, Berlin, 1984).
81. S. Bedanta, O. Petravic, M. Aderholz, and W. Kleemann, *Rev. Sci. Instrum.* 76, 083910 (2005).
82. J. Kerr, *Philos. Mag.* 3, 321 (1877).
83. M. Faraday, "On the magnetisation of light and the illumination of magnetic lines of force", *Philosophical Transactions of the Royal Society (London)* 136, 1-20 (1846).
84. S. D. Bader, *J. Magn. Magn. Mater.* 100, 440 (1991).
85. O. Idigoras, Thesis, CIC nanoGUNE, Spain (2013).
86. Z. Q. Qiu and S. D. Bader, *Rev. Sci. Instrum.* 71, 3, 1243 (2000).

87. S. Polisetty, J. Scheffler, S. Sahoo, Yi Wang, T. Mukherjee, Xi He, and Ch. Binek, *Rev. Sci. Instrum.* 79, 055107 (2008).
88. Z. J. Yang and M. R. Scheinfein, *J. Appl. Phys.* 74, 6810 (1993).
89. R. Schäfer, “Investigation of domains and dynamics of domain walls by the magneto-optical Kerr-effect,” in *Handbook of Magnetism and Advanced Magnetic Materials*, 3, 5, Helmut Kronmuller, Stuart Parkin (Editor), John Wiley& Sons, Ltd, (2007).
90. G. P. Felcher, *Phys. Rev. B* 24, 3, 1595 (1981).
91. S. J. Blundell and J. A. C. Bland, *Phys. Rev. B* 46, 3391 (1992).
92. H. Zabel, K. Theis-Bröhl, M. Wolff, and B. P. Toperverg, *IEEE Trans. Magn.*, 44, 7 (2008).
93. A. Paul and S. Mattauch *J. Phys. D: Appl. Phys.* 43, 185002 (2010).
94. J. F. Ankner and G. P. Felcher, *J. Magn. Magn. Mater.* 200, 741-754 (1999).
95. G. S. Bauer, *Nuclear Instruments and Methods in Physics Research Section A: Accelerators, Spectrometers, Detectors and Associated Equipment* 463, 505 (2001).
96. S. Mattauch and U. Rücker, *TREFF Reflectometer, Manual of the JCNS Laboratory Course Neutron Scattering* 107, (2015).
97. Y. Fukuma, Z. Lu, H. Fujiwara, G. J. Mankey, W. H. Butler, and S. Matsunuma, *J. Appl. Phys.* 106, 076101 (2009).
98. Y. P. Fang, W. He, H. L. Liu, Q. F. Zhan, H. F. Du, Q. Wu, H. T. Yang, X. Q. Zhang, Z. H. Cheng, *Appl. Phys. Lett.* 97, 022507 (2010).
99. S. V. Dijken, L. C. Jorritsma, B. Poelsema, *Phys. Rev. Lett.* 82, 4038 (1999).
100. V. Madurga, J. Vergara, C. Favieres, *J. Magn. Magn. Mater.* 272, 1681-1683 (2004).

101. Q. F. Zhan, C. V. Haesendonck, S. Vandezande, K. Temst, *Appl. Phys. Lett.* 94, 042504 (2009).
102. M. T. Umlor, *Appl. Phys. Lett.* 87, 082505 (2005).
103. J. B. Youssef, N. Vukadinovic, D. Billet and M. Labrune, *Phys. Rev. B* 69, 174402 (2004).
104. H. Kijima, S. Ohnuma, and H. Masumoto, *IEEE Trans. Magn.* 47, 3928 (2011).
105. J. Y. Kim, I.O. Hwang, H.C. Hong and D.H. Shin, *Proceedings of magneto-optical recording international symposium 96*, *Magn.Soc. Jpn.* 20, 165, s1 (1996).
106. M. Labrune, S. Andrieu, F. Rio, P. Bernstein, *J. Magn. Magn. Mater.* 80, 211-218 (1989).
107. H. Xi, K. Z. Gao, J. Ouyang, Y. Shi and Y. Yang, *J. Phys.: Condens. Matter* 20, 295220 (2008).
108. A. Adjanoh, R. Belhi, J. Vogel, M. Ayadi, K. Abdelmoula, *J. Magn. Magn. Mater.* 323, 504-508 (2011).
109. N. Chowdhury, S. Bedanta, and G. S. Babu, *J. Magn. Magn. Mater.* 336, 20-25 (2013).
110. W. Kleemann, *Annu. Rev. Mater. Res.* 37, 415–48 (2007).
111. P. Chauve, T. Giamarchi, P. Le Doussal, *Phys. Rev. B* 62, 6241 (2000).
112. S. Bedanta, E. Kentzinger, O. Petravic, W. Kleemann, U. Rücker, Th Brückel, A. Paul, S. Cardoso, P. P. Freitas, *Phys. Rev. B* 74, 054426 (2006).
113. J. A. Arregi, O. Idigoras, P. Vavassori, and A. Berger, *Appl. Phys. Lett.* 100, 262403 (2012).
114. C.S. Chi, B. Y. Wang, W. F. Pong, T. Y. Ho, C. J. Tsai, F. Y. Lo, M. Y. Chern, and W. C. Lin, *J. Appl. Phys.* 111, 123918 (2012).

115. H. Hoffmann IEEE Trans. Magn. 4, 32–38 (1968).
116. N. Chowdhury, S. Mallick, S. Mallik and S. Bedanta Thin Solid Film, (under Review).
117. S. S. P. Parkin, N. More, and K. P. Roche, Phys. Rev. Lett. 64, 19 (1990).
118. S. S. P. Parkin, Phys. Rev. Lett. 67, 25 (1991).
119. P. Bruno and C. Chappert, Phys. Rev. Lett. 67, 12, 1602 (1991).
120. P. Bruno and C. Chappert, Phys. Rev. Lett. 67, 2592(E) (1991).
121. P. Bruno and C. Chappert, Phys. Rev. B 46, 1, 261 (1992).
122. P. Bruno, Phys. Rev. B 49, 18, 13231 (1994).
123. R. P. Erickson, K. B. Hathaway, and J. R. Cullen, Phys. Rev. B 47, 5, 2626 (1993).
124. P. Bruno, Phys. Rev. B 52, 1, 411 (1995).
125. S. O. Demokritov, J. Phys. D: Appl. Phys 31, 925 (1998).
126. G. J. Strijkers, J. T. Kohlhepp, H. J. M. Swagten, and W. J. M. De Jonge, Phys. Rev. Lett. 84, 8, 1812 (2000).
127. S. Toscano, B. Briner, H. Hopster, and M. Landolt, J. Magn. Magn. Mater 114, L6-L10 (1992).
128. A. Brambilla, P. Sessi, M. Cantoni, M. Finazzi, N. Rougemaille, R. Belkhou, P. Vavassori, L. Duò, and F. Ciccacci, Phys. Rev. B 79, 172401 (2009).
129. P. Biagioni, A. Brambilla, M. Portalupi, N. Rougemaille, A.K. Schmid, A. Lanzara, P. Vavassori, M. Zani, M. Finazzi, L. Duo`, F. Ciccacci, J. Magn. Magn. Mater, 290–291, 153–156 (2005).
130. H. Xi and R. M. White, Phys. Rev. B 62, 6, 3933 (2000).
131. M. Björck and G. Andersson, J. Appl. Cryst. 40, 1174–1178 (2007).

132. J. Faure-Vincent, C. Tiusan, C. Bellouard, E. Popova, M. Hehn, F. Montaigne, and A. Schuhl, *Phys. Rev. Lett.* 89, 10 (2002).
133. C. L. Platt, M. R. McCartney, F. T. Parker and A. E. Berkowitz, *Phys. Rev. B* 61, 14 (2000).
134. M. Labrune and H. Niedoba, *Eur. Phys. J. B* 27, 103-109 (2002).
135. <http://genx.sourceforge.net>
136. L. G. Parratt, *Phys. Rev.* 95, 2, 359 (1954).
137. A. Aharoni, *Introduction to the Theory of Ferromagnetism* Clarendon, Oxford, (1996).
138. M. N. Baibich, J. M. Broto, A. Fert, F. Nguyen Van Dau, F. Petroff, P. Etienne, G. Creuzet, A. Friederich, and J. Chazelas, *Phys. Rev. Lett.* 61, 2472 (1988);
139. G. Binasch, P. Grünberg, F. Saurenbach, and W. Zinn, *Phys. Rev. B* 39, 7, R4828 (1989).
140. D. A. Allwood, G. Xiong, C. C. Faulkner, D. Atkinson, D. Petit, and R. P. Cowburn, *Science* 309, 1688 (2005).
141. D. A. Allwood, G. Xiong, M. D. Cooke, C. C. Faulkner, D. Atkinson, N. Vernier, and R. P. Cowburn, *Science* 296, 2003 (2002).
142. S. S. P. Parkin, M. Hayashi, and L. Thomas, *Science* 320, 190 (2008).
143. M. Hayashi, L. Thomas, R. Moriya, C. Rettner, and S. S. P. Parkin, *Science* 320, 209 (2008).
144. R. Alben, J. J. Becker, and M. C. Chi, *J. Appl. Phys.* 49, 1653 (1978).
145. M. Hehn, D. Lacour, F. Montaigne, J. Briones, R. Belkhou, S. El Moussaoui, F. Maccherozzi, and N. Rougemaille, *Appl. Phys. Lett.* 92, 072501 (2008).
146. H. Boeve, L. Esparbe, G. Gieres, L. Bär, J. Wecker, and H. Brückl, *J. Appl. Phys.* 91, 7962 (2002).

147. C. B. Muratov, and V. V. Osipov, *J. Appl. Phys.* 104, 053908 (2008).
148. H. S. Cho, C. Hou, M. Sun, and H. Fujiwara, *J. Appl. Phys.* 85, 8 (1999).
149. R. H. Wade, *Phil. Mag.* 103, 49-66 (1964).
150. M. S. Cohen, *J. Appl. Phys.* 34, 4, 1221 (1963).
151. A. L. G. Oyarce, T. Trypiniotis, P. E. Roy, and C. H. W. Barnes, *Phys. Rev. B* 87, 174408 (2013).
152. Y. Jang, S. R. Bowden, M. Mascaro, J. Unguris, and C. A. Ross, *APL* 100, 062407 (2012).
153. M. J. Liedke K. Potzger, A. H. Bothmer, J. Fassbender, B. Hillebrands, M. Rickart, and P. P. Freitas, *J. Appl. Phys.* 100, 043918 (2006).
154. M. Diegel, R. Mattheis, Member, IEEE, and E. Halder, *IEEE Trans. Magn.* 40, 4 (2004).
155. S. Bedanta, Ph. D. thesis, Universität Duisburg-Essen (2006).
156. S Bedanta and W. Kleemann, *J. Phys. D: Appl. Phys.* 42, 013001 (2009).
157. L. Néel, *Ann. Geophys. (C.N.R.S.)* 5, 99 (1949).
158. W. F. Brown, Jr., *Phys. Rev.* 130, 1677 (1963).
159. J. L. Dormann, R. Cherkaoui, L. Spinu, M. Nogués, F. Lucari, F. D’Orazio, D. Fiorani, A. Garcia, E. Tronc, and J. P. Jolivet, *J. Magn. Mater.* 187, L139 (1998).
160. W. Kleemann, O. Petravic, C. Binek, G. N. Kakazei, Y. G. Pogorelov, J. B. Sousa, S. Cardoso, and P. P. Freitas, *Phys. Rev. B* 63, 134423 (2001).
161. X. Chen, O. Sichelshmidt, W. Kleemann, O. Petravic, C. Binek, J. B. Sousa, S. Cardoso, and P. P. Freitas, *Phys. Rev. Lett.* 89, 137023 (2002).
162. S. Nakamae, Y. Tahri, C. Thibierge, D. L’Hôte, E. Vincent, V. Dupuis, E. Dubois, and R. Perzynski, *J. Appl. Phys.* 105, 07E318 (2009).

163. O. Petravic, X. Chen, S. Bedanta, W. Kleemann, S. Sahoo, S. Cardoso, and P. P. Freitas, *J. Magn. Magn. Mater.* 300, 192 (2006).
164. S. Sun, C. B. Murray, D. Weller, L. Folks, and A. Moser, *Science* 287, 1989 (2000).
165. X. Chen S. Bedanta, O. Petravic, W. Kleemann, S. Sahoo, S. Cardoso, and P. P. Freitas, *Phys. Rev. B* 72, 214436 (2005).
166. S. Sahoo, O. Petravic, W. Kleemann, S. Stappert, G. Dumpich, P. Nordblad, S. Cardoso, and P. P. Freitas, *Appl. Phys. Lett.* 82, 4116 (2003).
167. S. Sankar, D. Dender, J.A. Borchers, David J. Smith, R.W. Erwin, S.R. Kline, A.E. Berkowitz, *J. Magn. Magn. Mater.* 221, 1 (2000).
168. S. Bedanta, J. Rhensius, W. Kleemann, P. Parashar, S. Cardoso, and P. P. Freitas, *J. Appl. Phys.* 105, 07C306 (2009).
169. S. Bedanta, O. Petravic, E. Kentzinger, W. Kleemann, U. Rücker, A. Paul, Th. Brückel, S. Cardoso, and P. P. Freitas, *Phys. Rev. B* 72, 024419 (2005).
170. X. Chen, W. Kleemann, O. Petravic, O. Sichelshmidt, S. Cardoso, and P. P. Freitas, *Phys. Rev. B* 68, 054433 (2003).
171. K. Yamamoto, S. A. Majetich, M. R. McCartney, M. Sachan, S. Yamamuro, and T. Hirayama, *Appl. Phys. Lett.* 93, 082502 (2008).
172. L. J. Heyderman, H. H. Solak, C. David, D. Atkinson, R. P. Cowburn, and F. Nolting, *Appl. Phys. Lett.* 85, 4989 (2004).
173. M. Varón, M. Beleggia, T. Kasama, R. J. Harrison, R. E. Dunin-Borkowski, V. F. Puentes, and C. Frandsen, *Sci. Rep.* 3, 1234 (2013).
174. E. Y. Vedmedenko, N. Mikuszeit, H. P. Oepen, and R. Wiesendanger, *Phys. Rev. Lett.* 95, 207202 (2005).

175. N. Chowdhury, S. Bedanta, S. Sing, and W. Kleemann, *J. Appl. Phys.* 117, 153907 (2015).
176. J. F. Smyth, S. Schultz, D. R. Fredkin, D. P. Kern, S. A. Rishton, H. Schmid, M. Cali, and T. R. Koehler, *J. Appl. Phys.* 69, 5262 (1991).